Downloaded from orbit.dtu.dk on: Nov 02, 2026



DTU Library

Direct Catalytic Synthesis of Olefins and Aromatics by CO_2 Hydrogenation

Nikolajsen, Michael Thorstein

Publication date:
2023

Document Version
Publisher's PDF, also known as Version of record

Link back to DTU Orbit

Citation (APA):
Nikolajsen, M. T. (2023). *Direct Catalytic Synthesis of Olefins and Aromatics by CO_2 Hydrogenation*. Technical University of Denmark.

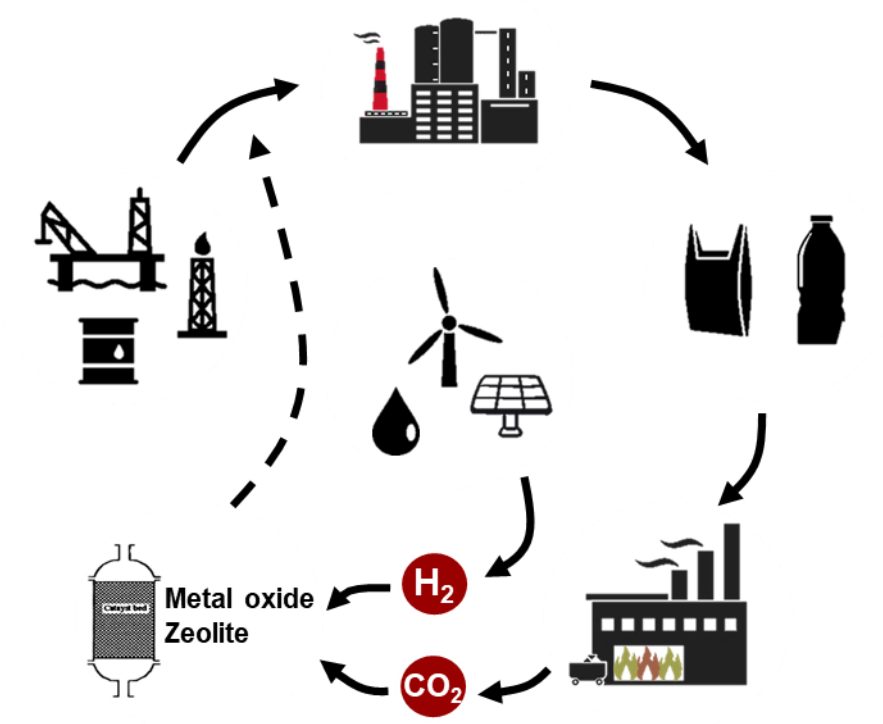
General rights
Copyright and moral rights for the publications made accessible in the public portal are retained by the authors and/or other copyright owners and it is a condition of accessing publications that users recognise and abide by the legal requirements associated with these rights.

- Users may download and print one copy of any publication from the public portal for the purpose of private study or research.
- You may not further distribute the material or use it for any profit-making activity or commercial gain
- You may freely distribute the URL identifying the publication in the public portal

If you believe that this document breaches copyright please contact us providing details, and we will remove access to the work immediately and investigate your claim.

Direct Catalytic Synthesis of Olefins and Aromatics by CO_2 Hydrogenation

Ph.D. Thesis written by Michael Thorstein Nikolajsen



Technical University of Denmark
Department of Chemical and Biochemical Engineering
CHEC research center 30. September 2023

DTU Chemical Engineering
Department of Chemical and Biochemical Engineering

DANMARKS FRIE FORSKNINGSFOND
INDEPENDENT RESEARCH FUND DENMARK

KIT Karlsruhe Institute of Technology
TOPSOE

DTU

Preface

This thesis is the outcome of the project carried out by Michael Thorstein Nikolajsen in the research group of **C**ombustions and **H**armful **E**mission **C**ontrol (CHEC) at the department of Chemical and Biochemical Engineering at the Technical University of Denmark (DTU). The Independent Research Fund Denmark funded the project (Grant no. 0136-00073B). The project was initiated 1. October 2020 and ended with the thesis submission the 30. September 2023 (3 years). Associate Professor Martin Høj from DTU has been the main supervisor for the work and Associate Professor Jakob Munkholt Christensen, also from DTU, has been co-supervisor. The project was conducted in close collaboration with Topsoe A/S (former known as Haldor Topsøe A/S) and Senior Principal Scientist Niels Christian Schjødt from Topsoe A/S has been co-supervisor. Uffe Vie Mentzel, Rasmus Yding Brogaard and Jens Sehested from Topsoe A/S have provided great guidance and have followed the project throughout all 3 years. I am grateful that I had the pleasure of getting to know and work with you. All of you have provided great enthusiasm, guidance, and support throughout the project period. Your great availability, friendliness, and idea sharing have provided me with great insight, constructive criticism, and knowledge that have evolved and encouraged me.

Topsoe A/S has provided an experimental high pressure flow setup and catalysts characterization techniques. The people responsible for these characterization techniques are greatly acknowledged, especially Lars Pilsgaard Hansen whom I spent two days with analyzing catalysts with the transmission electron microscope. I want to highlight the help provided by Said Rokni whose great knowledge of the high-pressure flow setup and fast problem solving allowed the setup to run continuously throughout the period. I will also acknowledge Mikkel Lerche Thordsen, Jeremy Burn and Dennis Roland Hansen who helped me constructing the GC method and calibrating the Dragon Software, which allowed accurate prediction of $C_{1\text{-}15}$ hydrocarbons.

The Karlsruhe Institute of Technology has provided me with the opportunity of an external visit where DRIFTS and XAS analysis could be conducted. Here I will especially acknowledge the friendliness and helpfulness in the group of Professor Jan-Dierk Grunwaldt. Great hospitality and guidance were provided by Jan-Dierk himself, Lorena Baumgarten, Abhijeet Gaur, and Dmitry Doronkin. I thank you for a constructive and pleasant visit.

I will also thank my present and former colleagues in the CHEC group for creating a nice working environment but also great scientific discussions. A special thanks is addressed to Jean-Claude Grivel

from the Department of Energy Conversion and Storage at DTU, who agreed to help me with conducting X-ray photoelectron spectroscopy.

At last, a big thank must go to my fiancée Caroline Holmegaard Dengsøe for her support, critical questions, and constructive feedback on my scientific work and grammar.



Michael Thorstein Nikolajsen

Abstract

The direct conversion of CO_2 into hydrocarbons in a process that combines the methanol synthesis and the methanol-to-hydrocarbon process in one reactor could facilitate efficient and sustainable production of valuable products, such as light olefins and aromatics. These hydrocarbons are primarily derived from oil refineries and are extensively used in the production of plastic materials and other important products. Capturing CO_2 produced from plastic waste incineration plants and converting it into new plastic monomers could create a new recycling pathway for plastic materials. This technology must, though, be sufficient to compete with the current production of plastic monomers from fossil resources.

In this work, Zn-based mixed oxides, such as ZnO/t-ZrO_2, $ZnAl_2O_4$, and $ZnGa_2O_4$, were found to be highly active for methanol synthesis at temperatures where the subsequent methanol-to-hydrocarbon process was active. Through catalyst characterization with BET, ICP, XRD, XPS, XAS, and TEM, it was identified that the primary active site was amorphous ZnO supported on the surface of the oxides. Modulation excitation spectroscopy, coupled with time-resolved QEXAFS for the ZnO/t-ZrO_2 catalyst, showed that these ZnO sites were capable of reversible, partial reduction under methanol synthesis conditions, forming ZnO_x, where x was approximately 0.98. XPS analysis revealed that an interaction between ZnO and ZrO_2 withdrew electrons from the Zn-O bond and likely induced the reducibility of the surface ZnO phase. The formation of methanol over the Zn-based mixed oxides was identified by in-situ DRIFTS to occur through a formate pathway, and the hydrogenation of the formate specie was the rate-determining step.

When combining the Zn-based mixed oxides with solid acids, such as the SAPO-34 or the ZSM-5, the direct production of light olefins or aromatics from CO_2 was possible. The local dehydration of the methanol with the catalyst bed ensured that the CO_2 hydrogenation equilibrium was exceeded, showing a higher conversion of CO_2 than expected from equilibrium calculations at the applied reactor conditions. High temperatures, pressures, and hydrogen partial pressures induced the hydrogenation activity for the bi-functional catalyst, increasing the hydrogen incorporation in the hydrocarbon product. The hydrogenation activity of the ZnO/t-ZrO_2+ZSM-5 was concluded to occur over the Brønsted acid sites, as the increase in the Si/Al ratio induced the hydrogen incorporation. The highest aromatic selectivity for the ZnO/t-ZrO_2+ZSM-5 catalyst was obtained at low temperature and pressure to minimize the hydrogenation. However, at these conditions a low hydrocarbon yield was obtained. This demonstrates a trade-off in the activity and the aromatic selectivity for the ZnO/t-

ZrO_2+ZSM-5 catalyst. A similar trade-off was observed for the light olefin production over the ZnO/t-ZrO_2+SAPO-34 and $ZnAl_2O_4$+SAPO-34 catalysts, showing that the current limitation for the bi-functional catalysts is the gap between activity and selectivity. Changing the CO_2/H_2 feed ratio showed improved hydrocarbon yield for the ZnO/t-ZrO_2 +SAPO-34 catalyst but at the expense of a slightly more hydrogenated product. It is believed that this strategy is only applicable at low operating pressure as the increase in pressure showed a great increase in hydrogenation activity. The hydrogenation activity is supposed to be induced at higher hydrogen partial pressure as well. Another strategy for improving the hydrocarbon yield without affecting the olefin selectivity was to co-feed CO over the $ZnAl_2O_4$+SAPO-34 catalyst. Higher CO concentration in the feed changed the thermodynamic driving force for the reverse-water-gas-shift reaction, reducing the production of water from this reaction. The lower water content improved the CO_2 hydrogenation activity significantly and improved the hydrocarbon yield of light olefins. The $ZnAl_2O_4$ or ZnO/t-ZrO_2 and SAPO-34 combination yielded a stable production of olefins that outperformed the stability of the methanol-to-olefin reaction. Deactivation of the bi-functional catalysts was observed when the CO_2 conversion to hydrocarbon and the hydrocarbon distribution changed with time on stream. Analysis of a spent bi-functional catalyst by XRD and TEM identified three deactivation phenomena: sintering of the surface ZnO specie, Zn migration into the SAPO-34 crystals, and formation of carbon deposits. It was not possible to decouple these deactivation phenomena effects on the bi-functional catalyst stability. Oxidative regeneration of the bi-functional catalysts resulted in sintering and creation of crystalline ZnO identified by TEM and in-situ XAS. Removal of the highly active ZnO surface domains resulted in a less active metal oxide component for the methanol synthesis reaction.

Kinetic modelling of the ZnO/t-ZrO_2+ZSM-5 catalyst showed that the water produced limited the methanol synthesis activity, even at very low residual concentrations of methanol. Higher water content at longer residence times will inhibit the CO_2 hydrogenation reaction by thermodynamics, causing the not linear increase in the CO_2 conversion as a function of residence time observed experimentally. It was found that to optimize the aromatic formation rate, the process should be operated far from equilibrium, which limits the CO_2 conversion.

Resumé

Den direkte omdannelse af CO_2 til kulbrinter i en proces, der kombinerer methanolsyntese og methanol-til-kulbrinteprocessen i en reaktor, kunne muliggøre en effektiv og bæredygtig produktion af værdifulde produkter, såsom lette olefiner og aromatiske forbindelser. Disse kulbrinter stammer i dag primært fra olieraffinaderier og anvendes i vid udstrækning i produktionen af plastmaterialer og andre vigtige materialer. Udnyttelse af CO_2 produceret fra forbrænding af plastaffald til produktion af nye plastmonomerer kunne skabe en ny genanvendelsesvej for plastmaterialer. Denne teknologi skal dog være konkurrencedygtig sammenlignet med den nuværende produktion af plastmonomerer fra fossile ressourcer.

I arbejdet beskrevet i denne rapport blev det fundet, at Zn-baserede blandingsoxider som ZnO/t-ZrO_2, $ZnAl_2O_4$ og $ZnGa_2O_4$ er meget aktive for methanolsyntese ved temperaturer, hvor den efterfølgende methanol-to-hydrocarbon proces også er aktiv. Gennem katalysatorkarakterisering med BET, ICP, XRD, XPS, XAS og TEM blev det identificeret, at det primære aktive site var amorft ZnO på overfladen af oxiderne. Modulation excitation spectroscopy, koblet med tidsopløst QEXAFS for ZnO/t-ZrO_2 katalysatoren, viste, at disse overflade ZnO specier er i stand til reversibel, delvis reduktion under betingelser for methanolsyntesen. Dette dannede ZnO_x, hvor x var cirka 0,98. XPS-analyse afslørede, at der var en interaktion mellem ZnO og ZrO_2, som trak elektroner fra Zn-O-bindingen og sandsynligvis øgede reduktionsevnen af overflade ZnO-fasen. Ved in-situ DRIFTS blev det identificeret, at dannelsen af methanol over de Zn-baserede blandingsoxider forekommer gennem overfladebundet formiat, hvor hydrogenering af formiat var det hastighedsbestemmende trin.

Det er muligt at omdanne CO_2 direkte til lette olefiner eller aromater, når Zn-baserede blandingsoxider blev kombineret med SAPO-34 eller ZSM-5. Den lokale dehydrering af methanol i katalysatorlaget sikrede, at CO_2-hydrogeneringsligevægten blev overskredet, hvilket resulterede i en højere omdannelse af CO_2 end ellers forventet ud fra ligevægtsberegninger ved de anvendte reaktorbetingelser. Høje temperaturer, tryk og brint partialtryk øgede hydrogeneringssaktiviteten for den bi-funktionelle katalysator og øgede hydrogenindholdet i kulbrinteproduktet. Det blev konkluderet, at hydrogeneringsaktiviteten for ZnO/t-ZrO_2+ZSM-5 forekommer over Brønsted syre-sites, da stigningen i Si/Al-forholdet øgede hydrogenindkorporeringen. Den højeste aromatiske selektivitet for ZnO/t-ZrO_2+ZSM-5 katalysatoren blev opnået ved lav temperatur og tryk for at minimere hydrogeneringen. Ved disse betingelser var der dog et lav udbytte af kulbrinte. Disse resultater demonstrerer et kompromis mellem aktivitet og aromatisk selektivitet for ZnO/t-ZrO_2+ZSM-5 katalysatoren. En lignende

afvejning blev observeret for produktionen af lette olefiner over ZnO/t-ZrO_2+SAPO-34 og $ZnAl_2O_4$+SAPO-34-katalysatorerne, hvilket viser, at den nuværende begrænsning for bi-funktionelle katalysatorer er forskellen mellem aktivitet og selektivitet. Ændring af CO_2/H_2 forholdet i indgangsgassen viste et forbedret kulbrinteudbytte for ZnO/t-ZrO_2+SAPO-34 katalysatoren, men på bekostning af et mere mættet kulbrinteprodukt. Denne strategi menes kun at være anvendelig ved lavt driftstryk, da en stigning i trykket viste en stor forøgelse i hydrogeneringsaktiviteten. Hydrogeneringsaktiviteten menes også at blive forøget ved højere brint partialtryk. En anden strategi for at forbedre kulbrinteudbyttet uden at påvirke selektiviteten til lette olefiner var at tilføre CO til fødegassen over $ZnAl_2O_4$+SAPO-34 katalysatoren. Den højere CO-koncentration i føden ændrede den termodynamiske drivkraft for reverse-water-gas-shift reaktionen og reducerede mængden af vand dannet fra denne reaktion. Det lavere vandindhold forbedrede CO_2 hydrogeneringsaktiviteten betydeligt og forbedrede kulbrinteudbyttet af lette olefiner. Kombinationen af $ZnAl_2O_4$ eller ZnO/t-ZrO_2 og SAPO-34 resulterede i en stabil produktion af olefiner, der overgik stabiliteten af methanol-to-olefin reaktionen. Deaktivering af de bi-funktionelle katalysatorer blev observeret, da CO_2 omdannelsen til kulbrinter og fordelingen af kulbrinteprodukter ændrede sig over tid. Analyse af brugte bi-funktionelle katalysatorer ved hjælp af XRD og TEM identificerede tre deaktiveringsfænomener: sammenklumpning af overflade ZnO, Zn migrering ind i SAPO-34 krystallerne og dannelse af kulstofaflejringer. Det var ikke muligt at bestemme og adskille de præcise effekter hvert enkelt deaktiveringsfænomen havde af indflydelse på stabiliteten af de bi-funktionelle katalysatorer. Oxidativ regenerering af de bi-funktionelle katalysatorer resulterede i sammenklumpning og dannelse af krystallinsk ZnO, som blev identificeret ved hjælp af TEM og in-situ XAS. Fjernelsen af de meget aktive ZnO overfladedomæner resulterede i en mindre aktiv metaloxid komponent for methanolsyntesereaktionen.

Kinetisk modellering af ZnO/t-ZrO_2+ZSM-5 katalysatoren viste, at det vand, som blev produceret, begrænsede methanolsynteseaktiviteten, selv ved meget lave restkoncentrationer af methanol. Højere vandindhold ved længere opholdstider hæmmer CO_2-hydrogeneringsreaktionen på grund af termodynamikken og forårsager den krumme kurve for CO_2-omdannelse som en funktion af opholdstiden, som blev observeret eksperimentelt. Det blev fundet, at for at optimere dannelseshastigheden af aromater skal processen køres langt fra ligevægt, hvilket vil begrænser CO_2-omdannelsen.

Publications and Conference Contributions

Submitted articles in peer-reviewed journals:

M. T. Nikolajsen, J.-C. Grivel, A. Gaur, L.P. Hansen, L. Baumgarten, N.C. Schjødt, U. V Mentzel, J.-D. Grundwaldt, J. Sehested, J.M. Christensen, M. Høj, Surface ZnO_x on Zirconia is Highly Active for High Temperature Methanol Synthesis, Journal of Catalysis, submitted september 2023

Articles in preparation for peer-reviewed journals:

M. T. Nikolajsen, E. S. Kold, A. B. Møller, N.C. Schjødt, U. V Mentzel, J. Sehested, R. Y. Brogaard, J.M. Christensen, M. Høj, Direct CO_2 Hydrogenation to Aromatics over Combined Catalysts Composed of Supported ZnO with Different Zeolite Topologies

M. T. Nikolajsen, K. Jordahn, L. D. Nilsson, N. C. Schjødt, U. V. Mentzel, J. Sehested, R. Y. Brogaard, J. M. Christensen and M. Høj, ZnO supported on Zinc Spinel Structures Enables the Direct Conversion of CO2 to Olefins when Combined with Acidic CHA Catalysts

M. T. Nikolajsen, N.C. Schjødt, U. V Mentzel, J. Sehested, R. Y. Brogaard, J.M. Christensen, M. Høj, Deactivation Phenomena for Bi-functional Catalysts Composed of ZnO/ZrO_2 and CHA Topology Solid Acid

Conference contributions:

The 27th North American Catalysis Society Meeting, 2022, New York, United States. Poster presentation: **M. T. Nikolajsen**, N.C. Schjødt, U. V Mentzel, J. Sehested, J.M. Christensen, M. Høj, Zinc Based High Temperature Methanol Synthesis Catalysts Enabling Direct Synthesis of Olefins and Aromatics from CO_2

19th Nordic Symposium on Catalysis, 2022, Espoo, Finland. Poster presentation: **M. T. Nikolajsen**, N.C. Schjødt, U. V Mentzel, J. Sehested, J.M. Christensen, M. Høj, Zinc Based High Temperature Methanol Synthesis Catalysts Enabling Direct Synthesis of Olefins and Aromatics from CO_2

The 28th North American Catalysis Society Meeting, 2023, Providence, United States. Oral presentation: **M. T. Nikolajsen**, N.C. Schjødt, U. V Mentzel, J. Sehested, J.M. Christensen, M. Høj, A Critical View on Direct Syngas to Aromatics over Combined Zinc Oxide on Zirconia and H-ZSM-5 Catalysts

15th European Congress on Catalysis, 2023, Prague, Czech Republic. Oral presentation: **M. T. Nikolajsen**, N.C. Schjødt, U. V Mentzel, J. Sehested, J.M. Christensen, M. Høj, A Critical View on Direct Syngas To Aromatics over Combined Zinc Oxide on Zirconia and H-ZSM-5 Catalysts

Other publications:

M. T. Nikolajsen, N.C. Schjødt, U. V Mentzel, J.M. Christensen, M. Høj, Grønnere plastikproduktion, Dansk Kemi, 103 (2022) 20-22.

Nomenclature

Abbreviations		Unit
ASF	Anderson-Schulz-Flory	
ATE	Approach To Equilibrium	
BET	Brunauer-Emmett-Teller	
DME	Dimethyl ether	
DRIFTS	Diffuse Reflactance Infrared Fourier Transform Spectroscopy	
EXAFS	Extended X-ray Absorption Fine Structure	
FID	Flame Ionization Detector	
FT	Fischer-Tropsch	
FTIR	Fourier Transform Infrared	
GC	Gas Chromatography	
GHSV	Gas Hourly Space Velocity	mL/g/h
HAADF	High-Angle Annular Dark Field	
HRTEM	High-Resolution Transmission Electron Microscopy	
ICP	Inductively Coupled Plasma	
MTA	Methanol to Aromatics	
MTH	Methanol to Hydrocarbons	
MTO	Methanol to Olefins	
RWGS	Reverse Water Gas Shift	
STEM	Scanning Transmission Electron Microscopy	
TCD	Thermal Conductivity Detector	
TOF	Turnover Frequency	
TPD	Temperature Programmed Desorption	
TPR	Temperature Programmed Reaction	
WHSV	Weight Hourly Space Velocity	g/g/h
XANES	X-ray Absorption Near Edge Structure	
XAS	X-ray Absorption Spectroscopy	
XPS	X-ray Photo-electron Spectroscopy	
XRD	X-ray Diffraction	
XRF	X-ray Fluorescence	

Content

1 Introduction 1

2 Literature Review 4

2.1 Methanol Synthesis 4

2.1.1 Reaction scheme 4

2.1.2 Reaction mechanism 5

2.1.3 Metallic methanol synthesis catalyst in bi-functional catalytic systems 9

2.1.4 Alternative catalyst for high temperature methanol synthesis 20

2.2 The Methanol to Hydrocarbons Process 35

2.2.1 Zeolite materials and the acid sites 37

2.2.2 The hydrocarbon pool dual cycle reaction mechanism 43

2.2.3 Introduction to the shape-selective nature of zeolite materials 45

2.2.4 Catalysts deactivation 49

2.3 Direct Conversion of Synthesis Gas to Hydrocarbons 56

2.3.1 Fischer-Tropsch 57

2.3.2 Bi-functional catalytic conversion of synthesis gas to light olefins 61

2.3.3 Acidity effect on the light olefin selectivity 66

2.3.4 Bi-functional catalytic conversion of synthesis gas to aromatics 69

2.3.5 Acidity effect on the aromatic selectivity 73

2.3.6 Feed gas composition effects on the bi-functional catalyst activity and selectivity 76

2.3.7 The stability of bi-functional catalysts 79

2.3.8 Catalyst bed configurations for the bi-functional catalyst 82

2.4 References 84

3 Surface ZnO_x on Zirconia is Highly Active for High Temperature Methanol Synthesis 102

4 Direct CO_2 Hydrogenation to Aromatics over Combined Catalysts Composed of Supported ZnO with Different Zeolite Topologies 135

5 ZnO supported on Zinc Spinel Structures Enables the Direct Conversion of CO_2 to Olefins when Combined with Acidic CHA Catalysts 163

6 Deactivation Phenomena for Bi-functional Catalysts Composed of ZnO/ZrO_2 and CHA Topology Solid Acid 193

7 Conclusions 212

8 Future work 216

9 Appendix I

9.1 Supporting information: Surface ZnO_x on Zirconia is Highly Active for High Temperature Methanol Synthesis I

9.2 Supporting information: Direct CO_2 Hydrogenation to Aromatics over Combined Catalysts Composed of Supported ZnO with Different Zeolite Topologies XV

9.3 Supporting information: ZnO supported on Zinc Spinel Structures Enables the Direct Conversion of CO2 to Olefins when Combined with Acidic CHA Catalysts XXIV

9.4 Supporting information: Deactivation Phenomena for Bi-functional Catalysts Composed of ZnO/ZrO2 and CHA Topology Solid Acid XXXIII

1 Introduction

In 2017 it was estimated that 6300 million tons of plastic waste were generated in the period from 1950 to 2015 worldwide. 12 % of the waste have been incinerated to avoid it being disposed on landfills [1]. By incineration of the plastic product, a fraction of the energy that went into producing the plastic can be recovered as heat. However, a higher level of value recovery could be obtained with direct recycling of the plastic by melting it into new products [2]. Only a fraction of the consumer sorted plastic is possible to recycle directly. The remaining plastic could be chemically recycled by depolymerization, purification and re-polymerization or pyrolysis to a liquid resembling crude oil. The struggle of sorting plastic for direct recycling and the energy costs associated with chemical recycling have resulted in that only 9 % of the plastic waste in the period from 1950 to 2015 have been recycled [1,3]. However, both the recycle and the incineration percentage have increased in recent years to deal with the problems associated with landfills disposal of the annual exponential rising amount of generated plastic waste.

The main monomers (or monomer precursors) in plastic manufacturing are light olefins (ethene, propene, and butene) and aromatic molecules (benzene, toluene, and xylene). Since these chemicals are mainly produced from crude oil, there is an increasing demand for reducing the dependency on finite oil resources for producing plastic monomers [3]. Additionally, to make the consumption of plastic products more sustainable, an increase in recycling and a reduction in greenhouse gas emissions are crucial. Capturing CO_2 from the plastic incineration and convert it back into plastic monomers (or monomer precursors) such as light olefins and aromatics can theoretically close this loop. The annual production of polypropylene plastic was in 2019 ~73 million tons, which shows that around 230 million tons of CO_2 could be stored in this product alone. This shows a great potential for CO_2 utilization and storage for the plastic manufacturing industry.

CO_2 can be converted to synthesis gas in the reverse water gas shift reaction when combined with H_2, as stated in eqn. (1) [4]. The required hydrogen can be obtained from water electrolysis potentially driven by excess renewable energy [5].

$$CO_2 + H_2 \rightleftharpoons CO + H_2O \quad (1)$$

Synthesis gas can then directly be converted to hydrocarbons in the Fisher-Tropsch process, typically using promoted Co or Fe based catalysts at 150 ℃ to 350 ℃ and a pressure near 1 atm and up to 100

atm [6,7]. In general, the product formation is accepted to be caused by surface polymerization reactions, which tend to follow the Anderson-Schulz-Flory distribution (ASF). The product selectivity can be tuned by changing reactor conditions, the type of catalyst, and promoters, but the theoretical maximum yield of C_2 and C_4 hydrocarbons is ~60 % according to the ASF [7–9]. Recent studies have indicated a C_2-C_4 olefin selectivity up to ~60% on a CO_2 free basis [7,10,11].

An alternative to the Fisher-Tropsch process is the indirect method where the synthesis gas is first converted to methanol via methanol synthesis and then to hydrocarbons over an acidic zeolite catalyst in the so-called methanol-to-hydrocarbons (MTH) process [12,13]. The product distribution of the MTH process is affected by the zeolite topology and operating conditions. In general, the reaction mechanism over zeolites is accepted to follow the hydrocarbon pool dual cycle concept consisting of an aromatic cycle and an alkene cycle [14]. Zeolites with large pores and relative low temperatures favours the aromatic cycle. High temperature and narrow pore zeolites are expected to lead to enhancement of the alkene cycle. At low partial pressure, the necessary coupling of several alkenes in sequence to form aromatic is less noticeable [15]. Further modifications of the zeolite, such as acidity, ion-exchange with metal ions (Ni and Zn), extra-framework metal oxides (Ag_2O, NiO and CuO), and framework substitutions with metal ions (Ni), have showed potential for tuning the product distribution [16–21]. To shift the equilibrium reaction in the methanol synthesis towards methanol, the reaction is operated at moderate temperatures of 200 to 250 ℃ and at pressures of 50 to 100 atm [12]. The MTH process is typically operated at temperatures around 340 to 400 ℃ and at pressures from 1 to 25 atm [13,22,23]. If methanol is immediately consumed in the MTH process, the equilibrium reaction of the methanol synthesis may be driven towards products, even at intermediate temperature and pressure, resulting in compatible conditions for the methanol synthesis and MTH process. This concept has recently been reported by the research groups Bao [24–26], Li [17,27], Wang [28] and Liu [29]. The research groups of Bao, Li and Wang all reported bi-functional catalysts consisting of the zeolite SAPO-34 and the methanol synthesis catalyst of ZnCr- or ZnZr-oxide for the conversion of synthesis gas to light olefins [24,25,27,28]. The groups Li and Liu reported the conversion of synthesis gas to aromatics by using a ZnZr- or ZnAl-oxide catalyst together with the H-ZSM-5 zeolite [17,29]. A combination of a Fischer-Tropsch catalyst Na-Fe_3O_4 and H-ZSM-5 has also demonstrated a potential for synthesis gas conversion to aromatics [30].

This project aims to develop new catalysts and catalyst systems for efficient and selective conversion of CO_2 and H_2 to olefins and aromatics at yields relevant for industrial applications. This means at least 15 % conversion of CO_2 pr. catalyst passed and 80% selectivity towards olefins or aromatics among the hydrocarbon products. Fulfilling these goals are necessary for the process to be competitive to petroleum-based processes in near future. In this project, the CO_2 to hydrocarbon conversion was conducted through bi-functional catalysts composed of a mixture of a methanol synthesis active component with a shape-selective solid acid (zeolite/zeotype) for the methanol dehydration reaction. To achieve a high CO_2 to hydrocarbon conversion, it is important to have an active methanol synthesis component for the production of methanol at elevated temperatures. For this purpose several metal oxides and mixed oxides were synthesized and tested for their methanol synthesis activity. Promising candidates, such as ZnO mixed oxides, were optimized by changing the oxide support and/or the Zn-loading and characterized through ex-situ XRD, XAS, BET, ICP, STEM and in-situ XAS to gain improved knowledge of the catalyst structure-activity relationship. Thus, enabling future rationale and knowledge-based improvements of the catalysts. The metal oxides showing high methanol synthesis activity were combined with solid acids. This was mainly the H-ZSM-5 zeolite and the H-SAPO-34 zeotype for the direct conversion of CO_2 into aromatics and olefins, respectively. The catalyst bed-configuration, mixing ratio of the two components, and the acid site density was investigated to optimize the catalyst performance. The reactor conditions, such as pressure, temperature, feed composition, and space velocity, were tested in order to find the optimal conditions. Additionally, kinetic analysis was conducted to help explaining the observed experimental trends and to optimize the hydrocarbon formation rate by changing the above-mentioned catalyst and reactor conditions. Other shape-selective zeolites with different pore sizes and channel structures were used for tuning the hydrocarbon selectivity. Lastly, Zn modified solid acids produced through impregnation were tested as well. These solid acids were characterized by XRD, XRF, NH_3-TPD, and Zn migration from the metal oxide to the solid acid was investigated by STEM.

2 Literature Review

2.1 Methanol Synthesis

The first part of the process for the bi-functional catalytic system using methanol as intermediate is the conversion of synthesis gas, a mixture of carbon dioxide, carbon monoxide, and hydrogen, to methanol. This process is known as the methanol synthesis, which is a widely commercialized process [12]. To activate the very stable CO_2 molecule with two C=O double bonds, a catalyst must be used to lower the activation energy. The first type of catalyst used in the industry by BASF was a mixed oxide consisting of ZnO and Cr_2O_3. This catalyst was operated at very high pressures of 250-350 bar to achieve acceptable reactivity at temperatures of 300-450 ºC. This was done in order to increase the thermodynamic driving force at these temperatures [31]. Innovation and development of the much more active $Cu/ZnO/Al_2O_3$ catalyst allowed low pressures at around 50-100 bar and production of methanol at temperatures of 200 to 250 ℃. This catalyst required more purified synthesis gas for especially sulphur that otherwise poisoned the catalyst. Even with this drawback, copper-based catalyst are still exclusively used in the industry for methanol synthesis [32].

2.1.1 Reaction scheme

Three reactions occur over copper-based catalyst under methanol synthesis, which are the carbon dioxide hydrogenation, carbon monoxide hydrogenation, and the reverse-water-gas-shift, as stated in Eq. (2) to (4) [32].

$$CO_2 + 3H_2 \rightleftharpoons CH_3OH + H_2O \quad \Delta H_{r,298K,50bar} = -40.9\ \mathrm{kJ/mol} \tag{2}$$

$$CO + 2H_2 \rightleftharpoons CH_3OH \quad \Delta H_{r,298K,50bar} = -90.7\ \mathrm{kJ/mol} \tag{3}$$

$$CO_2 + H_2 \rightleftharpoons CO + H_2O \quad \Delta H_{r,298K,50bar} = 49.8\ \mathrm{kJ/mol} \tag{4}$$

The reaction scheme shows that methanol can be formed by combining hydrogen with carbon dioxide (Eq. (2)) or carbon monoxide (Eq. (3)). The exothermic nature of these reactions and the stoichiometric ratio between the products and reactants show that production of methanol is favoured by high pressure and low temperature (Le Chatelier's principle). The reaction rate is favoured by an increase in temperature and to achieve a sufficient production of methanol, a trade-off between the reaction kinetic and the thermodynamic driving force has to be made [33]. The endothermic nature of the

reverse-water-gas-shift (Eq. (4)) improves the thermodynamic driving force for this reaction with increasing temperature, shifting the reaction towards production of carbon monoxide and water. As water is also a product from the carbon dioxide hydrogenation reaction (Eq. (2)), the formed water for the reverse-water-gas-shift reaction will additionally limit the thermodynamic driving force for this reaction. This limitation does not exist for the carbon monoxide hydrogenation reaction (Eq. (3)). Using catalysts able to actively produce methanol from the carbon monoxide hydrogenation reaction could potentially provide a more efficient production of methanol by by-passing the thermodynamic limitations of the carbon dioxide hydrogenation reaction. Another strategy to circumvent the thermodynamic limitation is to add carbon monoxide to the feed stream and thereby shift the reverse-water-gas-shift reaction towards water and carbon monoxide consumption. However, kinetic inhibition by competing adsorption with carbon monoxide and/or alteration of the active sites, caused by the highly reductive nature of carbon monoxide, could result in a less kinetic active catalyst [34]. For industrial methanol synthesis over the $Cu/ZnO/Al_2O_3$ catalyst, the optimal performance is achieved by feeding a mixture of carbon dioxide, carbon monoxide, and hydrogen.

2.1.2 Reaction mechanism

The proposed reaction pathways for the methanol formation from CO_2 hydrogenation are illustrated in Fig. 1. It has been proposed that the CO_2 hydrogenation can occur through a direct hydrogenation route (the formate pathway) or an indirect route where CO_2 is first converted into CO by reverse-water-gas-shift followed by CO hydrogenation steps [35,36].

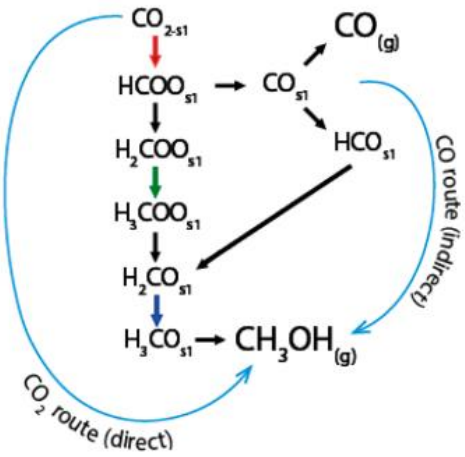
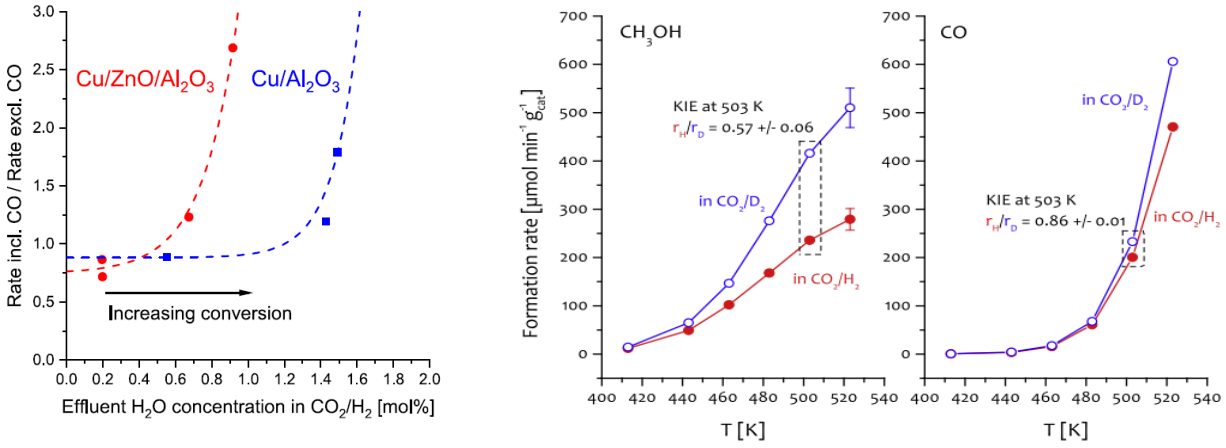


Fig. 1. Schematic of the direct CO_2 route to methanol through the formate pathway or the indirect route with formation of CO followed by CO hydrogenation reactions. Figure obtained from [35].

Several authors have identified the formation of surface formate from carbon dioxide and hydrogen and surface methoxy species from formate and hydrogen by using infrared spectroscopy techniques

[37–40]. This suggests that the reaction stated in eq. (2) occurs through a formate pathway, where adsorbed CO_2 hydrogenates into formate and further into methoxy surface species that desorb as methanol. This is illustrated as the direct route in Fig. 1. Kinetic studies on the role of CO and CO_2 in Cu catalysed methanol synthesis confirmed that the primary carbon source for methanol formation is CO_2, with the exception of Cu supported on MgO [34,41]. The results concluded that on $Cu/ZnO/Al_2O_3$ or Cu/Al_2O_3 catalysts, CO will inhibit the methanol synthesis, most likely due to competitive adsorption or less likely by removing oxygen from the catalyst surface at low conversion conditions. Interestingly, when conversion increases the formation of water (strong inhibitor), the methanol formation rate will reduce and by co-feeding CO (milder inhibitor), the reverse-water-gas-shift reaction will shift and water will be removed. Thus, CO has a beneficial role in removing a stronger inhibiting species and thereby increase the methanol formation rate at higher conversions conditions, as illustrated in Fig. 2 (a).



(a) (b)

Fig. 2. (a) The ratio between the methanol formation rate in $CO_2/CO/H_2$ and $CO_2/N_2/H_2$ as a function of the estimated effluent water concentration in the $CO_2/N_2/H_2$ atmosphere for Cu/Al2O3 and $Cu/ZnO/Al_2O_3$. Reaction conditions: 523 K, 50 bar, $(2.4\text{-}14.5)\cdot10^5$ and $(1.4\text{-}9.4)\cdot10^4$ for the $Cu/ZnO/Al_2O_3$ and Cu/Al_2O_3, respectively. (b) Formation rate of methanol (left) and CO (right) on a $Cu/ZnO/Al_2O_3$ catalyst as a function of temperature in CO_2/H_2 (red circles) and CO_2/D_2 (blue circles). Reaction conditions: 200 mg catalyst, 30 bar and 100 ml/min. Figures were obtained from [34] *and* [42]*, respectively.*

Stronger inverse kinetic isotope effect of hydrogen/deuterium substitution for the CO_2 hydrogenation into methanol than for the CO formation was observed from hydrogen/deuterium exchange experiments over a $Cu/ZnO/Al_2O_3$ catalyst [42], as illustrated in Fig. 2 (b). This suggest that the two reactions do not share a common intermediate, which questions that the reverse-water-gas-shift reaction occurs through a common intermediate as proposed by [43]. Furthermore, CO hydrogenation did not show a strong kinetic isotope effect, suggesting that methanol formation from CO_2 does not proceed

through consecutive reverse-water-gas-shift and CO hydrogenation steps [42]. In-situ infrared spectroscopy and kinetic analysis have demonstrated that the methanol synthesis primary occurs via the CO_2 and hydrogen through a formate pathway (Eq. (2)).

For the water-gas-shift reaction, two reaction mechanisms have been proposed, which are the surface redox mechanism [44,45] and the associative mechanism [46,47]. The associative mechanism describes the formation of an intermediate CH_xO_y species, such as carboxyl (COOH) [46,48,49] or formate (HCOO) [47,50], from adsorbed carbon monoxide and water that decomposes into carbon dioxide and hydrogen. The decomposition of surface formate seems unlikely if the carbon dioxide hydrogenation into methanol proceeds through the formate pathway and the formation of carbon monoxide from the reverse-water-gas-shift reaction does not share a common intermediate [43]. However, the formation of spectator formate species formed by hydrogenation of the formed carbon dioxide could explain the visible formation and accumulation of surface formate under in-situ diffuse reflectance infrared Fourier transform spectroscopy (DRIFTS) analysis [50]. Thus, leading to a false conclusion of formate being an important intermediate for the reaction. Even though the carboxyl and bidentate formate are isomers, Gokhale et al. [46] suggested that carboxyl intermediates could be formed by a single elementary reaction step that is not possible with formate formation. The hydroxyl binds to the surface through its oxygen atom and carbon monoxide through its C atom. The formate binds through its two oxygen atoms and not its carbon atom, suggesting that formate is formed by reaction of carbon dioxide with atomic hydrogen [46]. Thus, the carboxyl intermediate pathway could be the mechanism decoupled for the formate pathway, which allows the water-gas-shift reaction to occur through an associative mechanism without sharing important carbon dioxide hydrogenation intermediates. An alternative to the associative mechanism is the surface redox mechanism (also known as the regenerative mechanism), that proceeds via alternating reduction and oxidation of the catalyst surface [51]. This mechanism is generally accepted from iron-based catalyst, as redox coupled Fe^{2+}/Fe^{3+} can accommodate the dissociative adsorption of water by oxidising Fe^{2+} to Fe^{3+} [51]. The atomic oxygen can then oxidise the adsorbed carbon monoxide and reduce the iron again. It was proposed that the atomic oxygen is obtained either by two successive hydrogen abstractions steps or by hydrogen abstraction followed by disproportionation of two hydroxyl species [46]. Ovesen et al. [44] successfully described the water-gas-shift reaction over a Cu-based catalyst under industrial conditions using the surface redox mechanism as basis for their microkinetic model. Suggesting that the surface redox mechanism could apply for the Cu-based catalyst as well. Today, the surface redox and

associative reaction mechanism for the water-gas-shift reaction is still under debate in the literature [51]. The elementary reaction steps for the two reaction mechanism are stated in Table 1 [46].

Table 1. The proposed elementary reaction steps for the surface redox and the associative carboxyl mechanism over Cu(111). Adapted from [46].

Redox mechanism	Associative carboxyl mechanism
$CO + * \rightarrow CO*$	$CO + * \rightarrow CO*$
$H_2O + * \rightarrow H_2O*$	$H_2O + * \rightarrow H_2O*$
$H_2O* + * \rightarrow H* + OH*$	$H_2O* + * \rightarrow H* + OH*$
$OH* + * \rightarrow O* + H*$	$CO* + OH* \rightarrow COOH* + *$
$OH* + OH* \rightarrow H_2O* + O*$	$COOH* + * \rightarrow CO_2* + H*$
$CO* + O* \rightarrow CO_2* + *$	$COOH* + OH* \rightarrow CO_2* + H_2O*$
$CO_2* \rightarrow CO_2 + *$	$CO_2* \rightarrow CO_2 + *$
$H* + H* \rightarrow H_2 + 2*$	$H* + H* \rightarrow H_2 + 2*$

The understanding of the surface reaction mechanism for the carbon dioxide hydrogenation and water-gas-shift reaction is crucial for guiding the development of catalyst materials than can suppress the latter reaction. It would be impossible to completely remove the water-gas-shift reaction if it shares a common intermediate with the carbon dioxide hydrogenation, which was found unlikely to be the case [42]. The reversible change in the Cu oxidation state from Cu^{2+} to metallic Cu^0 could function as the active site for the water-gas-shift redox mechanism. Thus, a dynamic behaviour in the Cu oxidation state, if present, could be investigated by in-situ XPS or XAS coupled with modulation excitation spectroscopy. However, the methanol synthesis rate is linear dependent on the Cu surface area, where Cu bounded formate is crucial for the formate hydrogenation rate [37–40]. This questions the ability to completely supress the water-gas-shift reaction over a metallic based methanol synthesis catalyst.

2.1.3 Metallic methanol synthesis catalyst in bi-functional catalytic systems

The idea of combining methanol synthesis with methanol dehydration over solid acids to change the thermodynamic constraints for the former reaction is not new. This was the thought behind the development of the direct hydrogenation of carbon dioxide into dimethyl ether. This reaction can be achieved by combining a Cu-based catalyst with a solid acid within one reactor, which allows improved syngas conversion at lower pressure [52], as illustrated in Fig. 3 (a). This technology was the basis for the Topsøe Integrated GAsoline Synthesis (TIGAS) where the pressure used for the production of dimethyl ether corresponded to that of the methanol-to-gasoline reaction. This closed the loop without the need for isolating and storing of the oxygenate intermediate, as illustrated in the process flow diagram in Fig. 3 (b).

(a) (b)

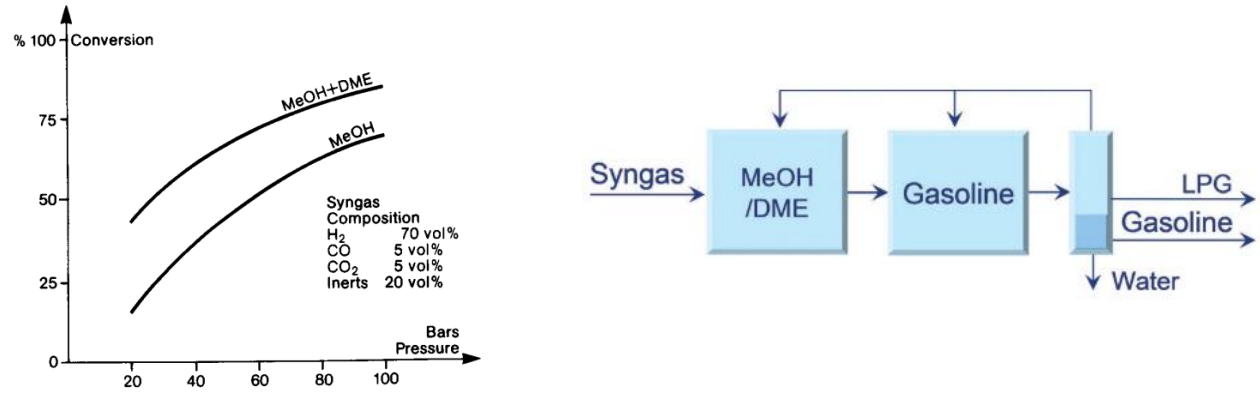


Fig. 3. (a) The conversion of syngas to oxygenate using the methanol synthesis or the combined methanol synthesis and methanol dehydration reaction. (b) Schematic of the Topsøe Integrated GAsoline Synthesis (TIGAS) process. Obtained from [14,52].

This concept was demonstrated in pilot scale (1 ton pr. day scale) in the 1980s [52], where the produced oxygenate and water from the first reactor together with unconverted syngas was directly fed to the methanol-to-gasoline reactor loaded with the H-ZSM-5 zeolite. These experiments lead to some interesting observations of the process performance when changing the feed gas composition. As shown in Fig. 4, the deactivation rate by coke formation was strongly influenced by the hydrogen partial pressure, where high hydrogen partial pressure (illustrated as the increase in the so-called gas module $(H_2\text{-}CO_2)/(CO+CO_2)$) significantly inhibits the coking rate. It was at that time suggested that the improved lifetime of the zeolite was due to hydrogenation of unsaturated coke precursor, which limited their ability to oligomerize into large coke molecules. High partial pressure of hydrogen also led to enhanced olefin hydrogenation producing mostly saturated hydrocarbons but resulted in a stable gasoline product. The olefin hydrogenation was believed to occur mainly over the Cu-based cat-

alyst as the product gas was recycled through the oxygenate reactor. Thus, changing the gas composition affected the hydrocarbon distribution, catalyst volume and recycle flow. To achieve optimized performance, it is necessary to balance these effects by optimizing the feed composition.

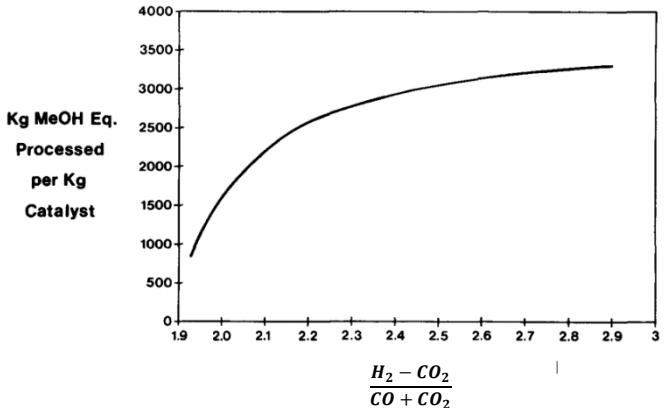


Fig. 4. The accumulated amount of methanol equivalent converted pr. mass of H-ZSM-5 catalyst. Adapted from [52].

2.1.3.1 Bi-functional catalyst for syngas to hydrocarbon conversion

Combining the solid acid for methanol dehydration to dimethyl ether allowed for a more efficient methanol production at pressures similar to the methanol-to-gasoline reactor. As the H-ZSM-5 catalyst itself is a solid acid, the need for using two reactors can be questioned. In 1979, the Mobil Research and Development Corporation's group Chang et al. [53,54] asked this question and found that it was possible to produce hydrocarbons within one reactor by combining the methanol synthesis and methanol-to-hydrocarbon reaction. It was discovered that by changing the methanol synthesis candidate, the carbon monoxide conversion and the hydrocarbon distribution could be altered. Upon combining a ZnO and Cr_2O_3 based catalyst with a H-ZSM-5 zeolite, a high selectivity towards aromatic products (~70 wt%) was obtained. This was achieved at a carbon monoxide conversion to hydrocarbon of ~16 % at relatively harsh conditions of 82 bar, 427 ºC and long residence time [54]. This inspired the groups of Fujimoto et al. and Bruce et al. to investigate the syngas conversion to aromatics under milder conditions by using nickel-cobalt-zirconia (Fischer-Tropsch catalyst) [55] and metallic palladium supported on silica (methanol synthesis component) [56] combined with H-ZSM-5. They achieved significantly lower aromatic selectivity at ~29 and ~35.7 wt%, respectively.

For obtaining sufficient syngas conversion at milder conditions, the optimal methanol synthesis candidate could be metallic Cu- or Pd-based catalysts [34,57]. These catalysts have higher CO_2 hydrogenation activity and allow the production of methanol at lower temperatures, which minimizes the pressure required for an efficient thermodynamic driving force. The group of Fujimoto et al. [58]

tried to replace the before mentioned Pd/SiO_2 catalyst with the state of the art $Cu/ZnO/Al_2O_3$ and combined it with the H-ZSM-5 catalyst. This significantly increased the hydrocarbon yield fromr 9.6 to 17 c. mol% but at the expense of a more saturated product low in aromatics (3.8 c. mol% within hydrocarbons). Several studies on varying the metallic based methanol synthesis and zeolite/zeotype catalyst have shown high selectivity to saturated hydrocarbons, where some of them are listed in Table 2.

Table 2. Listed operating parameters and results for synthesis gas (CO Con. or CO_2 Con.) conversion to hydrocarbons over bi-functional catalyst composed of a mixture of metallic methanol synthesis and a zeolite/zeotype catalyst. The conversion and selectivity are given in %. H_2/CO and the H_2/CO_2 ratio is 2 and 3, unless else stated.

Bi-functional catalyst	Si/Al	T [°C]	P [bar]	W/F [g_{cat} h mol^{-1}]	CO Con.	CO_2 Sel.	Ref.
$Cu/ZnO/Al_2O_3$/H-SAPO-5*	0.14	290	40	9600**	24.4***	NR	[59]
$Cu/ZnO/ZrO_2/Al_2O_3$/H-Beta*	150	260	20	20	62	44.0	[60]
$Cu/ZnO/ZrO_2/Al_2O_3$/Pd-Beta*	17.5	260	20	20	78.4	40.3	[60]
$Cu/ZnO/ZrO_2/Al_2O_3$/Pd-Beta	38	260	20	10	82.8	44.9	[61]
Pd/SiO_2/H-ZSM-5	25	300	21	3.4	25	41	[58]
$Cu/ZnO/Al_2O_3$/H-ZSM-5	25	300	21	3.4	34	48	[58]
$Cu/ZnO/Al_2O_3$/H-DAY	7.6	300	21	3.4	32	46	[58]
Pd/SiO_2/H-Y	4.8	350	20.6	10	9.2	29.3	[62]
Pd/SiO_2/H-ZSM-5	25	350	20.6	10	16.4	34.1	[62]
Pd/SiO_2/H-DAY	7.6	350	20.6	10	20.5	28.8	[62]
Pd/SiO_2/H-SDAY	7.6	350	20.6	10	22.7	44.1	[62]
Bi-functional catalyst	**Si/Al**	**T [°C]**	**P [bar]**	**W/F [g_{cat} h mol^{-1}]**	**CO_2 Con.**	**CO Sel.**	**Ref.**
$Cu/ZnO/Al_2O_3$/Pd-Beta	38	260	20	10	21.2	64.6	[61]
$Cu/ZnO/ZrO_2$/Pd-Beta	38	260	20	10	22.0	49.1	[61]
$Cu/ZnO/ZrO_2/Al_2O_3$/Pd-Beta	38	260	20	10	25.2	47.2	[61]
$Cu/ZnO/ZrO_2$/H-SAPO-5	0.6	340	28	20	25.0	61.6	[63]
$Cu/ZnO/Al_2O_3$/H-SAPO-5	0.6	340	28	20	24.3	71.2	[63]

* H_2/CO = 2.3 for $Cu/ZnO/Al_2O_3$/H-SAPO-5 and $H_2/CO/CO_2/Ar$ = 65/24/8/3 for $Cu/ZnO/ZrO_2/Al_2O_3$/H-Beta and $Cu/ZnO/ZrO_2/Al_2O_3$/Pd-Beta.
** The space velocity is reported as GHSV [$mL/g_{cat}/h$].

The results listed in Table 2 demonstrate that a bi-functional catalyst can convert CO or CO_2 into hydrocarbons at reasonable conversions at lower pressure and temperatures, making these catalytic systems more energy efficient. However, a high olefin hydrogenation activity was observed for all the above listed catalysts, resulting in high yields of saturated hydrocarbons. The research group Fujimoto et. al [58,61,64,65] found that their catalysts produced hydrocarbons mainly in the C_{2-4} range

and by changing the zeolite from H-DAY to H-Beta, the main product shifted from propane to butanes (Fig. 5 (a)). As illustrated in Fig. 5 (a), the main product of such reaction was found to be iso-butane with a selectivity 55.7 carbon mol% achieved at the CO conversion to hydrocarbons at 36.7 %. Iso-butane is an interesting molecule used as precursor for the synthesis of methyl tert-butyl ether (MTBE), which is used as an additive in gasoline to increase the octane rating. Upon adding metallic sites, such as Pd, into the beta zeolite, the increased hydrogenation activity within the zeolite pores inhibited the formation of C_{5+} and increased the isobutane selectivity to >80 carbon mol % [60]. CO_2 conversion over a similar catalyst did not result in a similar high selectivity towards isobutane, which indicates that changes in the gas atmosphere also have influence on the hydrocarbon selectivity, as illustrated in Fig. 5 (b).

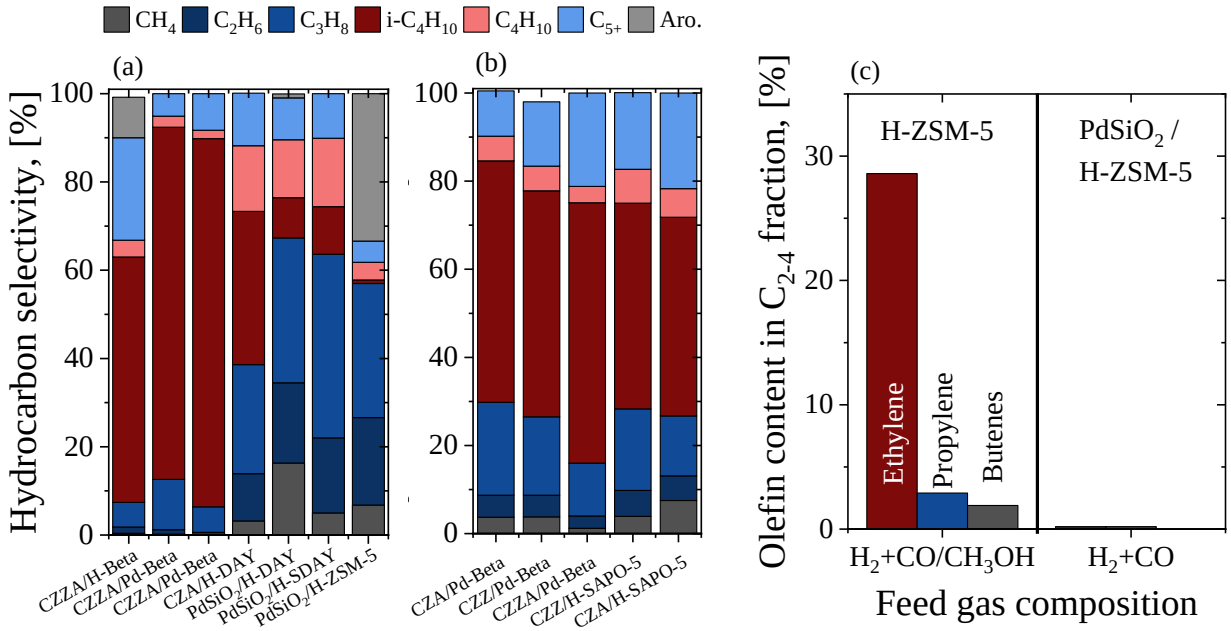
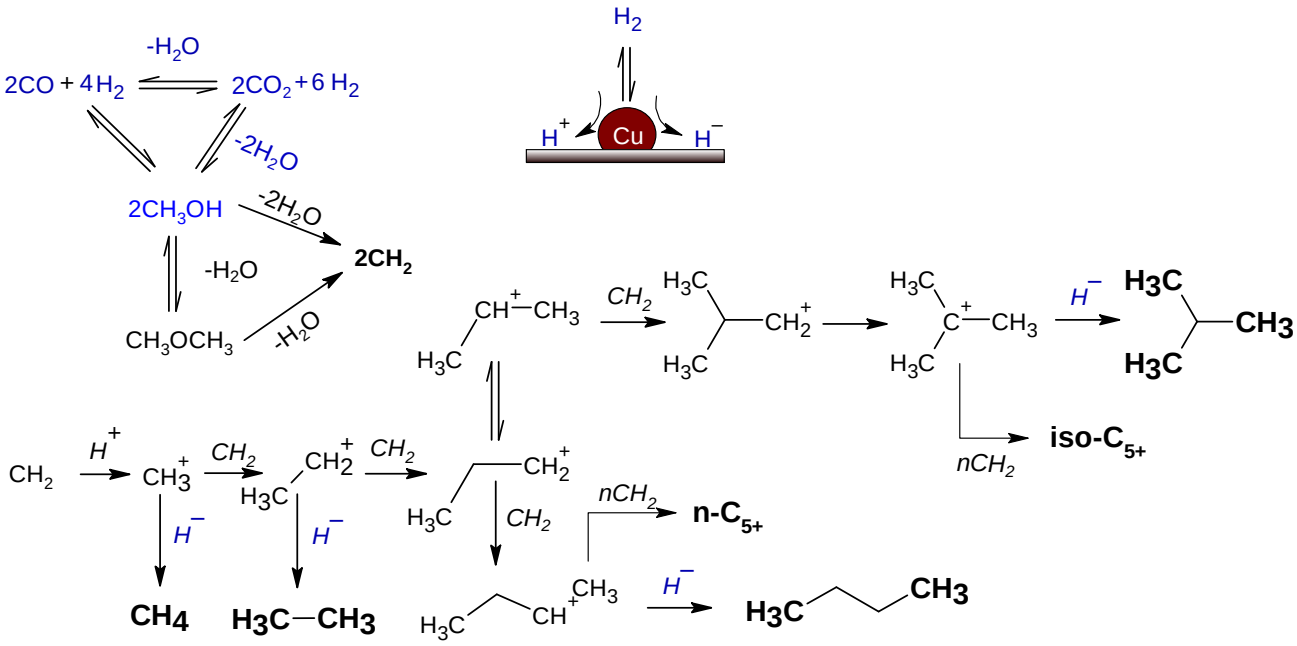


Fig. 5. Reported hydrocarbon selectivity for the bi-functional catalyst for (a) CO [60,62] *and (b) CO_2 conversion* [61,63] *. CZZA, CZZ and CZA denotes the Cu/ZnO/ZrO_2/Al_2O_3, Cu/ZnO/ZrO_2 and Cu/ZnO/Al_2O_3 catalyst, respectively. (c) The olefin content in the C_{2-4} fraction at methanol conversion with syngas co-feed in 1/9 ratio over H-ZSM-5 zeolite and syngas conversion over the bi-functional catalyst. Reaction conditions:638 K (628 K for the PdSiO2/H-ZSM-5), 20.6 bar and 8.8 g_{cat} h mol^{-1}* [56].

Co-feeding methanol and syngas (CO+H_2) over H-ZSM-5 alone resulted in formation of both olefins and aromatics, where syngas conversion over the combined $PdSiO_2$/H-ZSM-5 catalyst hydrogenated all the olefins (Fig. 5 (c)) and decreased the aromatic selectivity by ~9 wt% [56]. It is generally accepted that the conversion of methanol over zeolite catalysts first give lower olefins which in the dual cycle hydrocarbon pool mechanism converts to higher hydrocarbon products rich in olefins and aromatics [14,66–69]. However, the use of a methanol metallic based catalyst and zeolite for converting

synthesis gas (CO and H_2) to hydrocarbons in pressurized hydrogen atmosphere showed that the initially formed olefins are directly converted to paraffins by the hydrogenation reaction (Fig. 5 (c)) [56,58,62]. Thus, decreasing the possibility of further carbon chain growth resulting in a lower aromatic selectivity [56]. The hydrogenation of the olefins is believed to happen mainly on the metallic methanol synthesis catalysts, where adding metallic site within the zeolite pore can increase the hydrogenation activity of the zeolite as well. Therefore, the residence time of olefins in the zeolite catalyst has great influence on the obtained product distribution. The residence time of olefins in the zeolite is influenced by the diffusion rate determined by pore size, the crystal size, and the particle size of the zeolite catalyst [58]. Zeolites with larger pore size and smaller crystal and particle size will increase the effective diffusion rate of olefins, which will lower the molecular weight of the obtained hydrocarbon product. Fujimoto et. al [58] also reported that this will minimize the selectivity towards aromatics and formation of coke, resulting in increased stability of the catalyst. A schematic representation of the hydrogen activation on the metallic site and the following olefin hydrogenation are represented in Scheme 1.



Scheme 1. Proposed reaction mechanism over a copper-based methanol synthesis catalyst and large pore zeolite such as H-beta (low residence time for olefins). Draw from schemes discussed by the research group Fujimoto et. al [58,61,64,65].

Liu et al. [59] investigated the catalytic performance of $Cu/ZnO/Al_2O_3$ combined with SAPO-5 for direct conversion of CO to hydrocarbons. The product obtained at these conditions was predominantly propane and isobutane with a product selectivity of 28 and 35.5 wt%, where the methane and C_{6+} selectivity was <3.4 wt%. Liu et al. [59] reported great instability problems for the bi-functional

catalyst where the initial 24.4 % CO conversion started decreasing after 1.5 hours on stream and was <7 % after 4 hours on stream, as shown in Fig. 6 (a). This deactivation was suggested to be caused by significant sintering of the Cu particles for the CZA catalyst and it was recommended that a more sintering-resistant catalyst ($Pb/ZnO/Al_2O_3$) should be used. However, it is known that carbon deposits deactivate zeolite/zeotype catalyst by blocking the access to the acid sites. This would cause a higher concentration of unconverted methanol forcing the methanol synthesis closer to equilibrium, which could significantly inhibit the $Cu/ZnO/Al_2O_3$ conversion abilities. Liu et al. [59] demonstrated a linear tendency between the CO conversion and the density of Brønsted acid sites for the SAPO-5 zeolite, as illustrated in Fig. 6 (b). This is clearly indicating that a sufficient methanol dehydration reaction over the zeolite catalyst shifts the methanol synthesis equilibrium reaction, increasing the carbon monoxide conversion.

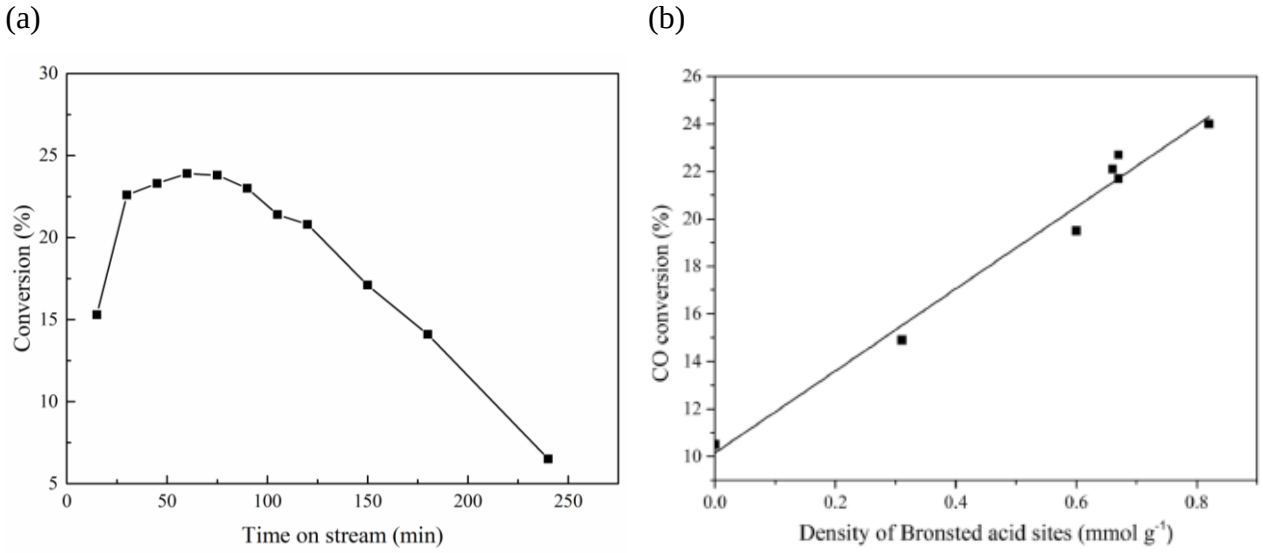


Fig. 6. (a) The CO conversion with time on stream and (b) linear correlation between CO conversion and the density of Brønsted acid sites during synthesis gas conversion to hydrocarbons over $Cu/ZnO/Al_2O_3$ and SAPO-5 catalyst. These results are obtained after 1 hour. Reactor conditions: 40 bar, 290 ºC, GHSV 9600 h^{-1}, H_2/CO = 2.3 and $Cu/ZnO/Al_2O_3$ /SAPO-5 = 4. Obtained from [59].

A synergy effect can be observed between the methanol synthesis and the methanol to hydrocarbon reaction where the activity of the methanol synthesis reaction is dependent on the ability of the zeolites to dehydrate the methanol. This suggests that to achieve high CO or CO_2 conversions, solid acids with high acid densities are required to maximize the number of active sites for the methanol dehydration reaction. Water is produced from the CO_2 hydrogenation to methanol, the reverse-water-gas-shift reaction, and from the methanol dehydration reaction. When using a bi-functional catalyst for the CO_2 conversion to hydrocarbons, high water partial pressure is expected. Competitive adsorption of water on the Brønsted acid site could result in lower methanol dehydration activity of the zeolite that could result in a less active bi-functional catalyst. Fujiwara et al. [70] used $Cu/ZnO/Al_2O_3$ in

combination with H-beta and found that the strong acid site of the zeolite was seriously deactivated. Grafting the zeolite with disilane (1,4-bis(hydroxydimethylsilyl)benzene) made the zeolite more hydrophobic (water contact angles more than 130^{o}), which remarkably improved the catalytic activity for the production of hydrocarbons, as illustrated in Fig. 7. This indicates that water production from the three reactions could have a negative impact on the performance of bi-functional catalysts.

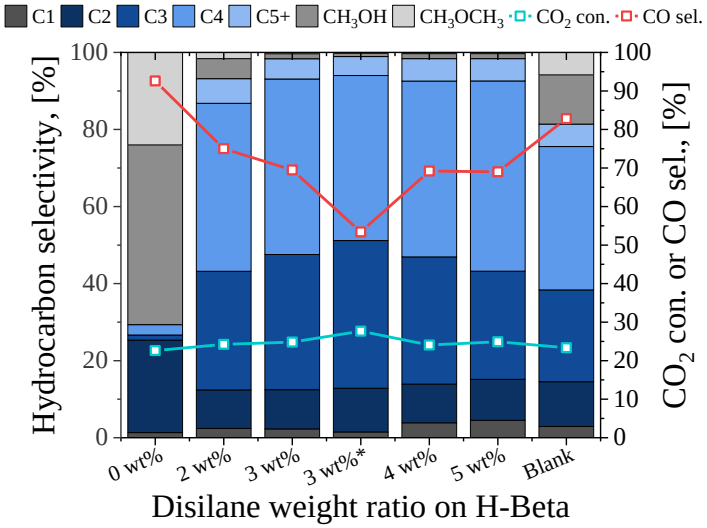


*Fig. 7. The change in product distribution with the weight ratio of disilane in H-beta for the bi-functional catalyst consisting of Cu/ZnO/Al2O3 (Cu/Zn/Al=6/3/1) and H-beta. Reaction Conditions: 300℃, 9.8 bar, GHSV 3000 mL/g_{cat}/h and CO_2/H_2 = 1/3. Blanks represent H-beta treated with the modification treatment in absence of disilane. * GHSV = 1500 mL/g_{cat}/h* [70].

Several authors have investigated the used of a metallic methanol synthesis catalyst together with the chabazite structure zeotype, H-SAPO-34 [71–75]. The H-SAPO-34 catalyst consist of small 8-ring pores (pore opening of 3.8 Å) connecting larger cavities (9.54 Å) and creating a 3-dimensional structure [76]. By restricting the pore opening of the solid acid to 3.8 Å, diffusion limitations cause lighter hydrocarbons to be the main product produced. When the H-SAPO-34 catalyst is used for the methanol dehydration reaction, the main product is light olefins such as ethylene, propylene and butenes [76–78], making it a good candidate for production of plastic monomers. However, these catalysts are prone to fast deactivation caused by that large carbon deposits can form within the cages, which inhibits the accessibility of the active sites [79,80]. Nieskens et al. [71] combined a commercial $Cu/ZnO/Al_2O_3$ catalyst with H-SAPO-34 for carbon monoxide conversion and found that the main product obtained was light paraffin, as illustrated in Fig. 8 (a). Similarly, Ramirez et al. [73] synthesized a $PdZn/ZrO_2$ catalyst and combined it with H-SAPO-34 for carbon dioxide conversion, where the main product obtained was propane (Fig. 8 (b)). Again, clearly indicating that using metallic based

methanol synthesis catalyst hydrogenates the produced olefins. As shown in Fig. 8 (b), the bi-functional catalyst has high CO_2 conversion (>20 %) with low selectivity towards CO (<30 %) at long residence time, showing high hydrocarbon productivity. In Fig. 8 (a), the performance of the $Cu/ZnO/Al_2O_3$ with H-SAPO-34 catalyst are visualized. Surprisingly, the bi-functional catalyst shows great stability and maintains high CO conversion for more than 250 g converted methanol pr. g H-SAPO-34 with no indication of oxygenate breakthrough. The deactivation of the H-SAPO-34 catalyst under methanol-to-olefins conditions is evident in the sudden oxygenate breakthrough, as coke formation inhibits the conversion of methanol. Converting methanol to olefins over the H-SAPO-34 in a fixed bed reactor have shown to convert approximately 20 g_{MeOH} pr $g_{SAPO-34}$ before the methanol conversion had dropped to 20 % [76]. Thus, indicating that operating the methanol dehydration under high partial pressures of hydrogen, water, carbon dioxide, and monoxide significantly enhances the lifetime of the H-SAPO-34 catalyst. The cause of the improved lifetime will be further elaborated in section 2.3.7.

(a) (b)

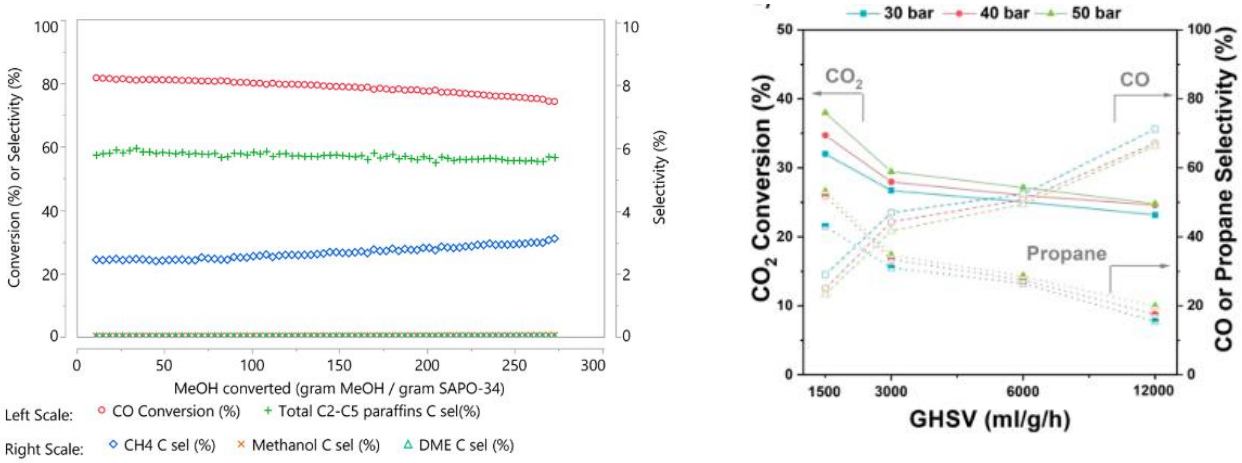


Fig. 8. (a) CO conversion and product selectivity as a function of the cumulative amount of methanol converted pr. amount of H-SAPO-34. Reaction Conditions: 390 ºC, 50 bar, GHSV = 4000h^{-1}, H2/CO = 3, catalyst composed of 75 wt% $Cu/ZnO/Al_2O_3$ and 25 wt% H-SAPO-34 [71]. *(b) CO_2 conversion, CO, and propane selectivity for the PdZn/ZrO2 at different space velocities and pressures. Reaction Conditions: 350 ºC and $H_2/CO_2 = 3$* [73].

2.1.3.2 Deactivation

As discussed in the previous section, combining a methanol synthesis component composed of metallic sites, such as Cu or Pd, will result in a highly hydrogenated product low in aromatics and olefins. Another concern with using the state of the art $Cu/ZnO/Al_2O_3$ as the methanol synthesis component for CO_2 hydrogenation is the increase in water partial pressure, which tend to increase catalyst sintering [81,82]. This problem only increases when such catalysts are combined with zeolite for the

direct conversion of CO_2 into hydrocarbons, as the methanol dehydration reaction contributes with additional water formation. As shown in Fig. 9 (a), the activity of the $Cu/ZnO/Al_2O_3$ (denoted CZA 1) decreases with time on stream when operated at equilibrium conditions at different temperatures. By increasing the temperature from 493 to 523 K, the stability of the catalyst increased, where further increase in temperature to 523 K forced the activity to drop faster [82]. The activity gained at 525 K was not expected because of pure thermal sintering. The equilibrium gas compositions are highly influenced by the reaction conditions and the methanol and water content decreases with increase in temperature. As shown in Fig. 9 (a), water has detrimental effect on the catalyst stability and the lower water content at 523 K could explain the improved stability. In Fig. 9 (b), the change in the specific Cu surface area with time on stream suggests that the improved stability at 523 K is related to better preservation of the Cu surface area. Co-feeding water in short hydro-treatments significantly induces the loss of Cu surface area showing that high water partial pressures promote thermal sintering of the $Cu/ZnO/Al_2O_3$ catalyst. Thus, lowering the water content by increasing the temperature to 523 K reduces thermal sintering, but enhanced sintering was observed even at low water concentration at 553 K (Fig. 9 (b)). This suggests that the deactivation by sintering is promoted at high temperature and high water concentration [82].

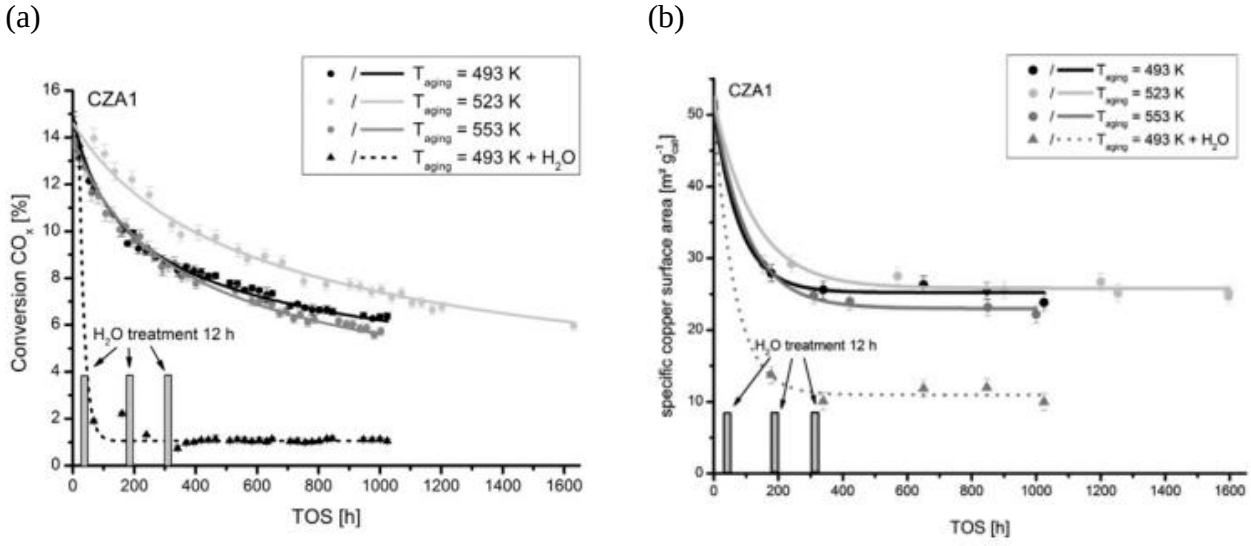


Fig. 9. (a) The CO_x (CO_2+CO) conversion with time on stream at different temperatures. Reaction conditions: 60 bar, GHSV =1260 h^{-1} and feed gas composition of $CO/CO_2/H_2/N_2$ = 13.5/3.5/73.5/9.5. (b) The specific Cu surface area determined by reactive N_2O frontal chromatography. Figures obtained from [82].

Kurtz et al. [83] investigated the deactivation of different Cu-based methanol synthesis catalyst, as shown in Fig. 10. They monitored the effluent methanol concentration with time on stream as they heated the reactor from 473 to 723 K, as illustrated in Fig. 10 (a). All catalysts deactivate with time on stream but the increasing temperature enhances the deactivation rate. The Cu support on ZnO

deactivates much faster than the $Cu/ZnO/Al_2O_3$ due to increased loss of the specific Cu surface area for the Cu/ZnO catalyst (Fig. 10 (b)). This suggest that adding Al_2O_3 to the catalyst provides two important effects for the methanol synthesis catalyst which are a promoting effect and a stabilizing effect. As demonstrated in Fig. 10 (b), with similar Cu surface area for the Cu/ZnO and $Cu/ZnO/Al_2O_3$ catalysts, the latter has higher methanol synthesis activity showing that having both ZnO and Al_2O_3 has a promoting effect. The $Cu/ZnO/Al_2O_3$ only loses ~60 % where Cu/ZnO loses ~88 % of the Cu surface area after the temperature experiment. This shows that the Al_2O_3 phase also provides a stabilizing effect.

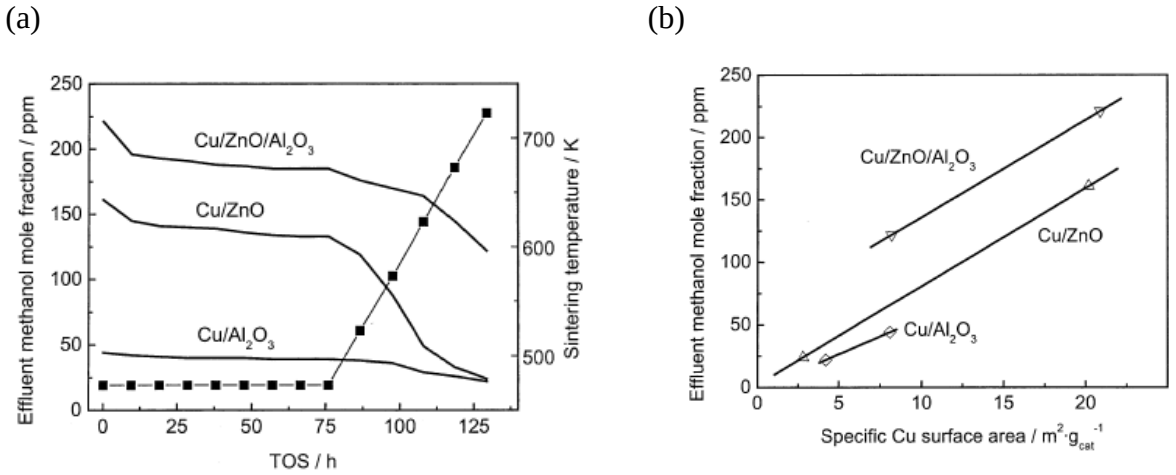


Fig. 10. (a) The effluent methanol mole fraction with time on stream and increasing temperature. (b) The effluent methanol mole fraction against the measured specific Cu surface area for fresh and spent Cu-based catalysts. Reaction conditions: 50 mL/min, 473 K, 1 bar and catalyst loading of 0.1 g. Figures obtained from [83].

Lunkenbein et al. [84] found that it is the ZnO species that is most dynamic under long-term stability test for the $Cu/ZnO/Al_2O_3$ catalyst. As shown in Fig. 11 (a), the phase composition of ZnO and $ZnAl_2O_4$ changes with time on stream showing that Zn ions migrate into the Al_2O_3 structure forming the Zn-spinel structure. Furthermore, all the phases sinter with time on stream where especially the ZnO and the $ZnAl_2O_4$ crystallites grow within the first 50 and 30 days, respectively. This causes a dramatic reduction in the catalyst surface area within the first 50 days, that results in a drop in the methanol synthesis rate (Fig. 11 (b)). This initial reduction in the methanol synthesis activity occurred without significant change in the actual Cu surface area determined H_2-isothermal adsorption. However, N_2O chemisorption shows that the reduction in the Cu surface area plus the redox active sites on ZnO correlated with the activity profile, indicating that a synergy effect between ZnO and the Cu surface is important for the methanol synthesis activity (Fig. 11 (b)) [85,86]. In Fig. 11 (c), TEM imaging of the catalyst suggests that Cu act as support for ZnO moieties and showed severe changes in the local surface composition of the catalyst resulting from the transformation of the Zn-containing

phases [84]. The sintering of the ZnO phase is visible by the densification of the ZnO on the Cu surface where the initial metastable ZnO crystallites are converted into stable wurtzite ZnO, which reduces the catalyst activity [84,87,88].

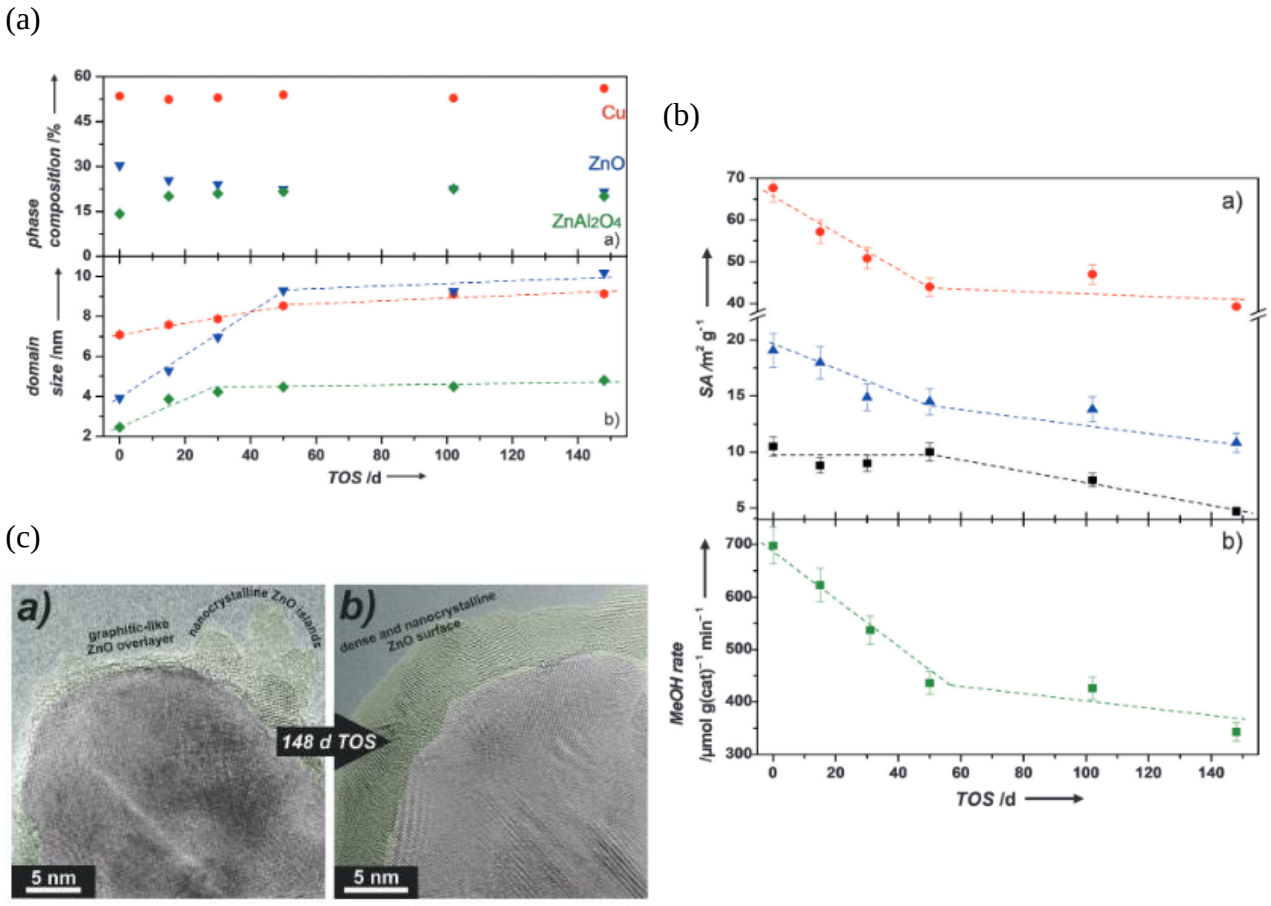


Fig. 11. (a) Quantitative analysis of neutron diffraction. a) Phase composition of Cu, ZnO and $ZnAl_2O_4$ and b) the domain sizes with time on stream. The phase composition was determined by Rietveld refinement and the domain size from width of the reflections. (b) a) The catalyst, Cu plus redox active sites on ZnO and actual Cu surface area and b) the methanol synthesis activity with time on stream. The catalyst surface area was determined by BET and the surface area of Cu plus redox active sites on ZnO was determined by N_2O measurements. The actual Cu surface area was determined by H_2-adsorption. (c) TEM image of a) fresh and b) spent catalyst.

2.1.4 Alternative catalyst for high temperature methanol synthesis

The activity measurements discussed in section 2.1.3 highlight that to achieve selective conversion of CO or CO_2 into unsaturated products, it is essential to use a methanol synthesis catalyst without metallic sites. These metallic sites either provide activated hydrogen by the hydrogen-spill-over effect, or can directly act as olefin hydrogenation sites, resulting in a saturated hydrocarbon mixture. The activation of the gaseous hydrogen is important to achieve high CO_2 hydrogenation activity, because it is the hydrogenation of surface formate into methoxy that is the rate determining reaction step [89]. Furthermore, limiting the production of water by inhibiting the reverse-water-gas-shift reaction could be important for the methanol dehydration activity, as water adsorption on acid sites could inhibit the active site *[70]*. This is important for complete removal of unconverted methanol which increases the thermodynamic driving force for the methanol synthesis reaction. The increased water partial pressure and the elevated temperatures for CO_2 hydrogenation into hydrocarbons will have a severe deactivating effect for bi-functional catalysts composed of $Cu/ZnO/Al_2O_3$. The higher temperature and the presence of water will cause faster Cu and ZnO sintering, which reduces the Cu surface area that will limit the methanol synthesis activity [82,84]. Thus, it is essential for sufficient production of olefins and aromatics by bi-functional catalysts to identify new methanol synthesis materials that can selectively produce methanol at methanol dehydration relevant temperatures and have low olefin hydrogenation activity.

2.1.4.1 Zinc based Catalyst

Pure ZnO without Cu is active for the methanol synthesis but requires harsh reaction conditions with temperatures in the range of 570-679 K and 250-300 bar [90]. The reaction mechanism over ZnO was found to go through a formate pathway under methanol synthesis conditions, similar to that observed for the Cu-based catalyst (section 2.1.2). Co-adsorbing CO_2 and H_2 resulted in formate formations while CO and H_2 did not form any formate species [91], suggesting that methanol is formed from CO_2 hydrogenation. Wilmer et al. [92] prepared several ZnO catalysts and found that the methanol synthesis activity was related to specific ZnO surfaces sites favoring the methanol synthesis. As shown in Fig. 12, a linear area-activity relationship for the highly crystalline materials was obtained where high surface area ZnO deviated from this trend. Wilmer et al. [92] suggested that the ZnO polar faces play an important role in the methanol synthesis activity.

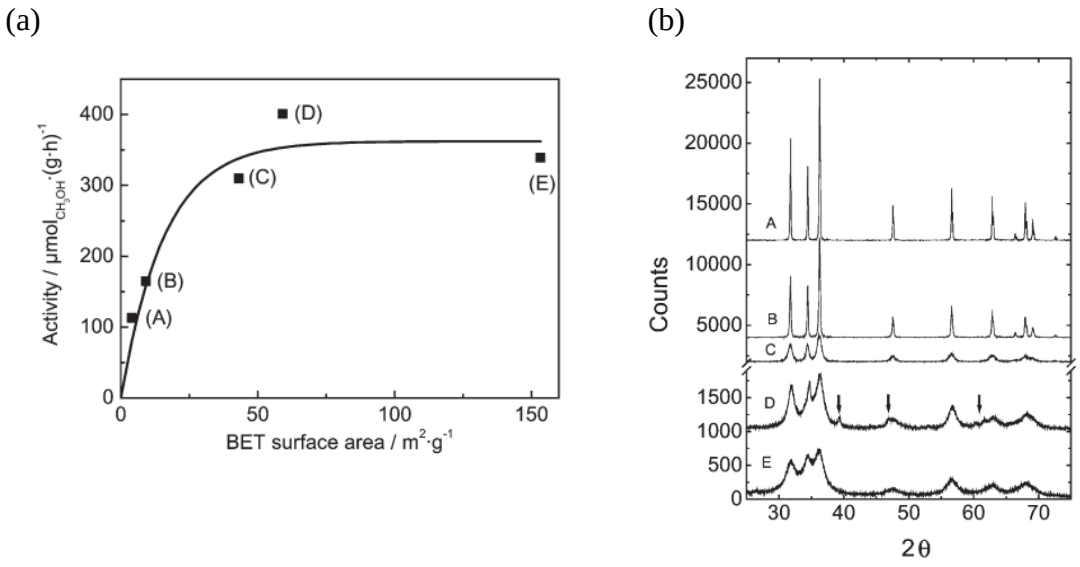


Fig. 12. (a) The methanol synthesis activity of ZnO with the change in the surface area. Reaction conditions: 573 K, 30 bar, 10 mL/min and gas composition of CO_2/CO/H_2/He = 8/6/64/22. (b) XRD pattern of the prepared ZnO catalysts. Obtained from [92].

Density functional theory (DFT) calculations by French et al. suggest that [93,94] oxygen vacancies on the polar oxygen-terminated ZnO (0001) surface act as the active site for CO_2 hydrogenation to methanol. As illustrated in Fig. 13, this reaction is thought to go through a formate pathway with formic acid and methoxy as intermediate for the production of methanol.

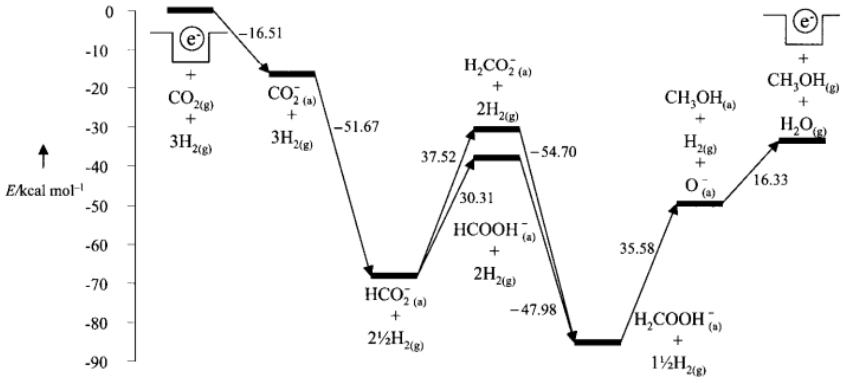


Fig. 13. The calculated reaction energy profile for the methanol synthesis over oxygen vacancies on the polar ZnO surface. Obtained from [94].

Recently Wang et al. [95] synthesized a mixed oxide catalyst composed of ZnO and ZrO_2 by the co-precipitation method. This significantly improved the CO_2 conversion and the methanol selectivity compared to pure ZnO. As shown in Fig. 14 (a), pure ZrO_2 has a negligible activity towards methanol formation but the CO_2 conversion and methanol selectivity improve by adding small amounts of Zn. An optimal performance was obtained with 13 mol% Zn-loading, which optimized the CO_2 conversion and methanol selectivity (>80 %). Introducing more Zn reduced the CO_2 conversion but the high

methanol selectivity was maintained until 33 mol% Zn-loading. Beyond this point, the catalytic performance started to resemble pure ZnO. The XRD analysis showed that by co-precipitating ZnO and ZrO_2, the only crystalline phase visible was the tetragonal ZrO_2 (t-ZrO_2) structure, as shown in Fig. 14 (b). The introduction of dopants is known to stabilize the meta-stable t-ZrO_2 structure at temperatures below 1170 °C [96], where the stable ZrO_2 structure is the monoclinic phase. Thus, showing that Zn interacts with the ZrO_2 phase to stabilize the formation of t-ZrO_2. By increasing the Zn-loading from 5 to 33 %, a systematic shift in the (101) Bragg reflection to higher degrees was seen (Fig. 14 (b)). This systematic shift is caused by the substitution of Zr^{4+} (84 Å) with Zn^{2+} (74 Å), which shrinks the tetragonal lattice. Using iron- and yttrium oxide as dopants for the ZrO_2 structure have shown similar trends where the ionic radius of 70 Å and 90 Å shifts the (101) Bragg reflection to higher and lower degrees, respectively [97,98]. Beyond the Zn-Zr solid solution saturation of 33 mol%, hexagonal ZnO starts to form and become visible in XRD, as shown in Fig. 14 (b). The activity data presented in Fig. 14 (a) suggests that the activity of the ZnO-ZrO_2 catalyst is related to the formation of a solid-solution of the two phases where the formation of hexagonal ZnO disrupts the solid-solution surface area, causing the decrease in CO_2 conversion and methanol selectivity. Several studies have investigated similar ZnO-ZrO_2 mixed oxide catalysts and have observed this systematic shift in the (101) Bragg reflection [95,99–101]. FTIR bands around 500 and 600-700 cm^{-1} for ZnO-ZrO_2 catalysts were associated with Zn-O-Zn and Zn-O-Zr vibrations [102]. UV-vis spectra of ZrO_2 changed with Zn as dopant where the shape of the absorption spectrum indicated the presence of isolated Zn^{2+} ions [103]. These findings suggest that it is the surface of a solid solution, where Zn^{2+} is embedded in the zirconia crystal lattice, which in synergy with Zr^{4+} is highly active for CO_2 hydrogenation. Wang et al. [95] suggested that this synergy is attributed to H_2 activation on Zn sites and simultaneous activation of CO_2 on the neighboring Zr site.

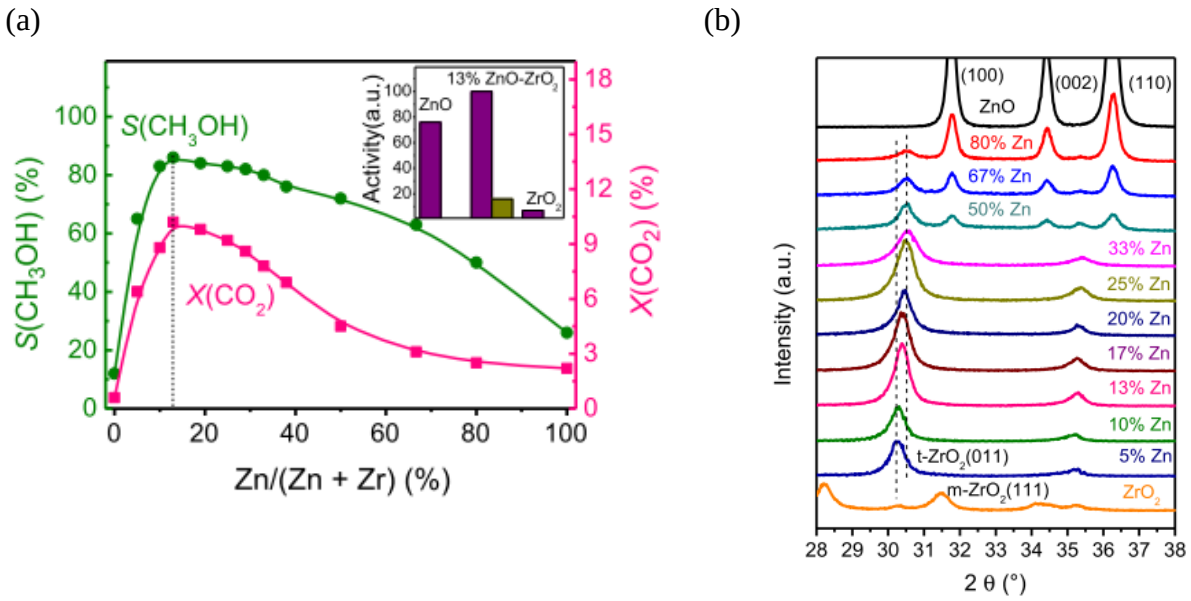


Fig. 14 (a) The methanol synthesis performance of the ZnO-ZrO2 catalyst with the Zn/(Zn+Zr) molar ration. Inset: purple, normalized activities for ZnO, 13% ZnO-ZrO_2, and ZrO_2 by specific surface area; dark yellow, normalized activities for mechanically mixed ZnO and ZrO_2 in the same composition: Reaction conditions: 320 ºC, 50 bar, H_2/CO_2 =3, GHSV = 24000 mL/g/h. (b) XRD pattern of the as prepared catalysts. Obtained from [95].

Salusso et al. [104] and Tada et al. [100] performed X-ray absorption spectroscopy (XAS) of the Zn K-edge of a ZnO-ZrO_2 catalyst. The shape and absorption edge of the XANES spectra revealed that only Zn^{2+} were present in the samples [100,104], as shown in Fig. 15 (a). The Fourier transformed K^3-weighted EXAFS spectra for ZnO-ZrO_2 samples with varying Zn-loadings is illustrated in Fig. 15 (b). At low Zn-loadings, the Zn-Zn backscattering is not visible which indicates that the Zn is not present in a repeated crystalline structure, as it is in crystalline ZnO. However, the Zn-Zn back-scattering signal increases with increasing Zn-loading due to formation of crystalline ZnO, which is in line with the observations obtained by XRD [100]. This clearly indicates that Zn can be present in different phases in the ZnO-ZrO_2 catalysts, which could be in the form of a Zn-Zr solid solution and in crystalline ZnO. Salusso et al. [104] observed a similar trend (Fig. 15 (a)) and they obtained a Zn-Zn coordination number close to 4 ± 3 by fitting the EXAFS spectra to the ZnO standard, indicating a disordered nature of the ZnO (Zn-Zn coordination number = 12 for bulk ZnO). This disorder could be explained by the presence of very small ZnO domains [104] or that some Zn is present in an isolated form and in crystalline ZnO, making the average coordination number less than 12. As Zn should dramatically enlarge its interatomic distance (Zn-Zn= 3.20 Å and Zr-Zr=3.59) with Zn^{2+} replacing the Zr^{4+} in the ZrO_2 lattice, it was pointed out by Salusso et al. [104] that an ideal solid solution seems unlikely. They suggest that ZnO nanoclusters were chemically bonded in the ZrO_2 matrix. Han et al. [105] performed similar EXAFS fittings for different ZnO-ZrO_2 catalysts and found

that the first shell Zn-O coordination number were close to 3. If Zn^{2+} species were present in the bulk t-ZrO_2 structure, a significantly higher coordination should be expected.

(a) (b)

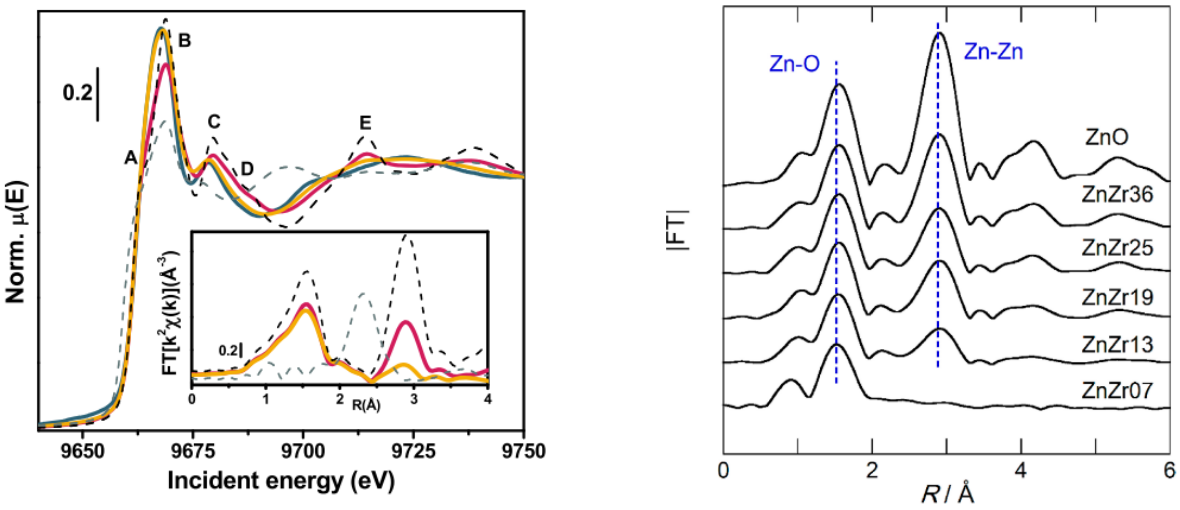


Fig. 15 (a) Zn K-edge XANES (main panel) and phase-uncorrected weighted FT-EXAFS (insert transformed in the 2-12 $Å^{-1}$ k range measured at room temperature (He atmosphere). ZrZn-5 (blue), ZrZn-15 (yellow), and ZrZn-30 (red) where 5, 15, 30 denotes the weight percentage Zn loading. h-ZnO reference (dashed black) and Zn metal foil (dashed-gray). (b) Zn K-edge FT-EXAFS of ZnO-ZrO_2 catalyst with different loadings (numbers represent the atomic Zn loading). Obtained from [100,104].

In Fig. 15, no clear evidence for Zn-Zr backscattering signal was observed in the EXAFS spectra, which could be suspected if an ideal Zn-Zr solid solution was formed. Salusso et al. [104] also investigated the Zr K-edge for their ZnO-ZrO_2 catalyst, which only revealed the Zr-O at 1.5 Å and Zr-Zr at 3.2 Å backscattering signals, as illustrated in Fig. 16. The first shell shows a similar intensity as the t-ZrO_2 reference, but a lower intensity can be observed for the second shell unveiling an enhanced structural disorder in the Zr local coordination environment. As the Zn-loading increases, the peak intensity progressively reduces, indicating some interactions between the ZnO on the ZrO_2 lattice that disrupt the t-ZrO_2 lattice. Chemical bound ZnO nanoclusters or Zn^{2+} migration into the ZrO_2 lattice explain these observation, showing that when preparing co-precipitated ZnO-ZrO_2, Zn species will migrate into the ZrO_2 lattice creating some kind of a solid solution. In Fig. 16, imaginary parts of the Zr-Zr and Zr-Zn scattering contributions show that they cancel each other out perfectly, which could explain the absence of such signals, making it difficult for observing Zn-Zr interactions from XAS analysis.

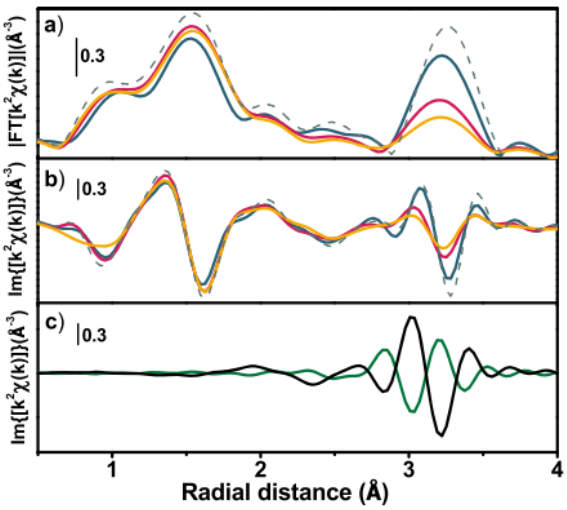


Fig. 16. a) The magnitude and b) imaginary parts of k^2-weighted phase-uncorrected Zr K-edge FT-EXAFS extracted in the k range of 2.5-12 $Å^{-1}$ for ZrZn-5 (blue), ZrZn-15 (red), ZrZn-30 (yellow), and reference t-ZrO_2 (dashed grey). c) imaginary part of the individual Zr-Zr (black and Zr-Zn (green) scattering paths generated by FEFF6 optimized after the fit of ZrZn-30. Obtained from [104].

In contrast to the theory of the solid solution being the main active sites, the low Zn-O coordination number by XAS [105] and surface enrichment of Zn determined by X-ray photoelectron spectroscopy [95,100] suggest that Zn is mostly present at the zirconia surface. This suggests that besides forming a solid solution, a surface ZnO species is being formed on the Zn stabilized t-ZrO_2 surface. Cheng et al. [106] used High-Resolution Transmission Electron Microscopy (HR-TEM) and found that even at low Zn content (1 mol%), individual lattice fringes of isolated ZnO were detected, as illustrated in Fig. 17. This suggests difficulties for the Zn^{2+} ions to substitute Zr^{4+} inside the ZrO_2 lattice and that Zn prefers to generate a separate ZnO phase. Thus, in the preparation of ZnO-ZrO_2 catalysts beside the generation of a Zn-Zr solid-solution, surface ZnO will be generated and will exist apart from the solid solution.

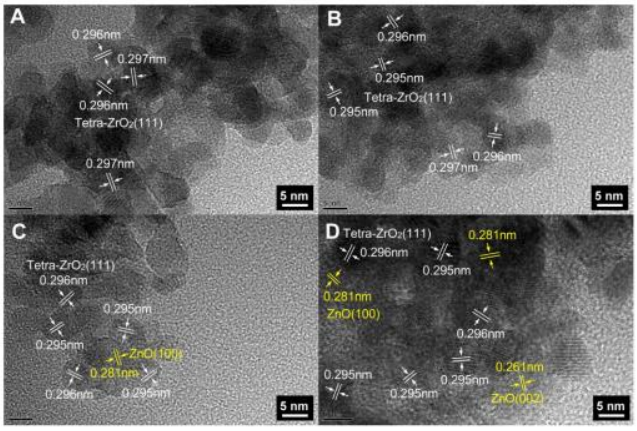


Fig. 17. High-Resolution Transmission Electron Microscopy of ZnO-ZrO_2 catalysts with different Zn loading of (A) 0 mol%, (B) 0.5 mol%, (C) 1 mol% and (D) 10 mol%. Obtained from [106].

Generally, ZrO_2 presents a low surface area compared to other catalyst supports, such as Al_2O_3 and SiO_2. Han et al. [99] managed to increase the surface area of the ZnO-ZrO_2 from 48.2 m^2/g from using the co-precipitation method to 109 m^2/g by preparing the catalyst with evaporation-induced self-assembly procedure. The higher surface area increased the CO_2 conversion from 3.8 % to 6.4 % and still maintained high selectivity towards methanol > 78 %. However, as illustrated in Fig. 18, the factor ~2 increase in the catalyst surface area only enhanced the methanol synthesis activity by 35 %. This indicates that the activity is not related to the total catalyst surface area, but to specific sites on the solid-solution surface or to surface ZnO species.

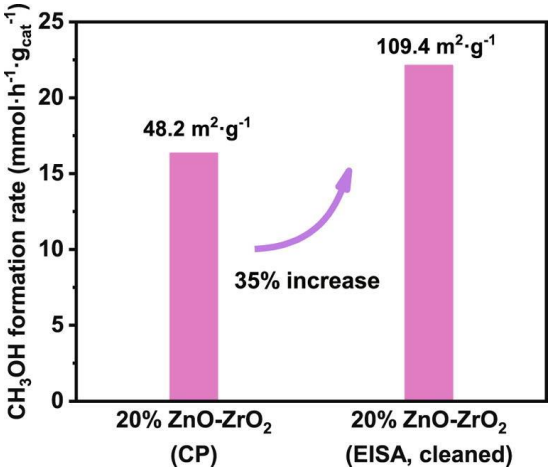


Fig. 18. The methanol synthesis activity for co-precipitated (CP) and evaporation-induced self-assembly (EISA) prepared ZnO-ZrO_2 catalysts. Reaction conditions: 320 ºC, 55 bar, GHSV 24000 mL/g/h and feed composition of $CO_2/H_2/Ar$ = 24/72/4. Obtained from [99]

Temvuttirojn et al. [107] and Lin et al. [108] investigated the effect of the ZrO_2 phase on the methanol synthesis activity of the ZnO-ZrO_2 catalyst. Temvuttirojn et al. [107] prepared ZrO_2 support and calcined the support at different temperatures from 600-1000 ºC, to which ZnO was impregnated. When ZnO was added to the amorphous ZrO_2 support, the t-ZrO_2 phase was formed. Upon calcination at different temperatures, the surface area of the ZrO_2 support significantly decreased, resulting in creation of more crystalline ZnO, when impregnated with same Zn-loading. This makes it hard to distinguish the effect of the crystalline ZnO phase to that of the difference in the ZrO_2 phase. However, a higher surface area of the ZrO_2 support seems to generate a catalyst low in crystalline ZnO content, which improves the CO_2 conversion and oxygenate (methanol and dimethyl ether) selectivity. Lin et al. [108] impregnated ZnO on three different ZrO_2 polymorphic phases; monoclinic, tetragonal and amorphous. In contracts to the group of Temvuttirojn et al. [107], no change in the ZrO_2 phase was observed by XRD analysis when ZnO were added to the supports. The difference in the surface area of the support influences the amount of crystalline ZnO forming on the catalyst, but the concentration

of the crystalline ZnO was not reported for the catalysts. Nevertheless, the change in the polymorphic phases of ZrO_2 seems to influence the CO_2 conversion and methanol selectivity. Going from tetragonal, monoclinic, and amorphous, the conversion was 4.3, 5.2 and 6.6 % with a methanol selectivity of 31, 58 and 43.7 % at 320 ºC and 20 bar.

The ZnO-ZrO_2 catalyst have high selectivity towards methanol but at the expense of lower CO_2 conversions. To improve the catalyst activity, Sha et al. [109] investigated the promoting effect of incorporating Ga into the ZnO-ZrO_2 catalyst. By 5 mol% Ga promotion, the CO_2 conversion was enhanced without changing the methanol selectivity, causing the activity to increase from 556 to 630 g kg^{-1} h^{-1}. Chemisorption and hydrogen/deuterium exchange experiments showed that Ga promotion increases the catalyst capacity for adsorption and activation of hydrogen, comparted to the un-promoted ZnO-ZrO_2 catalyst. As shown in Fig. 19 (a), in-situ diffuse reflectance infrared Fourier transform spectra (DRIFTS) under methanol synthesis from hydrogen and CO_2 over ZnO-ZrO_2 catalysts show evidence of formation of bidentate formate (HCOO*) assigned from the peaks at 2878, 1595, 1382 and 1370 cm^{-1} [95]. The peaks at 2931, 2824 and 1046 cm^{-1} were assigned to the methoxy specie (H_3CO*). The evolution of these peaks was followed by the peaks at 2878 and 2824 cm^{-1} for the HCOO* and H_3CO*, as illustrated in Fig. 19 (b). The surface concentration of HCOO* reached steady state after 30 min, where slower surface accumulation was observed for H_3CO*. The methanol formation reached steady state after 60 min. When shifting the hydrogen for deuterium, the amount of HCOO*, H_3CO* and methanol decreased with increase in DCOO*, D_3CO* and CD_3OD. The methanol synthesis is, therefore, believed to go through the formate pathway, where formate and methoxy are important intermediates [95]. A similar analysis was conducted by Sha et al. [109] which concluded that HCOO* and CH_3O* species are main intermediates. The Ga promotion to the ZnO-ZrO_2 catalyst lowered the CH_3O*/HCOO* ratio suggesting that the hydrogenation of HCOO* to CH_3O* is boosted by the improved hydrogen adsorption and activation. This improved activation of hydrogen could have negative impact on the hydrocarbon product obtained from the bi-functional catalyst when Ga promoted ZnO-ZrO_2 catalyst are mixed with zeolites. Improved activation of hydrogen seems essential for obtaining a more active methanol synthesis catalyst but could lead to higher saturation degree of the hydrocarbon product obtained over bi-functional catalysts. This potentially reveal a compromise between the CO_2 conversion and the saturation degree of the hydrocarbon product must be made.

(a) (b)

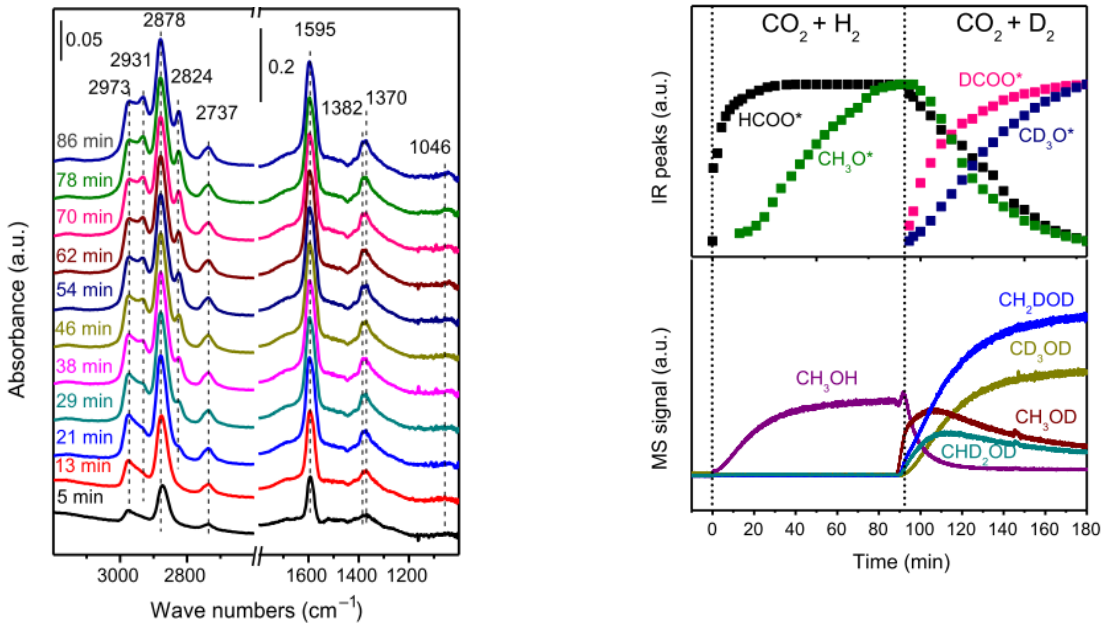


Fig. 19. (a) Characterization of surface species by in-situ DRIFTS under CO_2 and hydrogen reaction over ZnO-ZrO_2 catalyst. DRIFTS-MS for CO_2 and hydrogen reaction with subsequently switch of hydrogen to deuterium. Reaction conditions: 1 bar, 280 ºC, with 10 mL/min CO_2 and 30 mL/min H_2 or D_2. Obtained from [95].

Other interesting Zn-based methanol synthesis catalysts for selective production of methanol at higher temperature are the Zn-spinel catalysts. Liu et al. [110,111] studied both the $ZnAl_2O_4$ and the $ZnGa_2O_4$ catalysts for CO_2 hydrogenation to methanol. Similar to the ZnO-ZrO_2 catalyst, the activity of the Zn-spinel catalyst is related to the Zn-loading. This is illustrated for the $ZnAl_2O_4$ and $ZnGa_2O_4$ catalyst in Fig. 20 (a-b) and in Fig. 20 (d). Below the stoichiometric Zn-loading for the spinel structure, being the Zn-loading fulfilling the 1:2 ratio of Zn to Al or Ga (0.33 molar fraction), the catalyst is active for the methanol synthesis showing that the spinel structure itself has some activity. An optimum performance is obtained around the stoichiometric Zn-loading. Beyond this point, the performance declines again. Beyond the stoichiometric Zn-loading, crystalline ZnO starts to form and becomes visible by XRD where the fraction of this phase increases with the Zn-loading. Similar to the ZnO-ZrO_2, the formation of crystalline ZnO has a negative effect on the catalyst performance. The density of oxygen vacancies was determined by electron paramagnetic resonance (EPR) spectroscopy and revealed a relation to the concentration of the oxygen vacancies to the catalyst performance of the $ZnAl_2O_4$ and $ZnGa_2O_4$ catalysts, as shown in Fig. 20 (c) and (d). Higher concentration of oxygen vacancies correlated to the adsorption capacities of CO_2 and was therefore concluded to be

important for CO_2 adsorption and activation. The incorporation of Zn into the Al_2O_3 creates structural disorder that improves the oxygen vacancies concentration. In-situ DRIFTS studies showed that both the CO and CO_2 hydrogenation over the $ZnAl_2O_4$ catalyst proceed through the formate pathway, evident from the formation of formate and methoxy surface species [38,110,112]. Ye et al. [112] and Hu et al. [113] did DFT calculations of CO hydrogenation into methanol over $ZnAl_2O_4$ and found that the hydrogenation of the formate intermediate into methoxy is the rate determining step. This questions the effect of the higher oxygen vacancies concentration on the activity, as it is not the adsorption and activation of CO_2 that are the rate-determined step, if formate hydrogenation is the rate determining step for CO_2 hydrogenation as well.

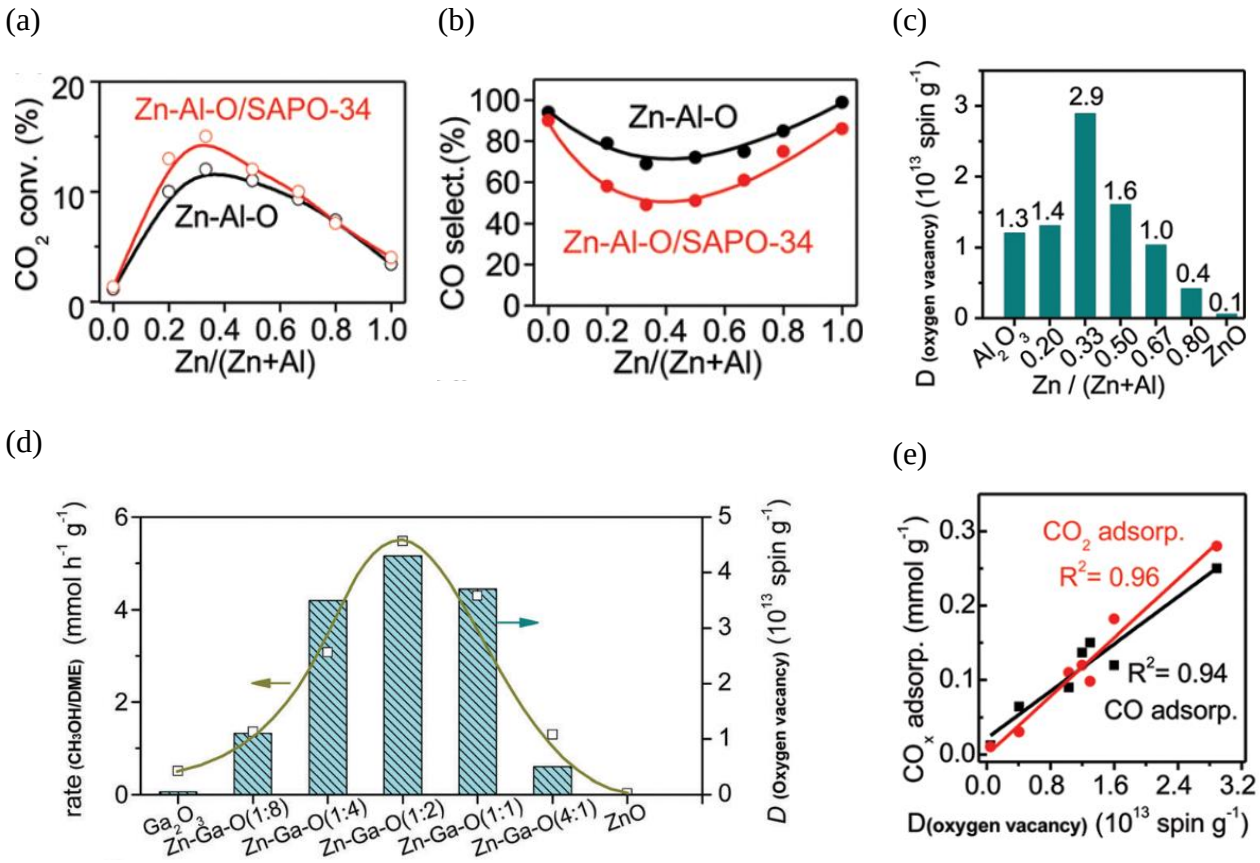


Fig. 20. The effect of Zn/Al molar ratio on catalytic behaviors of $ZnAl_2O_4$ and $ZnAl_2O_4$ mixed with H-SAPO-34 (a) CO2 conversion and (b) CO selectivity. Reaction conditions: 643 K, 30 bar, H_2/CO_2 = 3, 45 mL/min and catalyst loading of 0.17 $ZnAl_2O_4$ or 0.5 $ZnAl_2O_4$/SAPO-34. (c) Density of oxygen vacancies evaluated from EPR spectra for the $ZnAl_2O_4$ catalyst with different Zn/Al molar ratio. 1,1-Diphenyl-2-picryl-hydrazyl was used as an internal standard. (d) The effect of Zn/Ga molar ratio on the oxygenate formation rate and the density of oxygen vacancies determined from EPR analysis. Reaction conditions: 370 ºC, 30 bar, 45 mL/min, H_2/CO_2 =3, catalyst loading of 0.17 $ZnGa_2O_4$. (e) Correlation of CO and CO_2 (COx) chemisorption amounts against the density of oxygen vacancies. Obtained from [110,111].

Zhang et al. [114] prepared a similar $ZnAl_2O_4$ catalyst for the CO_2 hydrogenation into methanol and found that the activity of the catalyst increases with time on stream, as illustrated in Fig. 21. This trend was caused by a reconstruction of the $ZnAl_2O_4$ catalyst surface. XPS analysis of the fresh and

spent catalyst revealed an increase in the content of ZnO on the spinel surface from Zn/Al of 1.08 to 1.27. This shows that with time on stream, a surface enrichment in ZnO increase the methanol synthesis activity. The highest activity was obtained with a Zn-loading of 67 mol%, which outperformed the stoichiometric $ZnAl_2O_4$ catalyst [114]. Thus, having surface ZnO species seems to be important for the catalyst activity and preparing $ZnAl_2O_4$ with excess Zn to the stoichiometric Zn-loading increased the activity. However, as illustrated in Fig. 20 (a-b), too high loading causes formation of crystalline ZnO, which could remove the more amorphous surface ZnO species, causing the activity to decrease. The surface area of the prepared Zn-spinel catalyst could be important for the concentration of surface ZnO that can be constructed before larger ZnO crystals are formed. As shown in Fig. 21 (b) and (c), the reconstruction of the $ZnAl_2O_4$ surface shows faster hydrogenation of surface carbonates species into formate, showing that surface ZnO boosts the activity by promoting the activation of hydrogen.

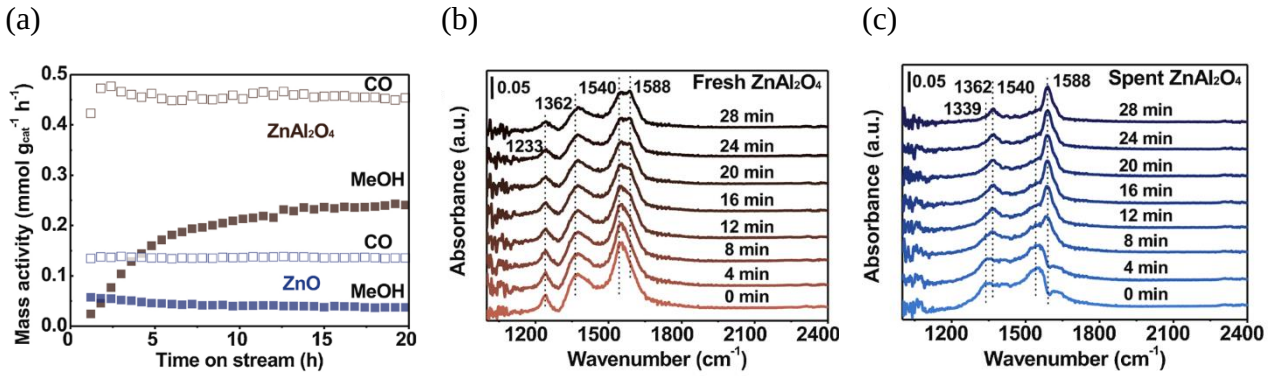


Fig. 21. (a) The product formation rate for ZnO and $ZnAl_2O_4$ catalysts with time on stream. Reaction conditions:553 K, 30 bar, 30 ml/min, 1g of catalyst and feed composition of $CO_2/H_2/N_2$ = 1/3/2. In situ FTIR spectra of the adsorbed carbonate species on the surface of (a) fresh $ZnAl_2O_4$ and (b) spent $ZnAl_2O_4$ in H_2/N_2(1/19) flow with a total rate of 20 mL/min at 573 K. Obtained from [114].

Several studies have shown that to achieve an active $ZnCr_2O_4$ catalyst for methanol synthesis a Zn-rich nonstoichiometric, $ZnCr_2O_4$ is essential [115–117]. Song et al. [115] prepared a series of ZnO/Cr_2O_3 catalysts with different Zn/Cr ratios, where the highest performance was achieved by a Zn/Cr ratio of 65/35. XRD analysis confirmed the formation of $ZnCr_2O_4$ spinel structure but with a low degree of crystallinity. DFT calculations showed that the (100) surface of the $ZnCr_2O_4$ spinel has a favorable oxygen vacancy formation energy of 1.58 eV. Doping this surface with excess Zn to give a 60 % Zn content, that are charge-balanced by oxygen vacancies, yields a catalyst composed of an amorphous ZnO layer support on the spinel, as illustrated in Fig. 22. The amorphous ZnO layer had the lowest oxygen vacancy formation energy yielding its reducibility and was therefore concluded to be the main active phase for the methanol synthesis catalyst. Similar amorphous ZnO sites constructed on the $ZnGa_2O_4$ and $ZnAl_2O_4$ catalyst surface could be important for the catalytic activity as well.

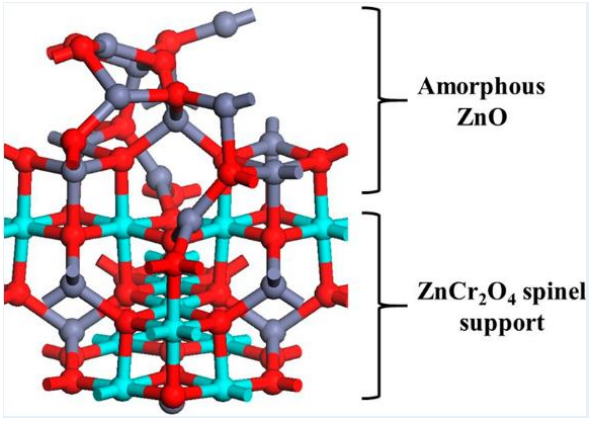


Fig. 22. Calculated local structure for 26.67% Zn doping (60% Zn content) in the (100) surface of the $ZnCr_2O_4$ spinel.

Souma et al. [118,119] prepared several ZnO/Fe_2O_3 catalysts with different Zn-loadings. XRD analysis revealed that at a Zn-loading lower than 33 mol%, two phases were present, the α-Fe_2O_3 and $ZnFe_2O_4$ spinel. Only ZnO and $ZnFe_2O_4$ were visible by XRD analysis at a Zn content higher than 33 mol%. As illustrated in Fig. 23, the catalytic performance changes with the Zn-loading. At low loadings, the α-Fe_2O_3 phase converts the CO_2 into methane and C_{2+} hydrocarbons through the Fischer-Tropsch process. Increasing the Zn-loading to obtain $ZnFe_2O_4$ and ZnO phases, changes the product to methanol where the optimal methanol synthesis activity is obtained with an excess Zn to the stoichiometric $ZnFe_2O_4$ spinel loading.

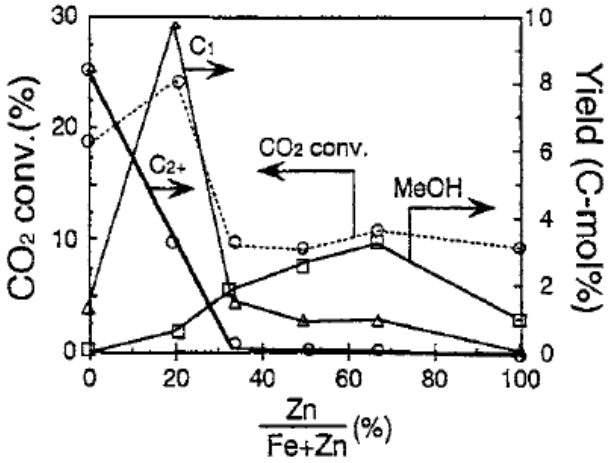


Fig. 23. Effect of zinc content on the activity of ZnO/Fe_2O_3. Reaction conditions: 350°C, 50 bar, GHSV = 3000 ml/g/h, H_2/CO_2=3. Obtained from [118,119].

2.1.4.2 Indium-based catalyst

The indium-based catalyst has gained great attention in recent years due to its great activity, selectivity, and stability for methanol production. Martin et al. [120] demonstrated pure In_2O_3 and In_2O_3/ZrO_2 activity and selectivity compared to the conventional $Cu/ZnO/Al_2O_3$ methanol synthesis activity, as illustrated Fig. 24 (a). The indium-based catalyst especially outperforms the $Cu/ZnO/Al_2O_3$ catalyst at higher temperatures due to its extraordinary methanol selectivity that stays close to 100 % in a temperature range of 480 to 580 K. The $Cu/ZnO/Al_2O_3$ catalyst has lower selectivity due to its high reverse-water-gas-shift activity and the methanol selectivity decrease with temperature. The In_2O_3/ZrO_2 catalyst exceeds the $Cu/ZnO/Al_2O_3$ catalyst at temperatures above 540 K and have shown to be stable for more than 1000 hours. The In_2O_3 is significantly promoted by ZrO_2 support, where TiO_2, ZnO, SiO_2 etc. showed a negligible or an inhibiting effect on the methanol synthesis activity (Fig. 24 (b)). The higher temperature required to outperform the conventional catalyst causes a higher energy input necessary for the replacing the $Cu/ZnO/Al_2O_3$ catalyst in industrial applications. However, the In-based catalyst is interesting in the application such as in bi-functional catalyst where higher temperature are required to ensure methanol dehydration activity. H_2-TPR showed features emerging at temperatures below bulk reduction, suggesting partial reduction of In_2O_3 forming oxygen vacancies. Furthermore, XPS analysis revealed possible oxygen atoms next to defect sites confirming the presence of oxygen vacancies. Martin et al. [120] proposed that the mechanism is rooted in the creation and annihilation of oxygen vacancies as active sites, which are boosted through electronic interaction created with ZrO_2 support.

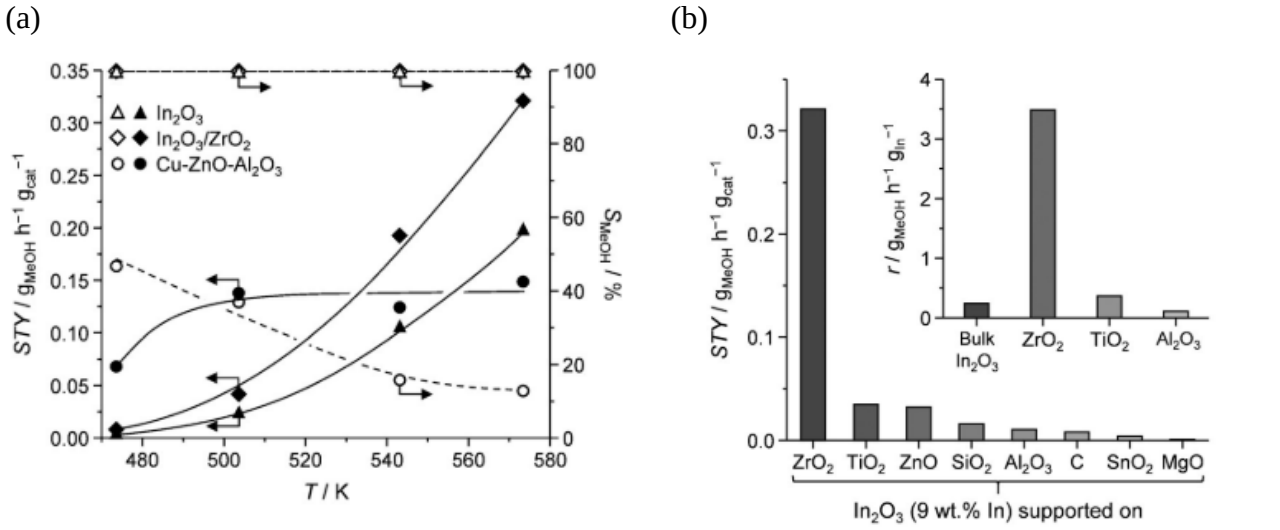
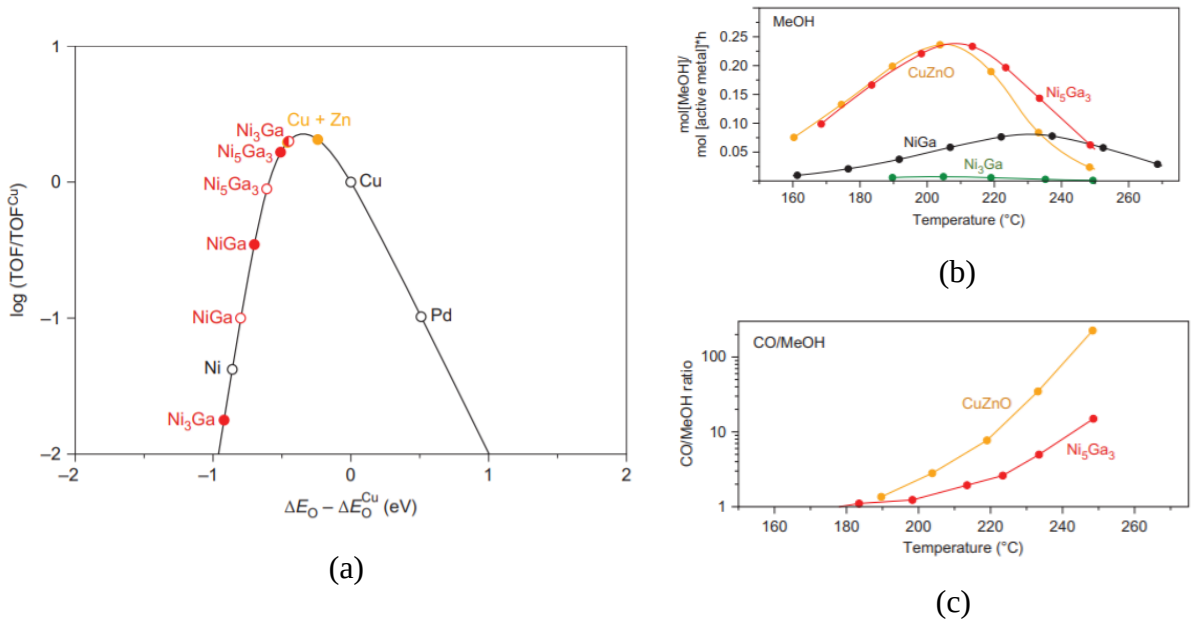


Fig. 24. The methanol synthesis activity and methanol selectivity for CO2 hydrogenation over In2O3, (9 wt% In) In2O3/ZrO2 and $Cu/ZnO/Al_2O_3$ at various temperatures. Reaction conditions: 50 bar, $H2/CO_2$ = 4 and GHSV = 16000 mL/g/h.

2.1.4.3 Nickel-gallium intermetallic catalyst

Studt et al. [121] synthesized a series of nickel-gallium based catalysts and tested their ability to reduce CO_2 to methanol at ambient pressure in a tubular fixed-bed reactor. Through descriptor-based analysis and computational methods nickel-gallium intermetallic compounds (here defined as a chemical compound of two or more metallic elements adopting ordered crystal structure that differs from those of the constituent metals) were identified to be a stable methanol synthesis candidate with good activity. This was made possible by the identification of a scaling relation between the oxygen adsorption energy, ΔE_O, the adsorption energies, and transition-state energies of all the hydrogenated forms of CO_2 on step sites fcc (211). These energies were mapped into a single parameter, ΔE_O. Predictions of the catalytic activity, calculated by a steady state microkinetic model with input of these scaling relations, revealed a relation with ΔE_O, as illustrated in Fig. 25 (a). These predictions showed that the highest reaction rate is a result of competition between too weak interactions with oxygen, causing unstable intermediates and high reaction barriers, and too strong interactions with oxygen, which causes surface poisoning by oxygen containing species, such as formate.



(a) (b) (c)

Fig. 25. (a) Theoretical CO_2 hydrogenation activity volcano plot. Open black circles represent the ΔE_O for the stepped 211 surfaces of cobber, nickel, and palladium. Closed orange circles are for the Cu+Zn surface. The red circles represent the predicted ΔE_O for the Ni-Ga intermetallic compounds, where closed circles represent nickel-rich sites, open circles represent gallium-rich sites and half-open circles represent mixed sites. The reaction condition was 227 °C, 1 bar and H_2/CO_2 ratio of 3. (b) The turnover frequency (TOF) and (c) the carbon monoxide to methanol ratio in the outlet stream for Ni-Ga intermetallic compounds as a function of temperature and compared to conventional cobber-based methanol synthesis catalyst. The reaction condition was 1 bar, GHSV 6000 mL/g_{cat}/h and H_2/CO_2 ratio of 3 [121].

Similar catalytic activity of the theoretical predicted nickel rich Ni_5Ga_3 intermetallic compound to the cobber-zinc based catalyst was experimentally confirmed. The activities of the synthesized Ni-

Ga catalysts compared to conventional Cu/Zn/Al catalysts at ambient pressures are illustrated in Fig. 25 (b). Here, the Ni_5Ga_3 catalyst showed similar or slightly enhanced performance (at higher temperature compared to the conventional type of catalyst). This is confirming the ability of the theoretical calculations proposed by Studt et al. [121] to screen for active methanol synthesis catalysts. One considerable advantage of the Ni-Ga based catalyst over the conventional catalyst is the significantly lower selectivity towards CO, as illustrated in Fig. 25 (c). This is an important factor for efficient production of methanol. The reason for the difference in reverse-water-gas-shift activity for the two catalysts was suggested to be caused by the gallium-rich sites and the nickel-rich sites catalyzes different reactions, in contrast to conventional cobber catalyst. The gallium-rich sites was believed to facilitate methanol synthesis where nickel-rich sites facilitate reverse-water-gas-shift and methanation, until the nickel-rich sites become self-poisoned by adsorbed CO and carbonates. This is interesting and may provide an efficient catalyst for the direct CO_2 hydrogenation to hydrocarbons, where the temperature is higher and the pressure lower compared to conventional methanol production plants. The higher temperature will shift the thermodynamic equilibrium of the water-gas-shift reaction towards CO and water formation, which will limit the production of methanol. However, if Ni-Ga based catalysts can suppress the formation of CO at these conditions, these catalyst could be ideal for this application. On the other hand, the metallic sites could function as olefin hydrogenation which has been observed for metallic Pd- and Cu-based catalysts [71–74].

2.2 The Methanol to Hydrocarbons Process

The research on conversion of oxygen containing compounds over a zeolite catalyst was initiated by the Mobil Research and Development Corporation. In the early 1970, they tried to selectively produce 1,3,5-trimetylbenzene from acetone over their newly synthesized **M**obil **S**ynthetic **Z**eolite, H-ZSM-5, solid acid. However, the conversion of acetone resulted in a gasoline-like mixture rich in 1,2,4-trimethylbenzene. Their next experiment was to investigate whether the ZSM-5 could catalyze the methylation of isobutene by methanol to higher branched alkanes, but again this yielded a gasoline-like product. It was found that methanol was completely converted, while isobutene was largely untouched. This led to the first experiment of only converting methanol over the ZSM-5 catalyst which confirmed that methanol can be converted into hydrocarbons rich in aromatics and iso-alkanes [23,122].

(a) (b)

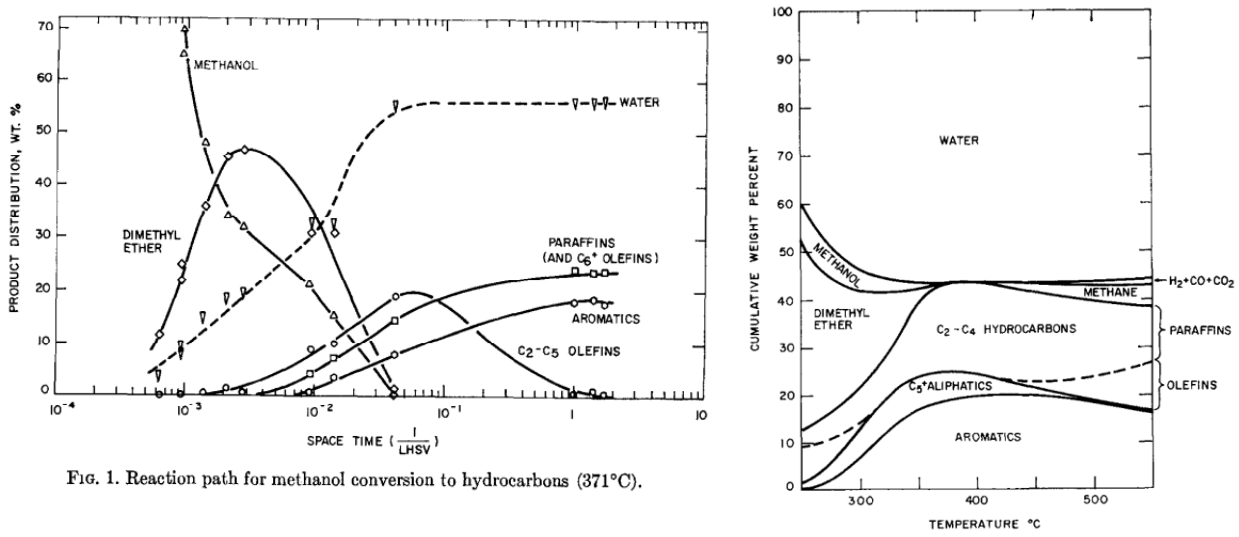


FIG. 1. Reaction path for methanol conversion to hydrocarbons (371°C).

Fig. 26. Product distribution from H-ZSM-5 catalyzed methanol conversion at (a) different space velocities and (b) different temperatures in a fixed bed microreactor. Reaction conditions: 371 ºC, 1 atm, LHSV at 0.6-0.7 hr^{-1}. Obtained from [23].

The hydrocarbon distribution obtained from methanol conversion over the H-ZSM-5 catalyst can be altered by residence time and temperature (Fig. 26). As illustrated in Fig. 26 (a), the methanol is initially converted into dimethyl ether at shorter residence time. Longer residence time converts the methanol/dimethyl ether into olefins and upon further increase in residence time the olefins are oligermized and cyclized into aromatics compounds. The parallel formation of aromatics and paraffins (Fig. 26 (a)) shows that in the formation of the benzene ring, olefins act as hydrogen acceptors forming an aromatic and paraffin rich product at high residence time [23,66,67]. At low space velocity, the main reaction at 260 ºC is the dehydration of methanol to dimethyl ether where the hydrocarbon

formed are predominantly $C_{2\text{-}5}$ olefins, as shown in Fig. 26 (b). At 340 to 370 ºC, the methanol and dimethyl ether conversion approaches completion with the main hydrocarbon product being aromatics. By further increase in temperature, the light olefins and methane selectivity rises as a result of a secondary cracking reaction. Above 500 ºC, methanol starts to decompose into hydrogen and carbon monoxide. These results lead to the proposed methanol reaction path by Chang et al. [23], as stated in Scheme 2.

$$2CH_3OH \underset{+H_2O}{\overset{-H_2O}{\rightleftharpoons}} CH_3OCH_3 \xrightarrow{-H_2O} C_{2-5}\ olefins \longrightarrow PIONA$$

Scheme 2. The reaction path going from methanol to hydrocarbons. PIONA denotes a hydrocarbon mixture composed of paraffins, iso-paraffins, olefins, naphthenes, and aromatics. Adapted from [23].

Chang et al. [16,22] also investigated the change in the hydrocarbon distribution with change in the zeolite acid site density and reaction pressure. Using pressures of 0.04, 1, and 50 atm showed that lower reaction pressures result in a higher olefin yield with low formation of aromatics, showing a decoupling of the olefin formation and aromatization at lower pressure. Opposite results were obtained at higher pressures, where increased overlap of the two reactions resulted in higher selectivity of poly-methylbenzenes [22]. The density of acidic sites in zeolites are altered by the concentration of Al_2O_3 within the zeolite structure as it is responsible for the creation of Brønsted acid sites, which are further elaborated in section 2.2.1. The result showed that using a H-ZSM-5 catalyst with low acid site density operated at high temperatures, decuples the formation of olefins from the aromatization given a hydrocarbon product rich in olefins. With the decrease in the acid site density, the methanol dehydration activity decreases and it is thereby necessary to apply high temperatures to achieve complete methanol conversion [16]. Upon changing the operating conditions and the acid site density of the H-ZSM-5 catalyst, the hydrocarbon distribution can be altered which is important for the selective production of olefins and aromatics.

Light olefins, such as ethene and propene, are used for the production of polyethylene and polypropylene plastic materials. In 2019, the worldwide production of these plastic materials was ~200 million tons [123]. Today, the plastic monomers are obtained from stream cracking of natural gas or naphtha and fluid catalytic cracking of heavier crude oil fractions [3]. Thus, using zeolites for the selective conversion of methanol produced from captured CO_2 and renewable hydrogen into light olefins could reveal a sustainable production pathway of plastic materials. This is essential for reducing the need for fossil resources and for reducing the CO_2 generated from plastic production and plastic waste incineration in the future, as the production of these plastic materials is forecasted to

increase by ~20% by 2030 [123]. Zeolites has shape-selective properties due to its well-defined pore structure, which limits diffusion of bulkier molecules in and/or out of the zeolites (section 2.2.3). Thus, by varying the pore structure of the zeolites, the selectivity of the hydrocarbons can be fine-tuned. The selectivity towards light olefins was significantly improved by the discovery of the H-SAPO-34 zeotype catalyst by the researchers at Union Carbide (now UOP) [14]. H-SAPO-34 consists of a Chabazite (CHA) structure that consist of small channels connecting larger cavities (cages). These small channels allow the diffusion of light hydrocarbons out of the zeolite crystal which improves the selectivity for light olefins >80 % [14]. In contract to the H-ZSM-5 catalyst, deactivation by carbon deposits (also referred to as coke molecules) occurs rapidly and therefore requires frequent regeneration. Thus, the zeolite/zeotype topology, the acid site density, acidic strength, and the reactor conditions can be altered to achieve different product distributions, from aromatics for the H-ZSM-5 catalyst rich in acid sites and light olefins for the pore restricted H-SAPO-34 catalyst.

2.2.1 Zeolite materials and the acid sites

Faujasite, mordenite, offretite, ferrierite, erionite, and chabazite are examples of natural occurring zeolites in nature. Zeolites have been known for over 250 years as aluminosilicate minerals. However, the use of zeolite material as heterogenous catalysts first became interesting when a synthetic faujasite (zeolite X and Y) was introduced, which had great influence in the petroleum refining industries [124]. The zeolite building blocks are $[SiO_4]^{4-}$ and $[AlO_4]^{5-}$ tetrahedra that can be described as TO_4 building blocks. The TiO_4 building blocks are linked at their corners via a common oxygen atom. As illustrated in Fig. 27, the TiO_4 units can be linked together in secondary building blocks, such as the sodalite or pentasil unit, which control the final zeolite structure, creating inorganic macromolecules with a well-defined framework composed of channels, channels intersections, and/or cages [124]. It will result in formation of the faujasite zeolite if the sodalite units are connected via their hexagonal faces. The faujasite has a spacious channel system with spherical cages with a diameter of 13 Å. These cages are connected tetrahedrally with four neighboring cages through pore openings with a diameter of 7.4 Å (Fig. 27). These pore openings are constructed by 12 TO_4-tetrahedra and faujasite zeolite is therefore classified as, 12-membered-ring pore system with a tree-dimensional structure due to the presence of both channel and cages. An example of a one-dimensional 12-membered-ring pore zeolite is the ZSM-12 zeolite having only straight channels in one direction as shown in Fig. 27 [124]. Ferrierite, also known as ZSM-35, is a 10 membered-ring pore zeolite with channels parallel to the [001] and [010] plane. It is, therefore, classified as a two-dimensional structure.

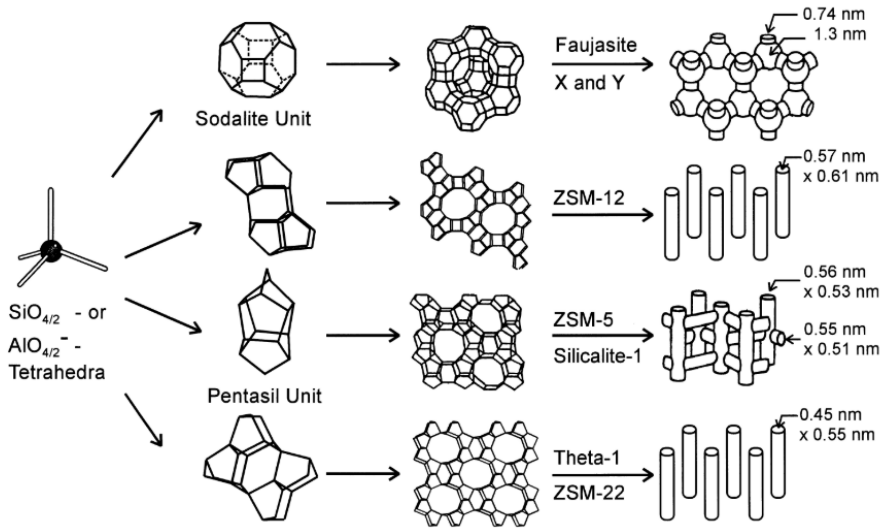


Fig. 27. The zeolite structures of faujasite, ZSM-12, ZSM-5, and ZSM-22. Obtained from [124].

The zeolite structures are additionally classified by a framework type code (FTC), which is a classification by the International Zeolite Association Structure Commission (IZA-SC). The ZSM-5, ZSM-11, and SSZ-13 zeolites have the FTC type code of MFI, MEL, and CHA, respectively [125]. The MFI framework contains two intersecting channel systems, one straight parallel to the [010] plane and the other sinusoidal (zigzag) parallel to the [001] plane [126]. The pore openings of the channel systems are 5.4 x 5.6 Å and 5.1 x 5.5Å for the straight and sinusoidal channels, respectively [124,127,128]. The channel intersections in the MFI structure construct cages (~9 Å) that can include bulkier molecules. The MEL structure is very similar to the MFI structure, as evident in the similar XRD pattern shown in Fig. 28 (a). However, the MEL structure consist only of straight channels parallel to the [001] and [010] plane with the pore openings of 5.3 x 5.4 Å, where the intersection creates larger cages of 11.7 Å compared to the MFI framework, as illustrated in Fig. 28 (b) [129].

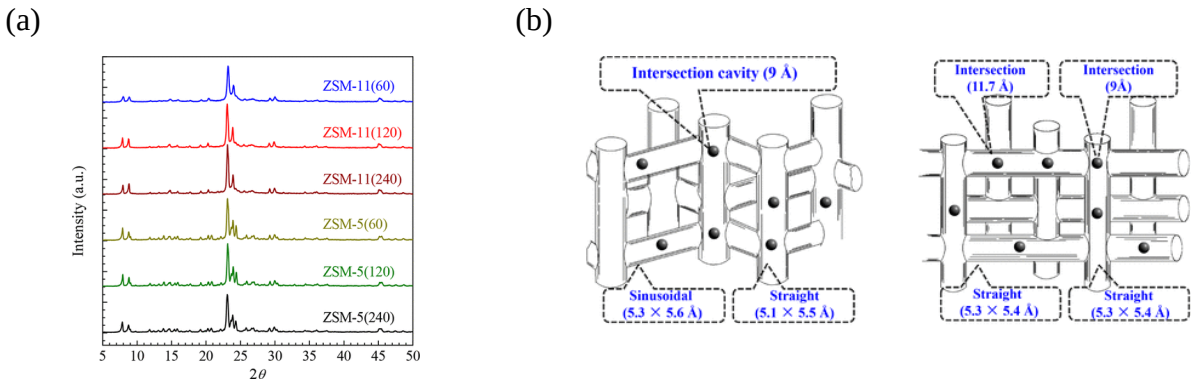


Fig. 28. (a) XRD pattern of the ZSM-5 and ZSM-11 catalyst with varying Si/Al ratios. (b) Topological structures of (left) ZSM-5 and (right) ZSM-11 zeolites with labeled pore sizes of corresponding channels. Obtained from [129].

The CHA framework is a three dimensional, 8 membered-ring pore zeolite, and similarly to the faujasite zeolite, it contains larger cages connected by narrow pore openings. The CHA pore openings are 3.8 x 3.8 Å, while the cages have a dimension of around 7.3 x 10 Å [130]. The different structures of the zeolites give them different shape-selectivity properties that control the hydrocarbon distribution obtained from these materials. This will be further elaborated in section 2.2.3.

2.2.1.1 The acid sites

The net change of the framework will be neutral if the only building block in zeolites is silicate, but a negative net charge will be constructed as Al^{3+} replaces Si^{4+} in the structure. This negative change must be compensated for by a cation, typically sodium, ammonium, or a proton in the most acidic form [124]. If the negative change is compensated for by a proton, a Brønsted acid site is created, as illustrated in Fig. 29 (a). Aluminosilicate zeolites can be synthesized over a range of aluminium content. The content affects the density of Brønsted acid sites, their strength, the thermal stability, and the hydrophilic or hydrophobic surface properties [124]. The Löwenstein's rule states that two contiguous tetrahedral containing aluminium with Al-O-Al linkages is forbidden which limits the Si/Al ratio to ≥1. However, other elements than silicon and/or aluminium can be used as the T-atom in the TO_4-building blocks, especially for construction of silicoaluminophosphates zeotype materials phosphate $[PO_4]^{3-}$ are used. The most common and the only conventionally used silicoaluminophosphate is used for the methanol-to-olefin process and is the H-SAPO-34 catalyst, having the CHA structure. The T-atoms in the TO_4 units are P^{5+} and Al^{3+} for silicoaluminophosphates. However, the charge will be balanced yielding a neural structure if only phosphate and aluminate are present in the structure. If Si^{4+} atoms replace P^{5+} atoms in the structure, a negative charge is created which is balanced by a proton, yielding the Brønsted acid sites, as shown in Fig. 29 (b) [131]. For the silicoaluminophosphates, it is the incorporation of silica into the structure that controls the acid site density.

(a) (b)



Fig. 29. Illustration of the construction of the Brønsted acid sites on (a) aluminosilicate and (b) silicoaluminophosphates. Adapted from [132].

The acid strength of the Brønsted sites are complex and are suggested to depend on; the distance and bond angle of the Al-OH-Si group (ZSM-5: 137-177°), the chemical composition of the zeolite structure, and the number of alumina atoms (the Si/Al ratio) [133]. By comparing the acidity of the H-SSZ-13 zeolite and the H-SAPO-34 zeotype with equal acid site densities, it is indicated that having phosphate in the structure reduces the acidity of the catalyst [134]. Bleken et al. [76] studied the H-SSZ-13 and H-SAPO-34 catalysts, with similar acid site density and crystal size, for the methanol conversion into olefins. The two catalysts produced nearly identical product distributions but the H-SSZ-13 catalyst had higher activity and more rapid deactivation compared to H-SAPO-34. This suggests that the higher acid strength is important for the activity but the acidity is also important for the coking rate as the deactivation is formed by carbon deposits, created by polymerization of product molecules (section 2.2.4). As illustrated in Fig. 30, the H-SSZ-13 catalyst showed higher conversion capacity at lower temperatures and the optimum temperature of the reaction shifted to lower temperatures. This shows that a more acidic H-SSZ-13 could be interesting for a more energy efficient methanol-to-olefins reaction [76].

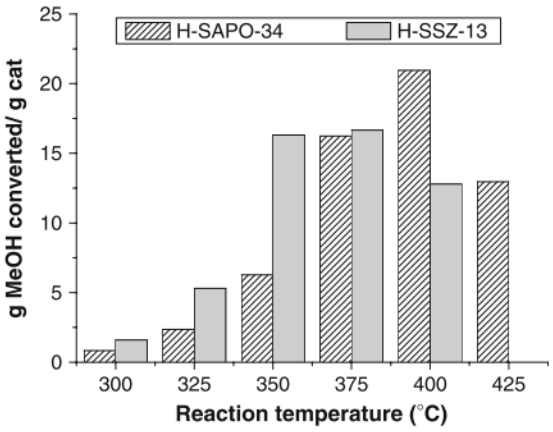
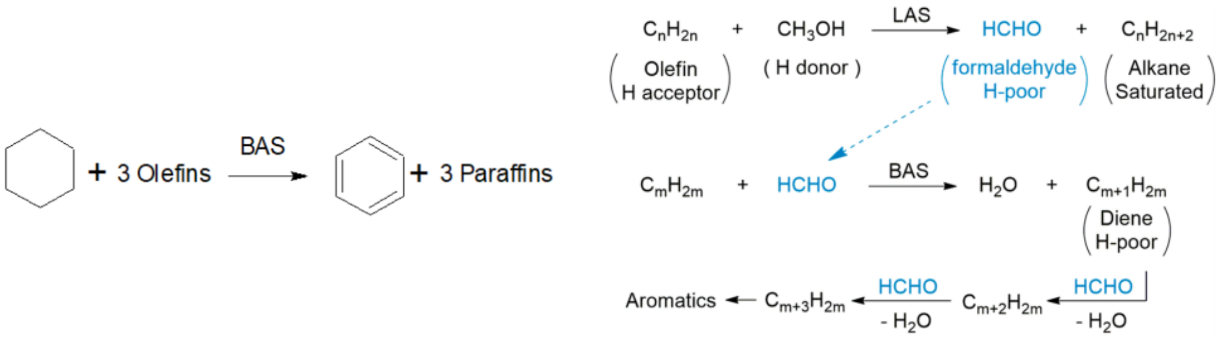


Fig. 30. The methanol conversion capacity by the time the catalyst was deactivated to 20% conversion in the accumulated methanol converted per gram of catalyst at various reaction temperatures. Obtained from [76].

The catalytic activity of zeolites stems from the Brønsted acid sites. Higher acid site density improves the zeolite activity and alters the hydrocarbon distribution [16]. In all zeolites, Lewis acid sites are constructed as well but the precise role of these sites on the catalyst activity, if any, is more uncertain. Müller et al. [135] have identified two separate hydrogen transfer pathways for the conversion of methanol into hydrocarbons over H-ZSM-5. In absence of methanol, the hydrogen transfer will occur between olefins and naphthenes via protonation of the olefins, as stated in Scheme 3 (a). This was concluded to only be dependent on the acidity of the Brønsted sites. The concentration of the Lewis sites involving Al^{3+} did not show any promoting effect on the hydrogen transfer between olefins

and/or napthenes, nor the methanol conversion activity. Thus, it was concluded that the overall activity of the catalyst to convert methanol is only determined by the concentration of Brønsted acid sites. In presence of methanol, a hydride transfer pathway including both the Lewis and Brønsted acid sites will dominate for the production of aromatics and paraffins. The pathway referred to as the methanol-induced hydrogen transfer pathway. Purely Lewis acidic ZSM-5 showed that methanol and propene react on Lewis acid sites to form propane and formaldehyde. Co-feeding methanol with formaldehyde clearly enhanced the production of aromatic species suggesting that formaldehyde reacts stepwise with olefins that eventually convert into aromatic molecules on the Brønsted acid sites. This leads to the proposal of the secondary methanol-induced hydrogen transfer pathway, as stated in Scheme 3 (b).



(a) (b)

Scheme 3. (a). Proposed reaction scheme for olefin-induced hydrogen transfer for the production of paraffins and aromatics. (b) The reaction network for methanol-mediated alkanes and aromatics formation involving alkanes from the methanol-induced hydrogen transfer reaction at the Lewis acid sites and aromatic formation from formaldehyde and alkene reaction over Brønsted acid sites. Obtained from [135].

At full methanol conversion the contribution of hydrogen transfer reactions between naphthenes and olefins for the formation of paraffins and aromatics will dominate (Scheme 3 (a)) and will be more pronounce at higher concentration of Brønsted acid site [135]. Whereas, at lower methanol conversion, the presence of methanol will inhibit olefin adsorption at the Brønsted acid site, resulting in this route to be insignificant [136]. Müller et al. [135] suggested that the majority of the hydrogen transfer product are formed via the methanol-induced hydrogen transfer pathway (Scheme 3 (b)) at partial methanol conversion. A correlation of the hydrogen transfer product (C_{1-4} paraffins and aromatics) for H-ZSM-5 zeolites with various Lewis acid site concentration, obtained at space velocities where 100 % methanol conversion is just reached, is illustrated in Fig. 31. This clearly indicates that the Lewis acidity plays a significant role for the selectivity of paraffins and aromatics for the methanol to hydrocarbon process, as long as methanol is present. This is evident in the increase in the hydrogen transfer product with the increasing Lewis acid site concentration at constant Brønsted acidity (Fig.

31). Interestingly, when complete methanol conversion is just reached, no significant effect on the selectivity of the hydrogen transfer product can be observed with increase or decrease in the Brønsted acid site acidity at ~constant Lewis acidity. This confirms that when methanol is present, the hydrogen transfer induced by olefins over Brønsted acid sites will be insignificant, compared to the methanol-induced hydrogen transfer over the Lewis acid sites.

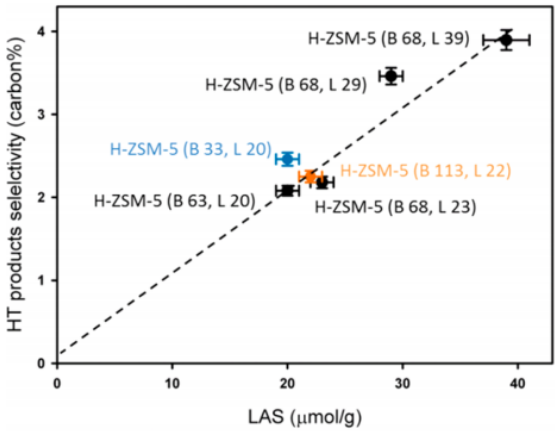
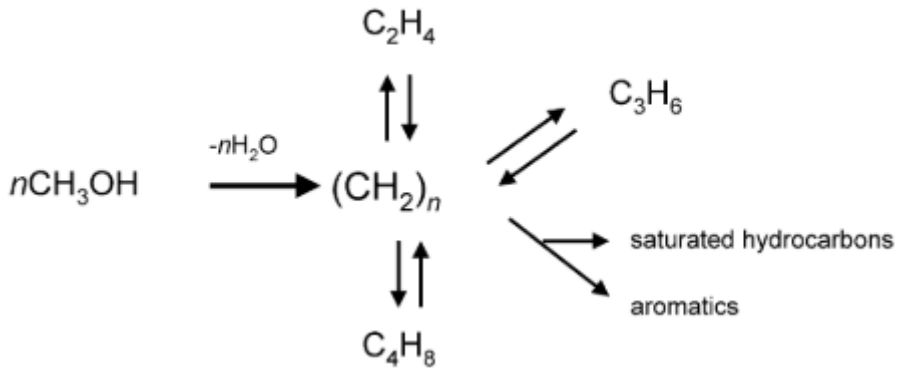


Fig. 31. Correlation of selectivity of hydrogen transfer products with different Lewis acid site concentrations for H-ZSM-5 samples, when complete methanol conversion is just reached. Reaction conditions: 450 °C, 178 mbar methanol, 2.8 h g_{cat}/mol_{MeOH} for (B113, L22) and 13.2 h g_{cat}/mol_{MeOH} for (B33, L20) and 6.6 h $g_{cat}/_{molMeOH}$ for the rest. Obtained from [135].

2.2.2 The hydrocarbon pool dual cycle reaction mechanism

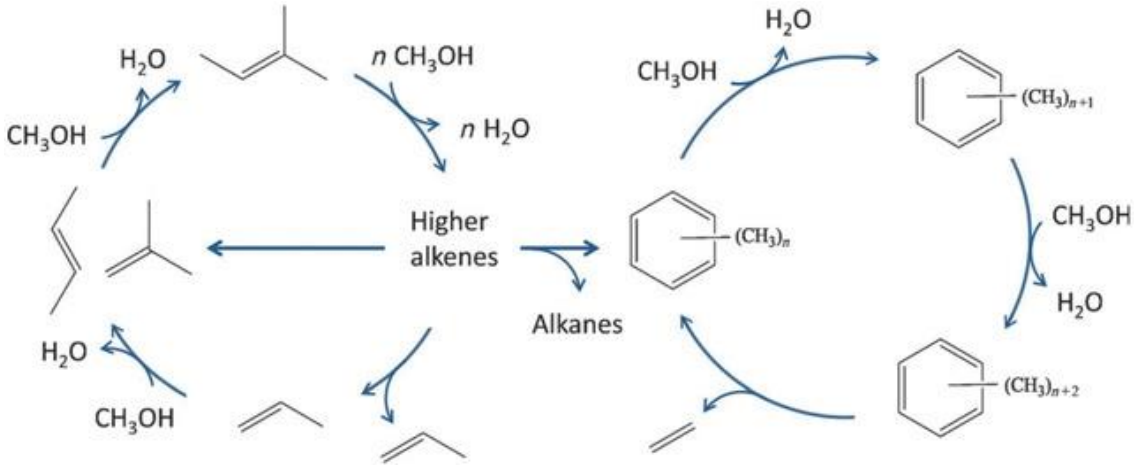
The hydrocarbon pool mechanism for describing the reaction mechanism from methanol to hydrocarbons over zeolite materials was first introduced by Dahl and Kolboe. This was a result of isotopic labelling experiments with ^{13}C-labelled methanol co-feed with ethylene, propylene, and ethanol over H-SAPO-34 catalyst [137,138]. The co-fed alkenes and ethanol were almost unreacted showing that the hydrocarbon products were exclusively formed from methanol. Based on this observation, the hydrocarbon pool mechanism was proposed as illustrated in Scheme 4. This mechanism is based on the assumption of an adsorbed hydrocarbon specie with the stoichiometry of $(CH_2)_n$. As shown in Scheme 4, methanol is continuously added to the reaction pool while olefins are entering and leaving the pool. The formation of paraffins and aromatics is considered end products.



Scheme 4. The hydrocarbon pool mechanism proposed by Dahl and Kolboe [137,138]. *The figure is obtained from* [14].

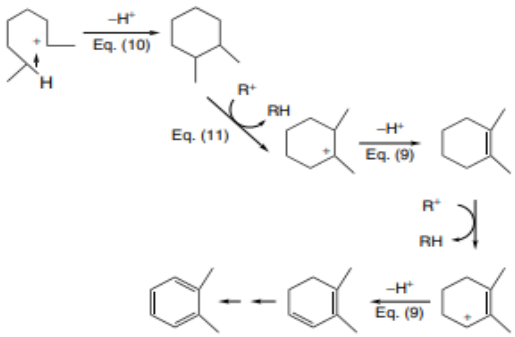
Studies on the confined hydrocarbon pool species found that methylbenzene is a key hydrocarbon pool intermediate which functions as catalytic centers for the methanol conversion to hydrocarbon reaction over SAPO-34 [139–141]. Haw et al. [142] used in-situ NMR with isotopic labeling to show that 1,3-dimethylcyclopenteny carbenium ions can function as intermediates in the synthesis of alkenes. For further understanding of the origin of the olefinic product formation, Svelle et al. [143,144] performed methanol conversion over a H-ZSM-5 zeolite with switching between $^{13}C/^{12}C$ methanol feed. The ^{13}C incorporation was slower for the ethylene and the aromatics as 0.5 min after the $^{12}C/^{13}C$ switching, the incorporation was only around 70-75%. This was in sharp contrast to the ^{13}C content in the C_{3-6} alkenes which at that time was 87-91%. However, the ^{13}C concentration in the aromatics and ethylene reached that of the heavier alkenes after 2 min. Similar isotopic switching between $^{12}C/^{13}C$ methanol co-fed with benzene and toluene showed that ethylene and propene contained 50 and 75 % ^{13}C [145]. The lower ^{13}C content in ethylene suggests that a large fraction of the ethylene

was formed via de-alkylation of methylbenzenes. These results show that the formation of ethylene is mechanical separated from the formation of higher alkenes. Propylene and higher alkenes are to a considerable extent formed from alkene methylation, where larger alkenes can be cracked to reintroduce lighter alkenes. This led to the proposal of the two mechanistic cycles (the dual cycle concept) that run simultaneously, as illustrated in Scheme 5.



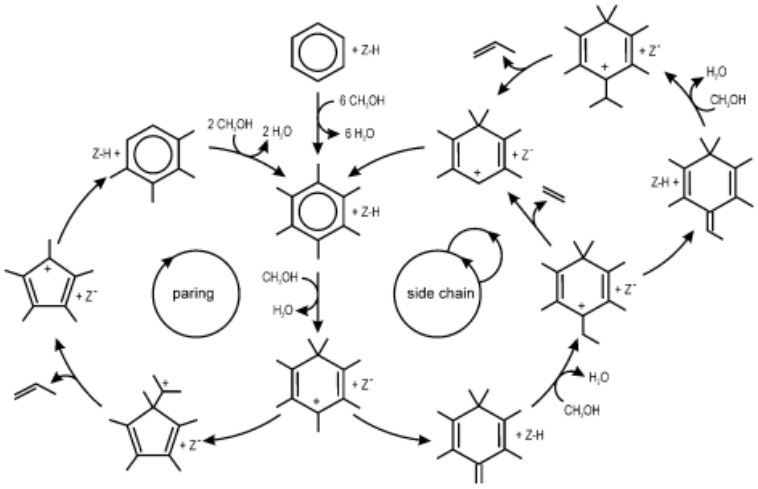
Scheme 5. The suggested dual-cycle hydrocarbon pool mechanism for the conversion of methanol over zeolites. Obtained from [14].

In the dual-cycle hydrocarbon pool mechanism, olefins oligomerize in the olefinic cycle to form hydrocarbons with sizes that allow the carbenium ion cyclization [66,67]. For the formation of aromatics, the carbenium ion cyclization is followed by a series of hydrogen transfer reactions where olefins act as hydrogen acceptors resulting in formation of aromatics and paraffins, as illustrated in Scheme 6. In Scheme 6, the aromatization starts with cyclization of carbenium ion followed by β-elimination and/or hydrogen transfer reactions [146].



Scheme 6. The reaction involved in the aromatization. Eq. (10), (11), (9) refer to the cyclization of carbenium ion, the β-elimination, and the hydrogen transfer reaction. Obtained from [146]

Olefins, that do not undergo carbenium ion cyclization, can be cracked through β-scission, which will form medium olefins [69]. The formation of light olefins, especially ethene and/or propene, occurs through the paring or/and the side chain methylation mechanism. These mechanisms are two distinct hypotheses for the formation of light olefins from aromatics and are illustrated in Scheme 7 [147]. The difference between the paring and the side-chain methylation mechanism is that the paring mechanism involves restructuring of the benzene ring to form a cyclopentadienyl carbenium ion that grows an alkyl chain. This alkyl chain can then be separated as an alkene. In the side-chain mechanism, the formation of an alkyl side chain occurs though methanol methylation of the benzene ring. In this mechanism, the aromatic ring is not broken during the formation of alkenes. Experimental evidence has been obtained for both mechanisms [14], and due to the differences in the pore architecture for the different zeolites, it could be expected that the mechanism may vary between the zeolites.



Scheme 7. The paring and the side-chain reaction pathways for de-alkylation of aromatics forming alkenes. Obtained from [147].

2.2.3 Introduction to the shape-selective nature of zeolite materials

The catalytic reaction in zeolites is happening in several steps. First, reactants diffuse through the zeolite pores to reach an active site. Then, the reactant is adsorbed on the active site, where a chemical reaction gives the adsorbed product. Lastly, the product is desorbed and diffuses out of the zeolite pores. Due to the well-defined size of the pore openings for the zeolite catalysts, they will act as molecular sieves [133].

The shape selectivity of zeolites can be divided into three types of shape selective phenomena: reactant selectivity, product selectivity, and restricted transition-state selectivity. Reactant selectivity occurs when molecules are too large to diffuse into the zeolite pores. This is visualized in Fig. 32, where iso-octane is too large to enter the zeolite pores, but the heptane molecule is not and cracks into butane

and propylene. Product selectivity is when some of the products formed are too bulky to diffuse out of the pores. These are either converted to less bulky molecules (by equilibration or cracking) or are assumed to be precursors for internal coke formation. An example is the methylation of toluene in Fig. 32, which will result in formation of 1,4-dimethylbenzene, rather than the 1,2-dimethylbenzene that is too bulky to diffuse out of the zeolite cages. Restricted transition-state selectivity is when certain reactions are prevented because the necessary transitions states are unable to form due to space limitations in the pores [148].

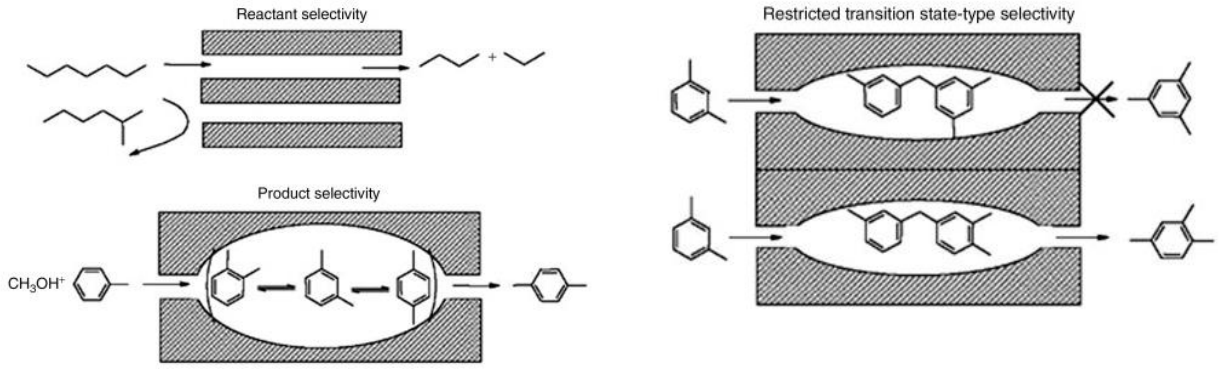


Fig. 32. Illustrations of three different types of shape selectivity phenomena. Obtained from [149].

The zeolite topology has through the shape selective phenomena great impact on the obtained hydrocarbon product. As illustrated in Fig. 33, the hydrocarbon product obtained from the small pore zeotype H-SAPO-34 is light hydrocarbons. By increasing the pore size, larger molecules can be formed, evident in the obtained product at higher retention time. Both the H-ZSM-5 and H-beta zeolites produce significant amounts of ethylene due to that the formation of ethylene primarily occurs through the aromatic cycle in the hydrocarbon pool mechanism (section 0). However, the larger pores of the H-beta zeolite enable the formation of more methylated aromatic hydrocarbon [150].

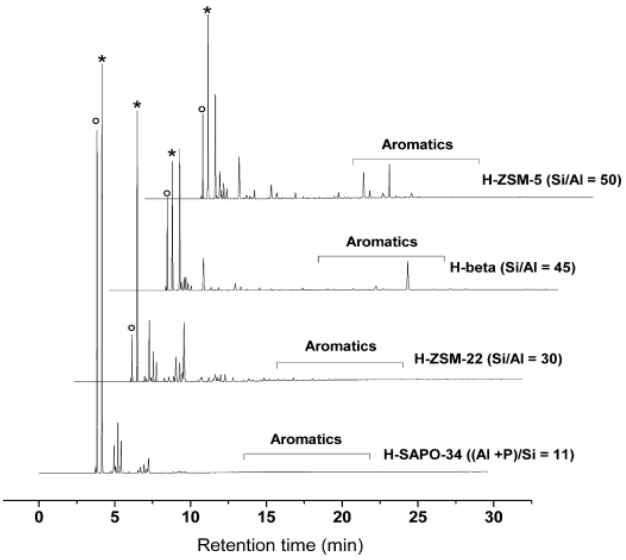


Fig. 33. GC chromatograms showing the hydrocarbon distribution at 100% methanol conversion over different zeolites topologies. Reaction conditions: 400 ºC and WHSV = 2 g/g/h. The reaction pressure was not reported and therefore assumed to be 1 atm. Obtained from [150].

The high selectivity of ethylene and propene obtained over the H-SAPO-34 catalyst is due to the product selectivity phenomena. In this catalyst, the narrow pores only allow smaller hydrocarbons to diffuse out, mainly ethylene and propylene. The formation of ethylene is believed to happen due to cracking of trapped aromatics species within its cage. Alshafei et al. [78] compared the product distribution from methanol conversion of the CHA and ERI zeolite frameworks and prepared both aluminosilicate (SSZ-13 and ERI) and silicoaluminophosphates (SAPO-34 and SAPO-17) versions of the structure. The obtained product distribution and the time to deactivate the catalyst, where the methanol conversion had dropped below 85 % or the dimethyl ether selectivity surpassed 50 %, is illustrated in Fig. 34. The stronger acidity of the zeolite catalyst enhances the deactivation rate, which has been previously discussed in section 2.2.1. The larger cages of the CHA structure and the low acidity of the H-SAPO-34 catalyst increase the catalyst stability with similar production of ethylene and propylene to the SSZ-13 catalyst. For the ERI structure, more selective production of ethylene was obtained at high acidity. The lower acidity of the SAPO-17 catalyst shifted the main product to propane and C_{5+} hydrocarbons. This is due to the shift in propagation of the olefinic cycle or the aromatic cycle in the hydrocarbon pool mechanism, where lower acidity reduces the propagation of the aromatic cycle and thus the formation of ethylene [78]. It is also evident form Fig. 34, that the slightly larger pores of the ERI structure compared to the CHA structure increases the average size of the hydrocarbon product.

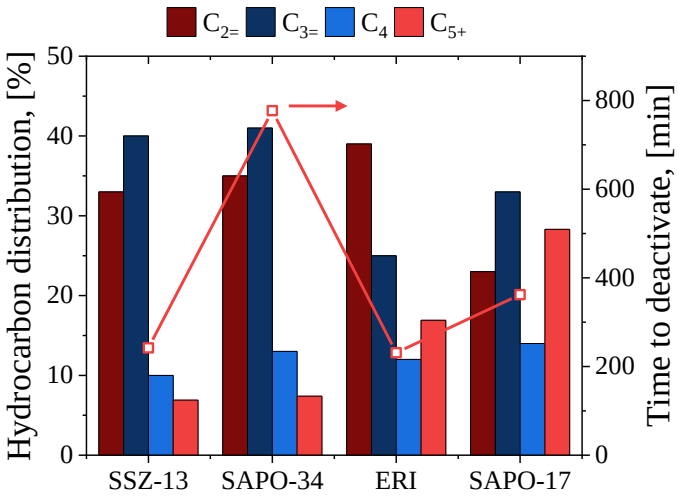


Fig. 34. The product distribution over different aluminosilicate (SSZ-13 and ERI) and silicoaluminophosphates (SAPO-34 and SAPO-17) catalysts at high methanol conversion (97-100%). The deactivation time is defined as the time it takes for the conversion to drop below 85 % or the dimethyl ether selectivity to surpass 50%, whichever occurs first. Reaction conditions: WHSV = 1.3 g/g/h and 400 °C. Obtained from [78].

Mikkelsen et al. [151] investigated the methanol conversion over H-ZSM-5 and H-beta zeolites. Similar to that observed by Teketel et al. [150], the larger pores of the H-beta zeolite promotes the aromatic cycle by allowing the formation of highly methylated benzene, such as the hexamethylbenzene. However, the result indicated that zeolite beta deactivates more rapidly than H-ZSM-5, as shown with the faster decline in the methanol conversion in Fig. 35. The formation rate of methyl- or polyaromatics species, that could be retained as carbon deposits blocking the active sites, are enhanced by larger pores allowing the formation of such species. This could explain the enhanced deactivation rate for the H-beta zeolite compared to the H-ZSM-5 catalyst, which are both three-dimensional structures with cages and intersecting channels [151,152]. These retained species further confine the space within the pore, increasing the product diffusion limitation and thereby changes the product selectivity to lighter hydrocarbons with time on stream [153]. This demonstrates that it is not only the acid site density and acidity of the zeolite/zeotype materials that affect the deactivation rate of the catalysts, but also the tonology of the catalyst.

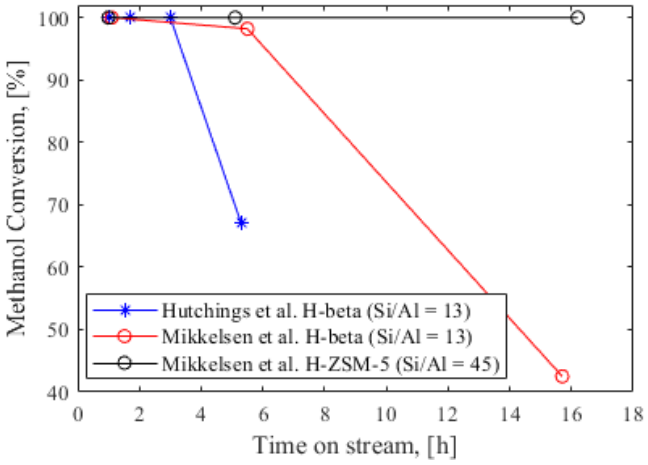


Fig. 35 Methanol Conversion as a function of time on stream over zeolite beta and ZSM-5. (*) represent data obtained from Hutchings et al. [152] *and (○) represent data obtained from Mikkelsen et al.* [151]. *Reaction conditions: 5 WHSV of 0.8 h^{-1} at 400℃ and 1 atm.*

2.2.4 Catalysts deactivation

Two deactivation phenomena are well established for the zeolite catalyst, the irreversible deactivation by dealumination and the reversible deactivation by carbon deposition, also known as coking. Dealumination is the permanent removal of the Brønsted acid site from the zeolite structure (structural damage), where coking is the deposition and accumulation of carbonaceous species that block the active sites. The formed coke can in large degree be removed by regeneration where the coke is burned off in a gas stream containing a small amount of oxygen [154].

2.2.4.1 Coke formation

The fast deactivation observed for the zeolite catalyst is caused by the formation of carbon deposits that creates large inactive molecules, called coke molecules. These large carbon structures are deposited on the inside and/or on the outer surface of the zeolite crystal. This phenomenon is also referred to as coking. The deactivation occurs due to steric blocking of the pores and/or by adsorption of coke species on the active site. This induces the diffusion limitation and inhibits the diffusion of reactants to the active site within the zeolite crystal [155]. The formation of coke molecules occurs through oligomerization and cyclization of olefinic products, which through hydrogen transfer reactions transform into mono-aromatics. Through alkylation, cyclization, and hydrogen transfer reactions, these mono-aromatics are transformed into bi-aromatics, tri-aromatics, and etc. [155]. In 2005, Haw et al. [156] introduced the “burning cigar” model for the methanol dehydration reaction over zeolite in a fixed bed reactor, as shown in Fig. 36 (a). The model describes how the deactivation over zeolite materials occurs inhomogeneously throughout the catalyst bed. The induction period (the lighting of the cigar) with very low methanol conversion consists until a sufficient concentration of reactive

hydrocarbon pool intermediates are formed. Hereafter, the catalyst bed is active and the deactivation proceeds from the inlet to the outlet of the catalyst bed. When the catalyst is fully deactivated, uncovered oxygenates will leave the reactor, referred to as the methanol slip, and the catalyst needs to be regenerated.

(a) (b)

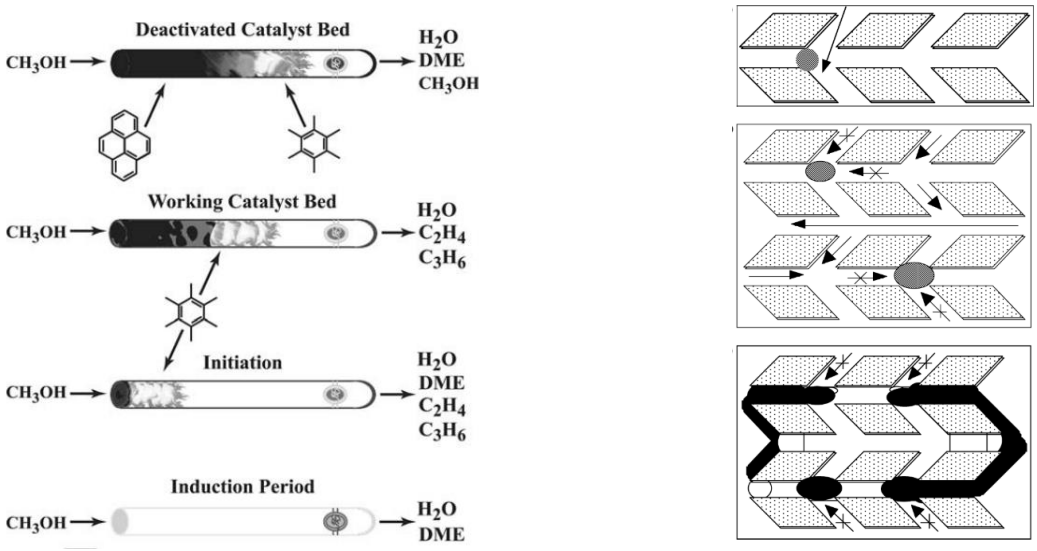


Fig. 36. (a) Illustration of the burning cigar model for the inhomogeneous deactivation of the zeolite in a fixed bed reactor. This demonstrates the movement of the catalytic zone with the coke formation. (b) Illustration of modes of deactivation by coke formation from n-heptane cracking over a H-ZSM-5 catalyst. First and second panel show site coverage by internal coke formation and the last panel show pore blockages formed by migration of internal coke molecules onto the zeolite surface forming external coke. Obtained from [156,157].

The pore structure of the zeolites has great influence on the deactivation rate from coke formation. For zeolites with no intersecting channels (one-dimensional or two-dimensional), the deactivation will occur more rapidly than for three-dimensional H-ZSM-5 zeolites [158]. As shown in Fig. 36 (b), the deactivation of a three-dimensional catalyst (H-ZSM-5) occurs initially through limitation of the access to the active sites, then blockage of the access to the sites for the channel intersection and lastly, at high coke content, coke molecules on the outer surface will block the access to the channels [155]. For zeolites composed of cages with narrow pore openings, such as the CHA structure, larger coke molecules are trapped inside the cage and deactivates the active sites within the cage. Thus, contributing to fast deactivation by the formation of trapped internal coke. Zeolites with larger pore size and/or with larger cages allow the creation of larger and more inactive coke molecules, such as methylated aromatics and poly-aromatics molecules (Fig. 37 (b)), which significantly contribute to faster deactivation [155,159,160]. Methanol conversion over a 10 membered-ring pore structured zeolite with similar crystal size and acid site density, but with different cage size, showed that larger cages induce the deactivation rate, as illustrated for the TNU-9 and IM-5 zeolite in Fig. 37 (a) [159].

By analyzing the retained material, it was found that zeolites with larger cages produced significantly larger coke molecules, as shown in Fig. 37 (b).

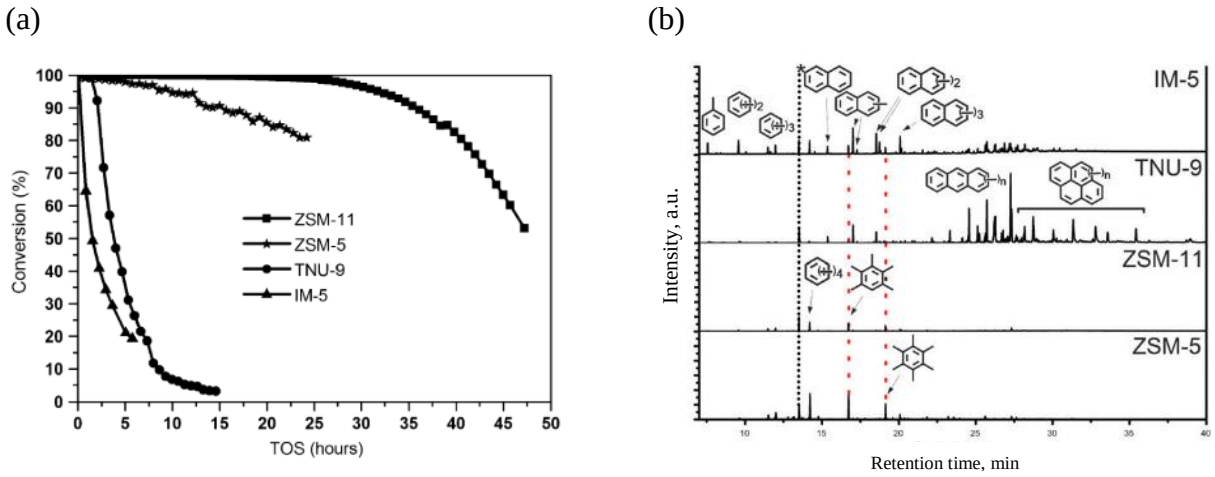


*Fig. 37. (a) Conversion of methanol over various zeolites with similar crystal size and acid site density. (b) Chromatogram of retained material at the end of the experiment for each zeolite. * indicates internal standard. Reaction conditions: 350 ºC, 1 atm and WHSV = 9 g/g/h. Obtained from* [159].

The deactivation rate by coke formation is not only influenced by the zeolite topology, but also by the acid site density and the acid strength. Strong acid sites result in faster coking rate due to an enhanced rate of reaction increasing the concentration of coke precursors [76,157]. By increasing the acid site density, the number of successive reaction steps along the diffusion path will similarly cause faster deactivation [157,161].

Molino et al. [162] synthesized a series of the one-dimensional ZSM-23 zeolite with different organic structure-directing agents, which created crystals with a large variety in crystal morphology and dimensions. Using these catalysts for methanol conversion showed that the catalytic lifetime is strongly influenced by the crystal size and morphology, as illustrated in Fig. 38 (a). Synthesizing the ZSM-23 catalyst with a small crystal size and with a spherical crystal morphology, reduced the diffusion path along the microchannel direction and improved the methanol conversion capacity, as shown in Fig. 38 (b). This clearly demonstrates that the zeolite crystal size is important for the deactivation rate, as the diffusion limitation worsens with increasing crystal size and thereby increases the retention of formed coke molecules within the pores. The formation of coke molecules will further limit the diffusion, creating a self-inducing effect that considerably increases the deactivation rate.

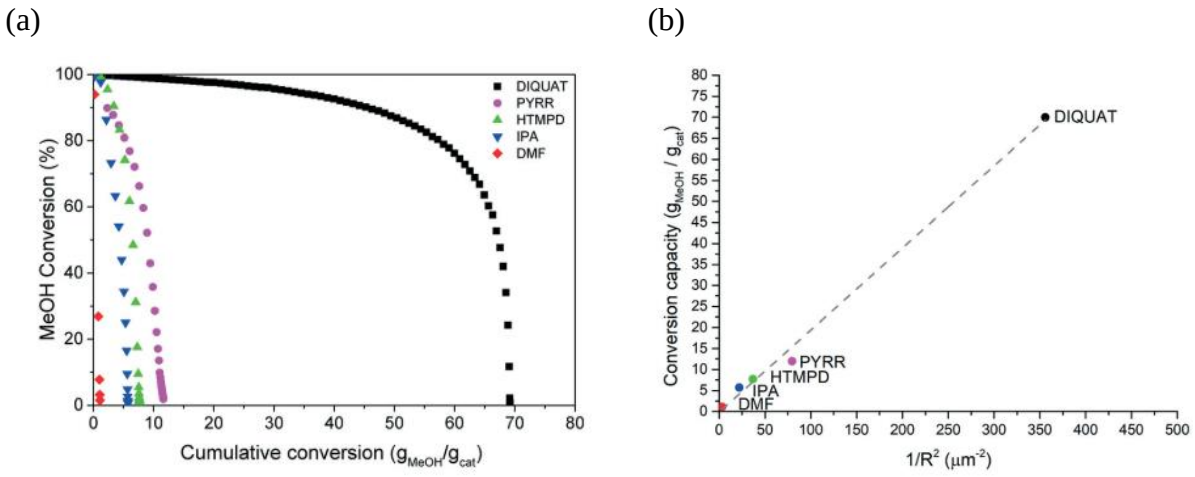


Fig. 38 The methanol conversion (a) and methanol conversion capacity (b) of ZSM-23 zeolites with different crystal size and morphology as a function of cumulative methanol conversion and the calculated reciprocal squared pore length, respectively. Reaction conditions: 400 ºC WHSV = 2 g/g/h. Obtained from [162].

Guisnet et al. [163] found that the composition and hence the formation of coke molecules depends strongly on the temperature, as illustrated in Fig. 39. At low temperature, condensation and rearrangement steps are involved in the formation of coke molecules, mainly resulting in non-polyaromatic species. The composition of the non-polyaromatic coke depends on the reactants. At higher temperatures (>350 ºC), the coke formation also includes various alkylation and hydrogen transfer reactions, resulting in the formation of polyaromatics coke species [163], where the composition are determined by the zeolite topology [159]. The proposed reaction path for coke molecules, shown in Fig. 39, suggests that coke molecules are directly formed from unsaturated species, such as alkenes, aromatics, cyclic alkenes, and particularly cyclic dienes, but not directly from alkanes and naphthenes.

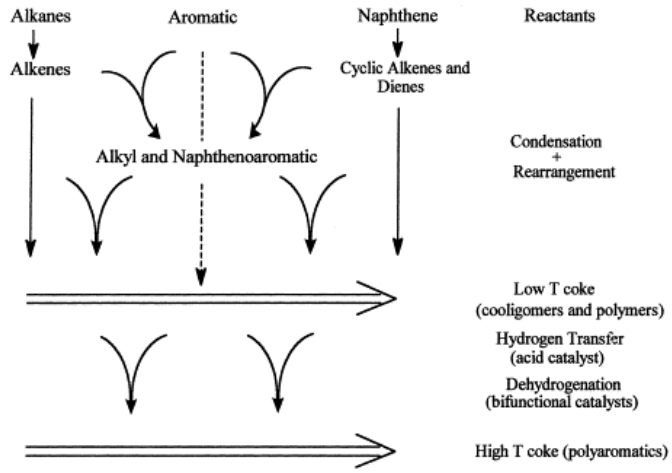


Fig. 39. The formation of coke from hydrocarbons over acid and bi-functional metal-acid catalysts. Obtained from [163].

The location of the deactivating coke, on the exterior surface of the zeolite crystals (external) or within the pore (internal coke), has been of great debate in literature. In 2008, Mores et al. [164] investigated

large H-SAPO-34 crystals with in-situ spectroscopy during the methanol-to-olefin reaction. They concluded that the coke deposition are mainly formed inside the H-SAPO-34 crystals. This is in contrasts to the H-ZSM-5 zeolite where both internal polyaromatic species and external graphite like carbon species were observed. Rojo-Gama et al. [165] investigated the deactivation of the H-ZSM-5 catalyst at different positions in a fixed bed reactor. As illustrated in Fig. 40, the analysis showed that a change in the length of the a- and b- unit cell vectors found through Rietveld refinement of XRD data correlated with coke content, acid site density, and catalyst surface area (BET). This indicates that trapped molecules within the zeolite crystal expands the unit cell, which makes XRD a powerful analysis technique for determining the degree of coking. Furthermore, these findings also suggest that the deactivation of the H-ZSM-5 catalyst is mainly caused by internal coke formation.

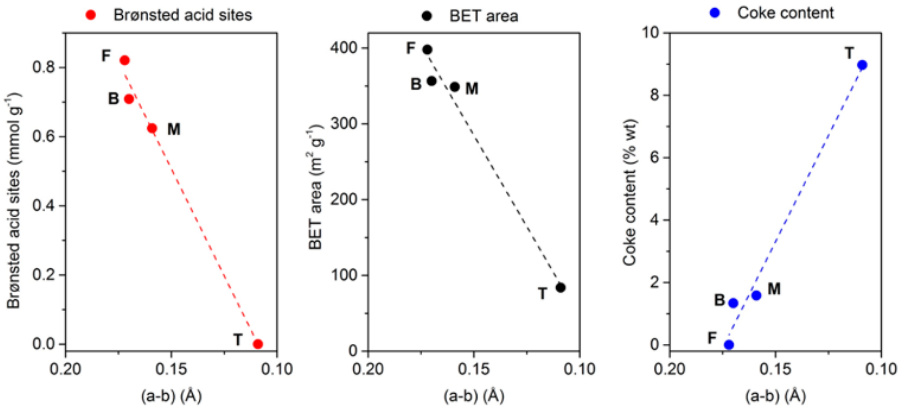


Fig. 40. Correlation between the acid site density, BET surface area, and coke content for the ZSM-5 with respect to the absolute change in the (a-b) unit cell parameter determined by Rietveld refinement of XRD data. F, T, M, and B correspond to the fresh catalyst and the catalyst extracted from the top, middle, and bottom of the fixed bed reactor. Reaction conditions: 400 ºC, 1 atm, and WHSV = 2 g/g/h

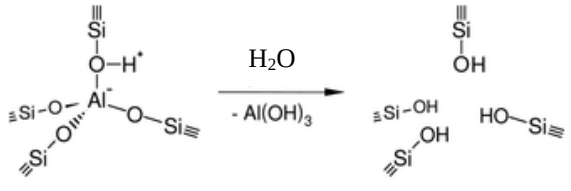
H-SAPO-34 is well known for its high catalytic activity for the methanol-to-olefin reaction and its fast deactivation due to coke formation. However, it is still considered to have the highest potential for conversion of methanol into light olefins among zeolite catalysts [79,80,166,167]. H-SAPO-34 can produce up to 80 % total yield of ethene and propene. As the H-SAPO-34 deactivates the $C_2^=/C_3^=$ ratio increases showing that carbon deposits influence the production of ethylene and propylene. Two hypotheses have been proposed to explain the increase in $C_2^=/C_3^=$ ratio as the catalyst deactivates. One hypothesis suggest that the change in $C_2^=/C_3^=$ ratio is due that carbon deposits limits the free space in the zeolite cages causing change to the transition-state shape selectivity. Thus, suppressing the formation of methyl benzenes with 5-6 methyl groups and thereby favoring ethylene formation [168,169]. The other hypothesis suggest that the carbon deposits limits the diffusion of larger products out of the zeolite causing changes in the product shape selectivity [170] or that it is a combination of

the two [171]. Hereijgers et al. [80] concluded, that the increase in the $C_2^=/C_3^=$ ratio is caused by product shape selectivity and not by transition-state shape selectivity, even for a severely deactivated catalyst. They concluded this based on experiments using $^{13}CH_3OH$.

The coke forms rapidly in H-SAPO-34 due to its large cages of 7.3Å x 10 Å and narrow pores with ring openings of 3.8 x 3.8 Å [80]. The deactivation is, therefore, generally accompanied by progressive formation of polyaromatic species, which limits the reactant diffusion and competitive adsorb to the active sites [79,80]. The main retained hydrocarbons from a spent H-SAPO-34 for methanol conversion has been identified as polymethylbenzene (trimethylbenzene, xylenes, and toluene), methylnaphthalenes, pyrene, and phenanthrene [80,172]. Analyses using visualization software by Marcus et al. [172] showed that pyrene and phenanthrene can exist within the cage, but there is little additional volume to accommodate reactants or transition states to convert phenanthrene to pyrene. This was confirmed by analysis of the retained hydrocarbons for a spent H-SAPO-34 where the pyrene/phenanthrene ratio was 0.414 which increased to 7.7 using H-SAPO-18 with larger cages.

2.2.4.2 Dealumination

The irreversible deactivation of zeolites under methanol conversion occurs through dealumination. The dealumination is defined as the removal of aluminium atoms from the zeolite framework causing the loss of Brønsted acid sites. Silaghi et al. [173] found through DFT calculations that water molecules adsorb on the aluminium atom in anti-position to the Brønsted acid site and force the breaking of the Al-O bond in the framework. The Al-O bonds hydrolyses until the Al atom is completely removed from the zeolite framework as $Al(OH)_3$. The activity of the dealumination is favored at a high water partial pressure and at high temperatures [154]. A simplified reaction scheme is illustrated in Scheme 8.



Scheme 8. Simplified reaction scheme of the dealumination of the Brønsted acid site in zeolites by water. Adapted from [174].

Dealumination removes the Brønsted acid sites resulting in a less active catalyst for methanol dehydration reactions. Aramburo et al. [175] found that by post-treating the H-ZSM-5 zeolite in steam, the activity dropped, but the stability significantly increased without altering the hydrocarbon distribution (Fig. 41). The decrease in the acid site density reduces the deactivation rate by coke formation,

as described in the previous section. However, the steaming post-treatment generated mesoporosity that together with the reduced acid site density limited the formation of polyaromatic coke molecules in the outer regions of the zeolite catalyst. Thus, dealumination of zeolite materials can reduce the coke formation rate and thereby improve the deactivation resistance. However, yielding a compromise between the catalyst activity and stability. Bjørgen et al. [161] reported that dealumination increased the stability of zeolite beta and changed the product selectivity towards alkenes. However, the gained stability also decreased the conversion and it was concluded that not much is gained if the lower acceptable limit is 80 % conversion to hydrocarbon.

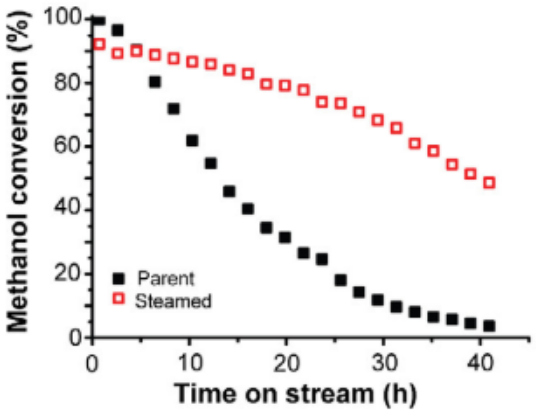


Fig. 41. Methanol conversion with time on stream for parent and steamed zeolite catalyst. Reaction Conditions: 350 ºC and WHSV = 5.56 g/g/h. Obtained from [175].

2.3 Direct Conversion of Synthesis Gas to Hydrocarbons

The growing interest for governments to reduce their emission of the greenhouse gas CO_2 have resulted in rising research for capture and converting CO_2 into synthetic fuel and usable chemicals. As illustrated in Fig. 42, CO_2 can be converted to CO by the reverse-water-gas-shift reaction or to alcohols, such as methanol, through the methanol synthesis (section 2.1). By combining the methanol synthesis and methanol-to-hydrocarbon process (section 2.2), the formed methanol from CO_2 is converted in the zeolite to form hydrocarbons. The hydrocarbon distribution is controlled by the reaction conditions but mainly from the zeolite topology and acidity. An obstacle for the methanol synthesis and methanol-to-hydrocarbon reaction is the substantial difference in optimal operating conditions. If methanol is immediately consumed in the methanol-to-hydrocarbon reaction, the equilibrium reaction of the methanol synthesis will be driven towards products, even at intermediate temperature and pressure, resulting in that the two reactions are compatible. An alternative to this pathway is the Fischer-Tropsch process where CO_2 is converted to CO, which further hydrogenates into hydrocarbon products. Through this process, hydrocarbons of various lengths are formed. To enhance the control of the hydrocarbon distribution, researchers have investigated the simultaneously cracking of the hydrocarbons in the zeolite pores [176,177]. However, one of the still existing challenges of the Fischer-Tropsch and the bi-functional catalytic processes, is the control over the carbon chain growth and to produce chemicals with desired properties; saturated, unsaturated, branch etc. It is required to overcome current challenges, such as low feed conversion, product selectivity, and catalyst stability, to synthetize olefins and aromatics from CO_2 with any conventional interest [178].

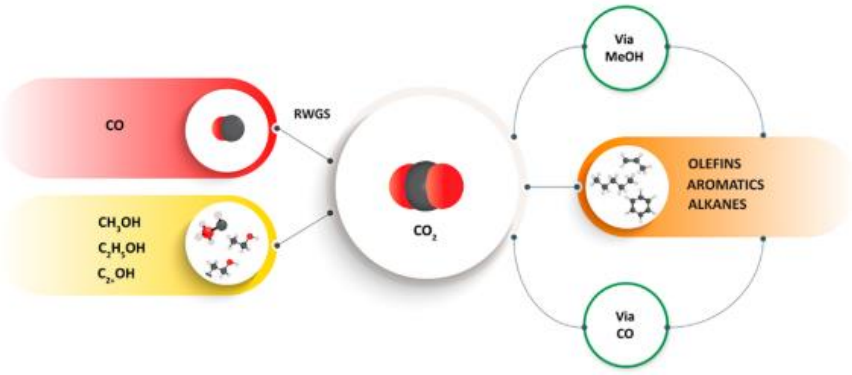
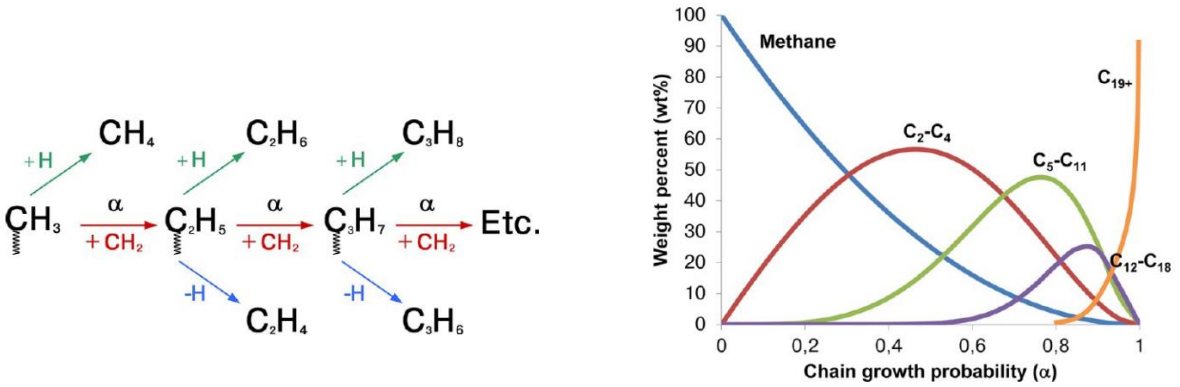


Fig. 42. Illustration of different routes for converting CO2 into CO, alcohols, or hydrocarbons through the Fischer-Tropsch or the combined methanol synthesis and methanol-to-hydrocarbon process. Obtained from [179].

2.3.1 Fischer-Tropsch

The Fischer-Tropsch process, FT, was published in 1923 by two German chemists, Fischer and Tropsch. In the early years, the FT process was used for the production of synthetic fuel from synthesis gas [6]. The catalysts for this process are iron or cobalt based, which irrespective of operation conditions produce a wide range of paraffins, olefins, and oxygenated products. The wide product distribution requires an energy-intense separation to achieve products with the desired properties. Thus, the selectivity control is the major challenge in FT synthesis, which is difficult to control on the metal surfaces due to a lack of confinement effects [180]. The product distribution can be altered by operation temperature, feed gas composition, pressure, catalyst type, and promotors [9]. In general, the product formation is accepted to be caused by surface polymerization reactions, and the mechanism is believed to follow a surface carbide mechanism, illustrated by a simplified scheme in Fig. 43 (a).



(a) (b)

Fig. 43. (a) Simplified surface carbide mechanism for the Fischer-Tropsch process. (b) The Anderson-Schulz-Flory model for prediction of the product distribution. Obtained from [7].

The polymerization reaction tends to follow the Anderson-Schulz-Flory distribution (ASF), which depends on the chain probability factor, α. The α parameter is controlled by the operation conditions of the FT process, as discussed above. The ASF model for prediction of the product distribution as a function of α is illustrated in Fig. 43 (b). According to ASF, the theoretical maximum yield of $C_{2\text{-}4}$ (paraffins and olefins), $C_{5\text{-}11}$ (gasoline), $C_{8\text{-}16}$ (jet fuel), and $C_{10\text{-}20}$ (diesel) are ~58 %, ~48 % , ~41 %, and ~40%, respectively [7–10,180]. The theoretical maximum yield of $C_{2\text{-}4}$ has long been considered the main constraint for industrialization of the FT process for effective and selective production of lower olefins. Methane and $C_{2\text{-}4}$ paraffins are considered undesirable products and studies have, therefore, mainly focused on improving the selectivity towards C_{5+} (liquid fuels) [180].

In recent years, some researchers have devoted their focus in to maximizing the lower olefin selectivity and to reduce the methane-, CO, or CO_2 selectivity. Studies have shown that promoted iron based FT catalysts with alkali metals, enhance the selectivity towards olefins and reduce the methane selectivity [181,182]. These alkali metals function as electron donors and increases the electron density on the catalyst while reducing the amount of adsorbed H_2 [178,181,182]. Hydrogenation of the formed olefins is minimized by controlling the adsorbed H_2 to be at a minimum. In general, iron based catalysts have shown a higher selectivity towards lower olefins than Co-based catalyst [7,181,183].

For direct conversion of CO_2 to olefins, the FT catalyst must include reverse-water-gas-shift reaction activity, which first converts the CO_2 to CO and water. The formed CO can further be converted to olefins through the FT synthesis [178]. Cobalt based FT catalysts exhibit no activity for the water-gas-shift reaction and must, therefore, be combined with a catalyst having this activity, such as manganese- or iron oxides [181]. Wang et al. [184] investigated the CO_2 hydrogenation on an alkali metal (Li, Na, K, Rb, and Cs) promoted iron catalysts supported on SiO_2, Al_2O_3, TiO_2, ZrO_2, mesoporous carbon (meso-C), and carbon nanotubes (CNT). The CO_2 conversion, CO selectivity, and hydrocarbon distribution of the different alkali promotions (with ZrO_2 as support) and oxides supports obtained at 340 ℃, 20 bar, H_2/CO of 3, and GHSV of 1200 mL/g_{cat}/h are illustrated in Fig. 44.

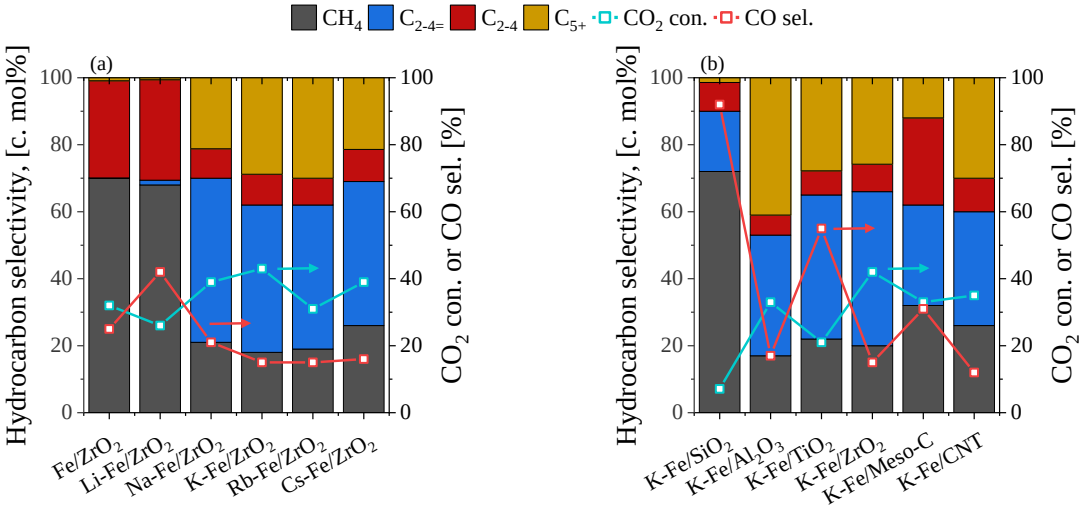


Fig. 44. (a) Catalytic performances of 1 wt% alkali metal promoted iron catalyst (10 wt% Fe) supported on ZrO_2 and (b) 1 wt% promoted iron catalyst (10 wt% Fe) on different supports. Meso-C and CNT denotes mesoporous carbon and carbon nanotube support, respectively. The supported Fe catalysts were prepared by the conventional impregnation method and the alkali metals were added by co-impregnation with aqueous solutions of an alkali metal salt. Reaction conditions: 340 ºC, 20 bar, H_2/CO = 3, and GHSV = 1200 mL/g_{cat}/h. Adapted from [184].

All alkali metals, except lithium, enhanced the light olefins selectivity. The sodium, potassium, and caesium promotion improved the conversion of CO_2. The best performance was obtained with 0.5-

1 wt% potassium promotion to iron catalyst supported on ZrO_2. In situ X-ray diffraction measurements suggested that the promotion with potassium accelerates the generation of the χ-Fe_5C_2 phase, which together with improved adsorption of CO_2 and decreased hydrogenation activity was concluded to cause the enhanced CO_2 conversion and light olefin selectivity. The SiO_2 support showed no activity towards formation of χ-Fe_5C_2, which was concluded to be the reason for the lower catalytic activity [184]. A possible explanation of this was that iron oxide supported on silicate does not undergo reduction easily and was, thereby, suspected to hinder the formation of χ-Fe_5C_2 [178]. Prior to reaction, the α-Fe_2O_3 was reduced to Fe_3O_4, FeO, or metallic iron (Fe^o), which in a CO/H_2 or CO_2/H_2 atmosphere can be converted into iron carbides, such as χ-Fe_5C_2, ε'-$Fe_{2.2}C$ and θ-Fe_3C. It was the χ-Fe_5C_2 iron carbide and Fe_3O_4 that was considered to be the active phase for the FT reaction and the reverse-water-gas-shift reaction [185].

Ramirez et al. [186,187] investigated the combination of a potassium oxide doped iron oxide with H-ZSM-5 and H-SAPO-34 catalysts for the conversion of CO_2 into hydrocarbons. The idea was to use highly acidic zeolites to fine-tune the product distribution and hopefully surpass the ASF distribution. In Fig. 45 (a), the product distribution upon adding H-ZSM-5 shows that a significant amount of aromatic product was formed with a selectivity of ~25 % achieved at a CO_2 conversion of ~50 %. The formation of the aromatic product occurs through the light olefins, especially ethylene and propylene, produced from the FT catalyst. The ethylene and propylene enter the zeolite crystal and forms a hydrocarbon pool species that reacts to form aromatics and butane (Fig. 45 (a)). That ethylene and propylene were intermediates of the aromatic formation was evident in the selectivity drop after the addition of the H-ZSM-5 catalyst. Furthermore, it was found that the aromatic selectivity was dependent on the acid site density and increased with increasing Si/Al ratio [186]. Smaller changes were observed with the use of a small pore zeotype H-SAPO-34 or a coated ZrS modified SAPO-34 catalyst, as illustrated in Fig. 45 (b). High olefin selectivity was observed with or without the addition of the solid acids, but a slight increase in the ethylene and propylene formation was obtained with the use of the SAPO-34 catalyst. The sulfated zirconia layer allowed the cracking of C_{5+} hydrocarbons which increased the lighter hydrocarbon selectivity. Diffusion limitations for the ethylene and propylene molecules caused by small pore openings of the SAPO-34 zeotype could limit the entering of such species into the cages. Thus, limiting the benefit of adding the zeotype, as ethylene and propylene are not forming significant amounts of hydrocarbon pool species. These results demonstrate that the use of zeolites with pores allowing olefins to diffuse to the acidic sites can alter the product distribution, when combined with a FT catalyst having high CO_2 hydrogenation activity. However, high

selectivity towards methane and low selectivity towards light olefins and aromatics is still a drawback of the FT process.

(a) (b)

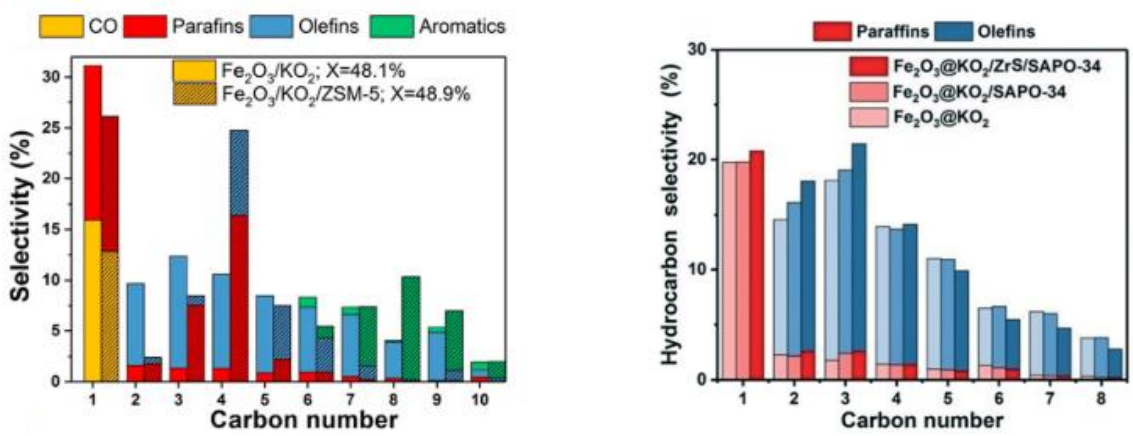


Fig. 45 The hydrocarbon selectivity for the (a) Fe_2O_3@KO_2/H-ZSM-5 and (b) Fe_2O_3@KO_2/H-SAPO-34 and Fe_2O_3@KO_2/ZrS/SAPO-34. Reaction conditions: 375 °C, 30 bar, H_2/CO_2 = 3, and 5000 mL/g/h. Obtained from [186,187].

2.3.2 Bi-functional catalytic conversion of synthesis gas to light olefins

In recent years a great interest for the conversion of CO or CO_2 into light olefins over the bi-functional catalyst have developed, and research studies are frequently published [24,27,28,110,111,188–204]. In the literature, a metal oxide capable of producing methanol at elevated temperatures with lower olefin hydrogenation activity, compared to a metallic-based methanol synthesis catalyts, are combined with zeolites/zeotypes having a topology with small pore openings. In this way, the methanol synthesis and the methanol-to-olefins process are combined. Mixing the catalysts in a mixed bed configuration (section 2.3.8) ensures immediate methanol conversion, allowing the methanol equilibrium to be exceeded at compromised reaction conditions. That the methanol equilibrium is exceeded shows the potential for having an efficient production of hydrocarbons in one step and minimizes the capital investment and the energy input for operating one reactor instead of two separate reactors (one at very high pressure). As we learned in section 2.1.3, metallic-based methanol synthesis catalysts have high CO_2 hydrogenation activity but also high olefin hydrogenation activity, causing the main product to be paraffins. For this reason, researchers have looked for other methanol synthesis candidates with lower olefin hydrogenation activity and have found Zn- and In-based mixed oxides to be interesting candidates for this application. This is due to their high methanol synthesis activity at elevated temperatures (section 2.1.4) where the subsequent methanol dehydration over solid acids are active. Especially, $ZnAl_2O_4$, $ZnGa_2O_4$, $ZnCr_2O_4$, ZnO-ZrO_2, and In_2O_3-ZrO_2 combined with the SSZ-13 or SAPO-34 catalysts have gained great attention for the direct production of light olefins [24,27,28,110,111,190–193,195,196,198–204].

Liu et al. [191] combined the ZnO-ZrO_2 and the SSZ-13 catalyst for the direct conversion of syngas into light olefins. Their results showed that high olefin selectivity above 80 % with a methane selectivity below 3 %. This demonstrates the superior light olefins selectivity, compared to that obtained by the Fischer-Tropsch process, but achieved at a low CO conversion of 10 %. It was demonstrated that the ZnO content, the acid site density of the SSZ-13, and the proximity of the two catalysts were crucial factors for the CO conversion and the light olefin selectivity. As shown in Fig. 46 (a), the optimal Zn-loading for the methanol synthesis activity was not beneficial for the light olefin selectivity. At Zn-loadings ≥ 1:4 Zn/Zr, the formation of hexagonal ZnO was confirmed by XRD analysis. The olefin hydrogenation activity increased with its formation and enhanced with increasing concentration of the crystalline ZnO phase. Similar to the results observed by Wang et al. [95], the methanol synthesis activity improves with Zn-loadings but declines with the substantial formation of crystalline ZnO at high Zn-loadings. Similar competition between the methanol synthesis activity and the olefin

selectivity with the Zn-content have been observed for the $ZnAl_2O_4$ and $ZnGa_2O_4$ mixed with the SAPO-34 catalyst [111,198]. This indicates a trade-off between the CO/CO_2 conversion and the light olefin activity. Li et al. [198] combined pure ZnO with SAPO-34 and found that the ZnO crystal size affects the olefin hydrogenation activity where smaller crystals have lower activity, as illustrated in Fig. 46 (b). These results suggest that it is important to maximize the Zn content without formation of large crystalline ZnO for improving the CO conversion and the olefin selectivity.

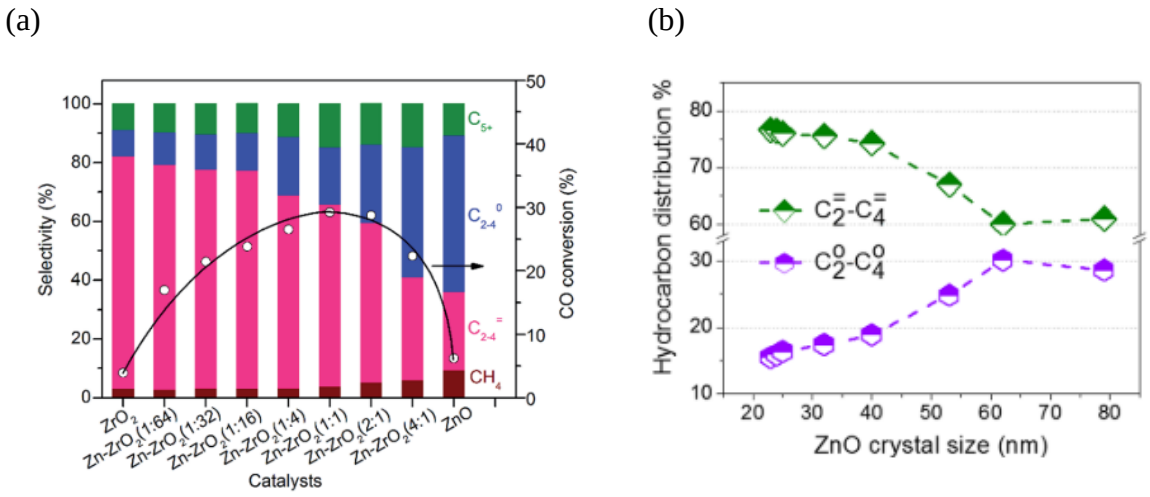


Fig. 46 (a) The effect of Zn/Zr molar ratio on the CO conversion and hydrocarbon distribution for the bi-functional ZnO-ZrO_2/H-SSZ-13 catalyst. The selectivity of CO2 did not change much with the Zn/Zr ratio and stayed at 41-45 %. Reaction conditions: 400 ºC, 30 bar, 30 mL/min, H_2/CO = 2 and 0.6 g of catalyst (oxide/zeolite = 1:2). (b) The light paraffin and light olefin selectivity with the change in the ZnO crystal size. The catalyst was a mixture of ZnO and SAPO-34 in a mass ratio of 2:1. Reaction conditions: 400 ºC, 40 bar, GHSV=1600 mL/g/h, and H_2/CO = 2.5. Obtained from [191] and [198].

By kinetic studies Liu et al. [191] concluded that the formation of oxygenates (methanol and dimethyl ether) was the rate-determining step for their bi-functional catalyst. The mass ratio between the oxide and zeolite in this study was 1:2 and it could be expected that increasing this ratio would improve the syngas conversion. However, if the metal oxide contributes significantly to the hydrogenation of olefins, the longer residence time over the metal oxide component could yield a more saturated product. The acidity and acid site density for the zeolite/zeotype catalyst have shown influence the olefin hydrogenation activity as well. DeWilde et al. [205] showed that under $CO_2/CO/H_2O/H_2$ atmospheres (products and reactants of the methanol synthesis), the main propene hydrogenation activity occurred through the acid sites in SAPO-34. In the literature [28,189,190] great inconsistencies in the optimal mixing ratio are reported, which could be a result of differences in where the primary olefin hydrogenation occurs, at the metal oxide or at the solid acid.

Similar to the Zn-based catalyst, the In_2O_3 catalyst have shown a great potential for the direct conversion of syngas to olefins when combined with SSZ-13 and SAPO-34 catalysts [192,193,196,199].

Gao et al. [190] studied the CO_2 conversion to light olefins over a In_2O_3-ZrO_2 mixed SAPO-34 catalyst and managed to achieve a light olefin selectivity of ~80 % at a CO_2 conversion of 35 %. The hydrocarbon distribution was affected by the bed configuration of the two catalysts where too close proximity made methane the main hydrocarbon product. This indicates some instability problems of the In-based catalysts and suggests some mobility of the indium [206].

2.3.2.1 Space velocity

The changes in the hydrocarbon distribution and CO_2 conversion with the residence time over ZnO and In_2O_3 supported on ZrO_2 mixed with SAPO-34 catalyst are shown in Fig. 47 (a) and (b) [27,190]. In both cases, the CO_2 conversion increases with increase in residence time showing that longer contact time over the metal oxide component increases the CO_2 conversion. On the other hand, longer residence time increases the light paraffin selectivity, creating a more saturated product. The thermodynamic equilibrium of the alkane dehydrogenation reaction in the hydrogen rich atmosphere shows that longer residence time should lead to more hydrogen incorporation [207]. A surprising result is that by doubling the residence time, the CO_2 conversion does not increase with the same factor. This suggests that there is some kind of inhibition of the methanol synthesis activity at higher residence time, which could be caused by product inhibition. The results in Fig. 47 shows that a compromise in residence time should be made for achieving a high olefin selectivity at a relevant CO_2 conversion.

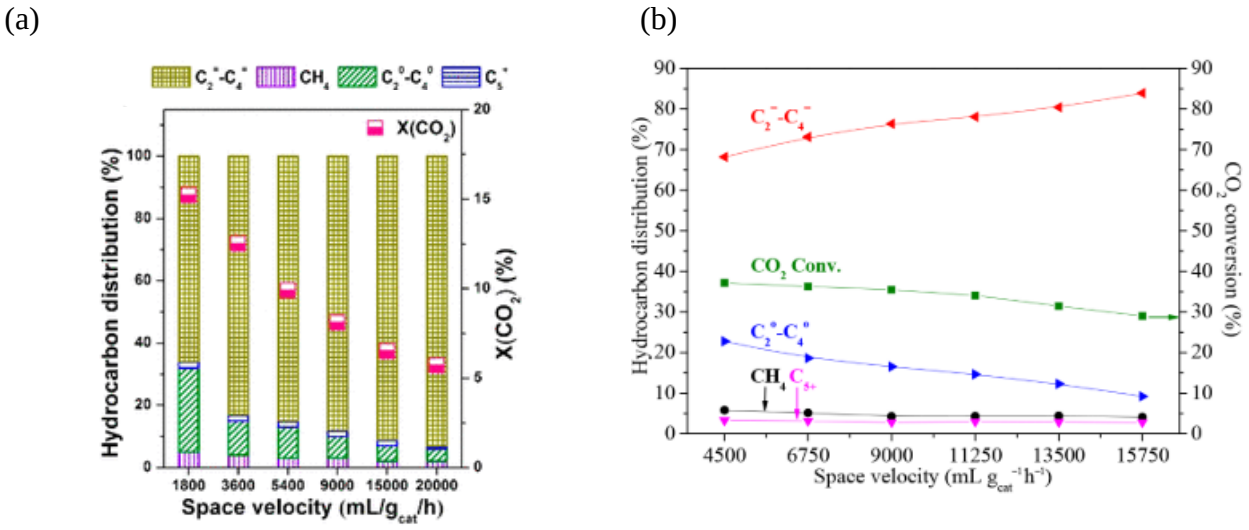


Fig. 47 The CO_2 conversion and hydrocarbon selectivity at different residence times for (a) ZnO-ZrO_2 and (b) In_2O_3-ZrO_2 mixed with H-SAPO-34. Reaction conditions: (a) 380 ºC, 20 bar, H_2/CO = 3, and oxide/zeolite = 1 and (b) 400 ºC, 30 bar, H_2/CO = 3, and oxide/zeolite = 2. Obtained from [27,190].

2.3.2.2 Reaction temperature

Higher temperature increases the olefin hydrogenation activity, evident in Fig. 48 with the increasing light paraffin selectivity. This occurs for both the ZnO-ZrO_2 and In_2O_3-ZrO_2 catalyst mixed with the SAPO-34 catalyst [27,190]. The endothermic nature of the reverse-water-gas-shift reaction result in improve thermodynamic driving force at higher temperatures resulting in higher CO productivity from CO_2. Even though the CO_2 conversion increases with temperature, the hydrocarbon yield will decrease as faster CO productivity reduces the CO_2 conversion to hydrocarbons. Therefore, there must be an optimal temperature range where a compromise between CO_2 conversion, CO selectivity, and olefin selectivity will yield the highest light olefin productivity.

(a) (a)

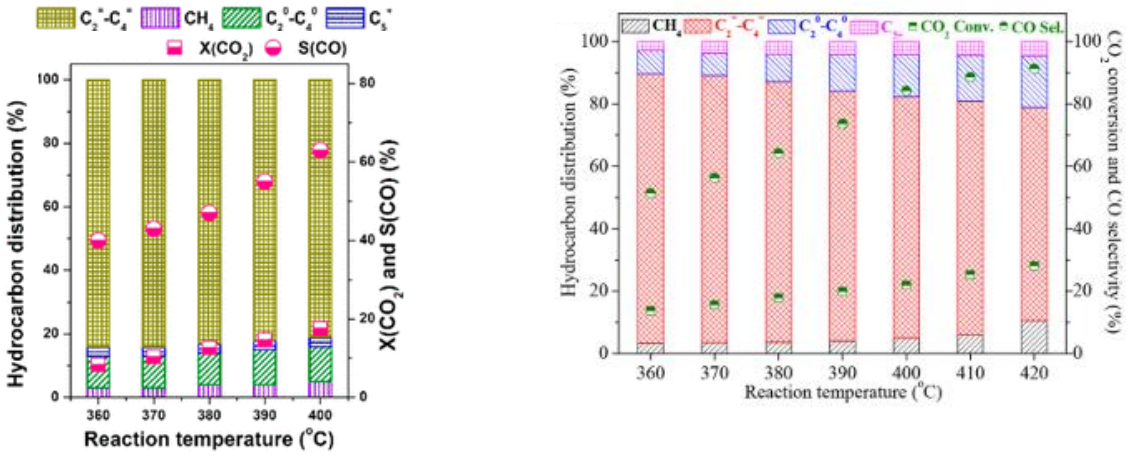


Fig. 48. The CO_2 conversion, CO selectivity, and hydrocarbon selectivity at temperatures for (a) ZnO-ZrO_2 and (b) In_2O_3-ZrO_2 mixed with H-SAPO-34. Reaction conditions: (a) 20 bar, H_2/CO = 3, GHSV =3600 mL/g/h, and oxide/zeolite = 1 and (b) 30 bar, H_2/CO = 3, GHSV =9000mL/g/h, and oxide/zeolite = 0.5. Obtained from [27,190].

In Fig. 49 (a), the calculated normalized yield for different metal oxides mixed with SAPO-34 indicates an optimal reaction temperature in the range of 360-400 ºC. The reaction conditions for the optimal production of light olefins for the different bi-functional catalyst are shown in Fig. 49 (b). These results indicate that despite differences in operating pressure and residence time, the highest productivity is obtained at temperatures in this range [27,111,190,194]. At lower temperatures, the methanol dehydration activity over SAPO-34 will be too low resulting in that unconverted oxygenate will leave the reactor. At higher temperatures, both the increase in the hydrogenation and reverse-water-gas-shift activity reduce the olefinic yield.

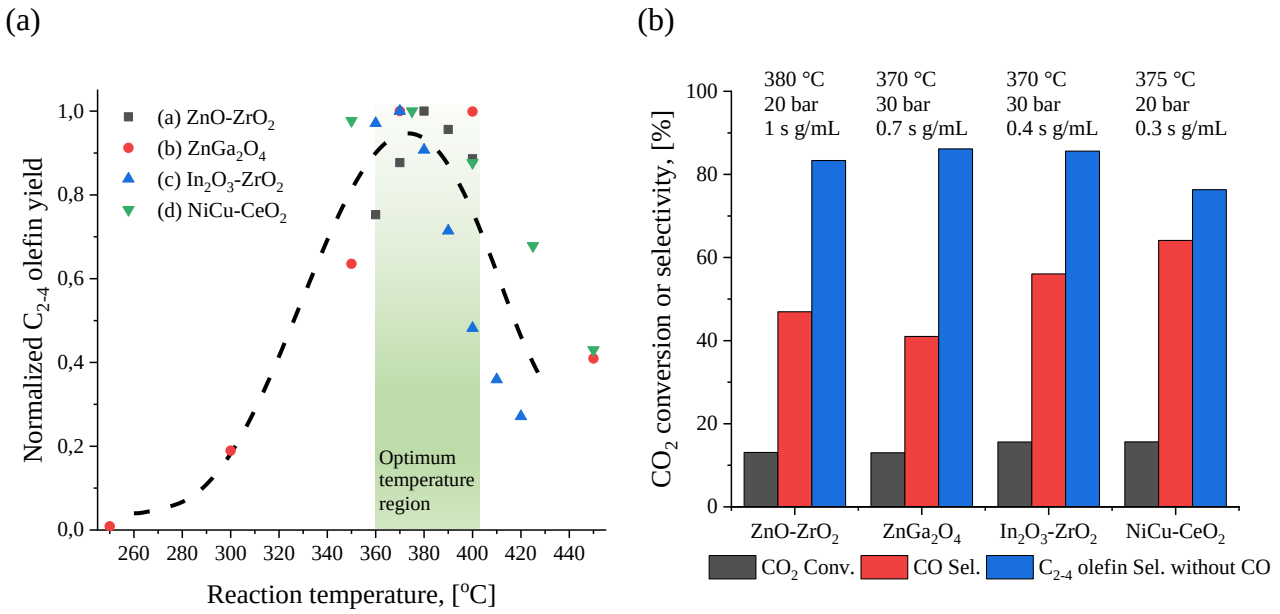


Fig. 49. (a) Normalized $C_{2-4=}$ yield for CO_2 hydrogenation over composite catalysts against reaction temperature. The $C_{2-4=}$ yield is calculated by: $Y_{C_{2-4=}} = X_{CO_2} \cdot (1 - S_{CO}) \cdot S_{C_{2-4=}}$ where the normalized yield is found by dividing the yield with the best obtained yield for that specific metal oxide/SAPO-34 catalyst. (b) The CO2 conversion, CO, and light olefin selectivity at the optimal temperature for light olefin productivity for the different metal oxide/SAPO-34 catalysts. Reaction conditions: (a-a) 20 bar, H_2/CO = 3, GHSV =3600 mL/g/h, and oxide/zeolite = 1, (a-b) 30 bar, H_2/CO = 3, GHSV = 5400 mL/g/h, and oxide/zeolite = 0.5, (a-c) 30 bar, H_2/CO = 3, GHSV = 9000 mL/g/h, and oxide/zeolite = 0.5, and (a-d) 20 bar, H_2/CO = 3, GHSV =12000 mL/g/h and oxide/zeolite = 0.5. Data obtained from [27,111,190,194].

2.3.2.3 Reaction pressure

Gao et al. [190] investigated the effect of the reaction pressure on the catalytic performance for the In_2O_3-ZrO_2 catalyst. The results are illustrated in Fig. 50. The results show that upon increasing the pressure, the CO_2 conversion increases and the CO selectivity decreases, which significantly improves the hydrocarbon yield. In the hydrogen rich atmosphere, the increasing pressure also leads to increased hydrogen incorporation into the hydrocarbon product. By increasing the pressure from 10 to 50 bar, the olefin selectivity decreases by ~20% where the CO_2 conversion to hydrocarbons increases from ~1.5 to ~11 %. This trend has also been observed on Zn-based catalysts [110,191,195] showing that a high olefins selectivity is obtained at low CO_x conversion. This demonstrates that the difference between the optimal operating conditions for the methanol-to-olefins and the methanol synthesis process limits the performance of the bi-functional catalysts. However, it still shows a high potential for improvement by synthesizing alternative materials to break these limitations. Altering the acidity or acid site density of the zeolite/zeotype materials may yield a solution for this problem.

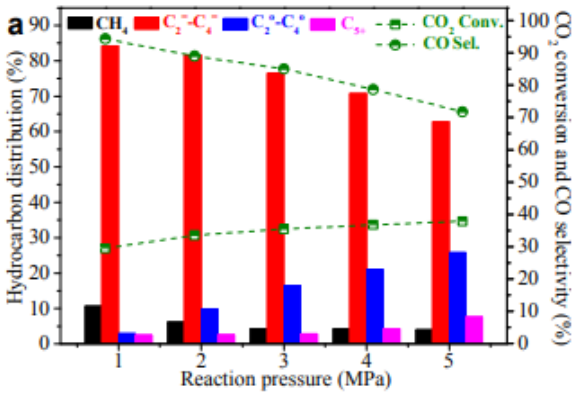


Fig. 50. The CO_2 conversion, CO selectivity, and hydrocarbon distribution at different reaction pressures over In_2O_3-ZrO_2/SAPO-34. Reaction conditions: 380 ºC, H_2/CO = 3, GHSV =9000mL/g/h, and oxide/zeolite = 0.5. Obtained from [190].

2.3.3 Acidity effect on the light olefin selectivity

The acidity of zeolites are dependent on factors such as the acid site density and the chemical composition of the zeolite [133]. As discussed in section 2.2.1, by synthesizing chabazite structured silicoaluminophosphates (zeotypes), the acid strength can be reduced even at similar acid site densities [76,134]. The SSZ-13 and SAPO-34 catalysts are examples of a zeolite and its counter zeotype with chabazite structure. Liu et al. [28,191] combined a ZnO-ZrO_2 binary oxide with these solid acids and varied the acid site density of both. Their results show that the acid site density is a key factor for achieving high light olefin selectivity, as illustrated Fig. 51 (a) and (d). The density of the Brønsted acid sites were determined by the high temperature peak from NH_3-temperature-programmed-desorption and by quantifying the ammonia adsorbed by Fourier transform infrared spectroscopy. The results shows that low acid site densities cannot fully convert the formed methanol synthesis into hydrocarbons, resulting in that unconverted oxygenates will leave the reactor. The low methanol dehydration activity hampers the CO conversion (Fig. 51 (a) and (c)) indicating that at low acid site densities, the rate-determining step is the methanol dehydration reaction. With the increase in the acid site density, both the CO conversion and the light olefin selectivity increase and the light olefin selectivity reaches an optimum around 0.1 mmol per g for both solid acids. Increasing the acid site density beyond this concentration showed a slower decrease in the light olefin selectivity for the SAPO-34 catalyst (Fig. 51 (a)) than observed for the SSZ-13 catalyst (Fig. 51 (b)). This indicates that the higher acid strength of the SSZ-13 catalyst leaves a smaller range in the acid site density to achieve the best olefin selectivity. In both cases, the decrease in the olefin selectivity was caused by an increase in selectivity towards light paraffins, indicating higher hydrogenation activity with increasing acid site density. As shown in Fig. 51 (b), methanol conversion over the SAPO-34 catalysts, under

same reaction conditions as used for the syngas conversion over the bi-functional catalyst, demonstrates that in a hydrogen rich atmospheres, the SAPO-34 itself has hydrogenation activity. The hydrogenation activity enhanced upon increasing the acid site densities. Having the right acid density to ensure complete methanol conversion is important for shifting the methanol equilibrium reaction and thereby increase the CO_x conversion. Having too high acid site density increases the olefin hydrogenation activity and thus again indicates a trade-off between CO_x conversion and the light olefin selectivity.

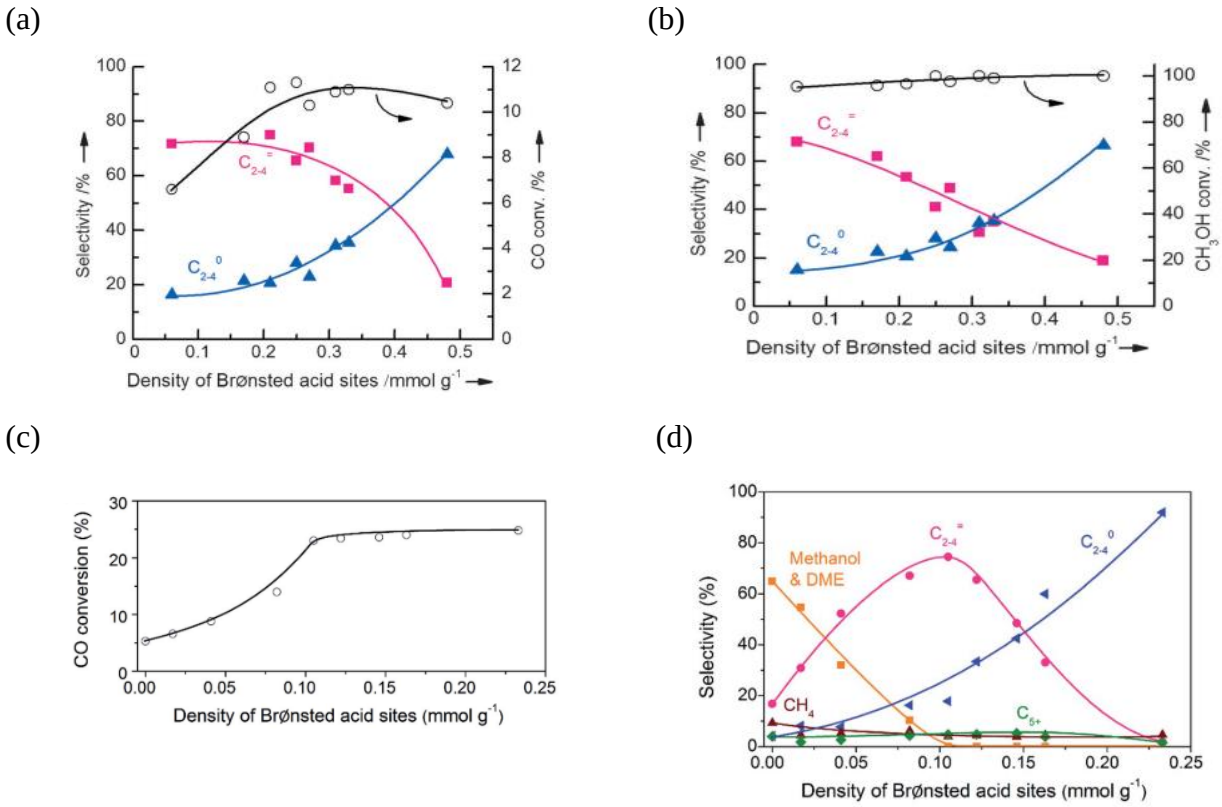


Fig. 51. (a) The hydrocarbon selectivity and the CO conversion with the change in acid site density for the SAPO-34 component in the ZnO-ZrO2/SAPO-34 bi-functional catalyst. (b) Methanol conversion over SAPO-34 with different acid site density. (c) The CO conversion and (d) the hydrocarbon selectivity with the change in acid site density for the SSZ-13 component in the ZnO-ZrO2/SSZ-13 bi-functional catalyst. Reaction conditions: (a-b) 400 ºC, 30 bar H2/CO = 2, GHSV = 3600 mL/g/h, and oxide/zeolite = 0.5 (c-d) 400 ºC, 30 bar H2/CO = 2, GHSV = 3000 mL/g/h, and oxide/zeolite = 0.5. Obtained from [76,134].

Very recently the research group of Bao et al. [208] showed that it was possible to break the trade-off between activity and selectivity for the bi-functional catalyst concept by incorporating germanium into the AlPO-18 zeotype framework, as illustrated in Fig. 52 (a). The germanium substitution into the framework attenuated the acid strength of the Brønsted acid sites that allowed for enhancing carbon-carbon coupling with increasing acid site density while inhibiting the olefin hydrogenation activity. In Fig. 52 (b), ethylene hydrogenation activity over the different AlPO-18 catalysts shows that

the addition of germanium significantly reduces this reaction. The lower hydrogenation activity allowed for optimizing the operation conditions and a light olefin selectivity of 83 % was achieved with a CO conversion of 85 %, which almost doubles the light olefins yield previously published in literature [208]. Thus, altering the acid strength of the solid acid to limit the olefin hydrogenation activity and combine it with metal oxides having high methanol synthesis activity could yield an efficient route for direct conversion of CO_2 into olefins.

(a) (b)

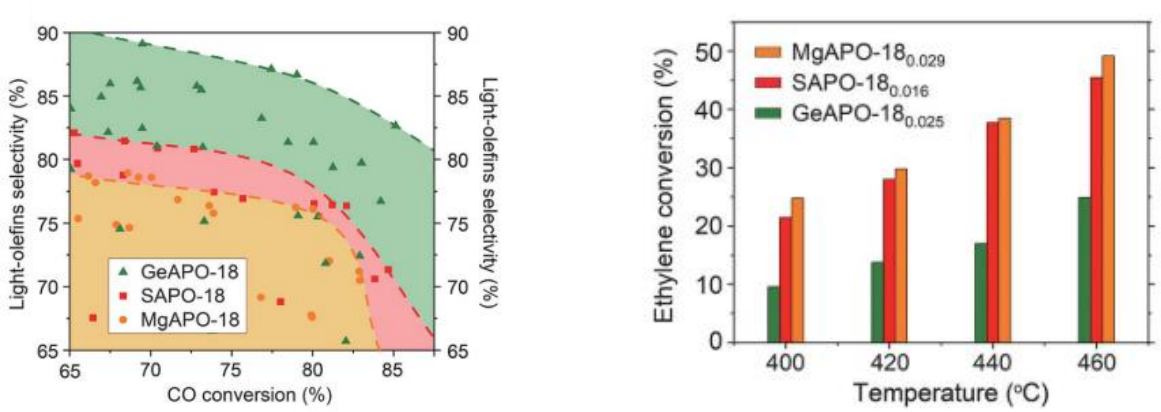


Fig. 52. (a) The selectivity of light olefins at different CO conversion. (b) Ethylene hydrogenation at different temperatures for the MgApO-18, SAPO-18, and GeAPO-18. Reaction conditions: (a) 410 to 480 ºC, 60 bar, H_2/CO = 2.5, and 1500-6000 mL/g/h. (b) 40 bar, 200 mL/min with 1.2 % ethylene in 66.6% hydrogen with the rest being argon. Obtained from [208].

2.3.4 Bi-functional catalytic conversion of synthesis gas to aromatics

Aromatic compounds such as para-xylene and styrene are used as monomers or monomer precursors for the production of plastic materials. Aromatics compounds have high anti-knock engine values making them good octane boosters for fuels. For this reason, fuels such as gasoline contain aromatic compounds to achieve a high-quality fuel. In Europe, the concentration of aromatic compounds in gasoline is restricted to 35 wt% due to environmental considerations [209,210], but still account for a larger portion of the fuel. The main production of aromatics comes from reforming of naphtha which is obtained as a product from oil refining [3] and it is, therefore, essential to find alternative reaction pathways for the production of these chemicals to ensure a more sustainable plastic and fuel production in the future.

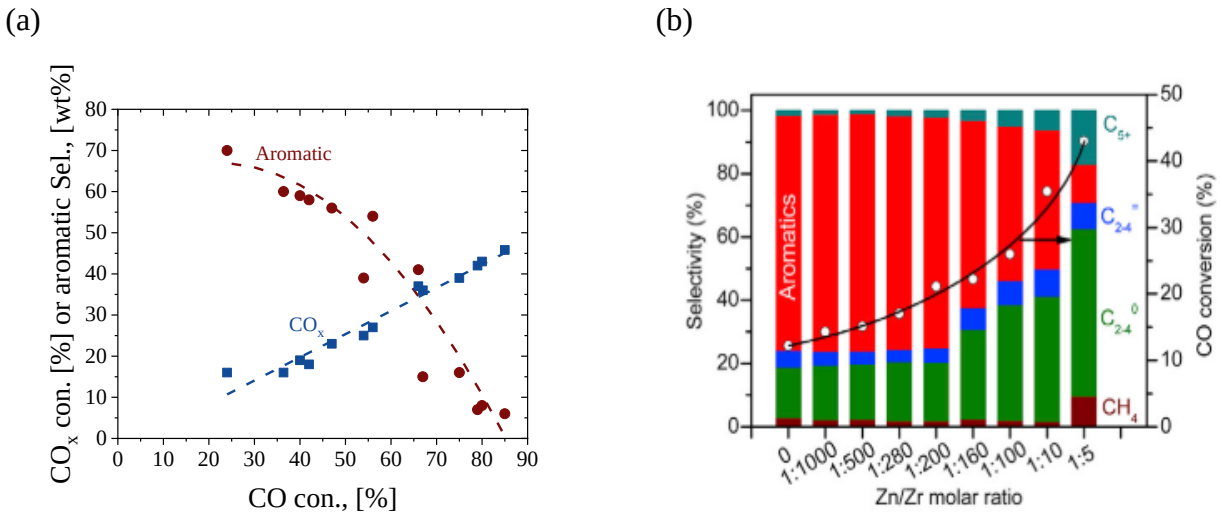


Fig. 53. (a) The aromatic selectivity as a function of CO_x conversion obtained with different ZnO-Cr_2O_3 mixed oxide for the ZnO-Cr_2O_3/H-ZSM-5 catalyst. (b) The hydrocarbon selectivity and the CO conversion with the Zn/Zr molar ratio for the ZnO-ZrO_2 catalysts in the ZnO-ZrO2/H-ZSM-5 bi-functional catalyst. Reaction conditions: (a) 427 ºC, 83 bar, H_2/CO =1, and GHSV = 1490-2845 mL/g/h (b) 430 ºC, H_2/CO = 2, 30 bar, and GHSV = 1500 mL/g/h. Obtained from [54] *and* [106].

As mentioned in section 2.1.3, the first selective production of aromatics over a bi-functional was published in the end of the 1970s [53,54]. This was achieved by combining a ZnO-Cr_2O_3 mixed oxide with the H-ZSM-5 catalyst yielding high selectivity of aromatics at ~70 wt%. Due to the low methanol synthesis activity of the ZnO-Cr_2O_3, high pressure, temperatures and residence time were used. Chang et al [54] synthesized alternative ZnO-Cr_2O_3 catalysts with various ZnO content to improve the methanol synthesis activity. However, as illustrated in Fig. 53 (a), increasing the methanol synthesis activity with higher content of ZnO significantly reduces the aromatic selectivity. A more recent study on syngas conversion to aromatics over the bi-functional catalyst composed for the H-ZSM-5 and the ZnO-ZrO_2 oxide, reveals a similar trade-off in the aromatic selectivity and the CO conversion with the change in ZnO content (Fig. 53 (b)) [106]. A similar trade-off was found for the bi-functional

catalyst for light olefin production (section 2.3.2) that could be related to the hydrogenation activity of large ZnO crystals.

Many research groups have investigated the bi-functional catalyst composed of ZnO-based catalysts and H-ZSM-5 for CO [106,211] or CO_2 hydrogenation [17,29,207,212–215] into aromatics. Others have focused on pure In_2O_3 or Cr_2O_3 as the methanol synthesis catalysts together with H-ZSM-5 [206,216,217]. The highest aromatic selectivity reported in these studies are summarized in Table 3, together with the CO_2 conversion and the reactor conditions applied.

Table 3. Listed operating parameters and results for CO_2 conversion to aromatics via bi-functional catalysts. The parameters reported are the Si/Al ratio of the zeolite used, reactor temperature, pressure, and space velocity (GHSV). The results are reported as the CO_2 conversion (denoted Con.), CO selectivity, and aromatic selectivity within hydrocarbons (denoted sel.).

Bi-functional catalysts (oxide:zeolite weight ratio)	**Si/Al**	**T [℃]**	**P [bar]**	**GHSV [mL/g_{cat}/h]**	**CO_2 Con. (%)**	**CO Sel. (%)**	**Aro. Sel. (%)**	**Ref.**
ZnO-ZrO_2/H-ZSM-5 (1:1)	100	320	40	1200	14	44.3	73	[17]
ZnO-ZrO_2/H-ZSM-5 (1:2)	56	340	40	7200	15.9	34.0	76	[213]
ZnO-ZrO_2/H-ZSM-5 (1:2)	600	340	30	4800	6.2	33.9	65.2	[212]
ZnO-ZrO_2/H-ZSM-5 (1:1)	360	350	30	~6695	~10	51.0	~31	[207]
Cr_2O_3/H-ZSM-5 (1:1)*	40	350	30	1200	34.5	33.0	75.9	[216]
Cr_2O_3/H-ZSM-5@S-1*	nr	350	30	1200	27.6	46.4	70.3	[216]
Cr_2O_3/Zn-ZSM-5 (2:1)@S-1	nr	350	30	1200	22.1	35.3	70.1	[217]
ZnO-Cr_2O_3/Zn-ZSM-5 (1:1)	140	320	50	2000	19.9	70.4	56.6	[214]
ZnO-Cr_2O_3/H-ZSM-5 (2:1)*	nr	350	40	1200	23.1	27.7	85.3	[215]
In_2O_3/H-ZSM-5 (1:2)	27	340	30	9000	13.1	45.0	14.6	[206]
$ZnAl_2O_4$/H-ZSM-5	97	320	30	2000	9.1	57.1	73.9	[29]

* CO co-feeding

As shown in Table 3, inconsistencies in the optimal residence time, pressure, oxide/zeolite mixing ratio, and acid site density for the optimal aromatic selectivity are reported. The optimal temperature seems to be more consistent and is in the range of 320-350 ºC for all the bi-functional catalysts. The highest CO_2 to hydrocarbon conversion was found to be 23 % with a 75.9 % aromatic selectivity and was obtained over the Cr_2O_3/H-ZSM-5 catalyst [216]. In contrast, the other studies found a CO_2 to hydrocarbon conversion less than 16 % with great variation in the aromatic selectivity between 85.3 to 14.6 %. This indicates that it is still a challenge to selectively produce aromatics at high conversions.

2.3.4.1 Space velocity

Ticali et al. [207] tested their ZnO-ZrO_2/H-ZSM-5 catalyst at space velocities from 6000 to 24000 mL/g/h which could be the reason for the low aromatic selectivity (>31 %) obtained compared to other similar bi-functional catalysts (Table 3). It was found that the longest residence time improved the aromatic selectivity and upon lowering contact time did not only minimize the aromatic selectivity but also the paraffins/olefins ratio. The higher paraffins/olefins ratio at shorter residence time is counterintuitive as the olefins are the first product of the hydrocarbon pool reaction and the thermodynamic equilibrium of the light alkene hydrogenation reactions shows that the main product should be alkanes. Therefore, opposite results should be expected where the paraffins/olefins ratio is increasing at longer residence time. Other studies have shown the opposite trend with a decrease in the olefin selectivity with increase in the residence time [17,106,213].

Zhou et al. [213] observed an optimum for the aromatic selectivity at 7200 mL/g/h for their aerogels integrated ZnO-ZrO_2 oxide with H-ZSM-5, as illustrated in Fig. 54. At low residence time, the main product was light olefins. When increasing the residence time, the light olefins are oligomerized and converted into aromatics. High residence time increases the paraffin selectivity with decrease in the aromatic selectivity. This could indicate that the olefins are removed before they can form aromatics or that hydrogen induced cracking of the aromatics convert it to light paraffins at high residence time. However, it is quite marveling that no C_{5+} species are reported in the hydrocarbon selectivity.

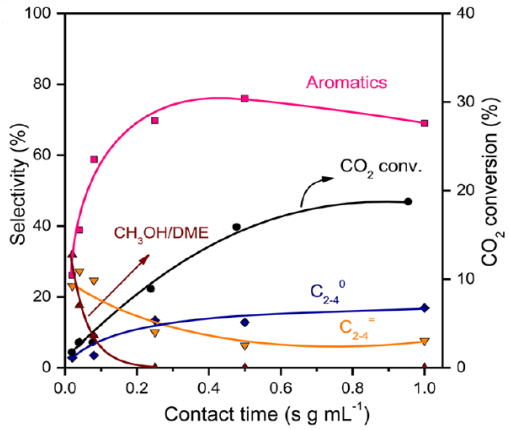


Fig. 54. The hydrocarbon selectivity and CO_2 as a function of contact time over the ZnO-ZrO_2 oxide/H-ZSM-5 catalyst. Reaction conditions: H_2/CO_2 = 3, 40 bar, and 340 ºC. Obtained from [213].

Increasing the residence time increases the CO_2 conversion but a compromise should be made between the CO_2 conversion and the aromatic selectivity due to the loss of aromatics at high residence time.

2.3.4.2 Reaction temperature

Investigation of the temperature effect on the CO_2 hydrogenation to aromatics over metal oxides mixed with H-ZSM-5 was conducted by several authors [17,29,212,217]. The research groups of Li et al. [17] and X. Zhang et al. [212] tested ZnO-ZrO_2 with H-ZSM-5 with a Si/Al ratio of 100 and 600, respectively. It was not only the acid density of the zeolite that differed between the two research groups. The mass ratio between the mixed metal oxide and zeolite was 1:1 and 1:2, the applied pressure was 40 and 30 bar, and the space velocity was 1200 and 4800 mL/g_{cat}/h. The two research groups tested the catalytic performance using reaction temperatures in the range of 260 to 400 ℃ and 280 to 420 ℃. Despite the differences between the two studies, the aromatic yield showed identical trends, where an optimum in the aromatic yield was obtained at 340 ºC.

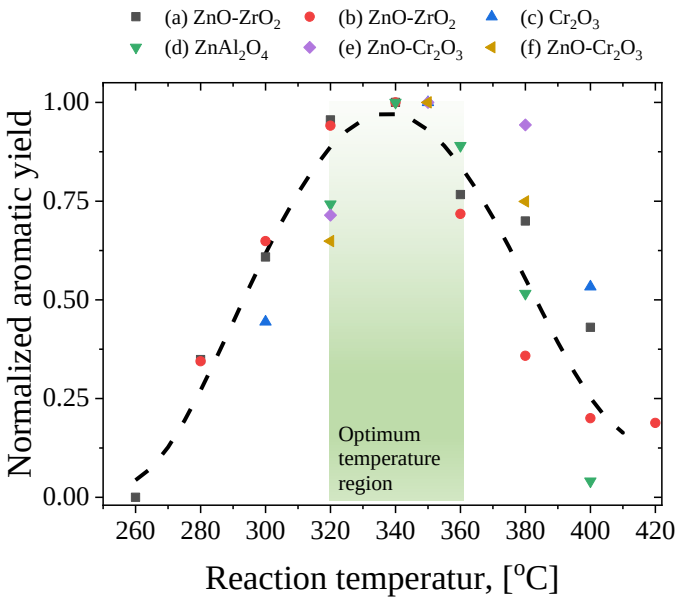


Fig. 55. Normalized aromatic yield for CO_2 hydrogenation over composite catalysts against reaction temperature. The aromatic yield is estimated as: $Y_{Aro} = X_{CO_2} \cdot (1 - S_{CO}) \cdot S_{Aro}$ where the normalized yield is found by dividing the yield with the best obtained yield for that specific metal oxide/H-ZSM-5 composite catalyst. The optimum in aromatic yield is marked with green. Reaction conditions: (a) H_2/CO_2 = 3, GHSV = 4800 mL/g_{cat}/h, P = 30 bar, and Si/Al = 600. (b) H_2/CO_2 = 3, GHSV = 1200 mL/g_{cat}/h, P = 40 bar, and Si/Al = 100. (c) H_2/CO_2 = 3 (5.42 vol% CO), GHSV = 1200 mL/g_{cat}/h, P = 30 bar, and Si/Al = 40. (d) H_2/CO_2 = 3, GHSV = 6000 mL/g_{cat}/h, P = 30 bar, and Si/Al = 97. (e-f) GHSV = 1200 mL/g_{cat}/h, P = 40 bar, Si/Al = nr, H_2/CO_2 = 3, and with 3.94 vol% CO co-feeding [215]. *The line is a guide to the eye, showing the trend in the average value of the normalized aromatic yield for the different temperatures by a best polynomial fit of 4th order. Data Obtained from* [17,29,212,215,217].

The normalized aromatic yields for ZnO-ZrO_2 [17,212], Cr_2O_3 [217], $ZnAl_2O_4$ [29], and $ZnGr_2O_4$ [215] mixed with H-ZSM-5 zeolites as a function of temperature are compared in Fig. 55. The normalized aromatic yield is calculated by dividing the yields with the best obtained yield for that specific composite catalyst. Thus, it only illustrates the temperature where the highest aromatic yield for a specific metal oxide/H-ZSM-5 catalyst is obtained and can thereby not be used for comparing the

performance of the catalysts. However, Fig. 55 clearly illustrates an optimum in aromatic yield in the temperature region of 320-360 ºC for the oxide/H-ZSM-5 composite catalysts. This suggests that the best compromise between the methanol synthesis reaction over the metal oxide and the methanol to aromatic reaction in the H-ZSM-5 zeolite is obtained using a reaction temperature within this range. This optimum temperature range was observed despite the differences in the metal oxides, zeolites acidities, applied pressure, and space velocities used in these studies, which ranges from Si/Al = 40-600, P = 30-40 bar and GHSV = 1200-4800 mL/g_{cat}/h.

Operating the bi-functional catalyst at lower reaction temperatures will result in low CO_2 to hydrocarbon conversion. Increasing the temperature above the optimal region will result in high formation of other C_{5+} products and light paraffins [17]. The change in the hydrocarbon distribution at high temperatures can be due to increased hydrogenation activity and/or cracking activity converting the aromatics back into smaller products.

2.3.5 Acidity effect on the aromatic selectivity

Ticali et al. [207] observed two effects on the product distribution with increasing acid site density for CO_2 hydrogenation into aromatics. Firstly, the CO selectivity reduced indicating formation of CO as a product from methanol decomposition or that conversion of CO is enhanced due to the change in the thermodynamic driving force for the methanol synthesis (section 0). Song et al. [218] have shown that excess oxygen vacancies on the metal oxides can promote decomposition of methanol back into CO. An alternative hypothesis is that CO itself could be converted to hydrocarbons in the zeolite catalyst [106,219,220] Secondly, the increase in the acid site density when using a H-ZSM-5 with Si/Al ratio of 360 (low density) and 25 (high density) increased the paraffin selectivity and reduced the aromatic selectivity.

In the methanol-to-hydrocarbon process, a higher acid site density increases the formation of aromatics and coke molecules (as aromatics are considered coke precursor) resulting in a significant rise in the deactivation rate [14]. To achieve high aromatic selectivity, it could be expected that zeolites with high acid site density and high acid strength would be needed. In Fig. 56, results for varying the acid site density of the H-ZSM-5 zeolite in the bi-functional catalyst with ZnO-ZrO_2 are shown [106]. The acid site density has an important effect on the aromatic selectivity and the CO conversion and increases initially with the increase in the acid site density, as expected. However, an optimum for the aromatic selectivity with a strong acid site density of 43 μmol/g was obtained. Higher acid site density showed that the Brønsted acid sites in a hydrogen rich atmosphere will reduce the aromatic selectivity

caused by enhanced hydrogenation of olefins. The olefin hydrogenation inhibits the polymerization and aromatization causing the decrease and increase in aromatic selectivity and in the paraffin selectivity.

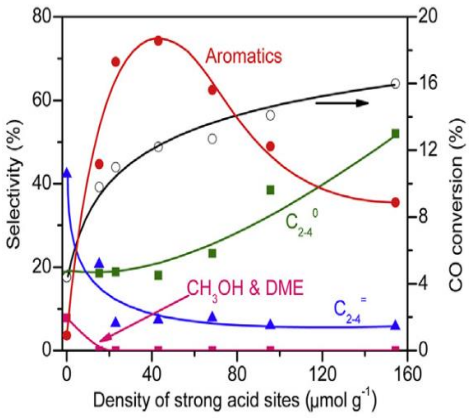


Fig. 56. The hydrocarbon selectivity with the density of strong acid sites over a ZnO-ZrO_2 oxide and H-ZSM-5 catalyst. Reaction conditions: H_2/CO = 2, 30 bar, 430 ℃, and 1500 GHSV (mL/g_{cat}/h). Obtained from [106].

Identical behavior for CO_2 hydrogenation over ZnO-ZrO_2/H-ZSM-5 was obtained by Li et al. [17] who observed an optimum for the acidity of zeolite at a Si/Al ratio of 100. This indicates that the acidity of the zeolite can be subjected to optimization of the aromatic selectivity. The poor aromatic selectivity by Ticali et al. [207] could maybe be improved by using a zeolite with intermediate acidity. Gao et al. [206] showed poor aromatic selectivity for the In_2O_3 combined with a highly acidity H-ZSM-5 catalyst. High degree of olefin hydrogenation reduced the aromatic selectivity but produce a hydrocarbon mixture rich in C_{5+} paraffins. A summary of the aromatic selectivity as a function of the Si/Al ratio of the H-ZSM-5 mixed with different metal oxides are illustrated in Fig. 57.

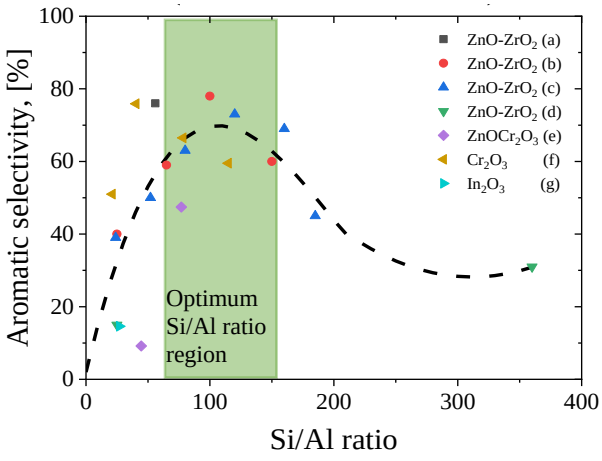


Fig. 57. The change in aromatic selectivity with different Si/Al ratio of the H-ZSM-5 zeolite combined with different metal oxides. Reaction conditions:GHSV of 9000-500 ml/g_{cat}/h, 320-350 ℃, and 50-30 bar with both CO/H_2, CO_2/H_2, and $CO_2/CO/H_2$ feed mixtures. Data obtained from [17,106,206,213,215,216].

Fig. 57 clearly indicates an optimum for the Si/Al ratio for the production of aromatics over metal oxides and the H-ZSM-5 zeolite. It should be noted that the operation conditions, such as temperature and space velocity, have shown significant effect on the aromatic selectivity and optimization of these parameters can tune the aromatic selectivity even more. The data used in Fig. 57 are obtained at a GHSV of 9000-500 ml/g_{cat}/h, 320-350 ℃, and 50-30 bar with both CO/H_2, CO_2/H_2, and $CO_2/CO/H_2$ feed mixtures. This confirms that the right acidity of the zeolite is crucial to obtain a high aromatic selectivity. Here the acidity is described by the Si/Al ratio, which is inversely proportional to the density of the Brønsted acid sites. The acid strength has been directly correlated to the cyclization and hydrogen transfer reactions in the zeolite [16]. Therefore, it is essential to have a certain acid site density to ensure high aromatization activity. As shown Fig. 57, high Si/Al ratios result in low aromatic selectivity as the aromatization activity is too low.

The drop and increase in the aromatics and paraffins selectivity for bi-functional catalytic systems are confirmed by several authors. In the traditional methanol-to-hydrocarbon process, the paraffins are considered to be a product from the formation of aromatics (section 2.2.2). The drop and increase in the aromatic and the paraffins selectivity with increase in acid site density suggest that gaseous hydrogen is activated and that hydrogenation occurs on the acid sites rather than on the metal oxide catalysts [200]. The hydrogenation of light olefins inhibits the formation of aromatic causing the observed drop in aromatic selectivity at low Si/Al ratio in Fig. 57.

The research group of Y. Wang et al. [216,217] investigated the Chromium (III) oxide in combination with H-ZSM-5 with additional modification by silicate-1, resulting in a core-shell structure of the zeolite. The purpose of the core-shell structure of the zeolite was to remove or minimize the density of external acid sites, which previously has shown indication of playing an important role in the methylation and oligomerization of the aromatics for the methanol-to-aromatic reaction [221–226]. By comparing the critical diameters (defined as the diameter of the smallest cylinder which a the molecule will fit inside) for the para-, meta-, and ortho-xylene 6.7, 7.4 and 7.4 Å, it could be hypothesized that mainly para-xylene is formed inside the well-defined pores of the H-ZSM-5 of ~6 Å. By removing the access to the external acid sites, a higher selectivity of para-xylene in the aromatic product was observed [216,217]. This shows that it is not only internal acid sites, but also external sites, that are important for the hydrocarbon distribution and that it can be further tuned by modifying the H-ZSM-5 catalyst.

2.3.6 Feed gas composition effects on the bi-functional catalyst activity and selectivity

The feed gas composition have shown to play an important role in the activity and selectivity of the bi-functional catalysts. As shown in Fig. 58 (a), increasing the H_2/CO_2 ratio improves the CO_2 conversion but at the expense of a decreasing olefin selectivity over the In_2O_3-ZrO_2/SAPO-34 catalyst [190]. Thus, increasing the hydrogen partial pressures improves both the methanol synthesis and olefin hydrogenation activity. This is also the case when co-feeding hydrogen for methanol conversion over the SAPO-34 catalyst at high pressure [190,202], as shown in Fig. 58 (b). The degree of hydrocarbon saturation can, therefore, be altered by the feed concentration of hydrogen at the expense of CO_2 conversion. The acidity of the zeolite and zeotype materials are important for the hydrogenation activity (section 2.3.3 and 2.3.5) where the acidity is also important for the methanol dehydration activity. Thus, an optimal feed concentration of CO_2/H_2 for achieving the maximum methanol synthesis activity and the lowest olefin hydrogenation activity must be dependent on the acidity of the solid acid applied. A similar trade-off between the aromatic selectivity and the CO_2 conversion was observed with higher H_2/CO_2 ratios over the ZnO-ZrO_2/H-ZSM-5 catalyst [17].

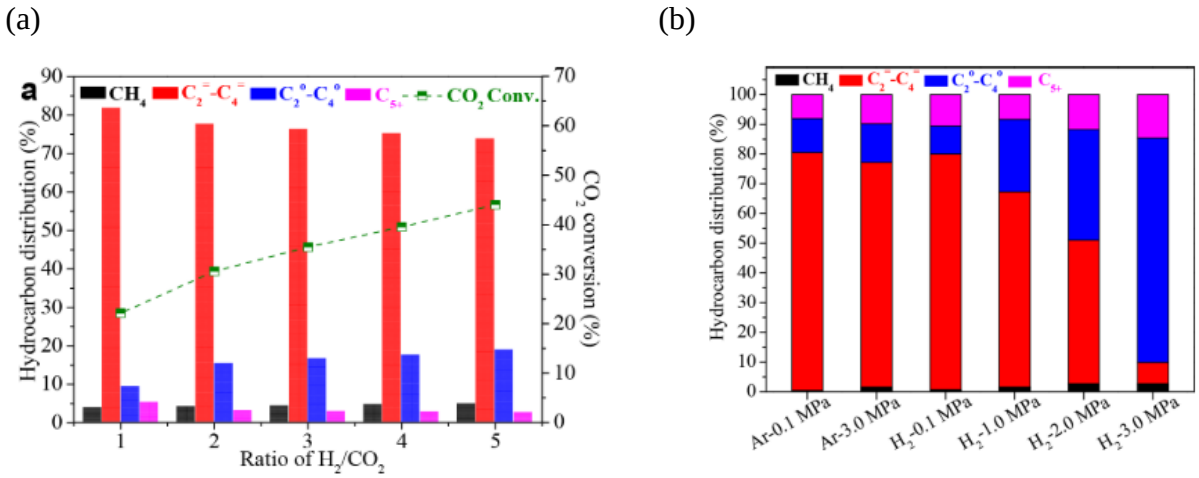


Fig. 58. (a) The hydrocarbon selectivity and CO2 conversion with different H_2/CO_2 ratio. (b) The influence of the atmosphere and H_2 pressure on the product selectivity for the conversion of methanol over the H-SAPO-34 catalyst. Reaction conditions: (a) 400 ºC, 30 bar, GHSV = 9000 mL/g/h, and oxide/zeolite = 2 (b) Ar or H_2 10-30 bar, GHSV = 9000 mL/g/h, and liquid methanol of 0.003 mL/min. Obtained from [190].

Interesting results have been obtained when using a feed mixture containing CO_2, CO, and hydrogen for the production of light olefins and aromatics [190,206,213,215,227]. By co-feeding CO, the selectivity towards CO can be minimized without affecting the CO_2 conversion and the light olefin selectivity, as illustrated in Fig. 59 for the In_2O_3-ZrO_2/SAPO-34 [190]. The decrease in the CO selectivity could be explained by the lower thermodynamic driving force reducing the reaction rate for the reverse-water-gas-shift reaction. This effect is not limited to the In_2O_3-ZrO_2/SAPO-34 bi-functional

catalyst as a similar trend in improved hydrocarbon yield has been observed for the $ZnO\text{-}ZrO_2$ and the $ZnO\text{-}Cr_2O_3$ mixed with H-ZSM-5 catalysts [213,215]. This is promising results as a mixture of $CO_2/CO/H_2$ could be obtained by simply recycling the unconverted syngas back to the reactor entrance. Another explanation for the improved hydrocarbon yield when adding CO to the feed, could be that surface oxygen vacancies are generated by the more reducible gas. This could boosts the CO_2 hydrogenation activity by counterbalancing the efficient annihilation of vacancies in the presence of CO_2 [120].

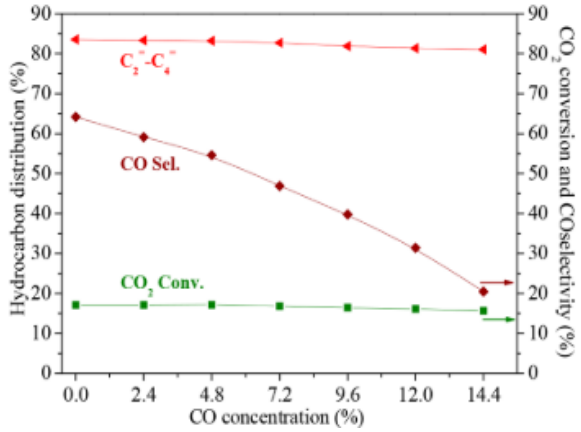


Fig. 59. The CO_2 conversion, CO, and light olefins selectivity as a function of the CO concentration in the feed. Reaction conditions: 380 ºC, 30 bar, H_2/CO_2 = 3, GHSV = 9000 mL/g/h, and oxide/zeolite = 0.5. Obtained from [190]

Gao et al. [215] found that co-feeding CO does not only improve the hydrocarbon yield but also improves the aromatic selectivity over the $ZnO\text{-}Cr_2O_3$/H-ZSM-5 catalyst. The aromatic selectivity increased with ~6 % by only adding ~4 vol% CO to the feed. Chen et al. [220] have shown that co-reacting CO with methanol over H-ZSM-5 improves the aromatic selectivity significantly from ~40% (CH_3OH) to ~80% (CO/CH_3OH). This indicates that methanol or dimethyl ether can be carbonylated to form acetic acid or methyl acetate that creates a new reaction pathway to the formation of aromatic compounds. The CO conversion was found to increase with increasing acid site density and it was observed that even at a Si/Al ratio of 314, small amounts of CO was converted. Cheng et al. [106] investigated the reaction between methanol and CO over the $ZnO\text{-}ZrO_2$/H-ZSM-5 catalyst. The aromatic selectivity improved with a change from inert N_2 to a gas containing CO and the selectivity also increased with higher CO pressures, as illustrated in Fig. 60 (a). In contrast to Chen et al. [220], no significant effect on the aromatic selectivity was observed when using the H-ZSM-5 catalyst alone but adding the $ZnO\text{-}ZrO_2$ had great effect on the aromatic selectivity. This suggests that the metal oxide phase plays a role in the incorporation of CO into the hydrocarbon product. By using isotopic

labelled ^{13}CO, the concentration of ^{13}C in the aromatic products will give an indication of the degree of CO incorporation. As illustrated in Fig. 60 (b), the CO incorporation increases with CO pressure.

(a) (b)

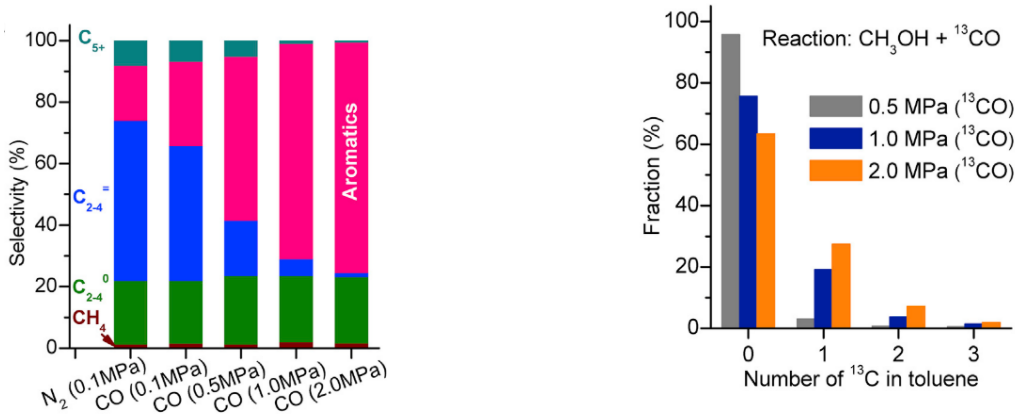


Fig. 60. (a) The effect of CO partial pressure on the product selectivity for methanol conversion over the ZnO-ZrO_2/H-ZSM-5 zeolite. (b) The incorporation of ^{13}C into toluene during methanol conversion with ^{13}CO at 100% methanol conversion. Reaction conditions: 400 ºC, liquid CH_3OH = 0.06 mL/h, N_2 or CO flow rate = 25 mL/min. Obtained from [220].

2.3.7 The stability of bi-functional catalysts

As described in section 2.2.4, an inherent feature of the methanol to hydrocarbons process is the steady deactivation caused by coke formation blocking the access to the active sites. Surprisingly, such deactivation phenomenon is rarely reported in literature for bi-functional catalysts [17,24,27–30,106,190,206,216,228]. However, Ticali et al. [207] demonstrated great instability problems for the combination of ZnO-ZrO_2 and H-SAPO-34, especially at 350 ℃ where it lost all activity in less than 20 hours, resulting in methanol being the major product. More stable performance was achieved using a H-ZSM-5 catalyst instead, which though significantly reduced the C_3 selectivity from ~60 % to~ 40 %. The ZnO-ZrO_2/H-ZSM-5 showed slight deactivation at 350 ℃ and 30 bar, which was concluded to be the most promising operation conditions. Zhang et al. [212] speculated that the de-activation they observed for their ZnO-ZrO_2/H-ZSM-5 catalyst was due to coke deposition rather than sintering of the metal oxide.

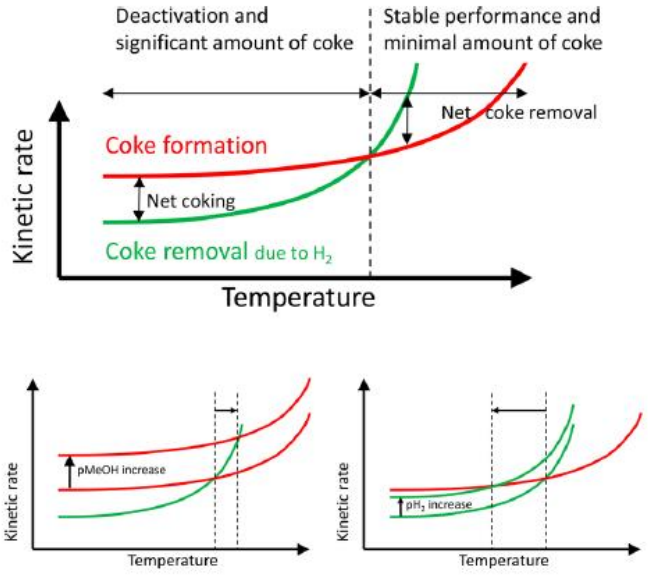


Fig. 61. Hypothesized model for coke formation and removal over a hybrid system composed of Cu/ZnO/Al_2O_3 and H-SAPO-34 at different process conditions such as increasing temperature (top,) methanol (bottom left), and hydrogen partial pressure (bottom right) [71].

Nieskens et al. [71] have recently showed that operating a bi-functional catalytic system, composed of a Cu/ZnO/Al_2O_3 and H-SAPO-34, under relative high hydrogen partial pressures, compared to the methanol intermediate partial pressure, significantly improves the deactivation rate. This improvement was reported to be caused by a reduced amount of formed coke and by the coke mostly consisted of mono- and diaromatics, as compared to tri- and tetraaromatic species formed under normal meth-

anol-to-olefin reaction conditions. Therefore, the smaller coke molecules formed over the bi-functional catalyst are easier to remove. Nieskens et al. [71] hypothesized that the performance for these bi-functional catalysts are the result of a balance between the competing reactions that form and remove coke species, as illustrated in Fig. 61. Here, coke formation is favored by low temperatures, low hydrogen- and high methanol partial pressures. Balancing these parameters could ensure a stable catalyst activity with minimal coke deposition.

The Nieskens research group have previously published results showing that co-feeding methanol with high hydrogen partial pressure of 3000 kPa can improve the lifetime with more than 70 times, while preserving the high C_{2-4} olefins selectivity of ~85 % during methanol-to-olefin reaction over H-SAPO-34. The results showed that increasing the hydrogen partial pressure enhanced the selectivity of methane, ethane, and propane and reduced the $C_2^=/C_3^=$ ratio. Thus, suggesting that high hydrogen partial pressures suppress the rate of aromatization and/or the propagation of the aromatic cycle, as ethylene is mainly formed as a product from dealkylation of aromatic species (section 2.2.2). The results also suggest that hydrogen participates in the hydrogen transfer reaction that hydrogenate olefinic species, as the selectivity of paraffin increases with the increase in hydrogen partial pressure [229].

By mixing the Cu-based methanol synthesis catalyst with SAPO-34, the main product obtained was paraffins [28,71,74,230]. This shows that the Cu-based methanol catalyst activates the hydrogen that hydrogenates the olefinic species. The removal of the olefinic species could inhibit the aromatic cycle in the dual-cycle hydrocarbon pool and, thereby, increase the bi-functional catalyst stability, as olefins and aromatics are assumed to be coke precursors. However, great stability of bi-functional catalysts, even with high selectivity towards both olefins and aromatics, are frequently reported [17,24,27–30,106,190,206,216,228]. This suggest that the great stability is not caused by the removal of olefin trough hydrogenation alone.

Castaño et al. [231] found that increasing the temperature and the hydrogen partial pressure, when methylcyclohexane was co-feed with hydrogen over the H-ZSM-5, increased the cracking and hydrogen incorporation into the products. With increasing hydrogen partial pressure, the aromatics selectivity decreased while the selectivity of saturated products such as paraffins and iso-paraffins increased. Thus, the stability of the bi-functional catalysts could be caused by the presence of high hydrogen partial pressures that changes the cracking mechanism for coke molecules as well. Zhao et al. [232] found that when co-feeding both hydrogen and water to methanol in the methanol-to-olefin

reaction over the SAPO-34 catalyst, the lifetime was prolonged and the methanol conversion capacity increased by 200 fold. They concluded that this improvement originated from an increased hydrogenation ability of heavier aromatic deposits that slowed down the evolution of coke species. A synergy between water and hydrogen was observed and believed to be caused by reduced barriers of hydrogenation reactions in the presence of water.

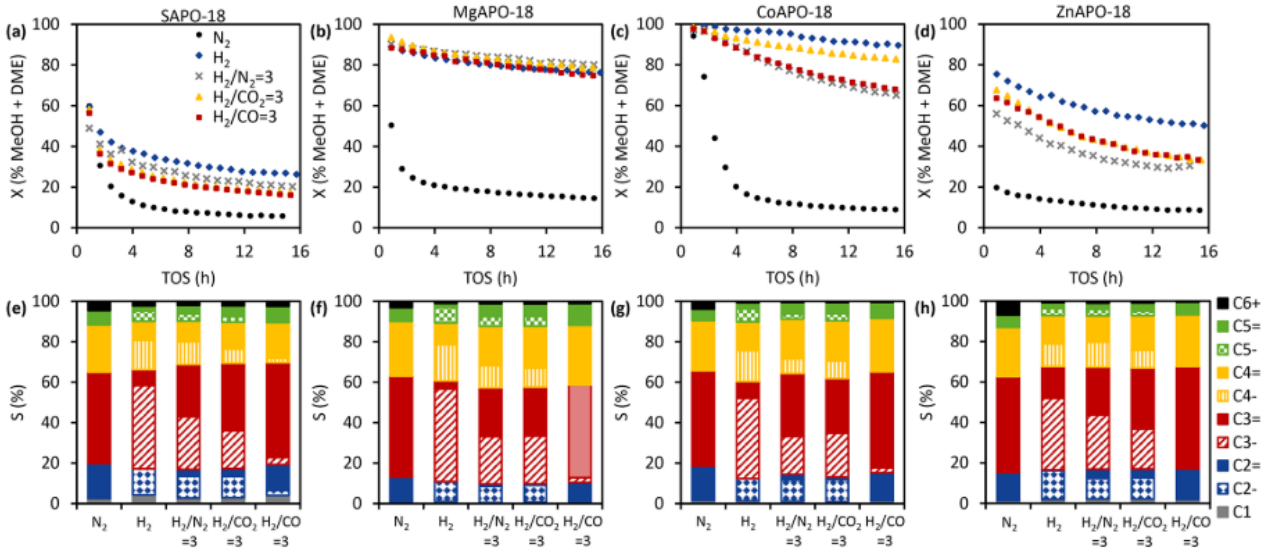
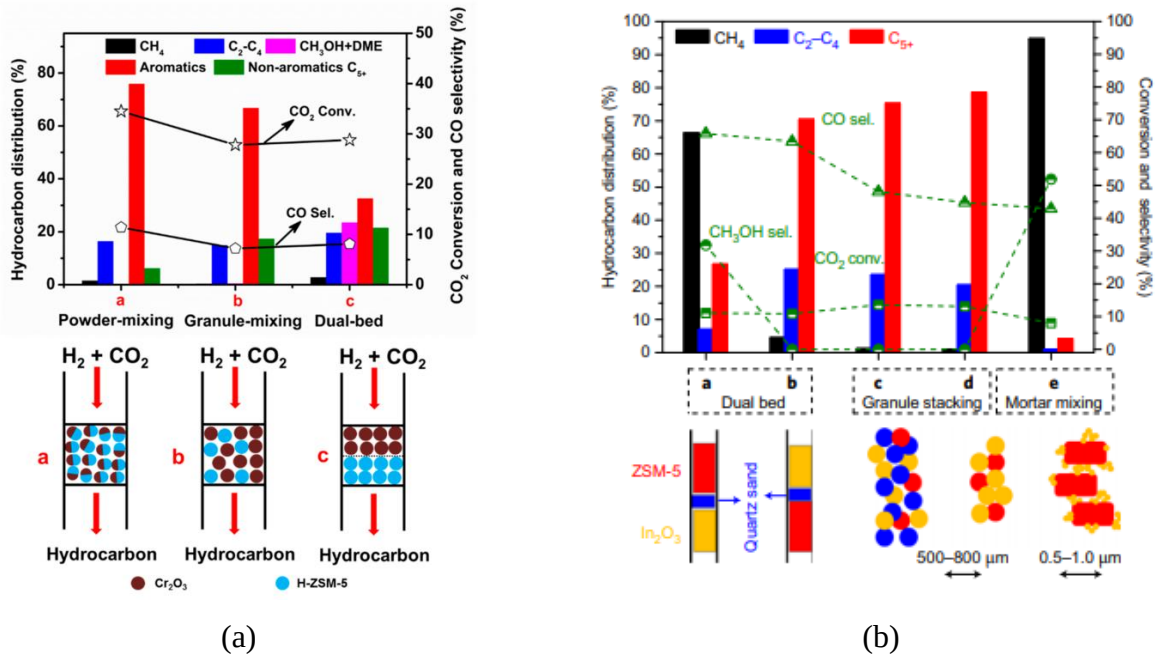


Fig. 62. (a-d) The methanol and dimethyl ether conversion with time on stream MAPO-18 (where M = Mg, Co, or Zn). (e-h) the hydrocarbon selectivity at time on stream. Reaction conditions: 350 ºC, 20 bar, 1 bar methanol (WHSV = 2 g/g/h), 0.6 bar Ar (internal standard), 18.4 bar N_2, H_2, or H2/CO_x = 3, and GHSV = 16000 mL/g/h. Obtained from [233].

Xie et al. [233] prepared a series of isomorphic substituted zeotypes with the AEI topology, denoted MAPO-18 were M is Mg, Co, or Zn. Methanol conversion over these materials were conducted with and without co-feed of hydrogen, CO, and/or CO_2. The results are show in Fig. 62. By adding Co, Mg, or Zn, a similar activity and lifetime as the SAPO-18 catalyst for methanol conversion were observed. These samples all showed improved activity and lifetime when hydrogen was co-fed but the effect was significantly higher for the samples containing Co, Mg, or Zn. This indicates that the presence of metal oxide sites where hydrogen can be activated further improves the stability of the solid acids. This synergetic effect could also be important for the great stability observed for the bi-functional catalyst, where hydrogen could be activated at the methanol synthesis component. Only co-feeding hydrogen resulted in a very saturated product for all catalysts, showing that the increased lifetime comes with a cost. However, when CO was added together with hydrogen and methanol, the olefin hydrogenation activity was inhibited and the main product was again olefins. This slightly affected the deactivation rate which increased with the formation of a more unsaturated product.

2.3.8 Catalyst bed configurations for the bi-functional catalyst

Several studies have suggested that the mixing and proximity of the two catalysts are crucial for the performance of bi-functional catalysts for converting synthesis gas or CO_2 into hydrocarbon products. Closer proximity plays a crucial role in minimizing any transport limitations and closer proximity induces the syngas conversion but can also alter the hydrocarbon distribution [17,24,27–30,106,190,206,216,228].



(a) (b)

Fig. 63. The effect on the CO_2 hydrogenation performance and hydrocarbon distribution for the different packing configuration: dual bed, granule- and powder-mixing for (a) Cr_2O_3/H-ZSM-5 and (b) In_2O_3/H-ZSM-5. Obtained from [206,216].

Typical configurations investigated are dual-bed, mixing of granules with sizes of several hundreds of micrometers, and mixing of fine powders with sizes on the nanometer scale [180]. In the dual-bed configuration, the methanol synthesis catalyst is placed upstream where the zeolite is placed down-stream and they are typically separated with quartz sand. This configuration will result in the lowest proximity between the two active components, which in general have resulted in the lowest CO or CO_2 conversion and selectivity towards desired hydrocarbons, as illustrated in Fig. 63. Increasing the proximity between the methanol synthesis catalyst, such as Zn-Zr, Zn-Al, Zn-Cr, and Cr oxides, and the zeolite, the conversion of CO or CO_2 enhances and the selectivity of olefins and aromatics increase [17,24,27–29,106,216]. This clearly indicates a synergistic effect between the methanol synthesis and the zeolite catalyst and shows the importance of immediate methanol conversion to alter the CO_2 hydrogenation equilibrium. However, studies have shown that fine powder mixing with a methanol synthesis catalyst based on In_2O_3 and zeolite increases the selectivity towards methane, as shown in

Fig. 63 (b). Thus, the optimal bed configuration of this type of bi-functional catalysts are granulate mixing. The main reason for this is believed to be caused by indium species poisoning the zeolite, which migrate from the metal oxide to the zeolite under these reaction conditions [190,206,228]. Similar poisoning have been observed for the Fe_2O_3/KO_2 and H-ZSM-5 mortar mixed catalytic systems. Solid-state titration of potassium into the zeolite reduced the activity of the Fischer-Tropsch catalyst and removed the Brønsted acid sites [186].

Wang et al. [234] investigated the migration of metals into the H-ZSM-5 catalyst for the conversion of syngas to hydrocarbons. They combined In_2O_3, ZnO, ZrO_2, or Cr_2O_3 with the H-ZSM-5 in different proximities to clarify the correlation between metal migration and the catalytic performance. It was found that both In and Zn could migrate into the zeolite and neutralize the Brønsted acid sites, destroying the bi-functionality. High reaction temperatures and close proximity were found to induce the metal migration and the migration was found irreversible. Ding et al. [235] also investigated the migration of Zn into the zeotype SAPO-34 from the $ZnO\text{-}Cr_2O_3$/SAPO-34 bi-functional catalyst. The proximity between the two catalysts also induces the Zn migration into the SAPO-34 catalysts. The migration of Zn increased the olefin hydrogenation activity resulting in a more saturated hydrocarbon product. As shown in Fig. 64, Ding et al. [235] found that the degree of Zn migration depends on the acidity of the SAPO-34 catalysts, showing that SAPO-34 with higher acid site density will induce the Zn migration. This is evident in the increased Zn concentration in the SAPO-34 catalysts after reaction. Close proximity increases the initial activity of the bi-functional catalysts, but too close proximity will increase deactivation by metal ion migration from the metal oxide to the solid acid. Therefore, an optimal proximity could reveal a compromise between activity, stability, and selectivity of the bi-functional catalysts.

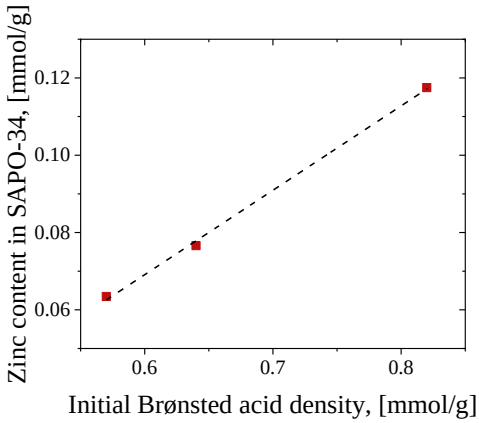


Fig. 64. The Zn concentration in the SAPO-34 catalysts after reaction as a function of the initial Brønsted acid site density. Reaction conditions: 400 ºC, 40 bar, H2/CO = 2.5, GHSV = 5000 mL/g/h, and the oxide/zeolite = 2. Data obtained from [235].

2.4 References

[1] R. Geyer, J.R. Jambeck, K.L. Law, Production, use, and fate of all plastics ever made, Sci. Adv. 3 (2017) 25–29. https://doi.org/10.1126/sciadv.1700782.

[2] P.H. Andersen, T. Duvold, B. Frølund, J. Lüneborg, K. Toft-Petersen, H. Vanthournout, C. Witte, The New Plastics Economy, 2019. https://innovationsfonden.dk/sites/default/files/2019-01/new-plastics-report-jan16-2019-vf.pdf.

[3] J.M. Garcia, M.L. Robertson, The future of plastics recycling, Science (80-.). 358 (2017) 870–872. https://doi.org/10.1126/science.aaq0324.

[4] D.S. Newsome, The Water-Gas Shift Reaction, Catal. Rev. 21 (1980) 275–318. https://doi.org/10.1080/03602458008067535.

[5] P.H. Borse, Hydrogen from water, Elsevier Inc., 2017. https://doi.org/10.1201/9781315153292.

[6] M.E. Dry, The Fischer-Tropsch (FT) Synthesis Processes, in: Handb. Heterog. Catal., 2005: pp. 2965–2994.

[7] H.M. Torres Galvis, K.P. De Jong, Catalysts for production of lower olefins from synthesis gas: A review, ACS Catal. 3 (2013) 2130–2149. https://doi.org/10.1021/cs4003436.

[8] L. Nowicki, D.B. Bukur, Kinetic modeling of the slurry phase Fischer-Tropsch synthesis on iron catalysts, Stud. Surf. Sci. Catal. 136 (2001) 123–128. https://doi.org/10.1016/s0167-2991(01)80291-3.

[9] M.E. Dry, The Fischer – Tropsch process : 1950 – 2000, 71 (2002) 227–241.

[10] H.M.T. Galvis, J.H. Bitter, C.B. Khare, M. Ruitenbeek, A.I. Dugulan, K.P. de Jong1, Supported Iron Nanoparticles as Catalysts for Sustainable Production of Lower Olefins, Science (80-.). 335 (2012) 835–838. https://doi.org/10.1126/science.1215614.

[11] H.M. Torres Galvis, J.H. Bitter, T. Davidian, M. Ruitenbeek, A.I. Dugulan, K.P. De Jong, Iron particle size effects for direct production of lower olefins from synthesis gas, J. Am. Chem. Soc. 134 (2012) 16207–16215. https://doi.org/10.1021/ja304958u.

[12] J. Ott, V. Gronemann, F. Pontzen, E. Fiedler, G. Grossmann, D.B. Kersebohm, G. Weiss, C. Witte, Methanol, in: Ullmann's Encycl. Ind. Chem., 2012.

[13] S. Kvisle, T. Fuglerud, S. Kolboe, U. Olsbye, P. Lillerud, B. V Vora, Methanol-to-Hydrocarbons, in: Handb. Heterog. Catal., 2008: pp. 2950–2965.

[14] U. Olsbye, S. Svelle, M. Bjørgen, P. Beato, T.V.W. Janssens, F. Joensen, S. Bordiga, K.P. Lillerud, Conversion of methanol to hydrocarbons: How zeolite cavity and pore size controls product selectivity, Angew. Chemie - Int. Ed. 51 (2012) 5810–5831. https://doi.org/10.1002/anie.201103657.

[15] S. Ilias, A. Bhan, Mechanism of the catalytic conversion of methanol to hydrocarbons, ACS Catal. 3 (2013) 18–31. https://doi.org/10.1021/cs3006583.

[16] C.D. Chang, C.T.W. Chu, R.F. Socha, Methanol conversion to olefins over ZSM-5. I. Effect

of temperature and zeolite SiO2 Al2O3, J. Catal. 86 (1984) 289–296. https://doi.org/10.1016/0021-9517(84)90374-9.

[17] Z. Li, Y. Qu, J. Wang, H. Liu, M. Li, S. Miao, C. Li, Highly Selective Conversion of Carbon Dioxide to Aromatics over Tandem Catalysts, Joule. 3 (2019) 570–583. https://doi.org/10.1016/j.joule.2018.10.027.

[18] M.A. Djieugoue, A.M. Prakash, L. Kevan, Catalytic study of methanol-to-olefins conversion in four small-pore silicoaluminophosphate molecular sieves: Influence of the structural type, nickel incorporation, nickel location, and nickel concentration, J. Phys. Chem. B. 104 (2000) 6452–6461. https://doi.org/10.1021/jp000504j.

[19] Y. Ono, H. Adachi, Y. Senoda, Selective conversion of methanol into aromatic hydrocarbons over zinc-exchanged ZSM-5 zeolites, J. Chem. Soc. Faraday Trans. 1 Phys. Chem. Condens. Phases. 84 (1988) 1091–1099. https://doi.org/10.1039/F19888401091.

[20] M. Conte, J.A. Lopez-Sanchez, Q. He, D.J. Morgan, Y. Ryabenkova, J.K. Bartley, A.F. Carley, S.H. Taylor, C.J. Kiely, K. Khalid, G.J. Hutchings, Modified zeolite ZSM-5 for the methanol to aromatics reaction, Catal. Sci. Technol. 2 (2012) 105–112. https://doi.org/10.1039/c1cy00299f.

[21] T. Inui, S. Phatanasri, H. Matsuda, Highly selective synthesis of ethene from methanol on a novel nickel-silicoaluminophosphate catalyst, J. Chem. Soc. Chem. Commun. 20 (1990) 205–206. https://doi.org/10.1039/C39900000205.

[22] C.D. Chang, W.H. Lang, R.L. Smith, The Conversion of Methanol and Other O-Compounds to Hydrocarbons over Zeolite Catalysts II. Pressure Effects, J. Catal. 56 (1979) 169.

[23] C.D. Chang, A.J. Silvestri, The conversion of methanol and other O-compounds to hydrocarbons over zeolite catalysts, J. Catal. 47 (1977) 249–259. https://doi.org/10.1016/0021-9517(79)90103-9.

[24] F. Jiao, J. Li, X. Pan, J. Xiao, H. Li, H. Ma, M. Wei, Y. Pan, Z. Zhou, M. Li, S. Miao, J. Li, Y. Zhu, D. Xiao, T. He, J. Yang, F. Qi, Q. Fu, X. Bao, Selective conversion of syngas to light olefins, Science (80-.). 351 (2016) 1065–1068. https://doi.org/10.1126/science.aaf1835.

[25] Y. Zhu, X. Pan, F. Jiao, J. Li, J. Yang, M. Ding, Y. Han, Z. Liu, X. Bao, Role of Manganese Oxide in Syngas Conversion to Light Olefins, ACS Catal. 7 (2017) 2800–2804. https://doi.org/10.1021/acscatal.7b00221.

[26] F. Jiao, X. Pan, K. Gong, Y. Chen, G. Li, X. Bao, Shape-Selective Zeolites Promote Ethylene Formation from Syngas via a Ketene Intermediate, Angew. Chemie - Int. Ed. 57 (2018) 4692–4696. https://doi.org/10.1002/anie.201801397.

[27] Z. Li, J. Wang, Y. Qu, H. Liu, C. Tang, S. Miao, Z. Feng, H. An, C. Li, Highly Selective Conversion of Carbon Dioxide to Lower Olefins, ACS Catal. 7 (2017) 8544–8548. https://doi.org/10.1021/acscatal.7b03251.

[28] K. Cheng, B. Gu, X. Liu, J. Kang, Q. Zhang, Y. Wang, Direct and Highly Selective Conversion of Synthesis Gas into Lower Olefins: Design of a Bifunctional Catalyst Combining Methanol Synthesis and Carbon-Carbon Coupling, Angew. Chemie - Int. Ed. 55 (2016) 4725–4728. https://doi.org/10.1002/anie.201601208.

[29] Y. Ni, Z. Chen, Y. Fu, Y. Liu, W. Zhu, Z. Liu, Selective conversion of CO2 and H2 into

aromatics, Nat. Commun. 9 (2018) 1–8. https://doi.org/10.1038/s41467-018-05880-4.

[30] J. Wei, Q. Ge, R. Yao, Z. Wen, C. Fang, L. Guo, H. Xu, J. Sun, Directly converting CO2 into a gasoline fuel, Nat. Commun. 8 (2017) 1–8. https://doi.org/10.1038/ncomms15174.

[31] G.H. Graaf, The Synthesis of Methanol in Gas-Solid and Gas-Slurry Reactors, 1988.

[32] J.B. Hansen, Methanol Synthesis, in: Handb. Heterog. Catal., 2008: pp. 1856–1876.

[33] P. Sharma, J. Sebastian, S. Ghosh, D. Creaser, L. Olsson, Recent advances in hydrogenation of CO2 into hydrocarbons via methanol intermediate over heterogeneous catalysts, Catal. Sci. Echnology. (2021). https://doi.org/10.1039/D0CY01913E.

[34] N.D. Nielsen, A.D. Jensen, J.M. Christensen, The roles of CO and CO2 in high pressure methanol synthesis over Cu-based catalysts, J. Catal. 393 (2021) 324–334. https://doi.org/10.1016/j.jcat.2020.11.035.

[35] S. Poto, D. Vico van Berkel, F. Gallucci, M. Fernanda Neira d'Angelo, Kinetic modelling of the methanol synthesis from CO2 and H2 over a CuO/CeO2/ZrO2 catalyst: The role of CO2 and CO hydrogenation, Chem. Eng. J. 435 (2022). https://doi.org/10.1016/j.cej.2022.134946.

[36] N.J. Azhari, D. Erika, S. Mardiana, T. Ilmi, M.L. Gunawan, I.G.B.N. Makertihartha, G.T.M. Kadja, Methanol synthesis from CO2: A mechanistic overview, Results Eng. 16 (2022) 100711. https://doi.org/10.1016/j.rineng.2022.100711.

[37] G.J. Millar, C.H. Rochester, K.C. Waugh, An in situ high pressure FT-IR study of CO2/H 2 interactions with model ZnO/SiO2 , Cu/SiO2 and Cu/ZnO/SiO2 methanol synthesis catalysts, Situ. 14 (1992) 289–295.

[38] F. Le Peltier, P. Chaumette, J. Saussey, M.M. Bettahar, J.C. Lavalley, In situ FT-IR and kinetic study of methanol synthesis from CO2/H2 over ZnAl2O4 and Cu-ZnAl2O4 catalysts, J. Mol. Catal. A Chem. 132 (1998) 91–100. https://doi.org/10.1016/S1381-1169(97)00235-5.

[39] Y. Wang, S. Kattel, W. Gao, K. Li, P. Liu, G.J. Chen, H. Wang, Exploring the ternary interactions in Cu–ZnO–ZrO2 catalysts for efficient CO2 hydrogenation to methanol, Nat. Commun. 10 (2019) 1–8. http://dx.doi.org/10.1038/s41467-020-16342-1.

[40] S.G. Neophytides, A.J. Marchi, G.F. Froment, Methanol synthesis by means of diffuse reflectance infrared Fourier transform and temperature-programmed reaction spectroscopy, Appl. Catal. A, Gen. 86 (1992) 45–64. https://doi.org/10.1016/0926-860X(92)80041-A.

[41] N.D. Nielsen, J. Thrane, A.D. Jensen, J.M. Christensen, Bifunctional Synergy in CO Hydrogenation to Methanol with Supported Cu, Catal. Letters. 150 (2020) 1427–1433. https://doi.org/10.1007/s10562-019-03036-7.

[42] E.L. Kunkes, F. Studt, F. Abild-Pedersen, R. Schlögl, M. Behrens, Hydrogenation of CO2 to methanol and CO on Cu/ZnO/Al2O3: Is there a common intermediate or not? This work is dedicated to the memory and achievements of Dr. Haldor Topsøe., J. Catal. 328 (2015) 43–48. https://doi.org/10.1016/j.jcat.2014.12.016.

[43] Y. Yang, C.A. Mims, D.H. Mei, C.H.F. Peden, C.T. Campbell, Mechanistic studies of methanol synthesis over Cu from CO/CO 2/H2/H2O mixtures: The source of C in methanol and the role of water, J. Catal. 298 (2013) 10–17. https://doi.org/10.1016/j.jcat.2012.10.028.

[44] C. V Ovesen, B.S. Clausen, B.S. Hammershøi, G. Steffensen, T. Askgaard, I. Chorkendorff, J.K. Nørskov, P.B. Rasmussen, P. Stoltze, P. Taylor, A Microkinetic Analysis of the Water – Gas Shift Reaction under Industrial Conditions, J. Catal. 158 (1996) 170–180.

[45] F. Polo-garzon, V. Fung, L. Nguyen, Y. Tang, F. Tao, Y. Cheng, L.L. Daemen, A.J. Ramirez-cuesta, G.S. Foo, M. Zhu, I.E. Wachs, D. Jiang, Z. Wu, Elucidation of the Reaction Mechanism for High-Temperature Water Gas Shift over an Industrial-Type Copper − Chromium − Iron Oxide Catalyst, J. Am. Chem. Soc. 141 (2019) 7990–7999. https://doi.org/10.1021/jacs.9b03516.

[46] A.A. Gokhale, J.A. Dumesic, M. Mavrikakis, On the Mechanism of Low-Temperature Water Gas Shift Reaction on Copper, J. Am. Chem. Soc. 130 (2008) 1402–1414.

[47] T. Shido, Y. Iwasawa, Regulation of Reaction Intermediate by Reactant in the Water-Gas Shift Reaction on CeO2 , in Relation to Reactant-Promoted Mechanism, J. Catal. 136 (1992) 493–503.

[48] Z. Li, N. Li, N. Wang, B. Zhou, P. Yin, B. Song, J. Yu, Y. Yang, Mechanism Investigations on Water Gas Shift Reaction over Cu(111), Cu(100), and Cu(211) Surfaces, ACS Omega. 7 (2022) 3514–3521. https://doi.org/10.1021/acsomega.1c05991.

[49] N.C. Nelson, M.T. Nguyen, V.A. Glezakou, R. Rousseau, J. Szanyi, Carboxyl intermediate formation via an in situ-generated metastable active site during water-gas shift catalysis, Nat. Catal. 2 (2019) 916–924. https://doi.org/10.1038/s41929-019-0343-2.

[50] L.F. Bobadilla, J.L. Santos, S. Ivanova, J.A. Odriozola, A. Urakawa, Unravelling the Role of Oxygen Vacancies in the Mechanism of the Reverse Water-Gas Shift Reaction by Operando DRIFTS and Ultraviolet-Visible Spectroscopy, ACS Catal. 8 (2018) 7455–7467. https://doi.org/10.1021/acscatal.8b02121.

[51] E. Baraj, K. Ciahotný, T. Hlinčík, The water gas shift reaction: Catalysts and reaction mechanism, Fuel. 288 (2021) 119817–119833. https://doi.org/10.1016/j.fuel.2020.119817.

[52] J. T.-Jørgensen, TOPSOE INTEGRATED GASOLINE SYNTHESIS - THE TIGAS PROCESS, Stud. Surf. Sci. Catal. 36 (1988) 293–305.

[53] C.D. Chang, W.H. Lang, A.J. Silvestri, Synthesis gas conversion to aromatic hydrocarbons, J. Catal. 56 (1979) 268–273. https://doi.org/10.1016/0021-9517(79)90113-1.

[54] D.C. Chang, H.W. Lang, Conversion of Synthesis Gas to Aromatic Hydrocarbons, 4188336, 1980.

[55] L.A. Bruce, G.J. Hope, J.F. Mathews, Conversion of Synthesis Gas to Aromatic-Containing Hydrocarbons Under mild Conditions, Appl. Catal. 9 (1984) 351–359.

[56] K. Fujimoto, Y. Kudo, H. o. Tominaga, Synthesis gas conversion utilizing mixed catalyst composed of CO reducing catalyst and solid acid. II. Direct synthesis of aromatic hydrocarbons from synthesis gas, J. Catal. 87 (1984) 136–143. https://doi.org/10.1016/0021-9517(84)90176-3.

[57] O.A. Ojelade, S.F. Zaman, A Review on Pd Based Catalysts for CO2 Hydrogenation to Methanol: In-Depth Activity and DRIFTS Mechanistic Study, Catal. Surv. from Asia. 24 (2020) 11–37. https://doi.org/10.1007/s10563-019-09287-z.

[58] K. Fujimoto, H. Saima, H.O. Tominaga, Hydrogenation of Carbon Monoxide on Carbon Monoxide Reducing Catalyst and Solid Acid. 6. Selective Production of C3 and C4 Hydrocarbons from Synthesis Gas, Ind. Eng. Chem. Res. 27 (1988) 920–926. https://doi.org/10.1021/ie00078a004.

[59] T. Liu, T. Lu, M. Yang, L. Zhou, X. Yang, B. Gao, Y. Su, Enhanced Catalytic Performance of CuO–ZnO–Al2O3/SAPO-5 Bifunctional Catalysts for Direct Conversion of Syngas to Light Hydrocarbons and Insights into the Role of Zeolite Acidity, Catal. Letters. 149 (2019) 3338–3348. https://doi.org/10.1007/s10562-019-02901-9.

[60] C. Li, K. Fujimoto, Synthesis gas conversion to isobutane-rich hydrocarbons over a hybrid catalyst containing Beta zeolite - Role of doped palladium and influence of the SiO2/Al2O3 ratio, Catal. Sci. Technol. 5 (2015) 4501–4510. https://doi.org/10.1039/c5cy00766f.

[61] C. Li, X. Yuan, K. Fujimoto, Direct synthesis of LPG from carbon dioxide over hybrid catalysts comprising modified methanol synthesis catalyst and β-type zeolite, Appl. Catal. A Gen. 475 (2014) 155–160. https://doi.org/10.1016/j.apcata.2014.01.025.

[62] K. Fujimoto, H. Saima, H. Tominaga, Synethesis Gas Conversion Utilizing Mixed Catalyst composed of CO reducing Catalyst and Solid Acid: IV. Selective Synthesis of C2, C3, and C4 Paraffins from Synthesis Gas, J. Catal. 94 (1985) 16–23.

[63] J.K. Jeon, K.E. Jeong, Y.K. Park, S.K. Ihm, Selective synthesis of C3-C4 hydrocarbons through carbon dioxide hydrogenation on hybrid catalysts composed of a methanol synthesis catalyst and SAPO, Appl. Catal. A, Gen. 124 (1995) 91–106. https://doi.org/10.1016/0926-860X(94)00258-4.

[64] C. Li, H. Ban, W. Cai, Y. Zhang, Z. Li, K. Fujimoto, Direct synthesis of iso-butane from synthesis gas or CO2 over CuZnZrAl/Pd-β hybrid catalyst, J. Saudi Chem. Soc. 21 (2017) 974–982. https://doi.org/10.1016/j.jscs.2017.05.003.

[65] C. Li, K. Fujimoto, Selective synthesis of isobutane from CO2-containing synthesis gas, Energy and Fuels. 28 (2014) 1331–1337. https://doi.org/10.1021/ef402393j.

[66] S. Ilias, A. Bhan, Mechanism of the Catalytic Conversion of Methanol to Hydrocarbons, ACS Catal. 3 (2013) 18–31.

[67] Y. V Joshi, K.T. Thomson, Brønsted Acid Catalyzed Cyclization of C7 and C8 Dienes in HZSM-5 : A Hybrid QM / MM Study and Comparison with C6 Diene Cyclization, (2008) 12825–12833.

[68] A. Sassi, M.A. Wildman, H.J. Ahn, P. Prasad, J.B. Nicholas, J.F. Haw, Methylbenzene Chemistry on Zeolite HBeta : Multiple Insights into Methanol-to-Olefin Catalysis, J. Phys. Chem. B. 106 (2002) 2294–2303.

[69] J.S. Buchanan, J.G. Santiesteban, W.O. Haag, Mechanistic Considerations in Acid-Catalyzed Cracking of Olefins, J. Catal. 158 (1996) 279–287.

[70] M. Fujiwara, T. Satake, K. Shiokawa, H. Sakurai, CO2 hydrogenation for C2+ hydrocarbon synthesis over composite catalyst using surface modified HB zeolite, Appl. Catal. B Environ. 179 (2015) 37–43. https://doi.org/10.1016/j.apcatb.2015.05.004.

[71] D.L.S. Nieskens, J.D. Lunn, A. Malek, Understanding the Enhanced Lifetime of SAPO-34 in a Direct Syngas-to-Hydrocarbons Process, ACS Catal. 9 (2019) 691–700.

https://doi.org/10.1021/acscatal.8b03465.

[72] P. Ticali, S. Morandi, G. Shterk, S. Ould-chikh, A. Ramirez, J. Gascon, S. Chung, J. Ruiz-martinez, S. Bordiga, PdZn/ZrO2 + SAPO-34 bifunctional catalyst for CO2 conversion : Further insights by spectroscopic characterization, Appl. Catal. A , Gen. 655 (2023) 1–9.

[73] A. Ramirez, P. Ticali, D. Salusso, T. Cordero-lanzac, S. Ould-chikh, C. Ahoba-sam, A.L. Bugaev, E. Borfecchia, S. Morandi, M. Signorile, S. Bordiga, J. Gascon, U. Olsbye, Multifunctional Catalyst Combination for the Direct Conversion of CO2 to Propane, JACS Au. 1 (2021) 1719–1732. https://doi.org/10.1021/jacsau.1c00302.

[74] M. Tong, E. Hondo, L. Gapu Chizema, C. Du, Q. Ma, S. Mo, C. Lu, P. Lu, N. Tsubaki, Hydrogenation of CO2to LPG over CuZnZr/MeSAPO-34 catalysts, New J. Chem. 44 (2020) 9328–9336. https://doi.org/10.1039/d0nj00907e.

[75] A. V. Kirilin, J.F. Dewilde, V. Santos, A. Chojecki, K. Scieranka, A. Malek, Conversion of Synthesis Gas to Light Olefins: Impact of Hydrogenation Activity of Methanol Synthesis Catalyst on the Hybrid Process Selectivity over Cr-Zn and Cu-Zn with SAPO-34, Ind. Eng. Chem. Res. 56 (2017) 13392–13401. https://doi.org/10.1021/acs.iecr.7b02401.

[76] F. Bleken, Æ.M. Bjørgen, Æ.L. Palumbo, S. Bordiga, Æ.S. Svelle, The Effect of Acid Strength on the Conversion of Methanol to Olefins Over Acidic Microporous Catalysts with the CHA Topology, Top Catal. 52 (2009) 218–228. https://doi.org/10.1007/s11244-008-9158-0.

[77] S. Wilson, P. Barger, The characteristics of SAPO-34 which influence the conversion of methanol to light olefins, Microporous Mesoporous Mater. 29 (1999) 117–126. https://doi.org/10.1016/S1387-1811(98)00325-4.

[78] F.H. Alshafei, Y. Park, S.I. Zones, M.E. Davis, Methanol-to-olefins catalysis on ERI-type molecular sieves: towards enhancing ethylene selectivity, J. Catal. 404 (2021) 620–633. https://doi.org/10.1016/j.jcat.2021.10.025.

[79] D. Chen, H.P. Rebo, K. Moljord, A. Holmen, Methanol conversion to light olefins over SAPO-34. Sorption, diffusion, and catalytic reactions, Ind. Eng. Chem. Res. 38 (1999) 4241–4249. https://doi.org/10.1021/ie9807046.

[80] B.P.C. Hereijgers, F. Bleken, M.H. Nilsen, S. Svelle, K.P. Lillerud, M. Bjørgen, B.M. Weckhuysen, U. Olsbye, Product shape selectivity dominates the Methanol-to-Olefins (MTO) reaction over H-SAPO-34 catalysts, J. Catal. 264 (2009) 77–87. https://doi.org/10.1016/j.jcat.2009.03.009.

[81] J. Sehested, Industrial and scientific directions of methanol catalyst development, J. Catal. 371 (2019) 368–375. https://doi.org/10.1016/j.jcat.2019.02.002.

[82] M.B. Fichtl, D. Schlereth, N. Jacobsen, I. Kasatkin, J. Schumann, M. Behrens, R. Schlögl, O. Hinrichsen, Kinetics of deactivation on Cu/ZnO/Al2O3 methanol synthesis catalysts, Appl. Catal. A Gen. 502 (2015) 262–270. https://doi.org/10.1016/j.apcata.2015.06.014.

[83] M. Kurtz, H. Wilmer, T. Genger, O. Hinrichsen, M. Muhler, Deactivation of supported copper catalysts for methanol synthesis, Catal. Letters. 86 (2003) 77–80.

[84] T. Lunkenbein, F. Girgsdies, T. Kandemir, N. Thomas, M. Behrens, R. Schlögl, E. Frei, Bridging the Time Gap: A Copper/Zinc Oxide/Aluminum Oxide Catalyst for Methanol Synthesis Studied under Industrially Relevant Conditions and Time Scales, Angew. Chemie -

Int. Ed. 55 (2016) 12708–12712. https://doi.org/10.1002/anie.201603368.

[85] M. Behrens, F. Studt, I. Kasatkin, S. Kühl, M. Hävecker, F. Abild-pedersen, S. Zander, F. Girgsdies, P. Kurr, B. Kniep, M. Tovar, R.W. Fischer, J.K. Nørskov, R. Schlögl, The Active Site of Methanol Synthesis over Cu/ZnO/Al2O3 Industrial Catalysts, Science (80-.). 336 (2012) 893–897.

[86] S. Kuld, M. Thorhauge, H. Falsig, C.F. Elkjær, S. Helveg, I. Chorkendorff, J. Sehested, Quantifying the promotion of Cu catalysts by ZnO for methanol synthesis, Science (80-.). 352 (2016) 969–974.

[87] V. Schott, H. Oberhofer, A. Birkner, M. Xu, Y. Wang, M. Muhler, K. Reuter, C. Wçll, Chemical Activity of Thin Oxide Layers : Strong Interactions with the Support Yield a New Thin-Film Phase of ZnO, Angew. Chemie - Int. Ed. 52 (2013) 11925–11929. https://doi.org/10.1002/anie.201302315.

[88] T. Lunkenbein, J. Schumann, M. Behrens, R. Schlçgl, M.G. Willinger, Formation of a ZnO Overlayer in Industrial Cu/ZnO/Al2O3 Catalysts Induced by Strong Metal – Support Interactions, Angew. Chemie - Int. Ed. 54 (2015) 4544–4548. https://doi.org/10.1002/anie.201411581.

[89] M. Bowker, R.A. Hadden, H. Houghton, J.N.K. Hyland, K.C. Waugh, The mechanism of methanol synthesis on copper/zinc oxide/alumina catalysts, J. Catal. 109 (1988) 263–273. https://doi.org/10.1016/0021-9517(88)90209-6.

[90] J. Frenzel, J. Kiss, N.N. Nair, B. Meyer, D. Marx, Methanol synthesis on ZnO from molecular dynamics, Phys. Status Solidi B. 6 (2013) 1174–1190. https://doi.org/10.1002/pssb.201248446.

[91] I. Chemical, I. Limited, T. Heath, Mechanism and Kinetics of Methanol Synthesis on Zinc Oxide, J. Chem. Soc., Faraday Trans. 2 (1981) 3023–3036.

[92] H. Wilmer, M. Kurtz, K. V Klementiev, O.P. Tkachenko, W. Grunert, O. Hinrichsen, A. Birkner, S. Rabe, K. Merz, M. Driees, C. Wöll, M. Muhler, Methanol synthesis over ZnO: A structure-sensitive reaction?, Phys. Chem. Chem. Phys. 5 (2003) 4736–4742. https://doi.org/10.1039/b304425d.

[93] S.A. French, A.A. Sokol, T. Bromley, C.R.A. Catlow, S.C. Rogers, F. King, P. Sherwood, From CO2 to Methanol by Hybrid QM/MM Embedding, Angew. Chem. Int. Ed. (2001) 4437–4440.

[94] S.A. French, A.A. Sokol, S.T. Bromley, C.R.A. Catlow, P. Sherwood, Identification and characterization of active sites and their catalytic processes — the Cu/ZnO methanol catalyst, Top. Catal. 24 (2003) 161–172.

[95] J. Wang, G. Li, Z. Li, C. Tang, Z. Feng, H. An, H. Liu, T. Liu, C. Li, A highly selective and stable ZnO-ZrO2 solid solution catalyst for CO2 hydrogenation to methanol, Sci. Adv. 3 (2017) 1–11. https://doi.org/10.1126/sciadv.1701290.

[96] R.P. INGEL, D.L. III, Lattice Parameters and Density for Y2O3-Stabilized ZrO2, J. Am. Ceram. Soc. 69 (1986) 325–332. https://doi.org/10.1111/j.1151-2916.1986.tb04741.x.

[97] S. Pradhan, B.G. Mishra, Catalytic application of SO42-/Fe-ZrO2 nanoparticles synthesized by a urea hydrolysis method for environmentally benign one pot synthesis of 1,8-

dioxodecahydroacridines, RSC Adv. 5 (2015) 86179–86190. https://doi.org/10.1039/c5ra11136f.

[98] S. Vasanthavel, S. Kannan, Structural investigations on the tetragonal to cubic phase transformations in zirconia induced by progressive yttrium additions, J. Phys. Chem. Solids. 112 (2018) 100–105. https://doi.org/10.1016/j.jpcs.2017.09.010.

[99] Z. Han, C. Tang, F. Sha, S. Tang, J. Wang, C. Li, CO2 hydrogenation to methanol on ZnO-ZrO2 solid solution catalysts with ordered mesoporous structure, J. Catal. 396 (2021) 242–250. https://doi.org/10.1016/j.jcat.2021.02.024.

[100] S. Tada, N. Ochiai, H. Kinoshita, M. Yoshida, N. Shimada, T. Joutsuka, M. Nishijima, T. Honma, N. Yamauchi, Y. Kobayashi, K. Iyoki, Active Sites on ZnxZr1– x O2– x Solid Solution Catalysts for CO2 -to-Methanol Hydrogenation, ACS Catal. 12 (2022) 7748–7759. https://pubs.acs.org/doi/10.1021/acscatal.2c01996.

[101] J. Ding, Z. Li, W. Xiong, Y. Zhang, A. Ye, W. Huang, Structural evolution and catalytic performance in CO2 hydrogenation reaction of ZnO-ZrO2 composite oxides, Appl. Surf. Sci. 587 (2022). https://doi.org/10.1016/j.apsusc.2022.152884.

[102] S. Aghabeygi, M. Khademi-Shamami, ZnO/ZrO2 nanocomposite: Sonosynthesis, characterization and its application for wastewater treatment, Ultrason. Sonochem. 41 (2018) 458–465. https://doi.org/10.1016/j.ultsonch.2017.09.020.

[103] C. Wang, G. Garbarino, L.F. Allard, F. Wilson, G. Busca, M. Flytzani-Stephanopoulos, Low-Temperature Dehydrogenation of Ethanol on Atomically Dispersed Gold Supported on ZnZrOx, ACS Catal. 6 (2016) 210–218. https://doi.org/10.1021/acscatal.5b01593.

[104] D. Salusso, E. Borfecchia, S. Bordiga, Combining X-ray Diffraction and X-ray Absorption Spectroscopy to Unveil Zn Local Environment in Zn-Doped ZrO2Catalysts, J. Phys. Chem. C. 125 (2021) 22249–22261. https://doi.org/10.1021/acs.jpcc.1c06202.

[105] S. Han, D. Zhao, T. Otroshchenko, H. Lund, U. Bentrup, V.A. Kondratenko, N. Rockstroh, S. Bartling, D.E. Doronkin, J.D. Grunwaldt, U. Rodemerck, D. Linke, M. Gao, G. Jiang, E. V. Kondratenko, Elucidating the Nature of Active Sites and Fundamentals for their Creation in Zn-Containing ZrO2-Based Catalysts for Nonoxidative Propane Dehydrogenation, ACS Catal. 10 (2020) 8933–8949. https://doi.org/10.1021/acscatal.0c01580.

[106] K. Cheng, W. Zhou, J. Kang, S. He, S. Shi, Q. Zhang, Y. Pan, W. Wen, Y. Wang, Bifunctional Catalysts for One-Step Conversion of Syngas into Aromatics with Excellent Selectivity and Stability, Chem. 3 (2017) 334–347. https://doi.org/10.1016/j.chempr.2017.05.007.

[107] C. Temvuttirojn, Y. Poo-arporn, N. Chanlek, C.K. Cheng, C.C. Chong, J. Limtrakul, T. Witoon, Role of Calcination Temperatures of ZrO2 Support on Methanol Synthesis from CO2 Hydrogenation at High Reaction Temperatures over ZnOx/ZrO2 Catalysts, Ind. Eng. Chem. Res. 59 (2020) 5525–5535. https://doi.org/10.1021/acs.iecr.9b05691.

[108] L. Lin, G. Wang, F. Zhao, CO2 Hydrogenation to Methanol on ZnO/ZrO2 Catalysts : Effects of Zirconia Phase, Chem. Sel. 6 (2021) 2119–2125.

[109] F. Sha, C. Tang, S. Tang, Q. Wang, Z. Han, J. Wang, C. Li, The promoting role of Ga in ZnZrOx solid solution catalyst for CO2 hydrogenation to methanol, J. Catal. 404 (2021) 383–392.

[110] X. Liu, M. Wang, H. Yin, J. Hu, K. Cheng, J. Kang, Q. Zhang, Y. Wang, Tandem Catalysis for Hydrogenation of CO and CO2 to Lower Olefins with Bifunctional Catalysts Composed of Spinel Oxide and SAPO-34, ACS Catal. 10 (2020) 8303–8314. https://doi.org/10.1021/acscatal.0c01579.

[111] X. Liu, M. Wang, C. Zhou, W. Zhou, K. Cheng, J. Kang, Q. Zhang, W. Deng, Y. Wang, Selective transformation of carbon dioxide into lower olefins with a bifunctional catalyst composed of ZnGa2O4 and SAPO-34, Chem. Commun. 54 (2017) 140–143. https://doi.org/10.1039/c7cc08642c.

[112] A. Ye, Z. Li, J. Ding, W. Xiong, W. Huang, Synergistic Catalysis of Al and Zn Sites of Spinel ZnAl2O4Catalyst for CO Hydrogenation to Methanol and Dimethyl Ether, ACS Catal. 11 (2021) 10014–10019. https://doi.org/10.1021/acscatal.1c02742.

[113] W. De Hu, C.M. Wang, Y.D. Wang, J. Ke, G. Yang, Y.J. Du, W.M. Yang, First-principles-based microkinetic simulations of syngas to methanol conversion on ZnAl2O4 spinel oxide, Appl. Surf. Sci. 569 (2021) 151064. https://doi.org/10.1016/j.apsusc.2021.151064.

[114] X. Zhang, G. Zhang, W. Liu, F. Yuan, J. Wang, J. Zhu, X. Jiang, A. Zhang, F. Ding, C. Song, X. Guo, Reaction-driven surface reconstruction of ZnAl2O4 boosts the methanol selectivity in CO2 catalytic hydrogenation, Appl. Catal. B Environ. 284 (2021) 119700. https://doi.org/10.1016/j.apcatb.2020.119700.

[115] H. Song, D. Laudenschleger, J.J. Carey, H. Ruland, M. Nolan, M. Muhler, Spinel-Structured ZnCr2O4 with Excess Zn Is the Active ZnO/Cr2O3 Catalyst for High-Temperature Methanol Synthesis, ACS Catal. 7 (2017) 7610–7622. https://doi.org/10.1021/acscatal.7b01822.

[116] T. Ferruccio, A. Vaccari, Non-stoichiometry as key to modify the activity and selectivity of spinel-type catalysts for hydrogenation reactions, Struct. Sel. Relationships Heterog. Catal. 67 (1991) 157–167.

[117] G. Del Piero, F. Trifiro, A. Vaccaria, Non-stoicheismetric Zn-Cr Spinel as Active Phase in the Catalytic Synthesis of Methanol, J. CHEM. SOC., CHEM. COMMUN. 3 (1984) 656–658.

[118] Y. Souma, F. M, R. Kieffer, H. Ando, Q. Xu, Hydrocarbon synthesis from CO2 over composite catalysts, Surf. Sci. Catal. 114 (1998) 327-.

[119] M. Fujiwara, R. Kieffer, H. Ando, Q. Xu, Y. Souma, Change of catalytic properties of Fe-ZnO/zeolite composite catalyst in the hydrogenation of carbon dioxide, Appl. Catal. A Gen. 154 (1997) 87–101. https://doi.org/10.1016/S0926-860X(96)00360-2.

[120] O. Martin, A.J. Martín, C. Mondelli, S. Mitchell, T.F. Segawa, R. Hauert, C. Drouilly, D. Curulla-Ferré, J. Pérez-Ramírez, Indium oxide as a superior catalyst for methanol synthesis by CO2 hydrogenation, Angew. Chemie - Int. Ed. 55 (2016) 6261–6265. https://doi.org/10.1002/anie.201600943.

[121] F. Studt, I. Sharafutdinov, F. Abild-Pedersen, C.F. Elkjær, J.S. Hummelshøj, S. Dahl, I. Chorkendorff, J.K. Nørskov, Discovery of a Ni-Ga catalyst for carbon dioxide reduction to methanol, Nat. Chem. 6 (2014) 320–324. https://doi.org/10.1038/nchem.1873.

[122] F.J. Keil, Methanol-to-hydrocarbons: process technology, Microporous Mesoporous Mater. 29 (1999) 49–66. https://doi.org/https://doi.org/10.1016/S1387-1811(98)00320-5.

[123] OECD, Global Plastics Outlook: Plastics use by polymer - projections, OECD Environ. Stat.

(2022). https://doi.org/10.1787/b9bae4d1-en (accessed September 22, 2022).

[124] J. Weitkamp, Zeolites and catalysis, Solid State Ionics. 131 (2000) 175–188. https://doi.org/10.1016/S0167-2738(00)00632-9.

[125] C. Baerlocher, L.B. McCusker, D.H. Olson, Atlas of Zeolite Framework Types, 6th Editio, Elsevier Science, 2007. https://doi.org/https://doi.org/10.1016/B978-0-444-53064-6.X5186-X.

[126] G. T. Kokotailo, S. L. Lawton, D. H. Olson, W. M. Meier, Structure of synthetic zeolite ZSM-5, Nature. 272 (1978) 437–438.

[127] D.H. Olson, G.T. Kokotailo, S.L. Lawton, W.M. Meier, Crystal structure and structure-related properties of ZSM-5, J. Phys. Chem. 85 (1981) 2238–2243. https://doi.org/10.1021/j150615a020.

[128] S.. I.Z. Association, Database of Zeolite Structures, (2017). https://europe.iza-structure.org/IZA-SC/material_tm.php?STC=MFI (accessed October 9, 2020).

[129] S. Wang, P. Wang, Z. Qin, Y. Chen, M. Dong, J. Li, K. Zhang, P. Liu, J. Wang, W. Fan, Relation of catalytic performance to the aluminum siting of acidic zeolites in the conversion of methanol to olefins, viewed via a comparison between ZSM-5 and ZSM-11, ACS Catal. 8 (2018) 5485–5505. https://doi.org/10.1021/acscatal.8b01054.

[130] M. Fischer, Template effects on the pressure-dependent behavior of chabazite-type fluoroaluminophosphates: a computational approach, Phys. Chem. Miner. 46 (2019) 385–401. https://doi.org/10.1007/s00269-018-1010-x.

[131] N.J. Tapp, N.B. Milestone, D.M. Bibby, Generation of acid sites in substituted aluminophosphate molecular sieves, Stud. Surf. Sci. Catal. 37 (1988) 393–402. https://doi.org/10.1016/S0167-2991(09)60616-9.

[132] J.S. Martínez-Espín, Mechanistic and kinetic investigations on the role of methanol and dimethyl ether in the Methanol-To-Hydrocarbons reaction Dissertation for the degree of Philosophiae Doctor, University of Oslo, 2017.

[133] A. Corma, Inorganic Solid Acids and Their Use in Acid-Catalyzed Hydrocarbon Reactions, Chem. Rev. 95 (1995) 559–614. https://doi.org/10.1021/cr00035a006.

[134] S. Bordiga, L. Regli, D. Cocina, C. Lamberti, M. Bjørgen, K.P. Lillerud, Assessing the acidity of high silica chabazite H-SSZ-13 by FTIR using CO as molecular probe: Comparison with H-SAPO-34, J. Phys. Chem. B. 109 (2005) 2779–2784. https://doi.org/10.1021/jp045498w.

[135] S. Müller, Y. Liu, F.M. Kirchberger, M. Tonigold, M. Sanchez-Sanchez, J.A. Lercher, Hydrogen Transfer Pathways during Zeolite Catalyzed Methanol Conversion to Hydrocarbons, J. Am. Chem. Soc. 138 (2016) 15994–16003. https://doi.org/10.1021/jacs.6b09605.

[136] W. Wu, W. Guo, W. Xiao, M. Luo, Dominant reaction pathway for methanol conversion to propene over high silicon H-ZSM-5, Chem. Eng. Sci. 66 (2011) 4722–4732. https://doi.org/10.1016/j.ces.2011.06.036.

[137] I.M. Dahl, On the reaction mechanism for propene formation in the MTO reaction over SAPO-34, Catal. Letters. 20 (1993) 329–336.

[138] I.M. Dahl, S. Kolboe, On the Reaction Mechanism for Hydrocarbon Formation from Methanol over SAPO-34 1. Isotopic labeling Studies of the Co-reaction of Ethene and Methanol, J. Catal. 149 (1994) 458–464.

[139] B. Arstad, S. Kolboe, The Reactivity of Molecules Trapped within the SAPO-34 Cavities in the Methanol-to-Hydrocarbons Reaction, (2001) 8137–8138.

[140] W. Song, J.F. Haw, J.B. Nicholas, C.S. Heneghan, P.O. Box, R. V June, Methylbenzenes Are the Organic Reaction Centers for Methanol-to-Olefin Catalysis on HSAPO-34, (2000) 10726–10727.

[141] B. Arstad, S. Kolboe, Methanol-to-hydrocarbons reaction over SAPO-34 . Molecules confined in the catalyst cavities at short time on stream, Catal. Letters. 71 (2001) 209–212.

[142] J.F. Haw, J.B. Nicholas, W. Song, F. Deng, Z. Wang, T. Xu, C.S. Heneghan, Roles for Cyclopentenyl Cations in the Synthesis of Hydrocarbons from Methanol on Zeolite Catalyst HZSM-5, J. Am. Chem. Soc. 122 (2000) 4763–4775.

[143] S. Svelle, F. Joensen, J. Nerlov, U. Olsbye, K.P. Lillerud, S. Kolboe, M. Bjørgen, Conversion of methanol into hydrocarbons over zeolite H-ZSM-5: Ethene formation is mechanistically separated from the formation of higher alkenes, J. Am. Chem. Soc. 128 (2006) 14770–14771. https://doi.org/10.1021/ja065810a.

[144] M. Bjørgen, S. Svelle, F. Joensen, J. Nerlov, S. Kolboe, F. Bonino, L. Palumbo, S. Bordiga, U. Olsbye, Conversion of methanol to hydrocarbons over zeolite H-ZSM-5: On the origin of the olefinic species, J. Catal. 249 (2007) 195–207. https://doi.org/10.1016/j.jcat.2007.04.006.

[145] Ø. Mikkelsen, P.O. Rønning, S. Kolboe, Use of isotopic labeling for mechanistic studies of the methanol-to-hydrocarbons reaction . Methylation of toluene with methanol over H-ZSM-5 , H-mordenite and H-beta, Microporous Mesoporous Mater. 40 (2000) 95–113.

[146] D.S. Santilli, B.C. Gates, Hydrocarbon Reaction Mechanisms, in: Handb. Heterog. Catal., 2008: pp. 1624–1637.

[147] D. Lesthaeghe, A. Horré, M. Waroquier, G.B. Marin, V. Van Speybroeck, Theoretical Insights on Methylbenzene Side-Chain Growth in ZSM-5 Zeolites for Methanol-to-Olefin Conversion, Chem. Eur. J. 15 (2009) 10803–10808. https://doi.org/10.1002/chem.200901723.

[148] S.M. Csicsery, Catalysis by Zeolites – Science and Technology, Stud. Surf. Sci. Catal. 58 (1986) 841–856. https://doi.org/10.1016/S0167-2991(08)63680-0.

[149] F.G. Cirujano, F.X. Llabrés i Xamena, Metal Organic Frameworks as Nanoreactors and Host Matrices for Encapsulation, Elsevier Inc., 2016. https://doi.org/10.1016/B978-0-12-801713-5.00010-0.

[150] S. Teketel, U. Olsbye, K.P. Lillerud, P. Beato, S. Svelle, Selectivity control through fundamental mechanistic insight in the conversion of methanol to hydrocarbons over zeolites, Microporous Mesoporous Mater. 136 (2010) 33–41. https://doi.org/10.1016/j.micromeso.2010.07.013.

[151] Ø. Mikkelsen, S. Kolboe, The conversion of methanol to hydrocarbons over zeolite H-beta, Microporous Mesoporous Mater. 29 (1999) 173–184. https://doi.org/10.1016/S0926-860X(01)00865-1.

[152] G.J. Hutchings, P. Johnston, D.F. Lee, A. Warwick, C.D. Williams, M. Wilkinson, The Conversion of Methanol and Other O-Compounds to Hydrocarbons over Zeolite beta, J. Catal. 147 (1994) 177–185.

[153] M. Guisnet, F.R. Ribeiro, Deactivation and Regeneration of Zeolite Catalyst, Imperial College Press, 2011.

[154] M.D.P. Søerensen, The establishment of a coke-burn kinetic model for zeolite catalysts, Chem. Eng. Sci. 168 (2017) 465–479. https://doi.org/10.1016/j.ces.2017.05.014.

[155] M. Guisnet, P. Magnoux, Coking and deactivation of zeolites. Influence of the Pore Structure, Appl. Catal. 54 (1989) 1–27. https://doi.org/10.1016/S0166-9834(00)82350-7.

[156] J.F. Haw, D.M. Marcus, Well-defined (supra)molecular structures in zeolite methanol-to-olefin catalysis, Top. Catal. 34 (2005) 41–48. https://doi.org/10.1007/s11244-005-3798-0.

[157] M. Guisnet, L. Costa, F.R. Ribeiro, Prevention of zeolite deactivation by coking, J. Mol. Catal. A Chem. 305 (2009) 69–83. https://doi.org/10.1016/j.molcata.2008.11.012.

[158] M. Zhang, S. Xu, Y. Wei, J. Li, J. Chen, J. Wang, W. Zhang, S. Gao, X. Li, C. Wang, Z. Liu, Methanol conversion on ZSM-22, ZSM-35 and ZSM-5 zeolites: Effects of 10-membered ring zeolite structures on methylcyclopentenyl cations and dual cycle mechanism, RSC Adv. 6 (2016) 95855–95864. https://doi.org/10.1039/c6ra08884h.

[159] F. Bleken, W. Skistad, K. Barbera, M. Kustova, S. Bordiga, P. Beato, K.P. Lillerud, S. Svelle, U. Olsbye, Conversion of methanol over 10-ring zeolites with differing volumes at channel intersections: Comparison of TNU-9, IM-5, ZSM-11 and ZSM-5, Phys. Chem. Chem. Phys. 13 (2011) 2539–2549. https://doi.org/10.1039/c0cp01982h.

[160] J.W. Park, J.Y. Lee, K.S. Kim, S.B. Hong, G. Seo, Effects of cage shape and size of 8-membered ring molecular sieves on their deactivation in methanol-to-olefin (MTO) reactions, Appl. Catal. A Gen. 339 (2008) 36–44. https://doi.org/10.1016/j.apcata.2008.01.005.

[161] M. Bjorgen, S. Kolboe, The conversion of methanol to hydrocarbons over dealuminated zeolite H-beta, Appl. Catal. A Gen. 225 (2002) 285–290. https://doi.org/10.1016/S0926-860X(01)00865-1.

[162] A. Molino, J. Holzinger, K.A. Łukaszuk, D. Rojo-Gama, A.E. Gunnæs, J. Skibsted, L.F. Lundegaard, S. Svelle, P. Beato, S. Bordiga, K.P. Lillerud, Synthesis of ZSM-23 (MTT) zeolites with different crystal morphology and intergrowths: Effects on the catalytic performance in the conversion of methanol to hydrocarbons, Catal. Sci. Technol. 9 (2019) 6782–6792. https://doi.org/10.1039/c9cy01068h.

[163] M. Guisnet, P. Magnoux, Organic chemistry of coke formation, Appl. Catal. A Gen. 212 (2001) 83–96. https://doi.org/10.1016/S0926-860X(00)00845-0.

[164] D. Mores, E. Stavitski, M.H.F. Kox, J. Kornatowski, U. Olsbye, B.M. Weckhuysen, Space-And time-resolved in-situ spectroscopy on the coke formation in molecular sieves: Methanol-to-olefin conversion over H-ZSM-5 and H-SAPO-34, Chem. - A Eur. J. 14 (2008) 11320–11327. https://doi.org/10.1002/chem.200801293.

[165] D. Rojo-Gama, M. Nielsen, D.S. Wragg, M. Dyballa, J. Holzinger, H. Falsig, L.F. Lundegaard, P. Beato, R.Y. Brogaard, K.P. Lillerud, U. Olsbye, S. Svelle, A Straightforward Descriptor for the Deactivation of Zeolite Catalyst H-ZSM-5, ACS Catal. 7 (2017) 8235–8246.

https://doi.org/10.1021/acscatal.7b02193.

[166] D. Chen, H.P. Rebo, A. Grønvold, K. Moljord, A. Holmen, Methanol conversion to light olefins over SAPO-34: Kinetic modeling of coke formation, Microporous Mesoporous Mater. 35–36 (2000) 121–135. https://doi.org/10.1016/S1387-1811(99)00213-9.

[167] D. Chen, K. Moljord, A. Holmen, A methanol to olefins review: Diffusion, coke formation and deactivation on SAPO type catalysts, Microporous Mesoporous Mater. 164 (2012) 239–250. https://doi.org/10.1016/j.micromeso.2012.06.046.

[168] W. Song, H. Fu, J.F. Haw, Supramolecular origins of product selectivity for methanol-to-olefin catalysis on HSAPO-34, J. Am. Chem. Soc. 123 (2001) 4749–4754. https://doi.org/10.1021/ja0041167.

[169] I.M. Dahl, R. Wendelbo, A. Andersen, D. Akporiaye, H. Mostad, T. Fuglerud, The effect of crystallite size on the activity and selectivity of the reaction of ethanol and 2-propanol over SAPO-34, Microporous Mesoporous Mater. 29 (1999) 159–171. https://doi.org/10.1016/S1387-1811(98)00328-X.

[170] P. Barger, Methanol to Olefins (MTO) and Beyond, in: Zeolites Clean. Technol., 202AD: pp. 239–260.

[171] D. Chen, K. Moljord, T. Fuglerud, A. Holmen, The effect of crystal size of SAPO-34 on the selectivity and deactivation of the MTO reaction, Microporous Mesoporous Mater. 29 (1999) 191–203. https://doi.org/10.1016/S1387-1811(98)00331-X.

[172] D.M. Marcus, W. Song, L.L. Ng, J.F. Haw, Aromatic hydrocarbon formation in HSAPO-18 catalysts: cage topology and acid site density, Langmuir. 18 (2002) 8386–8391. https://doi.org/10.1021/la011556i.

[173] M. Silaghi, C. Chizallet, J. Sauer, P. Raybaud, Dealumination mechanisms of zeolites and extra-framework aluminum confinement, J. Catal. 339 (2016) 242–255.

[174] K. Valdiviés-Cruz, A. Lam, C.M. Zicovich-wilson, Full Mechanism of Zeolite Dealumination in Aqueous Strong Acid Medium: Ab Initio Periodic Study on H - Clinoptilolite, J. Phys. Chem. C. 121 (2017) 2652–2660. https://doi.org/10.1021/acs.jpcc.6b09794.

[175] L.R. Aramburo, S. Teketel, S. Svelle, S.R. Bare, B. Arstad, H.W. Zandbergen, U. Olsbye, F.M.F. De Groot, B.M. Weckhuysen, Interplay between nanoscale reactivity and bulk performance of H-ZSM-5 catalysts during the methanol-to-hydrocarbons reaction, J. Catal. 307 (2013) 185–193.

[176] J. Wei, R. Yao, Q. Ge, Z. Wen, X. Ji, C. Fang, J. Zhang, H. Xu, J. Sun, Catalytic Hydrogenation of CO2 to Isoparaffins over Fe-Based Multifunctional Catalysts, ACS Catal. 8 (2018) 9958–9967. https://doi.org/10.1021/acscatal.8b02267.

[177] Y. Xu, C. Shi, B. Liu, T. Wang, J. Zheng, W. Li, D. Liu, X. Liu, Selective production of aromatics from CO2, Catal. Sci. Technol. 9 (2019) 593–610. https://doi.org/10.1039/c8cy02024h.

[178] D. Goud, R. Gupta, R. Maligal-ganesh, S.C. Peter, Review of Catalyst Design and Mechanistic Studies for the Production of Olefins from Anthropogenic CO2, (2020).

[179] S. De, A. Dokania, A. Ramirez, J. Gascon, Advances in the Design of Heterogeneous Catalysts

and Thermocatalytic Processes for CO2 Utilization, ACS Catal. (2020) 14147–14185. https://doi.org/10.1021/acscatal.0c04273.

[180] W. Zhou, K. Cheng, J. Kang, C. Zhou, V. Subramanian, Q. Zhang, Y. Wang, New horizon in C1 chemistry: Breaking the selectivity limitation in transformation of syngas and hydrogenation of CO2 into hydrocarbon chemicals and fuels, Chem. Soc. Rev. 48 (2019) 3193–3228. https://doi.org/10.1039/c8cs00502h.

[181] T. Riedel, M. Claeys, H. Schulz, G. Schaub, S.-S. Nam, K.-W. Jun, M.-J. Choi, G. Kishan, K.-W. Lee, Comparative study of Fischer–Tropsch synthesis with H /CO and H2 /CO2 syngas using Fe-and Co-based catalysts, Appl. Catal. A Gen. 186 (1999) 201–213.

[182] Y. Yang, H.W. Xiang, Y.Y. Xu, L. Bai, Y.W. Li, Effect of potassium promoter on precipitated iron-manganese catalyst for Fischer-Tropsch synthesis, Appl. Catal. A Gen. 266 (2004) 181–194. https://doi.org/10.1016/j.apcata.2004.02.018.

[183] D. Das, G. Ravichandran, D.K. Chakrabarty, iron and cobalt catalysts : Effect of manganese addition, 861 (1997).

[184] J. Wang, Z. You, Q. Zhang, W. Deng, Y. Wang, Synthesis of lower olefins by hydrogenation of carbon dioxide over supported iron catalysts, Catal. Today. 215 (2013) 186–193. https://doi.org/10.1016/j.cattod.2013.03.031.

[185] M. Ronda-lloret, G. Rothenberg, N.R. Shiju, A Critical Look at Direct Catalytic Hydrogenation of Carbon Dioxide to Olefins, (2019) 3896–3914. https://doi.org/10.1002/cssc.201900915.

[186] A. Ramirez, A. Dutta Chowdhury, A. Dokania, P. Cnudde, M. Caglayan, I. Yarulina, E. Abou-Hamad, L. Gevers, S. Ould-Chikh, K. De Wispelaere, V. Van Speybroeck, J. Gascon, Effect of Zeolite Topology and Reactor Configuration on the Direct Conversion of CO2 to Light Olefins and Aromatics, ACS Catal. 9 (2019) 6320–6334. https://doi.org/10.1021/acscatal.9b01466.

[187] A. Ramirez, A. Dutta Chowdhury, M. Caglayan, A. Rodriguez-Gomez, N. Wehbe, E. Abou-Hamad, L. Gevers, S. Ould-Chikh, J. Gascon, Coated sulfated zirconia/SAPO-34 for the direct conversion of CO2 to light olefins, Catal. Sci. Technol. 10 (2020) 1507–1517. https://doi.org/10.1039/c9cy02532d.

[188] P. Zhang, F. Meng, L. Yang, G. Yang, X. Liang, Z. Li, Syngas to Olefins over a CrMnGa/SAPO-34 Bifunctional Catalyst: Effect of Cr and Cr / Mn Ratio, Am. Chem. Soc. 60 (2021) 13214–13222.

[189] P. Zhang, F. Meng, X. Li, L. Yang, P. Ma, Z. Li, Excellent selectivity for direct conversion of syngas to light olefins over a Mn-Ga oxide and SAPO-34 bifunctional catalyst, Catal. Sci. Technol. 9 (2019) 5577–5581. https://doi.org/10.1039/c9cy01348b.

[190] P. Gao, S. Dang, S. Li, X. Bu, Z. Liu, M. Qiu, C. Yang, H. Wang, L. Zhong, Y. Han, Q. Liu, W. Wei, Y. Sun, Direct Production of Lower Olefins from CO2 Conversion via Bifunctional Catalysis, ACS Catal. 8 (2018) 571–578. https://doi.org/10.1021/acscatal.7b02649.

[191] X. Liu, W. Zhou, Y. Yang, K. Cheng, J. Kang, L. Zhang, G. Zhang, X. Min, Q. Zhang, Y. Wang, Design of efficient bifunctional catalysts for direct conversion of syngas into lower olefins: Via methanol/dimethyl ether intermediates, Chem. Sci. 9 (2018) 4708–4718.

https://doi.org/10.1039/c8sc01597j.

[192] T. Numpilai, C. Wattanakit, M. Chareonpanich, J. Limtrakul, T. Witoon, Optimization of synthesis condition for CO2 hydrogenation to light olefins over In2O3 admixed with SAPO-34, Energy Convers. Manag. 180 (2019) 511–523.

[193] S. Dang, S. Li, C. Yang, X. Chen, X. Li, L. Zhong, P. Gao, Y. Sun, Selective Transformation of CO2 and H2 into Lower Olefins over In2O3-ZnZrOx/SAPO-34 Bifunctional Catalysts, ChemSusChem. 12 (2019) 3582–3591. https://doi.org/10.1002/cssc.201900958.

[194] M. Ghasemi, M. Mohammadi, M. Sedighi, Sustainable production of light olefins from greenhouse gas CO2 over SAPO-34 supported modified cerium oxide, Microporous Mesoporous Mater. 297 (2020). https://doi.org/10.1016/j.micromeso.2020.110029.

[195] S. Wang, P. Wang, D. Shi, S. He, L. Zhang, W. Yan, Z. Qin, J. Li, M. Dong, J. Wang, U. Olsbye, W. Fan, Direct Conversion of Syngas into Light Olefins with Low CO2 Emission, ACS Catal. 10 (2020) 2046–2059. https://doi.org/10.1021/acscatal.9b04629.

[196] S. Wang, P. Wang, Z. Qin, W. Yan, M. Dong, J. Li, J. Wang, W. Fan, Enhancement of light olefin production in CO2 hydrogenation over In2O3-based oxide and SAPO-34 composite, J. Catal. 391 (2020) 459–470. https://doi.org/10.1016/j.jcat.2020.09.010.

[197] F. Meng, X. Liang, L. Wang, G. Yang, X. Huang, Z. Li, Rational Design of SAPO-34 Zeolite in Bifunctional Catalysts for Syngas Conversion into Light Olefins, Ind. Eng. Chem. Res. 61 (2022) 11397–11406.

[198] N. Li, F. Jiao, X. Pan, Y. Ding, J. Feng, X. Bao, Size Effects of ZnO Nanoparticles in Bifunctional Catalysts for Selective Syngas Conversion, ACS Catal. 9 (2019) 960–966. https://doi.org/10.1021/acscatal.8b04105.

[199] A.T. Aguayo, J. Bilbao, A. Ateka, A. Portillo, O. Parra, J. Ere, Effect of water and methanol concentration in the feed on the deactivation of In2O3 -ZrO2/SAPO-34 catalyst in the conversion of CO2/CO to olefins by hydrogenation, Fuel. 346 (2023) 128298–128307.

[200] L. Ren, J. Zhang, B. Wang, H. Xu, J. Jiang, Y. Guan, P. Wu, Syngas to light olefins over ZnAlOx and high-silica CHA prepared by boron-assisted hydrothermal synthesis, Fuel. 307 (2022) 121916–121926.

[201] Z. Liu, Y. Ni, T. Sun, W. Zhu, Z. Liu, Conversion of CO2 and H2 into propane over InZrOx and SSZ-13 composite catalyst, J. Energy Chem. 54 (2021) 111–117. https://doi.org/10.1016/j.jechem.2020.04.069.

[202] Y. Huang, H. Ma, Z. Xu, W. Qian, H. Zhang, W. Ying, Direct Conversion of Syngas to Light Olefins over a ZnCrOx+ H-SSZ-13 Bifunctional Catalyst, ACS Omega. 6 (2021) 10953–10962. https://doi.org/10.1021/acsomega.1c00751.

[203] J. Mou, X. Fan, F. Liu, X. Wang, T. Zhao, P. Chen, Z. Li, C. Yang, J. Gao, CO2 hydrogenation to lower olefins over Mn2O3-ZnO / SAPO-34 tandem catalysts, Chem. Eng. J. 421 (2021) 129978–129987.

[204] Z. Lui, Y. Ni, Z. Hu, Y. Fu, X. Fang, Q. Jiang, Z. Chen, W. Zhu, Z. Liu, Insights into effects of ZrO2 crystal phase on syngas-to-olefin conversion over ZnO/ZrO2 and SAPO-34 composite catalysts, Chinese J. Catal. 43 (2022) 877–884.

[205] J.F. Dewilde, C.R. Ho, J. Conner, A. Smith, A. V. Kirilin, A. Malek, P.M. Witt, Kinetics of Direct Olefin Synthesis from Syngas over Mixed Beds of Zn-Zr Oxides and SAPO-34, Ind. Eng. Chem. Res. 60 (2021) 14166–14175. https://doi.org/10.1021/acs.iecr.1c03246.

[206] P. Gao, S. Li, X. Bu, S. Dang, Z. Liu, H. Wang, L. Zhong, M. Qiu, C. Yang, J. Cai, W. Wei, Y. Sun, Direct conversion of CO2 into liquid fuels with high selectivity over a bifunctional catalyst, Nat. Chem. 9 (2017) 1019–1024. https://doi.org/10.1038/nchem.2794.

[207] P. Ticali, D. Salusso, R. Ahmad, C. Ahoba-Sam, A. Ramirez, G. Shterk, K.A. Lomachenko, E. Borfecchia, S. Morandi, L. Cavallo, J. Gascon, S. Bordiga, U. Olsbye, CO2 hydrogenation to methanol and hydrocarbons over bifunctional Zn-doped ZrO2 /zeolite catalysts, Catal. Sci. Technol. 11 (2021) 1249–1268. https://doi.org/10.1039/d0cy01550d.

[208] F. Jiao, B. Bai, G. Li, X. Pan, Y. Ye, S. Qu, C. Xu, J. Xiao, Z. Jia, W. Liu, T. Peng, Y. Ding, C. Liu, J. Li, X. Bao, Disentangling the activity-selectivity trade-off in catalytic conversion of syngas to light olefins, Science (80-.). 380 (2023) 727–730. https://doi.org/10.1126/science.adg2491.

[209] European Committe for Standardization, European standard EN 228, EN228 (2008).

[210] M.A. Quddus, S. Ahmed, S.N. Sarwar, Role of gasoline specifications in the control of environmental pollution, Pet. Sci. Technol. 25 (2007) 829–840. https://doi.org/10.1080/10916460500411705.

[211] J. Yang, X. Pan, F. Jiao, J. Li, X. Bao, Direct conversion of syngas to aromatics, Chem. Commun. 53 (2017) 11146–11149. https://doi.org/10.1039/c7cc04768a.

[212] X. Zhang, A. Zhang, X. Jiang, J. Zhu, J. Liu, J. Li, G. Zhang, C. Song, X. Guo, Utilization of CO2 for aromatics production over ZnO/ZrO2-ZSM-5 tandem catalyst, J. CO2 Util. 29 (2019) 140–145. https://doi.org/10.1016/j.jcou.2018.12.002.

[213] C. Zhou, J. Shi, W. Zhou, K. Cheng, Q. Zhang, J. Kang, Y. Wang, Highly Active ZnO-ZrO2 Aerogels Integrated with H-ZSM-5 for Aromatics Synthesis from Carbon Dioxide, ACS Catal. 10 (2020) 302–310. https://doi.org/10.1021/acscatal.9b04309.

[214] J. Zhang, M. Zhang, S. Chen, X. Wang, Z. Zhou, Y. Wu, T. Zhang, G. Yang, Y. Han, Y. Tan, Hydrogenation of CO2 into aromatics over a ZnCrOx-zeolite composite catalyst, Chem. Commun. 55 (2019) 973–976.

[215] W. Gao, L. Guo, Y. Cui, G. Yang, Y. He, C. Zeng, Selective Conversion of CO2 into para-Xylene over a ZnCr2O4-ZSM-5 Catalyst, ChemSusChem. 13 (2020) 6541–6545.

[216] Y. Wang, L. Tan, M. Tan, P. Zhang, Y. Fang, Y. Yoneyama, G. Yang, N. Tsubaki, Rationally Designing Bifunctional Catalysts as an Efficient Strategy to Boost CO2 Hydrogenation Producing Value-Added Aromatics, ACS Catal. 9 (2019) 895–901. https://doi.org/10.1021/acscatal.8b01344.

[217] Y. Wang, W. Gao, S. Kazumi, H. Li, G. Yang, N. Tsubaki, Direct and Oriented Conversion of CO2 into Value-Added Aromatics, Chem. Eur.J. 25 (2019) 5149–5153. https://doi.org/10.1002/chem.201806165.

[218] Q. Song, Y. Men, J. Wang, S. Liu, S. Chai, W. An, K. Wang, Y. Li, Y. Tang, Methanol steam reforming for hydrogen production over ternary composite ZnyCe1Zr9Ox catalysts, Int. J. Hydrogen Energy. 45 (2020) 9592–9602. https://doi.org/10.1016/j.ijhydene.2020.01.175.

[219] D.B. Rasmussen, J.M. Christensen, B. Temel, F. Studt, P.G. Moses, J. Rossmeisl, A. Riisager, A.D. Jensen, Ketene as a Reaction Intermediate in the Carbonylation of Dimethyl Ether to Methyl Acetate over Mordenite, Angew. Chemie - Int. Ed. 54 (2015) 7261–7264. https://doi.org/10.1002/anie.201410974.

[220] Z. Chen, Y. Ni, Y. Zhi, F. Wen, Z. Zhou, Y. Wei, W. Zhu, Z. Liu, Coupling of Methanol and Carbon Monoxide over H-ZSM-5 to Form Aromatics, Angew. Chemie - Int. Ed. 57 (2018) 12549–12553. https://doi.org/10.1002/anie.201807814.

[221] K. Miyake, Y. Hirota, K. Ono, Y. Uchida, N. Nishiyama, Selective Production of Benzene, Toluene and p-Xylene (BTpX) from Various C1-3 Feedstocks over ZSM-5/Silicalite-1 Core-Shell Zeolite Catalyst, ChemistrySelect. 1 (2016) 967–969. https://doi.org/10.1002/slct.201600172.

[222] J. Li, Y. Wang, W. Jia, Z. Xi, H. Chen, Z. Zhu, Effect of external surface of HZSM-5 zeolite on product distribution in the conversion of methanol to hydrocarbons, 23 (2014) 771–780. https://doi.org/10.1016/S2095-4956(14)60211-4.

[223] D.L. Green, J.S. Lin, Y.F. Lam, M.Z.C. Hu, D.W. Schaefer, M.T. Harris, Size, volume fraction, and nucleation of Stober silica nanoparticles, J. Colloid Interface Sci. 266 (2003) 346–358. https://doi.org/10.1016/S0021-9797(03)00610-6.

[224] K. Miyake, Y. Hirota, K. Ono, Y. Uchida, S. Tanaka, N. Nishiyama, Direct and selective conversion of methanol to para-xylene over Zn ion doped ZSM-5/silicalite-1 core-shell zeolite catalyst, J. Catal. 342 (2016) 63–66. https://doi.org/10.1016/j.jcat.2016.07.008.

[225] J. Zhang, W. Qian, C. Kong, F. Wei, Increasing para-Xylene Selectivity in Making Aromatics from Methanol with a Surface-Modified Zn/P/ZSM-5 Catalyst, ACS Catal. 5 (2015) 2982–2988. https://doi.org/10.1021/acscatal.5b00192.

[226] Y. Bi, Y. Wang, Y. Wei, Y. He, Z. Yu, Z. Liu, L. Xu, Improved selectivity toward light olefins in the reaction of toluene with methanol over the modified HZSM-5 catalyst, ChemCatChem. 6 (2014) 713–718. https://doi.org/10.1002/cctc.201301072.

[227] L. Tan, P. Zhang, Y. Cui, Y. Suzuki, H. Li, L. Guo, G. Yang, N. Tsubaki, Direct CO2 hydrogenation to light olefins by suppressing CO by-product formation, Fuel Process. Technol. 196 (2019). https://doi.org/10.1016/j.fuproc.2019.106174.

[228] J. Wang, A. Zhang, X. Jiang, C. Song, X. Guo, Highly selective conversion of CO2 to lower hydrocarbons (C2-C4) over bifunctional catalysts composed of In2O3-ZrO2 and zeolite, J. CO2 Util. 27 (2018) 81–88. https://doi.org/10.1016/j.jcou.2018.07.006.

[229] S.S. Arora, D.L.S. Nieskens, A. Malek, A. Bhan, Lifetime improvement in methanol-to-olefins Catalysis Over Chabazite Materials By High-Pressure H2 Co-feeds, Nat. Catal. 1 (2018). http://dx.doi.org/10.1038/s41929-018-0125-2.

[230] D.L.S. Nieskens, A. Ciftci, P.E. Groenendijk, M.F. Wielemaker, A. Malek, Production of Light Hydrocarbons from Syngas Using a Hybrid Catalyst, Ind. Eng. Chem. Res. 56 (2017) 2722–2732. https://doi.org/10.1021/acs.iecr.6b04643.

[231] P. Castaño, J.M. Arandes, M. Olazar, J. Bilbao, B. Pawelec, U. Sedrán, Effect of hydrogen on the cracking mechanisms of cycloalkanes over zeolites, Catal. Today. 150 (2010) 363–367. https://doi.org/10.1016/j.cattod.2009.09.013.

[232] X. Zhao, J. Li, P. Tian, L. Wang, X. Li, S. Lin, X. Guo, Z. Liu, Achieving a Superlong Lifetime in the Zeolite-Catalyzed MTO Reaction under High Pressure: Synergistic Effect of Hydrogen and Water, ACS Catal. 9 (2019) 3017–3025. https://doi.org/10.1021/acscatal.8b04402.

[233] J. Xie, D.S. Firth, T. Cordero-lanzac, A. Airi, C. Negri, S. Øien-ødegaard, K.P. Lillerud, S. Bordiga, U. Olsbye, MAPO-18 Catalysts for the Methanol to Olefins Process: Influence of Catalyst Acidity in a High-Pressure Syngas (CO and H2) Environment, ACS Catal. 12 (2022) 1520–1531.

[234] Y. Wang, G. Wang, L.I. van der Wal, K. Cheng, Q. Zhang, K.P. de Jong, Y. Wang, Visualizing Element Migration over Bifunctional Metal-Zeolite Catalysts and its Impact on Catalysis, Angew. Chemie - Int. Ed. 60 (2021) 17735–17743. https://doi.org/10.1002/anie.202107264.

[235] Y. Ding, F. Jiao, X. Pan, Y. Ji, M. Li, R. Si, Y. Pan, G. Hou, X. Bao, Effects of Proximity-Dependent Metal Migration on Bifunctional Composites Catalyzed Syngas to Olefins, Am. Chem. Soc. 11 (2021) 9729–9737.

3 Surface ZnO_x on Zirconia is Highly Active for High Temperature Methanol Synthesis

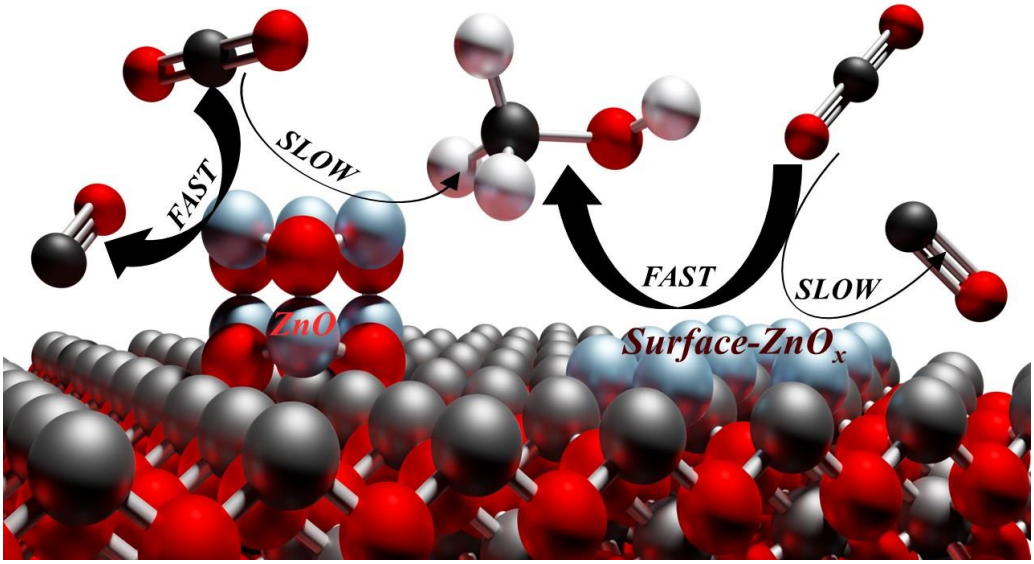
On the next page, the manuscript with the title: *Surface ZnO_x on Zirconia is Highly Active for High Temperature Methanol Synthesis* are reprinted.

This manuscript has been submitted to *Journal of Catalysis*.

The scientist highlights:

- Mixed oxides of ZnO and ZrO_2 prepared by impregnation or co-precipitation can selectively synthesize methanol at high temperature.
- XRD, XPS, XAS, and TEM identified that ZnO supported on the ZrO_2 surface is the main active site for methanol synthesis.
- In-situ DRIFT analysis showed that formation of methanol proceed through the formate path-way where Zn-HCO_2 were crucial for the methanol synthesis activity.
- XAS-MES analysis found that the surface ZnO underwent reversible reduction in syngas, creating local oxygen vacancies.

The graphical abstract:



Surface ZnO_x on Zirconia is Highly Active for High Temperature Methanol Synthesis

M. T. Nikolajsen[1], J.-C. Grivel[2], A. Gaur[3], L. P. Hansen[4], L. Baumgarten[3], N. C. Schjødt[4], U. V. Mentzel[4], J.-D. Grunwaldt[3], J. Sehested[4], J. M. Christensen[1] and M. Høj[1*]

[1] Department of Chemical Engineering, Technical University of Denmark (DTU), Kgs. Lyngby, 2800 (Denmark).

[2]Department of Energy Conversion and Storage, Technical University of Denmark (DTU), Kgs. Lyngby, 2800 (Denmark).

[3] Institute for Chemical Technology and Polymer Chemistry, Karlsruhe Institute of Technology, Karlsruhe, 76131, (Germany)

[4] Topsoe A/S, Kgs. Lyngby, 2800 (Denmark).

[*]Corresponding author: mh@kt.dtu.dk

Abstract

Zinc containing mixed metal oxides and supported zinc oxide are stable and selective methanol synthesis catalysts at temperatures where a subsequent methanol to hydrocarbons reaction can occur directly. This work provides fundamental insights into ZnO-based high temperature methanol synthesis catalysts. A pronounced support effect was observed, where ZrO_2 provided a beneficial effect while SiO_2 exerted a detrimental effect compared to bulk ZnO. Preparing co-precipitated ZnO-ZrO_2 catalysts showed that the initial activity correlated with the amount of amorphous ZnO on the surface of the support and that the catalytic activity increased with time on stream as zinc oxide migrated out of a solid solution with ZrO_2 and onto the support surface. Hence the active phase appeared to be ZnO surface species and not zinc oxide in a solid solution with ZrO_2. Operando XAS coupled with modulation excitation spectroscopy unravelled that the surface ZnO was partly reduced under operating conditions, as surface ZnO_x, with x approximately equal to 0.98. In-situ DRIFTS further uncovered that the surface ZnO_x activated CO_2 and formed methanol via carbonate, formate and methoxide species. XPS finally showed that ZrO_2 withdrew electrons from ZnO, facilitating oxygen abstraction to form the partly reduced ZnO_x, which in turn facilitated the activation of CO_2.

Keywords: carbon dioxide, methanol, zinc, zirconia

1 Introduction

Polymeric materials play an important role in society's permanently evolving needs and challenges because they are versatile, durable, and adaptable. From 1950 to 2019, the global production of polymeric materials increased from 2 Mt to 460 Mt, and the worldwide consumption is forecasted

to be 590 Mt in 2030 [1,2]. In 2019 polyethylene, polypropylene, polystyrene, and polyethylene terephthalate accounted for 229 Mt [3]. These products are directly related to the monomers ethylene, propylene, ethenyl benzene, and para-xylene. Since these chemicals are mainly produced from crude oil, the demand for an alternative feedstock is increasing as a part of an effort to reduce global CO_2 emissions[4].

CO_2 generated from biomass or captured from the atmosphere or at a point source can be utilized to produce these monomers or monomer precursors mentioned above. A route for utilizing CO_2 is the combination of methanol synthesis and methanol dehydration to hydrocarbons. The methanol synthesis is equilibrium limited, but a strategy to overcome this, is to combine a methanol synthesis catalyst with a zeolite methanol dehydration catalyst within one reactor [5,6]. The purpose of the zeolite is to ensure immediate conversion of the formed methanol and thereby shift the equilibrium towards the products. At the temperatures necessary for the zeolite to be active (300 to 420 °C), the traditional $Cu/ZnO/Al_2O_3$ methanol synthesis catalyst cannot be used because severe sintering of the metallic copper deactivates the catalyst [7]. Furthermore, the metallic copper causes hydrogenation of the olefins formed in the zeolite and thus disrupts the formation of unsaturated hydrocarbons [8]. For these reasons, there is currently a significant interest in finding metal oxides with high stability, high methanol synthesis activity and limited olefin hydrogenation activity.

A range of metal oxide catalysts, primarily based on ZnO, have shown high methanol synthesis activity at temperatures above 300 ºC [5,6,9–12]. Particularly catalysts combining ZnO and ZrO_2 have shown an improved performance. The solid solution of $ZnO\text{-}ZrO_2$ synthesized by Wang et al. [9] demonstrated high methanol selectivity of 86-91 %, achieved with a CO_2 single-pass conversion of more than 10 % (at 50 bar, H_2/CO_2 of 3 to 4, and at 315 to 320 ºC). The $ZnO\text{-}ZrO_2$ solid solution kept its activity for 500 hours on stream and was resistant to sintering at higher temperatures. Wang et al. [9] suggested that the high methanol selectivity is attributed to the synergetic effect of H_2 activation on zinc sites and simultaneous activation of CO_2 on the neighbouring zirconia site within a solid solution of the two components.

There has been clear evidence that the $ZnO\text{-}ZrO_2$ combination may form a solid solution. Co-precipitating zinc oxide and zirconia produces a material where zinc is stabilizing the tetragonal phase of zirconia. Zirconia exhibits a monoclinic crystal structure at temperatures below 1170 °C,

but the introduction of dopants is known to stabilize the meta-stable tetragonal structure [13]. Several studies have observed a systematic shift in the (101) Bragg reflection to higher 2θº with increasing zinc loading until zirconia-zinc saturation ~33 mol% Zn [9]. Beyond this saturation, hexagonal zinc oxide starts to form and become visible in XRD [9,14–16]. The systematic shift in the (101) Bragg reflection is caused by the substitution of Zr^{4+} (84 Å) with Zn^{2+} (74 Å), which shrinks the tetragonal lattice. Similar trends have been observed with the dopants iron- and yttrium oxide with an ionic radius of 70 Å and 90 Å, shifting the (101) Bragg reflection to higher and lower 2θº, respectively [17,18]. On ZnO-ZrO_2 catalysts, FTIR bands around 500 and 600-700 cm^{-1} were associated with Zn-O-Zn and Zn-O-Zr vibrations [19] and UV-vis spectra of ZrO_2 changed with Zn as dopant indicated the presence of isolated Zn^{2+} ions [20]. These findings have led to the belief that it is surface available Zn^{2+} embedded in the zirconia crystal lattice, as part of a solid solution, which in synergy with Zr^{4+} is the active site for CO_2 hydrogenation.

By contrast, low Zn-Zn or Zn-Zr coordination numbers found by X-ray absorption spectroscopy [21] and enrichment of Zn on the zirconia surface detected by X-ray photoelectron spectroscopy [9,15] suggest that ZnO is mostly present at the zirconia surface. Even at low Zn content (Zn/Zr = 1/100), individual lattice fringes of isolated ZnO were detected by high-resolution transmission electron microscopy, indicating difficulties for Zn^{2+} to be present inside the ZrO_2 lattice and a preference for generation of a separate ZnO phase [22]. The ZnO-ZrO_2 mixed oxides thus have surface ZnO, which exists apart from the solid solution. Currently there is no clear knowledge about whether the surface ZnO or the Zn^{2+} within a solid solution is the primary active species.

This study aims to bridge this gap by identifying the active species in ZnO-based methanol synthesis catalysts with particular emphasis on ZnO-ZrO_2 mixed oxides. The purpose is to identify good candidates for the bifunctional catalytic system and clarifying the metal oxide structure-activity relation, particularly the relative importance of Zn-Zr solid solution and ZnO surface domains. ZnO was deposited on silica (SiO_2), anatase titania (TiO_2), monoclinic zirconia (m-ZrO_2), and tetragonal zirconia (t-ZrO_2) by the incipient wetness impregnation method and ZnO-ZrO_2 was prepared by co-precipitation. The catalysts were characterized by X-ray diffraction (XRD), inductively coupled plasma optical emission spectroscopy (ICP-OES), X-ray absorption spectroscopy (XAS), X-ray photoelectron spectroscopy (XPS), high-resolution scanning transmission electron microscopy (HR-STEM) and N_2 adsorption/desorption (BET). Furthermore, the reaction species

involved in the CO_2 hydrogenation reaction on the surface of the catalyst were analysed by in-situ diffuse reflectance infrared Fourier transform spectroscopy (DRIFTS). The changes in the oxidation state of the supported ZnO was investigated by time resolved QEXAFS coupled with modulation excitation spectroscopy (MES).

2 Materials and Method

2.1 Catalyst Preparation

A series of ZnO-containing catalysts were prepared by the incipient wetness impregnation method. Firstly, the supports were dried overnight at 120 ºC and the precise water uptake was determined of the dried supports. The supports were then impregnated with a solution of $Zn(NO_3)_2{\cdot}6H_2O$ to produce catalysts with 13 mol% Zn (Zn/(M+Zn), where M is Si, Ti or Zr). Finally, the catalysts were dried overnight at 100 ºC and calcined in air at 500 ºC for five hours. The supports used were SiO_2 255 m^2/g, TiO_2 161 m^2/g, m-ZrO_2 57.2 m^2/g, t-ZrO_2 145 m^2/g (stabilized by Al_2O_3) and t-ZrO_2-CeO_2 105 m^2/g, all provided by Saint-Gobain NorPro. Furthermore, the ZnO content on t-ZrO_2 was varied from 13 to 44 mol%, all produced with the above-mentioned procedure. All impregnated samples are denoted with a forward slash as ZnO/support. All ZrO_2 supported catalysts showed HfO_2 impurity, typically 1-2 mol% Hf.

For comparison, a ZnO-ZrO_2 catalyst was prepared by the co-precipitation method proposed by Wang et al. [9], the hyphen is used here to denote co-precipitation. A 500 mL solution of 5.52 g $Zn(NO_3)_2{\cdot}6H_2O$ and 37.6 g $ZrO(NO_3)_2{\cdot}xH_2O$ was added to a beaker and heated to 70 ºC. A 500 mL solution of 15.3 g $(NH_4)_2CO_3$ was added dropwise to the warm precursor solution under vigorous stirring. The mixture was then aged for 120 min at 70 ºC, filtered and washed with demineralized water. The collected solid was dried at 100 ºC overnight and calcined in air at 500 ºC for five hours. Co-precipitation of a similar catalyst was repeated at a precipitation and ageing temperature of 100 ºC under reflux and this sample was denoted ZnO-ZrO_2-100.

Pure ZnO was prepared by precipitating $Zn(NO_3)_2{\cdot}6H_2O$ with a Na_2CO_3 solution at pH = 7 and 70 ºC. The precipitated ZnO was aged for 60 min at 70 ºC and pH = 7, then filtered and washed with demineralized water. The solid was collected and dried overnight at 80 ºC and calcined in air at 350 ºC for three hours.

2.2 Catalytic Activity Evaluation

The methanol synthesis activity tests were conducted in a high-pressure flow reactor setup using a quartz-lined reactor tube with an inner diameter of 4 mm. Typically, 300 mg of the catalyst with a grain size of 150-300 µm was loaded into the reactor tube. Synthesis gas $CO_2/H_2/Ar$ with the composition of 20/60/20 Vol% at 50 barg was introduced into the reactor at various temperatures in the range 280-400 ºC. The reaction temperature was controlled by a N-type thermocouple placed right above the catalyst bed inside the reactor tube and an electric furnace with three heating zones. It should be noted that no pre-treatment was given to the catalysts before the catalytic testing. The internal standard, argon, was used for accounting for the decrease in reaction volume. The carbon balance closed at an average of 99.95 % ± 0.99 % for all the experiments. The effluent gas was analysed by an online GC (ThermoFisher Trace 1300, assembled by Global Analyzer Solutions) equipped with a thermal conductivity detector (TCD) and a flame ionization detector (FID). The GC column connected to the flame ionization detector was Rtx-5 (60m, 0.32 mmID and 5µm df), which separated the formed products (methane, methanol, and dimethyl ether). A combination of Hayesep N, XL Sulfur and Molsieve 5A columns were connected to the TCD detector for quantification of CO, CO_2, and Ar. The CO_2 conversion, oxygenate (CH_3OH + CH_3OCH_3) selectivity, and oxygenate formation rate was calculated by Eq. (1) to (4).

$$\dot{F}_{i,out} = \dot{V}_{in} \cdot \frac{y_{Ar,in}}{y_{Ar,out}} \cdot y_{i,out} \cdot V_m^{-1} \tag{1}$$

$$X_{CO_2} = 1 - \frac{\dot{F}_{CO_2,out}}{\dot{F}_{CO_2,in}} \tag{2}$$

$$S_{CH4O+C_2H_6O} = \frac{\dot{F}_{CH_4O,out} + 2 \cdot \dot{F}_{C_2H_6O,out}}{\dot{F}_{CO_2,in} - \dot{F}_{CO_2,out}} \cdot 100\% \tag{3}$$

$$Rate = \frac{\left(\dot{F}_{CH_4O,out} + 2 \cdot \dot{F}_{C_2H_6O,out}\right) \cdot M_{w,CH_4O}}{m_c} \tag{4}$$

Where $\dot{V}$ is the volumetric flow rate at standard conditions, V_m is the molar volume, m_c is the weight of the catalyst, and M_w is the molar mass. $\dot{F}_i$ and y_i is the molar flow rate and molar fraction

of component i. Both methanol and dimethyl ether can be further dehydrogenated in zeolites to form hydrocarbons. Therefore, the production of both is relevant to consider when showing the activity of the catalysts.

2.3 Catalyst Characterization

XRD analysis was conducted with a PanAlytical X′Pert Pro instrument in Bragg-Brentano geometry in reflectance mode using a Cu K_α radiation source (λ = 1.541 Å) at ambient conditions. The scan range was 5–70° with a step size of 0.017°. The Rietveld analysis was performed using the Topas software. To analyse the elemental composition, ICP-OES analysis was conducted on an Agilent 700 Series instrument using argon as plasmogene. The specific surface area was analysed with the 3P instrument Sync440 and the N_2 adsorption isotherm was analysed by the Brunauer-Emmett-Teller method.

The XPS measurements were performed in an ultra-high vacuum with an ESCALAB Xi^+ instrument from ThermoFisher Scientific, employing a monochromatic Al K_α (1486.6 eV) X-ray source. The powdered samples were pressed onto a piece of adhesive copper tape (3M Electrical Tape). The diameter of the analysis area was approximately 650 μm. A low energy electron flood gun was used for the neutralization of surface charge buildup. The binding energies were calibrated by using Au foil ($4f_{7/2}$ binding energy of 83.95 eV). Etching was conducted in Ar cluster mode with an energy of 2000 eV during steps of 30 s and raster size of 3.25 x 3.25 mm^2. The data were analyzed with the Thermo Avantage software.

X-ray absorption spectroscopy (XAS) measurements at the Zn K absorption edge were done in transmission and fluorescence mode at the SuperXAS beamline10A, Swiss Light Source (SLS) synchrotron. QEXAFS spectra were recorded with a frequency of 1 Hz of the monochromator. Data importing and pre-processing involving energy calibration, rebinning, averaging and exporting was done using the ProQEXAFS software developed at the beamline [23]. Basic XAS data treatment of normalization, background subtraction and Fourier transformation has been conducted using Athena [24]. For the ex-situ measurements, pellets were prepared using cellulose diluted catalyst samples pressed as 13 mm diameter, self-sustaining wafers and the energy scanned in transmission mode. By taking average of 400 spectra, the k^3-weighted Fourier transformed EXAFS function (k range 3 to 12 $Å^{-1}$) was fitted in R – space (1 to 3 Å). The wurtzite ZnO structure

model (ICSD 67849) was used for fitting the amplitude reduction factor, $S_0^2 = 0.982$, to the obtained reference spectrum of the ZnO sample. This value of amplitude reduction factor was used in the refining of coordination number (CN), interatomic distances (R), energy shift (ΔE_0), and mean square deviation of interatomic distances (σ^2) for the first and second shell of ZnO on the catalyst samples. These fits were performed using Artemis by a least-square method in the R space between 1 and 3.7 Å [24]. The surface zinc oxide did not show a Zn-Zn interaction (CN = 0), meaning that the fraction of the surface sites can be estimated from the coordination number of the second shell as proposed by Han et al. [21] in Eq. (5).

$$\chi(\mathrm{ZnO_x}), [\%] = \left(1 - \frac{CN_{Zn-Zn}}{12}\right) \cdot 100\% \quad (5)$$

The coordination number of Zn-Zn in bulk ZnO is 12 and as XAS is a bulk method, the fitted coordination number is an average. The fitting results and the estimated fraction of surface ZnO_x for the catalyst samples can be found in Table S2. Linear combination fitting was conducted using the (0.13)ZnO/t-ZrO_2 (no ZnO was visible from XRD and no Zn-Zn back scattering in FT-EXAFS was observed) and ZnO as references for surface ZnO_x sites and crystalline ZnO respectively and compared to the results obtained by Eq. (5). The weight percentage of surface ZnO_x sites on the zirconia supports was used for calculating the amount of ZnO_x present on the zirconia surface by Eq. (6), as XPS and XRD results suggest no to hardly any incorporation of Zn into the zirconia lattice.

$$\mathrm{n_{ZnO_x}}, [\mu mol/g_{cat}\,] = \frac{b_{Zn} \cdot I_{Zn}}{Mw_{Zn}} \cdot 10^6 \quad (6)$$

Where $\mathrm{n_{ZnO_x}}$, b_{Zn}, I_{Zn}, and Mw_{Zn} are the concentration of surface ZnO_x pr. gram of catalyst, the bulk concentration of Zn determined by ICP-OES, the weight percentage of surface Zn determined by linear combination fitting and the molar mass of Zn, respectively.

For the in-situ experiments, quartz capillaries (length of 80 mm, o.d. 0.8 mm with 0.01 mm wall thickness) were loaded with 4.4 mg 100-200µm catalyst particles diluted 1:4 in inert α-Al_2O_3 giving a bed length of 7 mm. To ensure a pressure tolerance of 20 bar, the loaded capillaries were glued using Araldite Rapid Epoxy to a sample holder and cured for several hours. Hereafter, the sample holder was connected to the flow setup, where a downstream mass spectrometer and 10%

CO/He, CO_2, 10% O_2/He and He gasses were connected. The capillaries were heated by radiative heaters provided by the beamline. The experimental procedure included dehydration of the catalysts in O_2/He with a heating ramp of 10 °C /min to 400 °C at 15 bar, followed by cooling to room temperature. Then the gas was switched to a syngas mixture ($CO/CO_2/H_2$/He = 5/12/37/46, filtered through an active carbon filter to remove nickel carbonyls) and when a stable MS signal was achieved, the reactor was heated to 400 °C at 10 °C /min and kept at 400 °C for 2 hours. Thirdly, the modulation excitation spectroscopy (MES) coupled XAS experiments were performed where the gas was switched between O_2/He and syngas in intervals of 10 min at 400 °C and 15 bar. One cycle refers to the total time of O_2/He and syngas exposure (10 min in O_2/He and 10 min in syngas) and the switching was repeated for a total of 9 cycles. For the MES experiment, a four-way valve was used to switch the flow to the capillary between the two gas mixtures, allowing the flow of one gas mixture to the reactor and the other to a purge line. To avoid pressure fluctuations, the pressure of the purge line was adjusted by a backpressure valve to 15 bar, keeping the reactor and the purge line pressure almost equal. Time resolved spectra were continuously recorded in transmission as well as fluorescence mode in the middle of the catalytic bed through all the above-mentioned steps. For the MES analysis, florescence spectra were used due to high spectral quality. The oscillation frequency of the monochromator was fixed at 1 Hz, leading to a spectrum acquisition every 500 ms. Thus, the 20 min cycle (1 period) produced around 2400 spectra, meaning a total of 21600 spectra for 9 periods, were generated during each MES experiment. For the MES data analysis, normalized spectra were first averaged in 20s intervals to obtain 60 time-resolved spectra for each cycle. This averaging enhanced the signal-to-noise ratio for detection of small changes during the switching [25]. The time-resolved spectra were transformed into phase-resolved spectra $\mu(E, \Delta\phi)$ using Eq. (7) [26–28]. This creates a phase-resolved set of spectra at different phase shifts $0° \leq \Delta\phi < 360°$ based on the sine function of cycle time, T = 1200 s. Changes occurring at identical phase shifts during each cycle were added making small changes detectable. The changes observed from the phase-resolved spectra were analyzed qualitatively and quantitatively by comparing them to the spectra of ZnO and (0.13)ZnO/t-ZrO_2 subtracted by Zn foil.

$$\mu(E, \Delta\phi) = \frac{2}{T}\int_0^T \mu(E, t) \cdot \sin\left(\frac{360°}{T}t + \Delta\phi\right) dt \qquad (7)$$

Transmission electron microscopy imaging of the catalysts were performed on a Thermo Fisher Spectra 200 X-CFEG (S)TEM microscope equipped with Dual-X EDS detectors. The catalyst samples were crushed in a mortar and dispersed in absolute ethanol (99.9%) before drop casting on a Cu-TEM grid covered with lacey carbon film (SPI supplies). Images and energy dispersive X-ray (EDX) spectroscopy maps were acquired in scanning transmission mode (STEM) with a probe current of 0.2 nA and a probe convergence angle of 30 mrad. Detector collection angles of 0-22 mrad and 56-200 mrad were applied for the bright-field (BF) and high-angular annular dark field (HAADF) detector, respectively. The EDX maps were acquired continuously scanning for >10 minutes to obtain decent signals and were post-processed in Velox 3.8 to generate element composite images with pixel-averaged smoothing.

The reaction mechanism of CO_2 hydrogenation over (0.13)ZnO/t-ZrO_2 was probed by CO_2 adsorption, steady-state methanol synthesis, He and H_2 temperature-programmed-desorption/reaction with the use of in-situ diffuse reflectance infrared Fourier transform spectroscopy (DRIFTS). A Harrick high pressure Praying Mantis cell equipped with a high pressure dome and pure ZnSe windows was placed in a Vertex 70 infrared spectrometer with a liquid nitrogen cooled LN-MCT VP detector. The loaded sample was pretreated under He flow at 400 °C and 20 bar for 2 hours and then cooled to the reaction temperature, where a background spectrum was acquired. For the CO_2 adsorption experiment, the gas was switched to CO_2/He where the development of peaks was continuously monitored for 60 min. Hereafter, the gas was switched to H_2/He and the change and disappearance of surface species were continuously monitored for 60 min. For the steady-state methanol synthesis experiment, after the pretreatment, the gas was switched to CO_2/H_2/He (13/38/49 Vol%) and DRIFTS spectra were recorded for 60 min. After the steady-state methanol synthesis experiment, the reactor was cooled to room temperature and the gas was switched to either pure He or H_2. When a stable MS signal was achieved, the temperature was increased to 420 °C by ~6 °C/min.

3 Results and Discussion

3.1 Support effects in ZnO catalysed CO_2 hydrogenation

Firstly, the catalytic activity as function of temperature from 280 to 400 °C was measured (Fig. S1). These temperatures are above those applied in industrial methanol synthesis, but relevant

temperatures for subsequent methanol dehydration to hydrocarbons over zeolites. The results showed that at temperatures ≥ 360 °C the gas composition reached equilibrium, thus these results cannot be used for comparing the activity of the catalysts. The CO_2 hydrogenation activity results reported in the following were obtained at 320 °C, where both the reverse-water-gas-shift (RWGS) and the methanol synthesis were far from equilibrium (see calculations of approach to equilibrium in Table S1). Results with/without pre-reduction of the catalyst with hydrogen showed that the effect of this pre-treatment was negligible (see Fig. S2). Next, the effect of the feed gas composition was investigated, and it was found that the partial pressures of CO_2 and H_2 were crucial for the methanol synthesis activity over ZnO supported on zirconia. Shifting from a feed of CO/H_2 to CO_2/H_2 increased the activity dramatically (Fig. S3 and Fig. S5). Co-feeding or partially replacing CO_2 with CO did not improve the catalytic activity (Fig. S4), suggesting that the primary carbon source for methanol formation is CO_2, as also seen for Cu/ZnO based catalysts [29]. Increasing the H_2/CO_x ratio also increased the rate of methanol synthesis (Fig. S5).

The oxygenate (methanol + dimethyl ether (DME)) formation rate (Eq. (3)) and selectivity (Eq.(4)) over supported zinc oxide catalysts at 320 °C are shown in Fig. 1. The results reveal a clear support effect in the ZnO catalysed methanol synthesis. Supporting zinc oxide on anatase titania or monoclinic- and tetragonal zirconia significantly increased the oxygenate formation rate compared to bulk zinc oxide. This improvement was partly due to an increase in the CO_2 conversion, but mostly due to the enhanced oxygenate selectivity, which increased from 34 % for ZnO to 68-80 % for supported zinc oxide. The DME selectivity was lower than 0.5% on the zirconia supports, showing that these catalysts were highly selective towards methanol. Silica had a detrimental support effect on the methanol formation rate, which primarily resulted from a drop in the total CO_2 conversion compared to bulk ZnO. This silica support has previously shown a similar negative effect on the turn-over frequency for the methanol synthesis over Cu/SiO_2 compared to pure Cu (i.e. Raney Cu) [29]. Infrared spectroscopy of CO on Cu/SiO_2 showed a blueshift in the C-O frequency, hence the silica exerted an electron withdrawing effect upon Cu [30], which correlated to low activity of Cu/SiO_2. It is hypothesised that similar electronic interactions between SiO_2 and ZnO might cause the loss in activity when zinc oxide is supported on silica.

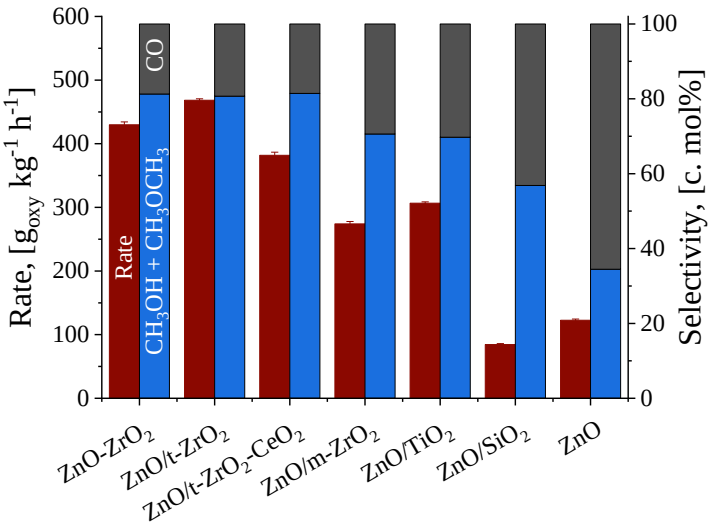


Fig. 1. The oxygenate (CH_3OH+ CH_3OCH_3) formation rate for ZnO supported on different metal oxides (Zn mol% = 13) compared to the co-precipitated ZnO-ZrO_2 and pure ZnO. Conditions: 320 °C, 50 barg, 15 NL/h, catalyst loading of 300 mg, feed gas composition of CO_2/H_2/Ar 20/60/20.

As illustrated in Fig. 1, the mass-based activity and oxygenate selectivity for zinc oxide supported on titania and monoclinic zirconia showed similar results, all exerting a beneficial support effect. It was, therefore, necessary to clarify whether the beneficial supports indirectly affected an active ZnO phase on the surface or created particularly beneficial Zn^{2+} sites that are part of a solid solution with the support.

3.2 The importance of a ZnO surface phase for the catalytic activity

To elucidate the support effects, several samples with zinc oxide impregnated on tetragonal zirconia were prepared to understand the relation between zinc loading, activity and selectivity as illustrated in Fig. 2.

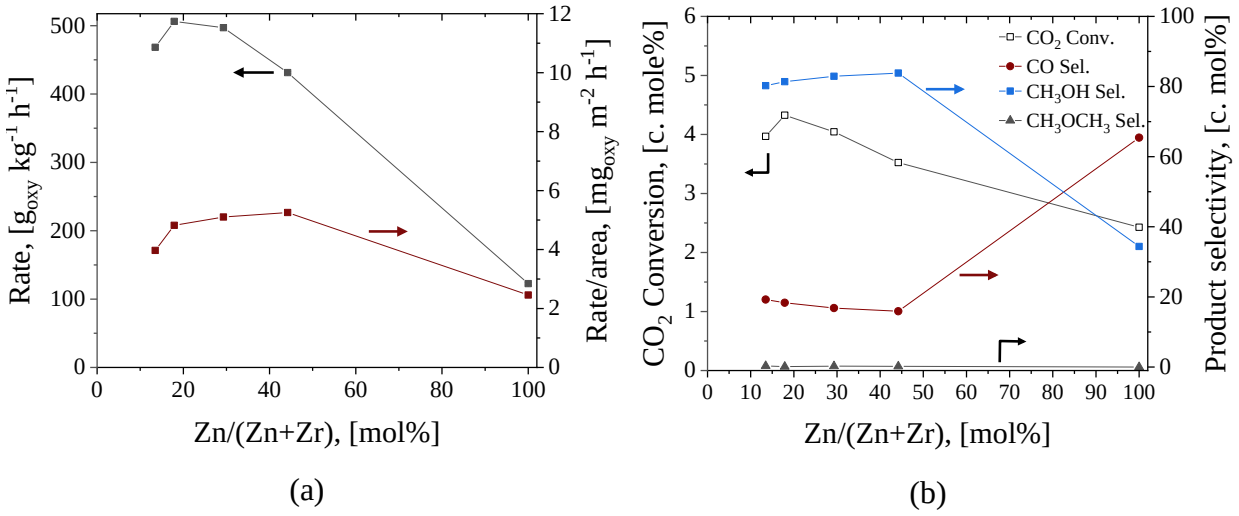


Fig. 2. (a) The oxygenate (CH_3OH+ CH_3OCH_3) formation rate against mol% of Zn for ZnO supported on t-ZrO_2 based on catalyst mass (black) and surface area (red). (b) The CO_2 conversion (left axis), CH_3OH, CH_3OCH_3 and CO selectivity (right axis) against the mol% of Zn supported on tetragonal zirconia. Conditions: 320 °C, 50 barg, 15 NL/h, catalyst loading of 300 mg, feed gas composition of CO_2/H_2/Ar 20/60/20.

In Fig. 2 (a) the oxygenate formation rate was improved when increasing the Zn loading from 13 to 18 mol%, due to enhanced CO_2 conversion. Further increasing the Zn loading reduced the CO_2 conversion while maintaining the high selectivity towards methanol (Fig. 2 (b)). The major changes in catalytic properties with ZnO loading reflected changes in physical properties of the samples. The BET surface area, the amount of crystalline ZnO determined by Rietveld refinement of the XRD data, and the elemental bulk and surface composition from ICP-OES and XPS analysis are summarized in Table 1. The XRD patterns for the impregnated and co-precipitated samples are shown in Fig. 3.

Table 1. Specific surface area (BET), bulk Zn mol%, surface Zn mol%, the weight% of crystalline hexagonal ZnO, and the amount of surface oxygen vacancies relative to the total amount of oxygen. Numbers in parentheses represent analysis of spent samples.

Catalyst name	**BET** [m^2/g]	**Bulk Zn/(M+Zn)**[a] [mol%]	**Crystalline ZnO**[b] [wt%]	**Surface Zn/(Zr+Zn)**[c] [mol%]	**O_v/O_T** [c] [%]
ZnO	49.9	100	100	100	29
(0.13)ZnO/t-ZrO_2	118	13.4	0 (0)	23	42
(0.18)ZnO/t-ZrO_2	105	17.9	0.7 (0.9)	30 (32)	43 (37)
(0.29)ZnO/t-ZrO_2	97.4	29.3	11 (7.9)	32	49
(0.44)ZnO/t-ZrO_2	82.1	44.2	21 (20)	38	39
ZnO/t-ZrO_2-CeO_2	77.3	13.4	2.2 (2.4)	-	-
ZnO/m-ZrO_2	44.8	13.5	5.4 (5.1)	-	-
ZnO/TiO_2	103	13.3	5.3 (6.5)	-	-
ZnO/SiO_2	165	13.0	1 (1.1)	-	-
ZnO-ZrO_2	40.3	10.7	0 (0)	33 (31)	45 (30)
ZnO-ZrO_2-100	145	12.0	0 (0)	22	37
t-ZrO_2	145	0	0	0	43

[a]*determined by ICP-OES,* [b]*determined by Rietveld refinement of XRD data,* [c]*determined by XPS*

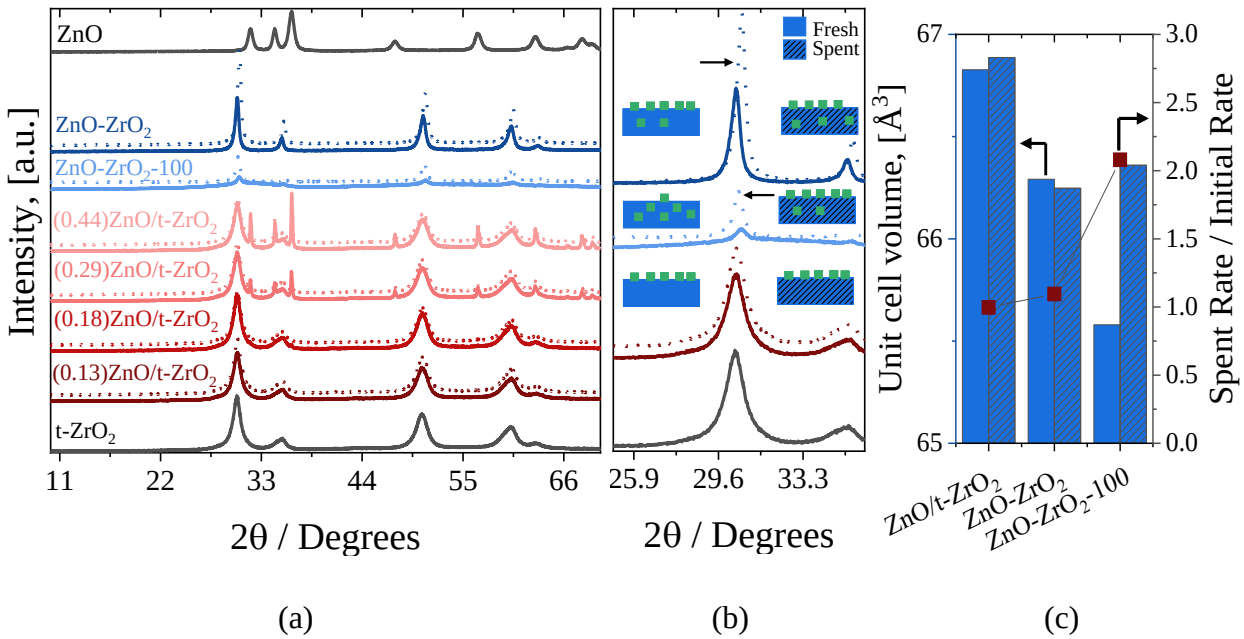


Fig. 3. (a) XRD patterns of ZnO supported on ZrO_2samples, bare t-ZrO_2 support and ZnO. (b) Zoom in on the (101) Bragg reflection of the fresh (solid line) and spent (dotted line) impregnated ZnO/t-ZrO2 (13 mol%), co-precipitated ZnO-ZrO2 at 70 °C and the co-precipitated ZnO-ZrO_2 at 100 °C. The arrow visualizes the (101) Bragg reflection movement from fresh to spent sample. The green boxes represent ZnO placed on the ZrO_2 surface or in the ZrO_2 structure, represented as blue box. (c) The unit cell volumes calculated from the lattice parameters obtained by Rietveld refinement and the spent to fresh reaction rate ratio at 300°C and 50 bar, after exposure for 42 hours to temperatures between 300 to 400 °C at 20 °C intervals.

Fig. 3 (a) shows that with increasing zinc loading by impregnation, the tetragonal (101) Bragg reflection, observed at $2\theta = 30.2°$, did not shift to higher angles, which is typically observed for ZnO in ZrO_2 solid solutions [9]. This shows that the tetragonal zirconia was unaffected and that no Zn was incorporated into the lattice. Furthermore, the high surface zinc fraction determined by XPS compared to the bulk zinc fraction suggests that zinc oxide was mainly deposited on the zirconia surface for the impregnated samples (Table 1). The fact that a comparatively high activity was achieved with the impregnated ZnO/t-ZrO_2 samples (Fig. 1 and Fig. 2) which on the basis of XPS/XRD did not show any sign of Zn incorporated as solid solution with the ZrO_2 support, suggests that the catalytic activity arised from a ZnO-type surface layer.

An increase from 13 to 18 mol% zinc enhanced the activity (Fig. 2 (a)) reflected in an increased CO_2 conversion at similarly high methanol selectivity (Fig. 2 (b)). At 18 mol% zinc, small amounts of crystalline ZnO were visible by XRD and the amount rose as the zinc loading increased (Fig. 3 (a)). Assuming an atom density like the bulk ZnO(0001) facet, ~19 mol% Zn would saturate the surface of the t-ZrO_2 support, with a specific surface area of 145 m^2/g, with a ZnO monolayer. Thus, it was consistent that this level marks the transition from a 2D ZnO surface phase to 3D ZnO nanoparticles. Scanning transmission electron microscopy with EDX of the impregnated sample with 13 mol% Zn (i.e. in the range of a 2D ZnO phase) showed well dispersed ZnO (Fig. S13). Fig. 4 (a) illustrates that the ZnO surface layer was in the form of surface domains with a diameter of ~5 nm. High-resolution transmission electron microscopy in Fig. 4 (b) showed a lattice spacing of 2.98Å, similar to the lattice spacing of the (101) Bragg reflection of tetragonal zirconia (Fig. S14). No evidence of any crystalline structure of ZnO was found, which supports that the ZnO surface layer is an amorphous phase without an ordered 3D structure.

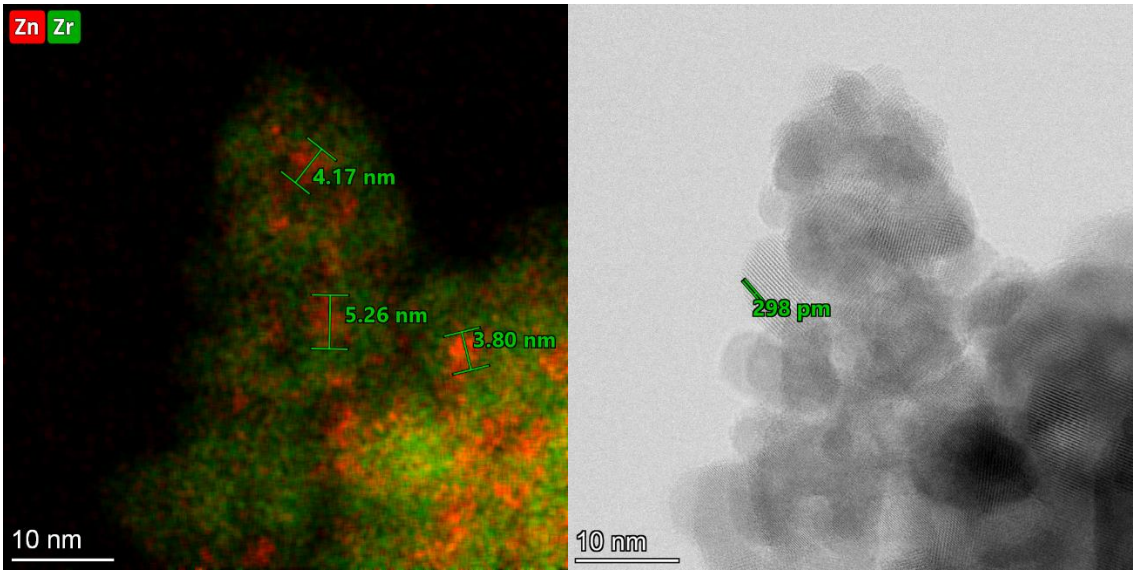


Fig. 4. (a) EDX element map of Zn and Zr of the image area in (b) high-resolution STEM image (bright field) of the (0.13)ZnO/t-ZrO_2 sample. The EDX quantification showed a mole fraction of Zn/(Zn+Zr) = 0.044 in this particular image area.

Fig. 2 (a) shows that the evolution of a 3D ZnO structure above 18 mol% Zn, did not improve the mass-based activity, but the activity per total catalyst surface area increased before dropping for bulk ZnO. The relative surface area occupied by crystalline ZnO nanoparticles increased as the zinc loading increased (Table 1), but the catalytic activity decreased, suggesting that the surface of the crystalline ZnO was less active. This shows that crystalline ZnO was of considerable activity on its own, but also that the ZnO surface layer dispersed on ZrO_2 was higher in activity, by a factor of at least 2 according to Fig. 2 (a). For the impregnated catalysts, XRD analyses of the spent samples showed a higher crystallinity, but no shift in the (101) Bragg reflection or changes in the tetragonal unit cell volume (Fig. 3 (a-c)), which remained close to the parent t-ZrO_2 support. This shows that the Zn in the samples remained as a ZnO surface phase during the reaction and did not migrate into the support, which was consistent with their activity being unaffected by the exposure to reaction conditions (Fig. 3 (c)).

The conclusion that activity arises from a ZnO surface layer and not from Zn^{2+} ions part of a solid solution with ZrO_2 is further substantiated by the behaviour of the co-precipitated ZnO-ZrO_2 samples. For the co-precipitated ZnO-ZrO_2 samples, the tetragonal zirconia unit cell volume was significantly lower than that for the impregnated samples (Fig. 3 (c)), suggesting that Zn^{2+} ions were present in the zirconia lattice, and this uptake of dopants that stabilized the tetragonal structure at temperatures below 1170 ºC [13]. TEM analysis of the ZnO-ZrO_2 sample (Fig. S15) also supported

that Zn was present as a mixture of both a highly dispersed Zn phase, consistent with isolated Zn^{2+} in a solid solution, and the ~5 nm ZnO surface domians seen for the impregnated samples. The co-precipitated samples thus had some zinc arranged inside the zirconia structure, as has also been observed in several other studies [9,14–16]. The ZnO-ZrO_2-100 sample, co-precipitated at 100 °C, had a particularly low unit cell volume (Fig. 3 (c)) and a relatively low surface ZnO content, close to the bulk composition (Table 1), which shows that this sample had a high degree of its Zn incorporated as solid solution. Two observations for the ZnO-ZrO_2-100 sample showed that Zn in the solid solution was not of particularly high catalytic activity. Firstly, Fig. 5 shows that ZnO-ZrO_2-100 had much lower initial activity than ZnO-ZrO_2, which had a higher surface enrichment of ZnO, although ZnO-ZrO_2-100 had a higher surface area. Secondly, the ZnO-ZrO_2-100 sample underwent a pronounced activation during the exposure to reaction conditions and after stabilization, the rate doubled compared to the initial level (Fig. 3 (c)). Analysis of the spent sample showed that this was mirrored by a downshift in the (101) Bragg reflection (Fig. 3 (b)) and a clear increase in unit cell volume (Fig. 3 (c)), which clearly shows that the increased activity occurred when Zn segregated out of the solid solution and formed a ZnO surface layer. Fig. 3 (b) shows an intensity increase in the XRD pattern for the t-ZrO_2 in ZnO-ZrO_2-100 during reaction. Possibly due to t-ZrO_2 becoming more crystalline or/and that the average crystallite size increased from about 100 to 186 Å according to Rietveld analysis, which would also result in a significant reduction of the specific surface area.

Changes in the crystalline phase of the zirconia have previously resulted in an effect on the methanol synthesis performance [31,32]. However, these effects are not comparable with the substantial improvement (a factor of >2) in the oxygenate formation rate observed from the fresh to the spent ZnO-ZrO_2-100 in Fig. 3 (c). These findings are summarized in Fig. 5, which clearly shows that it is the surface ZnO layer and not Zn^{2+} ions in a solid solution, which is responsible for catalysing the methanol synthesis.

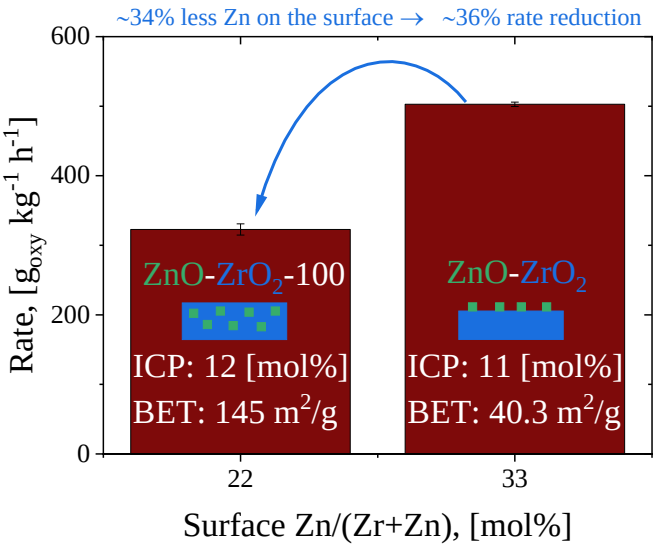


Fig. 5. The oxygenate (CH_3OH + CH_3OCH_3) formation rate against the mol% of ZnO supported on the ZrO_2 surface. Conditions: 320 °C, 50 barg, 32.1 NL/h, catalyst loading of 750 mg, feed gas composition of CO_2/CO/H_2/Ar 29/4/64/3.

3.3 Local Zinc Oxide Environment on the Zirconia Surface

Due to the amorphous nature of the ZnO surface domains on the ZrO_2 surface, XAS was conducted to characterize and quantify these species and evaluate their relation to the catalytic activity. The Zn K-edge X-ray absorption near edge structure (XANES) and the k^3-weighted Fourier-transformed extended X-ray absorption fine structure (FT-EXAFS) spectra of the as-prepared ZnO on ZrO_2 catalysts, Zn foil, and bulk ZnO are presented in Fig. 6(a) and (b), respectively. The XANES spectra (Fig. 6 (a)) shows the absorption edge at 9662 eV for the all ZnO/ZrO_2 samples, the same as bulk ZnO (9662 eV) rather than metallic Zn (9659 eV) [15,21]. The absence of a signal related to metallic Zn (Zn-Zn at approximately 2.2 Å) in the FT-EXAFS spectra (Fig. 6 (b)) confirmed that Zn^{2+} was the only oxidation state present in all the catalysts. At low Zn loadings ≤ 18 mol%, trends associated with ZnO were observed in the shape of the XANES spectra, but no signal related to the backscattering of the next nearest neighbour Zn-Zn was visible in the FT-EXAFS spectra. This indicated that the ~5 nm ZnO_x surface domains were a defective ZnO-phase with no repeating crystalline structure. As mentioned, the XPS evidence for surface enrichment of Zn (Table 1) revealed that these domains were present on the ZrO_2 surface. As the Zn loading increased > 18 mol% for the impregnated samples, the shape of the XANES spectra resembled that of bulk, hexagonal ZnO. This confirmed that an increasing fraction of the Zn created crystalline ZnO nanoparticles, as also detected with XRD. The co-precipitated ZnO-ZrO_2 sample showed similar trends as the Zn impregnated samples, but with more features in the XANES spectrum (Fig. 6 (a)). The

combination of XRD (Fig. 3), XPS (Table 1) and TEM (Fig. S15) suggested that this sample had most of its Zn in the form of ZnO surface domains and a minority of its Zn in solid solution, where different atomic positions may not result in regular Zn-Zr distances. Therefore, no clear Zn-Zr backscattering at distance ≈ 3.5 Å was observed for this sample [33].

Fitting the EXAFS spectra (reported in Table S2) resulted in an interatomic distance of Zn-O ≈ 1.98 Å and of Zn-Zn ≈ 3.23 Å (only for Zn loadings > 18 mol%), similar to the distances observed for these two shells in pure hexagonal ZnO. Coordination numbers for the first Zn-O shell for the impregnated samples were close to 4, similar to bulk ZnO. A higher Zn-O coordination number would be expected if Zn^{2+} was incorporated into the zirconia lattice [34] or if the ZnO was hydrated. A decrease in the coordination number was seen with increasing Zn loading, which was caused by the strong correlation with the refined mean square deviation of interatomic distances (σ^2). The coordination number fit of the co-precipitated ZnO-ZrO_2 sample was lower. However, the standard deviation did not suggest any significant difference from the impregnated samples, suggesting that most of the Zn in this sample was in the presence of ZnO surface domains.

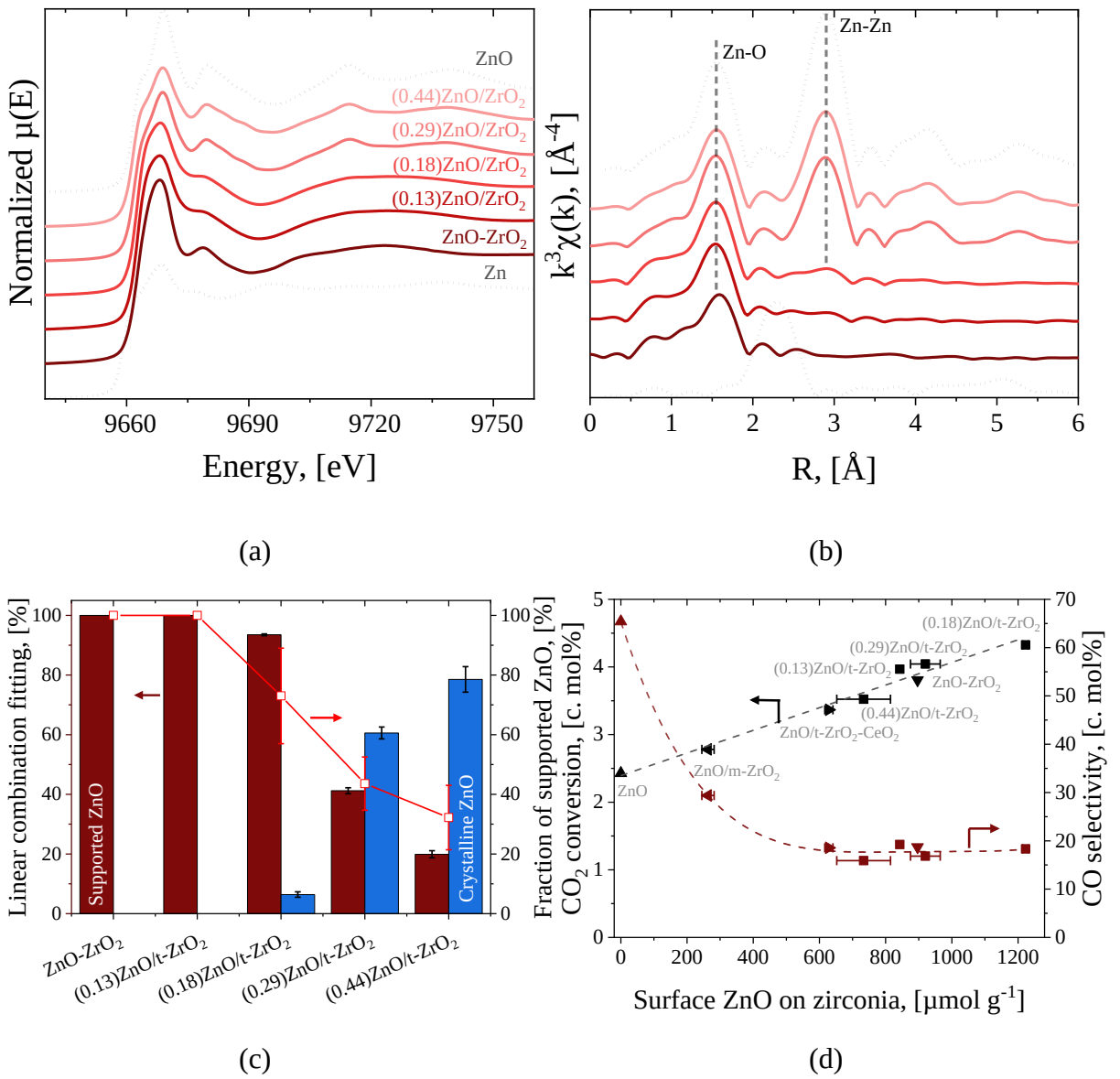


Fig. 6. (a) Zn K-edge XANES and (b) Fourier-transformed k^3-weighted EXAFS spectra of ZnO supported on zirconia catalysts with Zn foil and ZnO as references. (c) The fraction of surface ZnO determined by linear combination fitting and by the coordination number of the Zn-Zn second shell using Eq.(5). (d) The CO_2 conversion and CO selectivity against the calculated amount of surface ZnO species from Eq. (6). Reaction conditions: 320 °C, 50 barg, 15 NL/h, catalyst loading of 300 mg, feed gas composition of $CO_2/H_2/Ar$ 20/60/20.

The fractions of Zn in the disordered ZnO domains and in crystalline 3D ZnO, respectively, were estimated by Eq. (5) using the coordination number of the Zn-Zn shell and by linear combination fitting of the XANES spectra between samples having only isolated domains (here (0.13)ZnO/t-ZrO_2) and bulk ZnO. Fig. 6 (c) shows the fraction of Zn in ZnO surface domains using both methods, which yielded in similar results. With increasing Zn loading, more crystalline ZnO was formed, but a significant amount of the Zn was still present as ZnO surface domains. The amount

of Zn present as ZnO surface domains was thus be determined from the results in Fig. 6 (c) and the total Zn loading of the sample using Eq. (6). On this basis, Fig. 6 (d) shows the CO_2 conversion and CO selectivity as function of the amount of surface ZnO. This illustrate that the surface ZnO was highly selective towards methanol formation and that the amount controlled the CO_2 conversion. Crystalline ZnO showed methanol formation activity, but, as illustrated in Fig. 6 (d), these sites had lower selectivity towards methanol. Assuming that the ZnO domains are 2D structures with all Zn-atoms exposed and that their site density was that of the crystalline ZnO(0001) facet, the results in Fig. 6 (d) show that the turnover frequency per Zn surface atom was 17 h^{-1} for ZnO domains and 4 h^{-1} for crystalline ZnO, respectively. Other Zn-containing catalysts have been prepared for other catalytic processes, where similar surface or isolated Zn^{2+} sites have been concluded to be the main active site [35–38], supporting the conclusion that supported ZnO provided the active sites for methanol synthesis.

As discussed in Section 3.3 the 18 mol% Zn sample contained an appropriate amount of Zn to cover the available ZrO_2 surface area, and above this value 3D ZnO nanoparticles of lower activity began to occupy part of the surface. Fig. 6 (d) illustrates that this sample was also the most active as it maximized the amount of ZnO surface sites. The results in Fig. 1 and Fig. 6 (d) thus reveal that activity of ZnO based methanol synthesis catalysts was maximized by choosing the optimal support, of which t-ZrO_2 was the best tested here, and loading with Zn to the maximal level at which a 2D ZnO surface layer could be maintained.

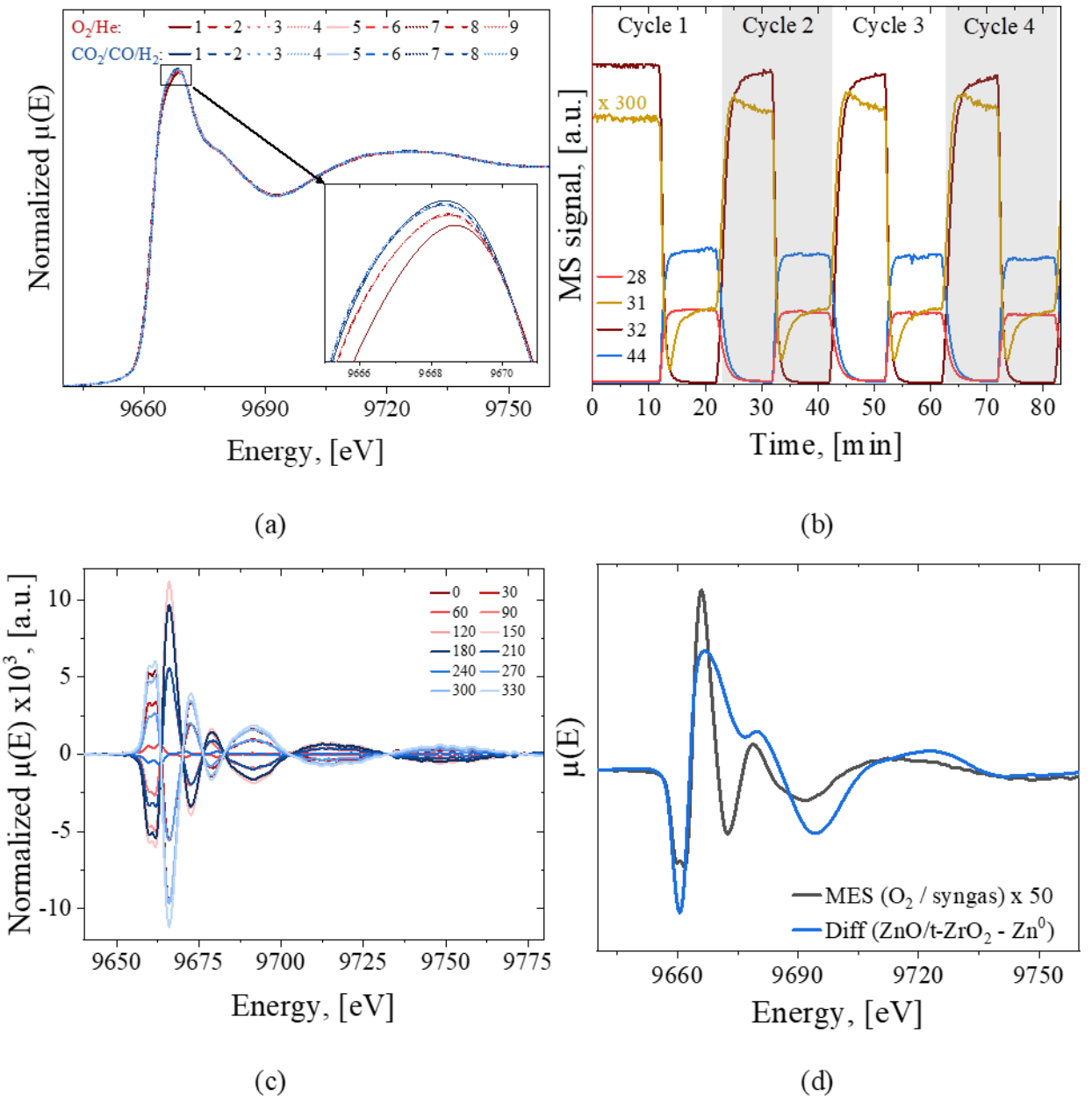


Fig. 7. (a) Zn K-edge XANES spectra of the (0.13)ZnO/t-ZrO_2 sample for cycles 1 to 9, where the gas was switched between O_2/He and syngas. (b) MS signal for the first 4 cycles showing the switch between gasses and the methanol formation. (c) The phase-resolved spectra obtained by Eq. (7) at different phase angles. (d) Comparison between the phase-resolved spectrum with the highest intensity (150°) with the difference spectrum of (0.13)ZnO/t-ZrO_2 minus Zn foil. Reaction conditions: 400 °C, 15 barg, 50 NmL/h, catalyst loading of ~2.5 mg (diluted 1:4 in inert α-Al_2O_3), feed gas composition of CO_2/CO/H_2/He 12/5/37/46.

3.4 State of the ZnO surface domains and the nature of the support effect

Time resolved QEXAFS, coupled with modulation excitation spectroscopy (MES) to amplify spectral changes, was conducted to investigate the stability of the catalysts and to determine minute changes in the Zn oxidation state under methanol synthesis conditions. An initial dehydration step in O_2/He did not show any changes for the Zn oxidation state, but changes in the Zn K-edge

XANES when switching to syngas could suggest partial Zn reduction (Fig. S10). To amplify this effect, MES experiments with periodic switching between a syngas mixture of CO_2/CO/H_2 (reducing gas) and an O_2/He mixture (oxidizing gas), with simultaneous measurements of spectra, were conducted. To conduct the MES analysis, the changes that occur when modulating the gas phase composition must be reversible. However, irreversible formation of crystalline ZnO was observed when switching between reducing and oxidizing atmospheres for the (0.18)ZnO/t-ZrO_2 and ZnO-ZrO_2 samples, which resulted in reduced methanol synthesis activity (Fig. S11). For the (0.13)ZnO/t-ZrO_2 sample, the first cycle resulted in an irreversible change in the XANES spectra, which stabilized from cycles 2 to 9, as illustrated in Fig. 7 (a), which shows the averaged time resolved spectra for 9 periods. The catalytic performance was stable throughout the 9 cycles, illustrated for the first 4 cycles in Fig. 7 (b), showing stable methanol synthesis activity (MS signal at m/z = 31, due to mass overlap O_2 also showed intensity at this mass). The averaged time resolved intensity at 9660 eV (for cycles 2 to 9) showed clear reversible changes in the intensity going from reducing to oxidizing conditions (Fig. S12). This allowed for the phase-domain analysis.

The phase-resolved spectra as obtained from averaged time resolved spectra shown in Fig. S12 (averaging cycles 2-9) are given in Fig. 7(c) at selected phase angles. The maximum intensity of phase resolved spectra was obtained at 150°, which was used for further comparison. The decreasing intensity at 9658-9660 eV, the edge position of metallic zinc, indicated reversible changes in the Zn oxidation state. In Fig. 7 (d), the phase-resolved spectrum at 150° phase angle scaled by a factor of 50 is compared to the difference spectrum between the as prepared sample and Zn foil. This shows a reversible partial reduction of Zn under reaction conditions, where approximately 1 out of 50 Zn atoms was reduced to a state closer to metallic Zn^0 than to Zn^{2+}. Thus, under reaction conditions, the ZnO surface species were partly reduced ZnO_x species with *x* approximately equal to 0.98. The partially reduced ZnO_x likely played an important role for the methanol synthesis activity. The thermodynamic reduction potentials of bulk ZnO to metallic Zn^0 from H_2 (ΔG = 78.5 kJ/mol) and CO (ΔG = 63.8 kJ/mol) show that this reaction is unlikely for bulk ZnO. The MES results thus indicated that the ZnO surface phase had an increased reducibility compared to crystalline bulk ZnO.

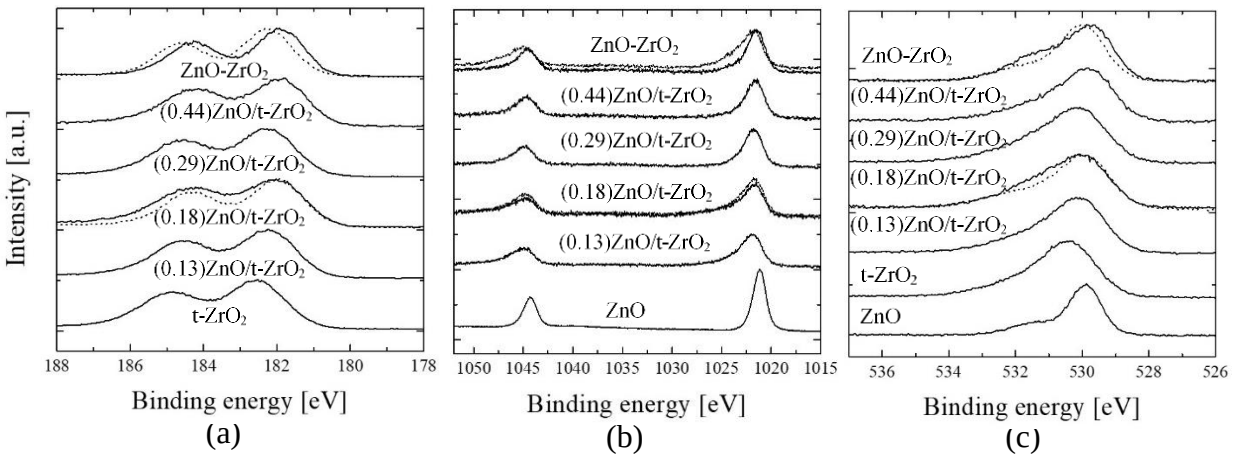


Fig. 8. XPS spectra of (a) Zr 3d, (b) Zn 2p and (c) O 1s. Solid lines represent fresh catalysts samples, ZnO and bare t-ZrO_2 support, while dotted lines represent spent samples.

Fig. 8 shows the Zr 3d, Zn 2p and O 1s XPS spectra for selected samples. In Fig. 8 (a), the spin-orbit doublet of the Zr 3d core level into Zr $3d_{5/2}$ and Zr $3d_{3/2}$ with binding energy around 182.5 and a splitting of ~2.5 eV, shows that the oxidation state was Zr^{4+} [39]. The impregnation of ZnO onto the zirconia support resulted in a shift for the Zr $3d_{5/2}$ to lower binding energies, indicating a charge enrichment of the ZrO_2 phase. In Fig. 8 (b), a spin-orbit doublet of Zn $2p_{3/2}$ and Zn $2p_{1/2}$ for pure ZnO were found at 1021 and 1044 eV, which shifted to higher binding energy when ZnO was supported on zirconia. This shift suggested that Zn^{2+} became more electron deficient. The position of the Zn LMM Auger peaks (Fig. S13) confirmed that Zn^{2+} was the only oxidation state present for all the samples. In Fig. 8 (c), the O 1s peaks also shifted to lower binding energies compared to the bare t-ZrO_2 support, which supported that Zn^{2+} became more electron deficient. Lorentz peak fitting to the O 1s peak for oxygen vacancies and lattice oxygen showed no relation between surface oxygen defects and the activity of the catalysts (Table 1). However, the binding energy values for all metals showed that there was an interaction between Zn and Zr. This interaction created a more electron deficient ZnO. Withdrawal of electrons from Zn-O bonds in the surface ZnO likely correlated with the increased partial reducibility of this phase to ZnO_x. This is further linked to the superior catalytic performance when ZnO was supported on ZrO_2, because it was easier to abstract oxygen from a more reducible ZnO_x surface and in that process oxophilic sites were created, that activated CO_2.

3.5 CO_2 Hydrogenation Reaction Mechanism

In-situ DRIFTS was used to study the ZnO/t-ZrO_2 and t-ZrO_2 surface reaction intermediates for methanol formation from CO_2 and H_2. In Fig. 9 (a), the CO_2 adsorption on the t-ZrO_2 support lead to observation of bicarbonate and bridging carbonate species (HCO_3*, CO_3* with at 1404, 1484, 1604 and 1640 cm^{-1}) [37,40–42]. When ZnO was added to the support, strong signals attributed to bidentate formate (HCO_2^* at 1360, 1382, 1595 and 2880 cm^{-1}) and zinc bonded carbonate (at 1508 cm^{-1}) adsorbates appeared [15,40,43]. The formation of formate species without H_2 present in the feed gas suggested that hydrogen was available at the zinc surface and that hydroxyl groups could play a role in the adsorption and activation of CO_2 [37]. After the CO_2 adsorption, the feed gas was changed to a H_2/He mixture and the intensity of the formate signal intensified and additional formate peaks at 2734, and 2978 cm^{-1} became visible. The carbonate signals (at 1404, 1484, 1508 and 1640 cm^{-1}) decreased, demonstrating hydrogenation of the carbonate species into formate [44]. With t-ZrO_2 alone, the formate signals were observed at lower wavenumbers and the carbonate species were still visible after 60 min (Fig. S18). Thus, having ZnO on the zirconia surface provided alternative formate and carbonate binding sites and improved the hydrogenation of the carbonate species into formate. This shows that the surface ZnO_x domains were able to bind and activate CO_2, while Zr-sites did not activate CO_2. Furthermore, no correlation between surface oxygen defects and activity was found by XPS analysis. In combination, the XPS and DRIFTS results contradicted that Zr should provide oxygen vacancies that operate in synergy with Zn for the formation of methanol as suggested elsewhere [33,45–47].

Fast removal of the carbonate species by hydrogenation into formate and further into methanol occurred when switching from CO_2 to H_2 at 320 °C. As the methanol formation subsided, the intensity of the formate peaks decreased, which suggested a pathway from HCOO to CH_3OH. However, formate signals were still visible at the catalyst surface at low methanol concentration (Fig. S17).

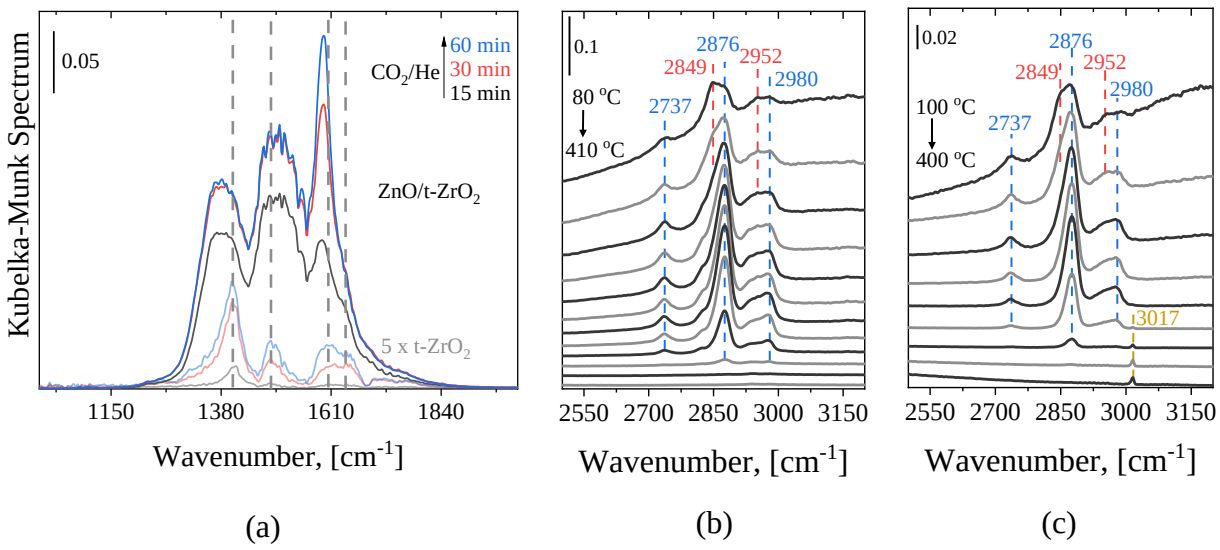


Fig. 9. In-situ DRIFTS measurements. (a) CO_2 adsorption on (0.13)ZnO/t-ZrO2 and bare t-ZrO_2 support at 20 bar and 320 °C. (b) TPD in He and (c) TPR in H_2 at 20 bar after steady-state methanol formation at 320 °C and 20 bar.

The (0.13)ZnO/t-ZrO_2 catalyst was subjected to steady-state methanol synthesis at 320 °C and 20 bar and then cooled to room temperature. Upon cooling, methoxy species (2849 and 2952 cm^{-1}) became visible at the catalyst surface [15,43]. Fig. 9 (b) and (c) show the results when this cooled sample was subjected to either temperature programmed desorption (TPD) in He or temperature programmed reaction (TPR) in H_2. The methoxy signals quickly disappeared when the reactor was heated in He or H_2, and were completely removed around 140 °C. This indicated that the pathway to methanol proceeds via methoxy, but that the hydrogenation of such species was so rapid that they were only visible at low temperatures. By further heating in He the carbonate species desorbed and were removed at around 220 °C. In H_2 atmosphere, the removal of carbonate species occurred at 180 °C (Fig. S19). The lower temperature for carbonate removal in the presence of H_2 suggested that carbonate was hydrogenated to formate instead of desorbing from the surface. Around 370 °C, the formate signals disappeared showing the bonding strength order of HCO_2*>CO_3*/HCO_3*>CH_3O*. As illustrated in Fig. S19, additional carbonate signals (at 1437 and 1573 cm^{-1}) became visible after formate desorption in He. These were concluded not to be relevant for the methanol synthesis activity as they are too strongly adsorbed on the surface, needing more than 410 °C to desorb. However, these signals were not observed in the H_2 atmosphere, suggesting that these carbonate species could be important for the methane formation.

These findings lead to the proposed reaction mechanism consisting of CO_2 adsorption as carbonate, hydrogenation into formate and further into methoxy and finally methanol. Formate was

strongly adsorbed and accumulated on the catalyst surface. Hydrogenation of formate formed short lived adsorbed methoxy, which rapidly hydrogenated and desorbed as methanol. The loosely adsorbed methoxy and the fact that carbonate hydrogenates into formate in H_2 atmosphere before desorption, suggested that the hydrogenation of formate into methoxy was the rate-determining step, similar to that found for the $Cu/ZnO/Al_2O_3$ catalyst [48].

4 Conclusions

ZnO supported on zirconia materials were highly active and selective catalysts for high temperature methanol synthesis, making them good candidates for combinations with zeolites in a bifunctional process for direct conversion of CO_2 into hydrocarbon products. Impregnated samples showed similar selective performance towards methanol formation as the co-precipitated samples, without any integration of Zn into the zirconia lattice as detected by XRD. Hence, a solid solution of ZnO in ZrO_2 was not important for the catalytic activity or selectivity. Both preparation methods resulted in catalysts where ZnO was mainly present on the zirconia surface, as determined by XPS. Furthermore, only amorphous, surface ZnO was detected by XAS at low Zn loadings. Activity measurements of two co-precipitated samples with the same bulk Zn mol%, but with a significant difference in the surface Zn concentration, demonstrated the importance of ZnO located on the zirconia surface. TEM analysis showed well-dispersed ZnO as domains of ~5 nm size on the zirconia surface for the co-precipitated and impregnated samples, without ZnO adopting any crystalline structure. Modulation excitation spectroscopy coupled time resolved QEXAFS showed that these Zn sites were capable of reversible, partial reduction under methanol synthesis conditions forming ZnO_x, where x was approximately 0.98. In-situ DRIFTS analysis of CO_2 adsorption under methanol synthesis conditions showed a shift in the formed carbonate and formate species on the ZnO containing zirconia, compared to the bare zirconia support. Together, these findings suggested that the active phase was the partly reduced surface ZnO_x, which adsorbed CO_2, hydrogenated it into formate and further into methanol.

Declaration of Competing Interest

The authors declare that they have no known competing financial interests or personal relationships that could have appeared to influence the work reported in this paper.

Acknowledgment

This work was funded by the Independent Research Fund Denmark (Grant no. 0136-00073B). We acknowledge the Paul Scherrer Institut, Villigen, Switzerland for provision of synchrotron radiation beamtime at beamline SuperXAS of the SLS. Funding for travels to SLS was provided by DanScatt. Special thanks are given to Eva S. Kold, Amalie B. Møller and Dr. Thomas Eldridge for their support overseeing experiments conducted at SLS and Simon Ingeman Hansen for his help making the graphical abstract.

References

[1] R. Geyer, J.R. Jambeck, K.L. Law, Production, use, and fate of all plastics ever made, Sci. Adv. 3 (2017) 25–29. https://doi.org/10.1126/sciadv.1700782.

[2] OECD, Global Plastics Outlook: Plastics use by region - projections, OECD Environ. Stat. (2022). https://doi.org/10.1787/913b14f3-en (accessed September 22, 2022).

[3] OECD, Global Plastics Outlook: Plastics use by polymer - projections, OECD Environ. Stat. (2022). https://doi.org/10.1787/b9bae4d1-en (accessed September 22, 2022).

[4] J.M. Garcia, M.L. Robertson, The future of plastics recycling, Science (80-.). 358 (2017) 870–872. https://doi.org/10.1126/science.aaq0324.

[5] X. Liu, M. Wang, H. Yin, J. Hu, K. Cheng, J. Kang, Q. Zhang, Y. Wang, Tandem Catalysis for Hydrogenation of CO and CO2to Lower Olefins with Bifunctional Catalysts Composed of Spinel Oxide and SAPO-34, ACS Catal. 10 (2020) 8303–8314. https://doi.org/10.1021/acscatal.0c01579.

[6] X. Liu, M. Wang, C. Zhou, W. Zhou, K. Cheng, J. Kang, Q. Zhang, W. Deng, Y. Wang, Selective transformation of carbon dioxide into lower olefins with a bifunctional catalyst composed of ZnGa2O4 and SAPO-34, Chem. Commun. 54 (2017) 140–143. https://doi.org/10.1039/c7cc08642c.

[7] M.B. Fichtl, D. Schlereth, N. Jacobsen, I. Kasatkin, J. Schumann, M. Behrens, R. Schlögl, O. Hinrichsen, Kinetics of deactivation on Cu/ZnO/Al2O3 methanol synthesis catalysts, Appl. Catal. A Gen. 502 (2015) 262–270. https://doi.org/10.1016/j.apcata.2015.06.014.

[8] D.L.S. Nieskens, J.D. Lunn, A. Malek, Understanding the Enhanced Lifetime of SAPO-34

in a Direct Syngas-to-Hydrocarbons Process, ACS Catal. 9 (2019) 691–700. https://doi.org/10.1021/acscatal.8b03465.

[9] J. Wang, G. Li, Z. Li, C. Tang, Z. Feng, H. An, H. Liu, T. Liu, C. Li, A highly selective and stable ZnO-ZrO2 solid solution catalyst for CO2 hydrogenation to methanol, Sci. Adv. 3 (2017) 1–11. https://doi.org/10.1126/sciadv.1701290.

[10] Y. Wang, L. Tan, M. Tan, P. Zhang, Y. Fang, Y. Yoneyama, G. Yang, N. Tsubaki, Rationally Designing Bifunctional Catalysts as an Efficient Strategy to Boost CO2 Hydrogenation Producing Value-Added Aromatics, ACS Catal. 9 (2019) 895–901. https://doi.org/10.1021/acscatal.8b01344.

[11] H. Song, D. Laudenschleger, J.J. Carey, H. Ruland, M. Nolan, M. Muhler, Spinel-Structured ZnCr2O4 with Excess Zn Is the Active ZnO/Cr2O3 Catalyst for High-Temperature Methanol Synthesis, ACS Catal. 7 (2017) 7610–7622. https://doi.org/10.1021/acscatal.7b01822.

[12] O. Martin, A.J. Martín, C. Mondelli, S. Mitchell, T.F. Segawa, R. Hauert, C. Drouilly, D. Curulla-Ferré, J. Pérez-Ramírez, Indium oxide as a superior catalyst for methanol synthesis by CO2 hydrogenation, Angew. Chemie - Int. Ed. 55 (2016) 6261–6265. https://doi.org/10.1002/anie.201600943.

[13] R.P. INGEL, D.L. III, Lattice Parameters and Density for Y2O3-Stabilized ZrO2, J. Am. Ceram. Soc. 69 (1986) 325–332. https://doi.org/10.1111/j.1151-2916.1986.tb04741.x.

[14] Z. Han, C. Tang, F. Sha, S. Tang, J. Wang, C. Li, CO2 hydrogenation to methanol on ZnO-ZrO2 solid solution catalysts with ordered mesoporous structure, J. Catal. 396 (2021) 242–250. https://doi.org/10.1016/j.jcat.2021.02.024.

[15] S. Tada, N. Ochiai, H. Kinoshita, M. Yoshida, N. Shimada, T. Joutsuka, M. Nishijima, T. Honma, N. Yamauchi, Y. Kobayashi, K. Iyoki, Active Sites on $Zn_xZr_{1-x}O_{2-x}$ Solid Solution Catalysts for CO_2-to-Methanol Hydrogenation, ACS Catal. 12 (2022) 7748–7759. https://pubs.acs.org/doi/10.1021/acscatal.2c01996.

[16] J. Ding, Z. Li, W. Xiong, Y. Zhang, A. Ye, W. Huang, Structural evolution and catalytic performance in CO2 hydrogenation reaction of ZnO-ZrO2 composite oxides, Appl. Surf.

Sci. 587 (2022). https://doi.org/10.1016/j.apsusc.2022.152884.

[17] S. Pradhan, B.G. Mishra, Catalytic application of SO42-/Fe-ZrO2 nanoparticles synthesized by a urea hydrolysis method for environmentally benign one pot synthesis of 1,8-dioxodecahydroacridines, RSC Adv. 5 (2015) 86179–86190. https://doi.org/10.1039/c5ra11136f.

[18] S. Vasanthavel, S. Kannan, Structural investigations on the tetragonal to cubic phase transformations in zirconia induced by progressive yttrium additions, J. Phys. Chem. Solids. 112 (2018) 100–105. https://doi.org/10.1016/j.jpcs.2017.09.010.

[19] S. Aghabeygi, M. Khademi-Shamami, ZnO/ZrO2 nanocomposite: Sonosynthesis, characterization and its application for wastewater treatment, Ultrason. Sonochem. 41 (2018) 458–465. https://doi.org/10.1016/j.ultsonch.2017.09.020.

[20] C. Wang, G. Garbarino, L.F. Allard, F. Wilson, G. Busca, M. Flytzani-Stephanopoulos, Low-Temperature Dehydrogenation of Ethanol on Atomically Dispersed Gold Supported on ZnZrOx, ACS Catal. 6 (2016) 210–218. https://doi.org/10.1021/acscatal.5b01593.

[21] S. Han, D. Zhao, T. Otroshchenko, H. Lund, U. Bentrup, V.A. Kondratenko, N. Rockstroh, S. Bartling, D.E. Doronkin, J.D. Grunwaldt, U. Rodemerck, D. Linke, M. Gao, G. Jiang, E. V. Kondratenko, Elucidating the Nature of Active Sites and Fundamentals for their Creation in Zn-Containing ZrO2-Based Catalysts for Nonoxidative Propane Dehydrogenation, ACS Catal. 10 (2020) 8933–8949. https://doi.org/10.1021/acscatal.0c01580.

[22] K. Cheng, W. Zhou, J. Kang, S. He, S. Shi, Q. Zhang, Y. Pan, W. Wen, Y. Wang, Bifunctional Catalysts for One-Step Conversion of Syngas into Aromatics with Excellent Selectivity and Stability, Chem. 3 (2017) 334–347. https://doi.org/10.1016/j.chempr.2017.05.007.

[23] A.H. Clark, J. Imbao, R. Frahm, M. Nachtegaal, ProQEXAFS: A highly optimized parallelized rapid processing software for QEXAFS data, J. Synchrotron Radiat. 27 (2020) 551–557. https://doi.org/10.1107/S1600577519017053.

[24] B. Ravel, M. Newville, ATHENA, ARTEMIS, HEPHAESTUS: data analysis for X-ray absorption spectroscopy using IFEFFIT, J. Synchrotron Rad. 12 (2005) 537–541.

[25] A. Gaur, T.M. Hartmann Dabros, M. Høj, A. Boubnov, T. Prüssmann, J. Jelic, F. Studt, A.D. Jensen, J.D. Grunwaldt, Probing the Active Sites of MoS 2 Based Hydrotreating Catalysts Using Modulation Excitation Spectroscopy, ACS Catal. 9 (2019) 2568–2579. https://doi.org/10.1021/acscatal.8b04778.

[26] A. Gaur, M. Stehle, M. Serrer, M.Z. Stummann, C. La Fontaine, J. Grunwaldt, M. Høj, Using Transient XAS to Detect Minute Levels of Reversible S - O Exchange at the Active Sites of MoS 2 - Based Hydrotreating Catalysts : E ff ect of Metal Loading , Promotion , Temperature , and Oxygenate Reactant, ACS Catal. 12 (2022) 633–647. https://doi.org/10.1021/acscatal.1c04767.

[27] D. Baurecht, U.P. Fringeli, Quantitative modulated excitation Fourier transform infrared spectroscopy, Rev. Sci. Instrum. 72 (2001) 3782–3792. https://doi.org/10.1063/1.1400152.

[28] A. Urakawa, T. Bürgi, A. Baiker, Sensitivity enhancement and dynamic behavior analysis by modulation excitation spectroscopy : Principle and application in heterogeneous catalysis, Chem. Eng. Sci. 63 (2009) 4902–4909. https://doi.org/10.1016/j.ces.2007.06.009.

[29] N.D. Nielsen, A.D. Jensen, J.M. Christensen, The roles of CO and CO2 in high pressure methanol synthesis over Cu-based catalysts, J. Catal. 393 (2021) 324–334. https://doi.org/10.1016/j.jcat.2020.11.035.

[30] N.D. Nielsen, T.E.L. Smitshuysen, C.D. Damsgaard, A.D. Jensen, J.M. Christensen, Characterization of oxide-supported Cu by infrared measurements on adsorbed CO, Surf. Sci. 703 (2021). https://doi.org/10.1016/j.susc.2020.121725.

[31] L. Lin, G. Wang, F. Zhao, CO 2 Hydrogenation to Methanol on ZnO / ZrO 2 Catalysts : Effects of Zirconia Phase, (2021) 2119–2125.

[32] Z. Lui, Y. Ni, Z. Hu, Y. Fu, X. Fang, Q. Jiang, Z. Chen, W. Zhu, Z. Liu, Insights into effects of ZrO2 crystal phase on syngas-to-olefin conversion over ZnO/ZrO2 and SAPO-34 composite catalysts, Chinese J. Catal. 43 (2022) 877–884.

[33] D. Salusso, E. Borfecchia, S. Bordiga, Combining X-ray Diffraction and X-ray Absorption Spectroscopy to Unveil Zn Local Environment in Zn-Doped ZrO2Catalysts, J. Phys. Chem. C. 125 (2021) 22249–22261. https://doi.org/10.1021/acs.jpcc.1c06202.

[34] G. Teufer, The crystal structure of tetragonal ZrO2., Aeta Cryst. (1962). 15 (1962) 1187.

[35] N.M. Schweitzer, B. Hu, U. Das, H. Kim, J. Greeley, L.A. Curtiss, P.C. Stair, J.T. Miller, A.S. Hock, Propylene hydrogenation and propane dehydrogenation by a single-site Zn2+ on silica catalyst, ACS Catal. 4 (2014) 1091–1098. https://doi.org/10.1021/cs401116p.

[36] J. Camacho-Bunquin, P. Aich, M. Ferrandon, A. "Bean" Getsoian, U. Das, F. Dogan, L.A. Curtiss, J.T. Miller, C.L. Marshall, A.S. Hock, P.C. Stair, Single-site zinc on silica catalysts for propylene hydrogenation and propane dehydrogenation: Synthesis and reactivity evaluation using an integrated atomic layer deposition-catalysis instrument, J. Catal. 345 (2017) 170–182. https://doi.org/10.1016/j.jcat.2016.10.017.

[37] Y. Zro, E. Ko, M. Kogler, T. Bielz, B. Klo, S. Penner, In Situ FT-IR Spectroscopic Study of CO2 and CO Adsorption on Y2O3, ZrO2 and Yttria-Stabilized ZrO2, J. Phys. Chem. C. 117 (2013) 17666–17673.

[38] I. Pinilla-Herrero, E. Borfecchia, J. Holzinger, U. V. Mentzel, F. Joensen, K.A. Lomachenko, S. Bordiga, C. Lamberti, G. Berlier, U. Olsbye, S. Svelle, J. Skibsted, P. Beato, High Zn/Al ratios enhance dehydrogenation vs hydrogen transfer reactions of Zn-ZSM-5 catalytic systems in methanol conversion to aromatics, J. Catal. 362 (2018) 146–163. https://doi.org/10.1016/j.jcat.2018.03.032.

[39] S. Tsunekawa, K. Asami, S. Ito, M. Yashima, T. Sugimoto, XPS study of the phase transition in pure zirconium oxide nanocrystallites, 252 (2005) 1651–1656. https://doi.org/10.1016/j.apsusc.2005.03.183.

[40] S.E. Collins, M.A. Baltanás, A.L. Bonivardi, An infrared study of the intermediates of methanol synthesis from carbon dioxide over Pd/β -Ga2O3, J. Catal. 226 (2004) 410–421. https://doi.org/10.1016/j.jcat.2004.06.012.

[41] K. Pokrovski, K.T. Jung, A.T. Bell, Investigation of CO and CO 2 Adsorption on Tetragonal and Monoclinic Zirconia, Langmuir. 17 (2001) 4297–4303.

[42] S.M. Fehr, K. Nguyen, I. Krossing, Realistic Operando-DRIFTS Studies on Cu/ZnO Catalysts for CO2 Hydrogenation to Methanol – Direct Observation of Mono-ionized Defect Sites and Implications for Reaction Intermediates, ChemCatChem. 14 (2022).

https://doi.org/10.1002/cctc.202101500.

[43] Y. Wang, S. Kattel, W. Gao, K. Li, P. Liu, G.J. Chen, H. Wang, Exploring the ternary interactions in Cu–ZnO–ZrO2 catalysts for efficient CO2 hydrogenation to methanol, Nat. Commun. 10 (2019) 1–8. http://dx.doi.org/10.1038/s41467-020-16342-1.

[44] L.F. Bobadilla, J.L. Santos, S. Ivanova, J.A. Odriozola, A. Urakawa, Unravelling the Role of Oxygen Vacancies in the Mechanism of the Reverse Water-Gas Shift Reaction by Operando DRIFTS and Ultraviolet-Visible Spectroscopy, ACS Catal. 8 (2018) 7455–7467. https://doi.org/10.1021/acscatal.8b02121.

[45] P. Ticali, D. Salusso, R. Ahmad, C. Ahoba-Sam, A. Ramirez, G. Shterk, K.A. Lomachenko, E. Borfecchia, S. Morandi, L. Cavallo, J. Gascon, S. Bordiga, U. Olsbye, CO2 hydrogenation to methanol and hydrocarbons over bifunctional Zn-doped ZrO2 /zeolite catalysts, Catal. Sci. Technol. 11 (2021) 1249–1268. https://doi.org/10.1039/d0cy01550d.

[46] C. Zhou, J. Shi, W. Zhou, K. Cheng, Q. Zhang, J. Kang, Y. Wang, Highly Active ZnO-ZrO2 Aerogels Integrated with H-ZSM-5 for Aromatics Synthesis from Carbon Dioxide, ACS Catal. 10 (2020) 302–310. https://doi.org/10.1021/acscatal.9b04309.

[47] Y. Yang, G. Wang, M. Gong, F. Zhao, Effect of preparation methods of ZnO/ZrO2 catalysts for methanol synthesis from CO2 hydrogenation, React. Kinet. Mech. Catal. 135 (2022) 2993–3005. https://doi.org/10.1007/s11144-022-02298-4.

[48] M. Bowker, R.A. Hadden, H. Houghton, J.N.K. Hyland, K.C. Waugh, The mechanism of methanol synthesis on copper/zinc oxide/alumina catalysts, J. Catal. 109 (1988) 263–273. https://doi.org/10.1016/0021-9517(88)90209-6.

4 Direct CO_2 Hydrogenation to Aromatics over Combined Catalysts Composed of Supported ZnO with Different Zeolite Topologies

On the next page, the manuscript with the title: *Direct CO_2 Hydrogenation to Aromatics over Combined Catalysts Composed of Supported ZnO with Different Zeolite Topologies* are reprinted.

This manuscript is still under preparation.

The scientist highlights:

- Combining ZnO/ZrO_2 mixed oxide with zeolites with pores size ≥5.5 Å enables the direct production of aromatics from CO_2.
- A disconnect between the aromatic selectivity and CO_2 conversion to hydrocarbons was found and high aromatic selectivity was favoured at low CO_2 conversions obtained at low temperature and pressure.
- A crucial factor for improving the aromatic selectivity was identified to be the zeolite topology where larger pores and cages induce the benzene methylation reactions.
- Kinetic analysis revealed that the activity of the bi-functional catalyst is hampered by high production of water.

Direct CO_2 Hydrogenation to Aromatics over Combined Catalysts Composed of Supported ZnO with Different Zeolite Topologies

M. T. Nikolajsen[1], E. S. Kold[1], A. B. Møller[1], N. C. Schjødt[2], U. V. Mentzel[2], J. Sehested[2], R. Y. Brogaard[2], J. M. Christensen[1] and M. Høj[1*]

[1] Department of Chemical Engineering, Technical University of Denmark (DTU), Kgs. Lyngby, 2800 (Denmark).

[2] Topsoe A/S, Kgs. Lyngby, 2800 (Denmark).

[*]Corresponding author: mh@kt.dtu.dk

Abstract

The potential to annually sequester approximately 170-200 million tons of CO_2 through the utilization of captured CO_2 in the synthesis of aromatic-based plastic monomers, such as para-xylene, demonstrates the huge potential for the direct hydrogenation of CO_2 into aromatics by bi-functional catalysts. Here we map out the potential for the production of aromatics in CO_2 hydrogenation with combinations of a ZnO/t-ZrO_2 methanol synthesis catalyst and ZSM-type zeolite. The simultaneous methanol synthesis and subsequent dehydration allow the methanol synthesis equilibrium to be exceeded. High hydrogen partial pressures favour the methanol synthesis equilibrium and thus CO_2 conversion but lead to a high cracking and hydrogenation activity that lowers the selectivity towards aromatics. Relatively low temperatures and pressures thus favour the aromatics selectivity, where the conversion is low. By using H-ZSM-5 and operating at low temperature and pressure (320 ºC and 10 bar) the hydrogenation activity was moderated resulting in an aromatics selectivity of 33.2 carbon mol%, at a CO_2 conversion to hydrocarbons of 4.5 %. Replacing the H-ZSM-5 with the larger pore zeolite H-ZSM-12 resulted in an aromatics selectivity of 42.4 carbon mol%, which was achieved by promoting the aromatic cycle and producing a more methylated benzene product, hexamethylbenzene. This was achieved at 340 ºC and 30 bar ensuring a high CO_2 to hydrocarbon conversion of 9.8 %. Kinetic analysis shows that water produced from the RWGS, CO_2 hydrogenation to methanol, and methanol dehydration limit the methanol synthesis activity even when residual methanol concentrations are exceedingly low. This represents another intrinsic competition between conversion and aromatics selectivity in the direct reaction. An analysis based on the hydrocarbon pool mechanism suggests that the realistically achievable upper limit on aromatics selectivity is 45-52 carbon mol%, which indicates that using a larger pore ZSM-12 zeolite at moderate temperature and pressure leads to the realistically achievable limit of aromatics selectivity.

1 Introduction

Polystyrene and polyethylene terephthalate are examples of plastic materials produced from the aromatic monomers ethenylbenzene and para-xylene. The collective annual output of these materials approximates 50 million tons, with projections anticipating an escalation to approximately 60 million tons by the year 2030 [1]. Currently, the main production of aromatic comes from the reforming of naphtha, a product from oil refining [2]. However, the utilization of CO_2, whether extracted from the atmosphere or generated through biomass processes, for the synthesis of these plastic monomers holds the theoretical potential to store an estimated 170-200 million tons of CO_2 on an annual basis.

Recent research has demonstrated that combining the methanol synthesis with an oxide catalyst and the methanol-to-hydrocarbon reaction with a zeolite catalyst enables the direct conversion of CO_2 into hydrocarbon products. Metal oxide catalyst such as In_2O_3 [3,4], ZnO [5], Cr_2O_3 [6,7] and mixed oxide such as ZnO/ZrO_2 [8–12], $ZnAl_2O_4$ [13,14], $ZnGa_2O_4$ [15] and $ZnCrO_4$ [16,17] have shown promising methanol synthesis activity at elevated temperatures necessity for the methanol dehydration over solid acids, with minimal olefin hydrogenation activity. Methanol synthesis catalysts based on metallic sites such as Cu or Pd [18–21] produce methanol at a higher rate but a high hydrogenation activity predominantly results in saturated hydrocarbon products. Thermodynamically, the following reactions occur during syngas conversion to methanol (R1 to R3).

$$CO + 2H_2 \rightleftharpoons CH_3OH \quad \Delta H_{r,298K,50bar} = -90.7\ \mathrm{kJ/mol} \qquad \text{R1}$$

$$CO_2 + H_2 \rightleftharpoons CO_2 + H_2O \quad \Delta H_{r,298K,50bar} = 49.8\ \mathrm{kJ/mol} \qquad \text{R2}$$

$$CO_2 + 3H_2 \rightleftharpoons CH_3OH + H_2O \quad \Delta H_{r,298K,50bar} = -40.9\ \mathrm{kJ/mol} \qquad \text{R3}$$

With the ZnO-catalysts commonly applied in the combined system, methanol can be formed in a faster reaction from CO_2 and a slower reaction from CO [22,23]. Additionally, CO_2 can be converted into CO and H_2O in the endothermic reverse water-gas shift (RWGS) reaction (Eq. (2)), and with increasing temperature the equilibrium would shift towards CO and water formation. The water produced from this reaction will force the CO_2 hydrogenation reaction (Eq. (3)) closer to

equilibrium, which significantly reduces the thermodynamic driving force for this reaction. Furthermore, more water is formed as the methanol is dehydrated over the solid acid. Therefore, it is essential to minimize the production of water formed by the RWGS reaction to have an efficient bi-functional catalytic CO_2 hydrogenation activity.

The combination of the zeolite H-ZSM-5 together with metal oxides such as $ZnO\text{-}ZrO_2$, Cr_2O_3, $ZnCrO_4$, $ZnAl_2O_4$, In_2O_3 have demonstrated varying results for direct conversion of CO_2 into aromatic products [3,6–11,13,16,17]. Li et al. [8] reported a CO_x conversion of 7.8 % with an aromatic selectivity of 73 %. This was obtained using the combination of $ZnO\text{-}ZrO_2$/H-ZSM-5 mixed in the mass ratio 1:1 and operated at 320 ºC, 40 bar and GHSV of 1200 mL g^{-1} h^{-1}. This surprisingly high selectivity towards aromatics was observed with no apparent deactivation over 100 hr on stream. By contrast, Ticali et al. [11] studied essentially the same catalyst system and reported a CO_x conversion of 4.9 % with an aromatic selectivity of 31 % obtained with a similar mixture of catalysts, however, operated 350 ºC, 30 bar and GHSV of 6695 mL g^{-1} h^{-1}. They observed a slight deactivation with time on stream, which is an inherent feature of methanol conversion in zeolites [24]. Ticali et al. [11] tested the influence of space time and did not find any remarkable difference, so the discrepancies cannot be related to residence time effects. These results show great inconsistency in the reported aromatic selectivity over similar bi-functional catalyst components [8–11]. To properly assess the potential of the direct CO_2 hydrogenation into aromatics it is vital to clarify if the wide variations in achieved selectivity arise from an incomplete understanding of the importance of the various operating parameters or trivial issues such as an incomplete characterization of the products.

Here we have used a $ZnO/t\text{-}ZrO_2$ methanol synthesis component optimized in our previous work [23] and combined it with solid acids such as H-ZSM-5, H-ZSM-11, H-ZSM-12 and TS-1. We have then evaluated the performance of the bi-functional system in the direct conversion of CO_2 into aromatics. We have used catalytic tests, catalyst characterization and kinetic modelling in order to map out the potential of the direct CO_2 conversion to aromatics and the importance of the various operating parameters.

2 Materials and Method

2.1 Catalyst preparation

The ZnO/t-ZrO_2 catalysts were prepared by the incipient wetness impregnation method on t-ZrO_2 support provided by Saint-Gobain NorPro. The support was dried overnight at 120 ºC as the first step. The water uptake for the dried support was determined and a solution with the water uptake volume of $Zn(NO_3)_2 \cdot 6H_2O$ to produce a 18 mol% Zn/(Zr+Zn) catalyst. Hereafter, the support was impregnated, dried overnight at 100 ºC, and calcined in air at 500 ºC for five hours.

NH_4-ZSM-5 and NH_4-ZSM-12 zeolites were obtained from Zeolyst C. V. The TS-1 and the H-ZSM-11 sample was obtained from ACS Material®. All samples were pelletized and calcined for three hours at 550 ºC to ensure the formation of H-cation and to increase the pellet strength.

The bi-functional catalysts were physically mixed as granulates of 300-600 µm with 80 wt% metal oxide catalyst unless otherwise stated.

2.2 Catalyst characterization

XRD analysis was conducted with a PanAlytical X'Pert Pro instrument in Bragg-Brentano Geometry in reflectance mode using a Cu K_α radiation source (λ = 1.541 Å) at ambient conditions. The scan range was 5–70° with a step size of 0.017°. Rietveld analysis was performed using the Topas software.

XRF was measured on a Bruker S2 Puma instrument using a silver anode and an energy dispersive HighSense XP detector. The spot size was limited by an 18 mm mask and the powder samples were loaded as prepared in 20 mm plastic sample cups with 4 µm polypropylene foil. Quantification was done using Bruker's standardless methods in the Spectra Elements software.

For the NH_3-TPD, the samples were first dehydrated by increasing the temperature to 550 °C for 2 h in 60 NmL/min He. Hereafter, the reactor was cooled to 100 °C and 15 NmL/min calibration gas of 500 ppm NH_3 in N_2 was bypassed the reactor for calibration of the MS. After the calibration, the NH_3 gas was redirected to the reactor and adsorption was performed for 1 h at the same flow, ensuring NH_3 saturation by stable MS signal. Excess NH_3 was flushed with 60 NmL/min He for 380 min. To ensure minimal NH_3 adsorption to the piping, the exit pipe to the MS was heat traced to 150 °C. The temperature of the reactor was lowered by 10 °C before the desorption to improve the baseline. The desorption was performed in 60 NmL/min of He with a ramp of 10 °C/min until

800 °C. The MS was tracking single ions, He (m/z = 4) and H_2O (m/z = 18) on the Faraday detector and NH_3 (m/z = 17) on the SEM detector. The ratio between the responses on the MS for m/z = 17 and m/z = 18 when flowing He was used to subtract the water contribution to m/z = 17. Quantification of the ammonia desorption by integration was performed in the Origin software.

2.3 Catalytic activity evaluation

The activity tests were conducted in a high-pressure flow reactor setup using a copper-lined reactor tube with an inner diameter of ¼ inch. For the methanol synthesis tests, typically 750 mg of the catalyst with a grain size of 300-600 µm diluted in 750 mg inert α-Al_2O_3 was loaded into the reactor. For the bi-functional catalysts, typically a total of 2 g was loaded into the reactor. The synthesis gas CO_2/CO/H_2/Ar with a composition of 29/4/64/3 Vol% was introduced into the reactor at various temperatures in the range of 280-400 ºC and pressures of 10-50 barg. The reaction temperature was adjusted by an electric furnace controlled by a K-type thermocouple placed right below the catalyst bed inside the reactor tube. No pre-treatment was given to the catalysts before the catalytic testing. The internal standard, argon, was used to account for the decrease in reaction volume. The effluent gas was analysed by an online GC (Agilent 7890B) equipped with a thermal conductivity detector (TCD) and a flame ionization detector (FID). The GC column connected to the flame ionization detector was RTX-DHA-150 (150m, 0.25 mmID and 1.0µm df). This column allowed for detailed analysis of oxygenates, paraffins, olefins, isoparaffins, naphthalene, and aromatics from $C_{1\text{-}13}$ formed from the reaction. Typically > 60 products were detected. The GC was calibrated with DHA standards from Restek of paraffins ($C_{10\text{-}15}$, 11 components), olefins ($C_{5\text{-}10}$, 25 components), aromatics ($C_{6\text{-}13}$, 35 components) and calibration gas containing $C_{1\text{-}5}$. The chromatograms were analysed using the Dragon DHA software and the obtained molar flow rates of hydrocarbons were corrected based on known CH_4, C_2H_6 and C_3H_8 molar flows from gas calibration (Eq. (6)). The piping towards the GC was heat traced to a minimum temperature of 180 °C.

A combination of Shincarbon ST and MS5A columns using helium or argon carrier gas were connected to the TCD detectors for quantification of CO, CO_2, Ar and H_2. The CO_2 conversion, oxygenate (CH_3OH + CH_3OCH_3) selectivity, and oxygenate formation rate were calculated by Eq. (1) to (4).

$$\dot{F}_{i,out} = \dot{V}_{in} \cdot \frac{y_{Ar,in}}{y_{Ar,out}} \cdot y_{i,out} \cdot V_m^{-1}, where\ i = CO_2, CO, H_2, CH_3OH\ or\ CH_3OCH_3 \quad (1)$$

$$X_{CO_2} = 1 - \frac{\dot{F}_{CO_2,out}}{\dot{F}_{CO_2,in}} \quad (2)$$

$$S_{Oxy} = \frac{\dot{F}_{CH_3OH,out} + 2 \cdot \dot{F}_{CH_3OCH_3,out}}{\dot{F}_{CO_2,in} - \dot{F}_{CO_2,out}} \cdot 100\% \quad (3)$$

$$Rate = \frac{\left(\dot{F}_{CH_3OH,out} + 2 \cdot \dot{F}_{CH_3OCH_3,out}\right) \cdot M_{w,CH_3OH}}{m_c} \quad (4)$$

Where $\dot{V}$ is the volumetric flow rate at standard conditions, V_m is the molar volume, m_c is the weight of the catalyst, and M_w is the molar mass. $\dot{F}_i$ and y_i is the molar flow rate and mole fraction of component i. The hydrocarbon selectivity within hydrocarbons (oxygenates included) was calculated by Eq. (5) to (8).

$$F_{HC,i,D} = (1 - S_{CO}) \cdot X_{CO_2} \cdot \dot{F}_{CO_2,in} \cdot y_{HC,i,D} \quad (5)$$

$$f = \frac{\frac{\dot{F}_{CH_4,D}}{\dot{F}_{CH_4,C}} + \frac{\dot{F}_{C_2H_6,D}}{\dot{F}_{C_2H_6,C}} + \frac{\dot{F}_{CH_4,D}}{\dot{F}_{CH_4,C}}}{3} \quad (6)$$

$$\dot{F}_{HC,i} = \frac{F_{HC,i,D}}{f} \quad (7)$$

$$S_{HC,i} = \frac{n_{c,i} \cdot \dot{F}_{HC,i}}{\sum_{i=1}^{N} n_{c,i} \cdot \dot{F}_{HC,i}} \cdot 100\% \quad (8)$$

Where $y_{HC,i,D}$ and $F_{HC,i,D}$ is the mole fraction and molar flow rate found from the Dragon software analysis of hydrocarbon (HC) i. $\dot{F}_{HC,C}$ is the flow rate found through GC calibrations and f is the average factor between the flow rate obtained from Dragon software and calibrations. $n_{c,i}$ is the number of carbon atoms within the hydrocarbon product.

2.4 Kinetic modelling

The kinetic rate equations are given as Eq. (9) to (10) based on the Langmuir-Hinshelwood mechanism proposed by Ghosh et al. [25] for CO_2 hydrogenation and reverse-water-gas-shift over metal oxides. Eq. (11) defines the dehydration of methanol to hydrocarbons over the zeolite.

$$R1: CO_2 + 3H_2 \rightleftharpoons CH_3OH + H_2O, \qquad r_{R1} = \frac{k_1 \left(f_{CO_2} \cdot f_{H_2} - \frac{f_{CH_3OH} \cdot f_{H_2O}}{K_{eq,1} \cdot f_{H_2}^2} \right)}{\left(1 + K_{CO_2} \cdot f_{CO_2} + \sqrt{K_{H_2} \cdot f_{H_2}}\right)^2} \tag{9}$$

$$R2: CO_2 + H_2 \rightleftharpoons CO + H_2O, \qquad r_{R2} = \frac{k_2 \left(f_{CO_2} \cdot f_{H_2}^{2.5} - \frac{f_{CH_3OH} \cdot f_{H_2O}}{K_{eq,2} \cdot f_{H_2}^{0.5}} \right)}{\left(1 + K_{CO_2} \cdot f_{CO_2} + \sqrt{K_{H_2} \cdot f_{H_2}}\right)^2} \tag{10}$$

$$R3: CH_3OH \rightleftharpoons "CH_2" + H_2O, \qquad r_{R3} = \frac{k_3 \cdot f_{CH_3OH}}{(1 + K_{H_2O} \cdot f_{H_2O})} \tag{11}$$

Where k_i is the reaction rate constants for the reaction R_i, and K_{CO_2}, K_{H_2} and K_{H_2O} are the adsorption constants for CO_2, H_2 and H_2O. f_i is the fugacity of component i and the equilibrium constants $K_{eq,i}$ are calculated based on empirical correlations of experimental equilibrium data for copper based catalysts [26]. The hypothetical molecule "CH_2" represents hydrocarbons broadly. To correct for the non-ideal behaviour of the gas mixtures, fugacity was used instead of partial pressure. A toolbox for calculating the fugacity coefficient for each component in the gas phase was constructed. This toolbox was based on the Soave-Redlich-Kwong equation of state modified by correction factors for polar components introduced by Mathias [27–29].

A reparameterized form of the Arrhenius equation, as stated in Eq. (12) was used to calculate the reaction rate constant.

$$k_i = k_i^* \cdot Exp\left(-\frac{E_{A,i}}{R} \left(\frac{1}{T} - \frac{1}{T^*} \right) \right) \tag{12}$$

Where $E_{A,i}$ and k_i^* are the activation energy and reference rate constant at 300 °C for the three reactions R1 to R3, which were determined through iteration. The adsorption constants for CO_2,

H_2 and H_2O were found to be constant within the relevant temperature interval [25,30]. This resulted in 6 parameters (K_{CO_2}, K_{H_2}, K_{H_2O} $E_{A,1}$, $E_{A,2}$, and $E_{A,3}$) which were fitted to the experimental data listed in Table S1.

The rates of production of methanol and hydrocarbons were calculated by Eq. (13) to (14).

$$R_{CH_3OH} = (r_{R1} + r_{R2}) \cdot RM - r_{R3} \cdot (1 - RM) \tag{13}$$

$$R_{HC} = r_{R3} \cdot (1 - RM) \tag{14}$$

Where RM is the weight ratio of metal oxide assuming uniform and ideal mixing of the two catalyst components in the reactor. The parameter estimation was done using the built in function *lsqnonlin* in MATLAB, which minimizes the sum of square errors of the objective function as stated in Eq. (15).

$$F_{obj} = \sum_{i=1}^{i} \sum_{j=1}^{j} \omega_i \left(Y_{i,j}^{model} - Y_{i,j}^{data}\right)^2 \tag{15}$$

Where ω_i was the weight of each component and set to get numerical equal fitting of each component (CO_2, CO, CH_3OH and "CH_2"). i and j are the number of components and experiments, respectively.

Limited data was obtained for the kinetic model parameter estimation and, therefore, a bootstrap method was performed, where 200 synthetic data pairs were generated within the parameter uncertainty of the initially performed sum of square error (Eq. (15)) [31].

The reactions were assumed to occur in an isothermal fixed bed reactor loaded with a fixed amount of catalyst in each experiment. The reactor model was calculated based on the differential equation describing the change in molar flow rate for component *i* (F_i) through the catalyst bed weight (w) in ideal plug flow, as stated in eqn. (16).

$$\frac{dF_i}{dw} = R_i \tag{16}$$

3 Results and Discussion

3.1 Characterization of employed zeolite samples

For the direct conversion of CO_2 into aromatic products, the metal oxide was combined with zeolite catalysts that convert methanol/DME into hydrocarbons. Prior to the catalytic tests, the structure and acid site distribution of the employed zeolite materials was characterized. In Fig. 4 (a), the XRD patterns confirmed the presence of pure MFI structured zeolite crystals for the ZSM-5 and TS-1 samples. Furthermore, it confirmed that the ZSM-11 and ZSM-12 samples consisted of pure MEL and MTW structures. The MFI and MEL structures are both 3D structures with pore openings of ~5.5 Å, however, the placement of the straight channels in the MEL structure results in the creation of larger cages than observed for the MFI structure. The similarities between the MFI and MEL structures were evident from the XRD patterns in Fig. 4 (a), where the MEL structure can be distinguished from the MFI structure by the reflections between 22.5 and 25 2θ degrees (Fig. 4 (b)) [32]. MTW is a 1D structure with a pore size of ~6 Å, allowing larger molecules to diffuse out of the channels compared to the MFI and MEL structures. Fig. 4 (c) shows the NH_3-TPD results and the Si/Al ratio for the zeolites and the amount of weak and strong acid sites are listed in Table 2.

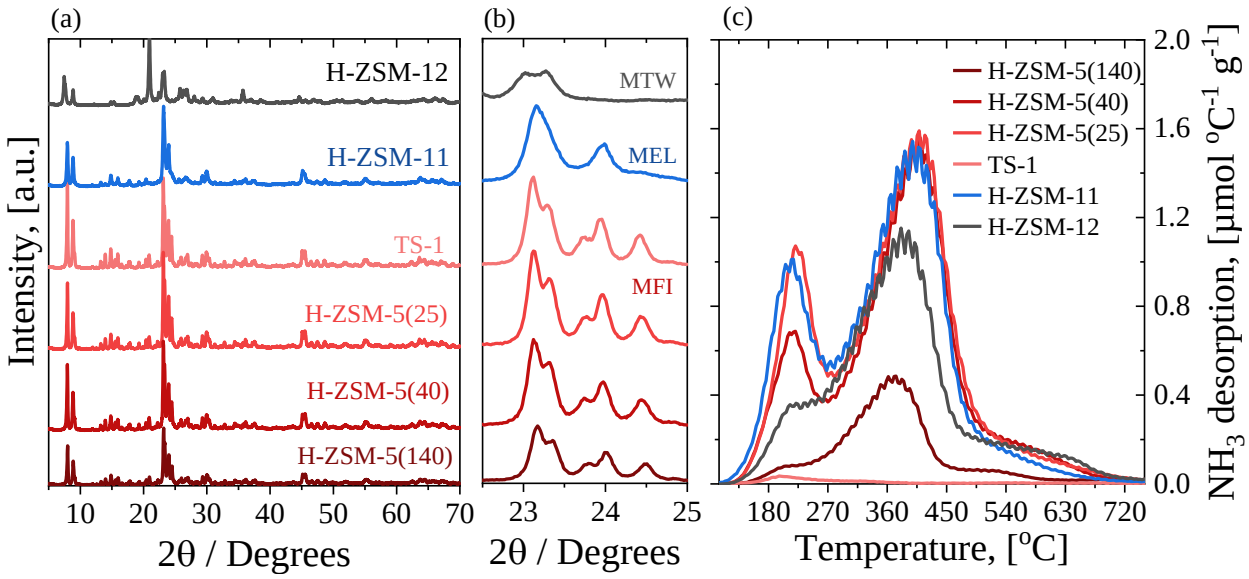


Fig. 4. (a) XRD patterns and (b) NH_3-TPD of the zeolite samples.

Table 2. The Si/Al ratio, weak and strong acid density for the zeolite samples.

Catalysts	Si/Al ratio[a]	Weak acid sites[b], [µmol g^{-1}]	Strong acid sites[b], [µmol g^{-1}]	Total acid sites[b], [µmol g^{-1}]
H-ZSM-5 (25)	22	79 ± 1.3	215 ± 2.0	294
H-ZSM-5 (40)	30	60 ± 2.3	198 ± 2.7	258
H-ZSM-5 (140)	66	5 ± 0.3	56 ± 0.7	61
H-ZSM-11 (25)	22	82 ± 1.6	208 ± 2.1	290
H-ZSM-12	29	30 ± 2.5	147 ± 2	177
TS-1	97/3/1[c]	1.6 ± 0.1	1.6 ± 0.2	3.2

[a]determined by XRF, [b]determined by NH_3-TPD and [c] the Si/Ti/Al ratio.

3.2 Direct CO_2 hydrogenation into aromatics

The methanol activity of the ZnO/t-ZrO_2 catalyst was in previous work found to correlate with the concentration of amorphous ZnO surface domains on the ZrO_2 surface [23]. The concentration of the ZnO surface domains was optimized at the Zn-loading of 18 mol% and therefore used as the methanol synthesis component in this study. Fig. 5 shows the development in conversion and selectivity as a function of the accumulated methanol conversion when a physical mixture of ZnO/t-ZrO_2 and H-ZSM-5(25) is used for CO_2 hydrogenation into hydrocarbons. Changes in the hydrocarbon selectivity and slight deactivation evident in decreasing CO_2 conversion were observed for the bi-functional catalyst with time on stream/accumulated methanol conversion. The fast initial drop in the aromatics selectivity with the amount of methanol converted is believed to be caused by carbon deposits blocking the acid sites responsible for aromatization [10,33]. Partial blockage of the zeolite pores may also inhibit diffusion of the bulky aromatics out of the zeolite and increase the risk of aromatics being cracked and hydrogenated into iso-paraffins in the hydrogen rich atmosphere. The drop in aromatics selectivity was mainly accompanied by an increase in isoparaffins and naphthenes selectivity (Fig. S2). As the reaction proceeded, the selectivity towards light olefins increased, showing that the hydrogenation activity decreased as carbon deposits blocked access to the acid sites. This could suggest that the hydrogenation occurs at the acid sites of the zeolite. A steady drop in the CO_2 conversion occurred with increasing time on stream/accumulated conversion, which shows a steady deactivation of the catalyst system. However, there could be multiple parallel causes of deactivation: sintering of amorphous ZnO into crystalline ZnO, Zn migration into the zeolite, carbon deposits blocking the active sites, and a decrease in zeolite activity

that slows down methanol conversion and causes local equilibrium limitations on the methanol synthesis.

An inherent feature of the methanol dehydration in zeolites is the steady deactivation caused by carbon deposits (coke) blocking the accessibility to the Brønsted acid sites and removing such carbon deposits is done by oxidative treatment [24]. Surprisingly, this deactivation phenomenon is rarely reported in literature for bi-functional catalytic systems [3,6,8,12,13,34–39]. However, the work of Zhang et al. [10] and Ticali et al. [11] reported deactivation of their bi-functional catalytic systems by carbon deposits. The H-ZSM-5 catalysts can typically convert ~90 g_{MeOH} pr. $g_{zeolite}$ before the catalyst is significantly deactivated and a fast drop in the methanol conversion occurs [40,41]. With the high amount of zeolite in the catalyst bed when mixed 1:1 or even 1:2 (metal oxide : zeolite) and with the low CO_2 to hydrocarbon conversion [6,8,10,11], these systems could operate for more than ~400 h before reaching the 90 g_{MeOH} pr. $g_{zeolite}$ limit. As illustrated in Fig. 5, no drop in the methanol conversion was observed, even at 60 g_{MeOH} pr. $g_{zeolite}$. The cracking mechanism of cycloalkanes and hydrogenation activity was altered when applying high partial pressure of hydrogen [42], which could improve the zeolite lifetime and explain the missing deactivation.

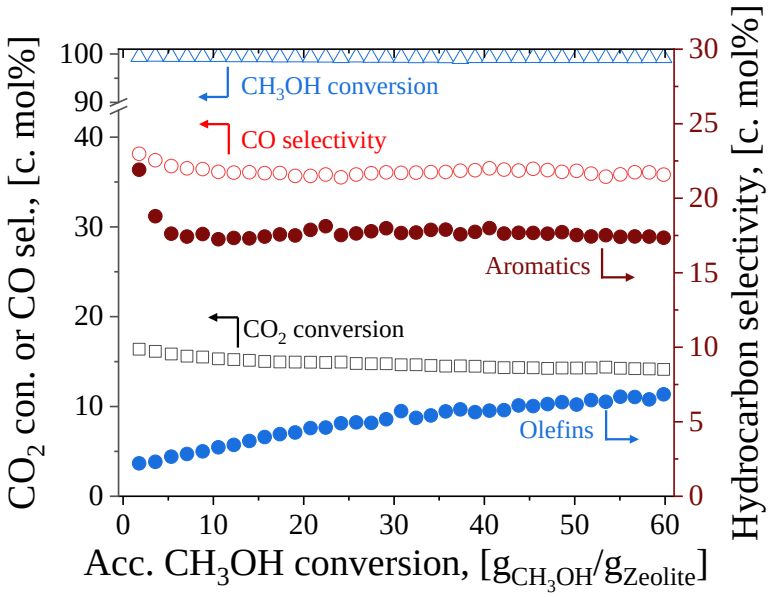


Fig. 5. CO_2 conversion, CO, aromatics and olefins selectivities with the accumulated (Acc.) amount of converted methanol pr. gram of zeolite (operated for 60 hours). Reaction conditions: 30 bar, 340°C, 20 NL h^{-1}, feed composition CO_2/CO/H_2/Ar of 24/4/64/3 vol% and catalyst loading of 4 g with 80 wt% ZnO/t-ZrO_2 and 20 wt% H-ZSM-5 (25).

3.3 The role of bed configuration and reaction conditions

A compromise in the reaction conditions [12,43], bed configuration [3,6], and catalyst mixing [44,45] could optimize the CO_2 conversion and aromatics selectivity by enhancing the synergy between the two catalytic systems. In Fig. 6 the hydrocarbon distribution, CO_2 conversion and CO selectivity are illustrated for different bed configurations, different ratios of the two components and different acid site densities for the H-ZSM-5 zeolite.

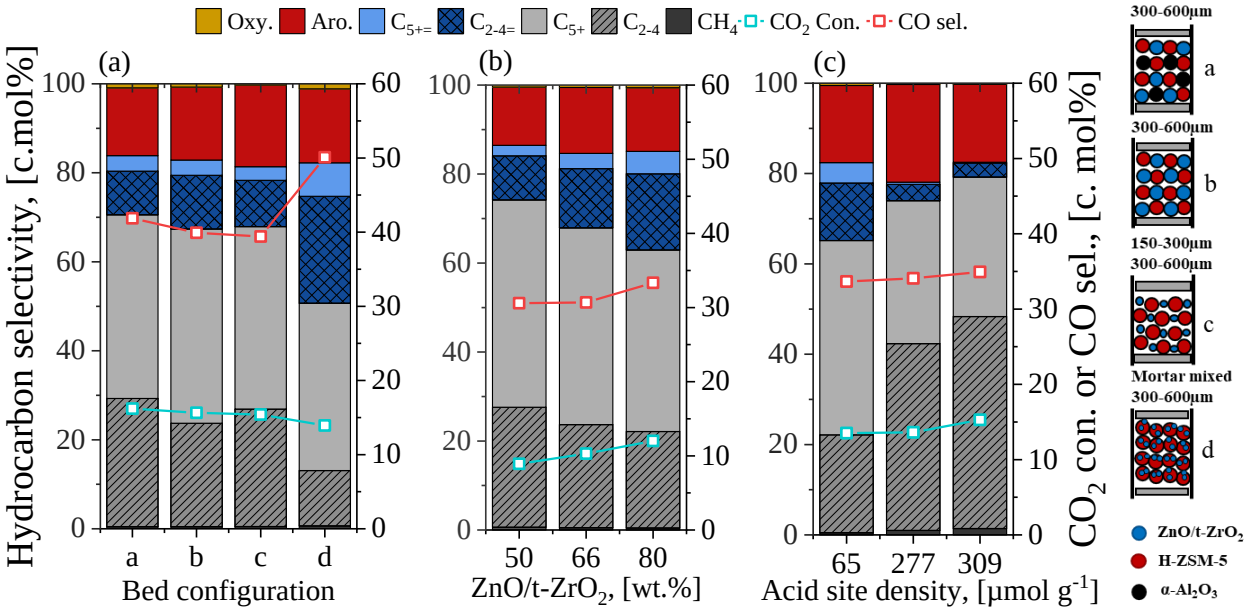


Fig. 6. Hydrocarbon selectivity, CO_2 conversion (CO_2 con.) and CO selectivity (CO sel.) after 10 g_{MeOH} pr. $g_{H\text{-}ZSM\text{-}5}$ over the combined bed of ZnO/t-ZrO_2 and H-ZSM-5: (a) mixed in different bed configurations, (b) mixed in different mass fractions (weight of ZnO/t-ZrO2 / total catalyst weight) and (c) mixed with H-ZSM-5 with different acid site densities determined by NH_3-desorption. The notations Oxy. and Aro. describe the oxygenate (MeOH and DME) and aromatic fraction. The number subscript describes the carbon chain length included in the fraction and for olefinic products it is followed by =. The C_{5+} fractions are without aromatics. The bed configuration a to c consists of a granulate mixtures of ZnO/t-ZrO_2 and H-ZSM-5, where d consists of mortar mixed powders pressed as pellet and sieved to granulate. Reaction conditions: 30 bar, 340°C, 10 NL h^{-1} (a and c) or 20 NL h^{-1} (b), feed composition CO_2/CO/H_2/Ar of 24/4/64/3 vol% and catalyst loading of 2g with 80 wt% ZnO/t-ZrO_2 and 20 wt% H-ZSM-5 (140) with acid site density 65 µmol g^{-1}, unless otherwise stated.

No significant change in the aromatic selectivity (<20 mol% of the carbon in hydrocarbon products) was observed when diluting the mixed catalytic bed in inert α-Al_2O_3 (configuration a), or when decreasing the metal oxide granulate size from 300-600 µm to 150-300 µm (bed configuration c). Mortar mixing oxide and zeolite (bed configuration d) improved the amount of olefins, which potentially could be converted into aromatics by olefin oligomerization and aromatization [40,46]. However, the closer proximity in the CO_2 conversion into hydrocarbons demonstrated a faster decrease in activity with time on stream (Fig S3). This can be explained by removal of CO_2 hydrogenation sites caused by either Zn migration into the zeolite [47,48] or by external coke

(poly-aromatics) molecules blocking/interfering with the active ZnO on the zirconia surface [23]. The increased olefin selectivity at closer proximity (bed configuration d) cannot be explained by zinc migration from the metal oxide to the zeolite, as zinc in zeolites has shown improved hydrogenation activity [47]. It is more likely that the build-up of light olefins was limited by the supply of methanol molecules and that a greater localized concentration of methanol near the zeolite favours this initial C-C bond formation.

Increasing the weight percentage of ZnO/t-ZrO_2 in the catalyst mixture increased the light olefin fraction and slightly increased the aromatics selectivity (Fig. 6 (b)). This again points to the supply of methanol molecules as the limiting factor in the build-up of light olefins. A larger fraction of ZnO/t-ZrO_2 in the catalyst mixture, and hence longer residence time over this oxide, enhanced the CO_2 conversion to hydrocarbons, which increased from 6.2 to 8.0 mol% carbon. The concurrent increase in olefins selectivity with increasing amount of metal oxide showed that olefin hydrogenation over the ZnO/t-ZrO_2 component played a secondary role, and most olefin hydrogenation occurred over the zeolite acid sites [49]. Furthermore, Fig. 6 (c) shows that increasing the acid site density of the zeolite component lowered the olefin selectivity greatly and increased the selectivity towards light paraffins as result of light olefins hydrogenation in agreement with prior observations [50]. This observation substantiates that the hydrogenation of unsaturated products over the oxide+zeolite system mainly occurs at the acid sites of the zeolite.

As illustrated in Fig. 6 (c), increasing the acid site density from 65 to 258 μmol g^{-1} optimized the aromatic selectivity, showing the importance of the acid sites for the aromatization reaction (Fig. 6 (c)) [51,52]. A loss in the aromatic selectivity was observed when the acid site density was further increased to 309 μmol g^{-1}. This can be attributed to the more severe hydrogenation of lighter olefins, which prevents the olefin oligomerization [8,12] to ~C_{5-8} that is needed for the carbenium ion cyclization [53,54]. Thus, a compromise in the acid site density is necessary for optimizing the aromatic selectivity, since acid sites are required for the aromatization but also involved in the hydrogenation of olefins, which interrupts the build-up of aromatics.

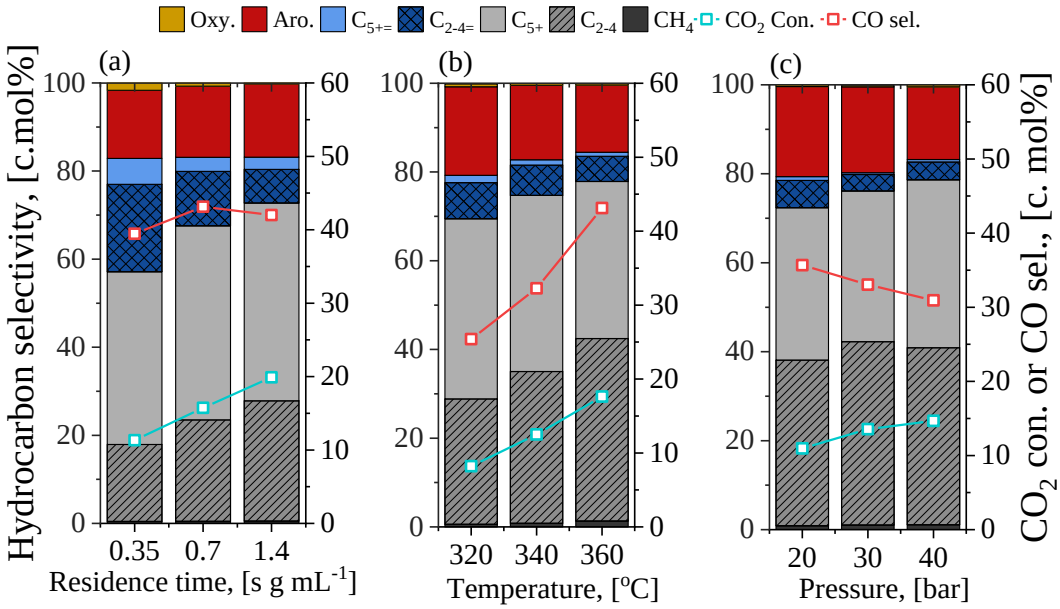


Fig. 7. Hydrocarbon selectivity, CO_2 conversion (CO_2 con.) and CO selectivity (CO sel.) over the combined bed of ZnO/t-ZrO_2 and H-ZSM-5: (a) change in residence time with change in total catalyst loading form 2, 4 and 6 g, (b) reaction temperature and (c) reaction pressure. Reaction conditions, unless otherwise stated: 30 bar, 340°C, 20 NL h^{-1}, feed composition CO_2/CO/H_2/Ar of 24/4/64/3 vol% and catalyst loading of 4g with 80 wt% ZnO/t-ZrO_2 mixed with (a) H-ZSM-5(140) or (b-c) H-ZSM-5(40).

Fig. 7 (a) shows that an increased residence time increases CO_2 conversion without altering the CO selectivity significantly. A 4-fold increase in residence time causes the CO_2 conversion to increase by a factor of only 1.8, which indicates that kinetic or thermodynamic inhibition slows down the reaction as conversion increases. For all residence times, the methanol synthesis reaction was far from equilibrium (Fig S4), but the RWGS reaction approached equilibrium with increasing residence time and reached equilibrium at 1.4 s g mL^{-1}. The water produced from the formation of methanol, methanol dehydration, and RWGS reaction created an increasing water concentration down through the catalyst bed. The progressively increasing water concentration inhibits the methanol formation thermodynamically by accelerating the reverse reaction and could also cause kinetic inhibition. This will be elaborated in Section 3.7. The improved yield of hydrocarbons by increasing the residence time came with the cost of a higher hydrogenation activity, which hydrogenated the light olefins to light paraffins (Fig. 7 (a)). No change in the aromatic selectivity was observed, meaning that the light olefins was hydrogenated rather than oligomerized.

The selectivity towards aromatics was favoured by low temperature (Fig. 7 (b)) and low pressure (Fig. 7 (c) and Fig S5). This can be attributed to increased hydrogenation and cracking activity at higher temperatures and pressures [42]. The main products from the bi-functional catalyst system

were paraffins and isoparaffins (Fig. 7 (c) and Fig S5), confirming that cracking and hydrogenation reactions occurred in parallel to the oligomerization and aromatization reactions. Applying operating conditions that increased the CO_2 conversion to hydrocarbons, such as long residence time, high temperature ≥360 °C (highest temperature investigated), high pressure and high hydrogen partial pressure, increased cracking and hydrogenation activity, reducing the amount of aromatics formed. The highest aromatic selectivity of 33.2 carbon mol% at a CO_2 conversion to hydrocarbons of 4.5 % for the ZnO/t-ZrO_2 + H-ZSM-5(40) catalyst mixture (Fig S6) was obtained at 320 °C, 10 bar, 10 NL/h, 2 g catalyst with 80 wt% ZnO/t-ZrO_2.

3.4 The role of zeolite topology

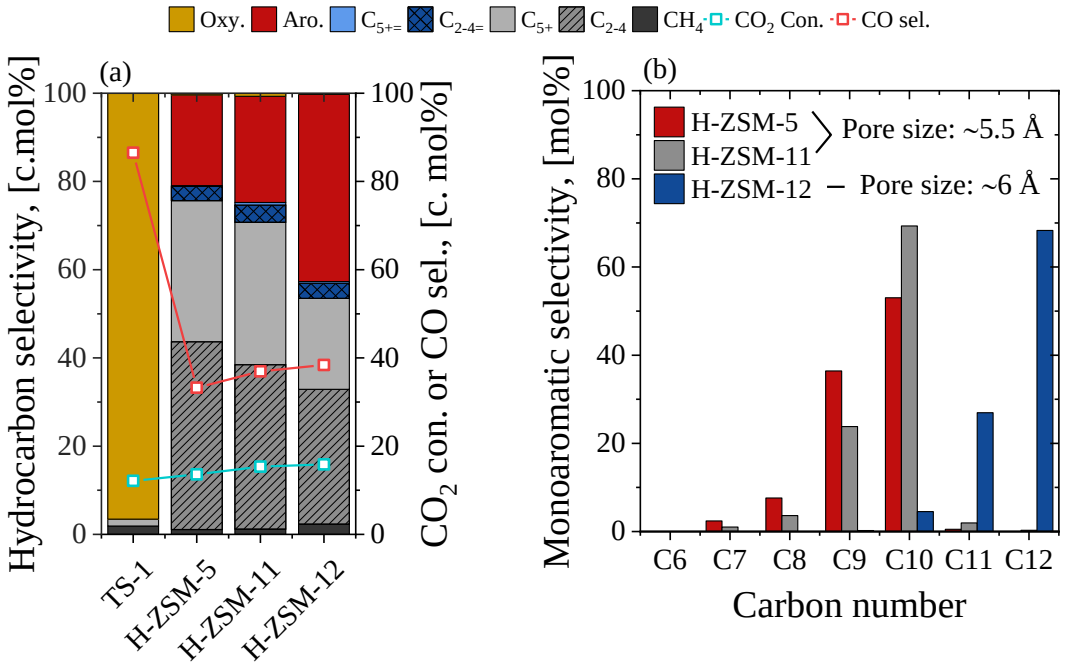


Fig. 8. (a) Hydrocarbon selectivity, CO_2 conversion (CO_2 con.) and CO selectivity (CO sel.) over the combined bed of ZnO/t-ZrO_2 and TS-1, H-ZSM-5, H-ZSM-11 and H-ZSM-5. (b) The carbon number selectivity within monoaromatics. Reaction conditions, unless otherwise stated: 30 bar, 340°C, 20 NL h^{-1}, feed composition CO_2/CO/H_2/Ar of 24/4/64/3 vol% and catalyst loading of 4g with 80 wt% ZnO/t-ZrO_2.

Another strategy for optimizing the yield of aromatics could be to adjust the zeolite topology. Zeolites with bigger intersections (H-ZSM-11) and bigger pores (H-ZSM-12) could potentially enhance the propagation of the aromatic cycle in the dual cycle hydrocarbon pool mechanism by allowing the production of more methylated aromatics. Fig. 8 shows that both H-ZSM-11 and H-ZSM-12 provide a considerably increase in the aromatic selectivity in the form of poly-methylated C_7-C_{12} species. The bigger pore of the H-ZSM-12 allows the formation of hexamethylbenzene,

which was the main product among the aromatics produced (Fig. 8 (b)). Thus, at a CO_2 conversion to hydrocarbons of 9.8 %, an aromatics selectivity of 42.4 carbon mol% was achieved at 340 °C, 30 bar, 10 NL/h, 2 g catalyst with 80 wt% ZnO/t-ZrO_2 and 20 wt% H-ZSM-12. The zeotype TS-1 had no significant activity for hydrocarbon formation (Fig. 8 (a)) which is attributable to the near-absence of acid sites in this material (Table 2). The zeotype does cause some methanol dehydration to DME and shifts the equilibrium compared to the methanol synthesis alone (Fig S1) [8].

3.5 Kinetic analysis of the bi-functional catalytic system

In order to assist the optimization of the yield in the hydrocarbon synthesis a kinetic model was developed. The kinetics of CO_2 hydrogenation over the ZnO/t-ZrO_2 and the combined ZnO/t-ZrO_2 and H-ZSM-5(40) catalysts were studied in an isothermal fixed bed reactor in a wide range of operating conditions (Table S1). The parameters obtained from the fitting procedure described in section 2.4 are listed in Table 3.

Table 3. Fitted kinetic parameters and adsorption constants for the kinetic model.

Parameter	
Ea_1 [kJ/mol]	77.7 ± 1.7
Ea_2 [kJ/mol]	98.1 ± 4.9
Ea_3, [kJ/mol]	38.6 ± 14.3
K_{CO2}, [bar^{-1}]	0.48 ± 0.05
K_H, [bar^{-1}]	4.5 ± 0.3
K_{H2O}, [bar^{-1}]	1.9 ± 0.64

The experimental results were described by fitting the parameters in the rate expressions (eq. (9)-(12)) for methanol synthesis, RWGS and methanol dehydration to hydrocarbons. Parity plots of the measured and modelled mole fractions of reactants and products can be found in Fig. S8. It

was found that the parameters in Table 3 make a reasonable prediction, which is evident in the relative low root mean square errors (Fig. S8).

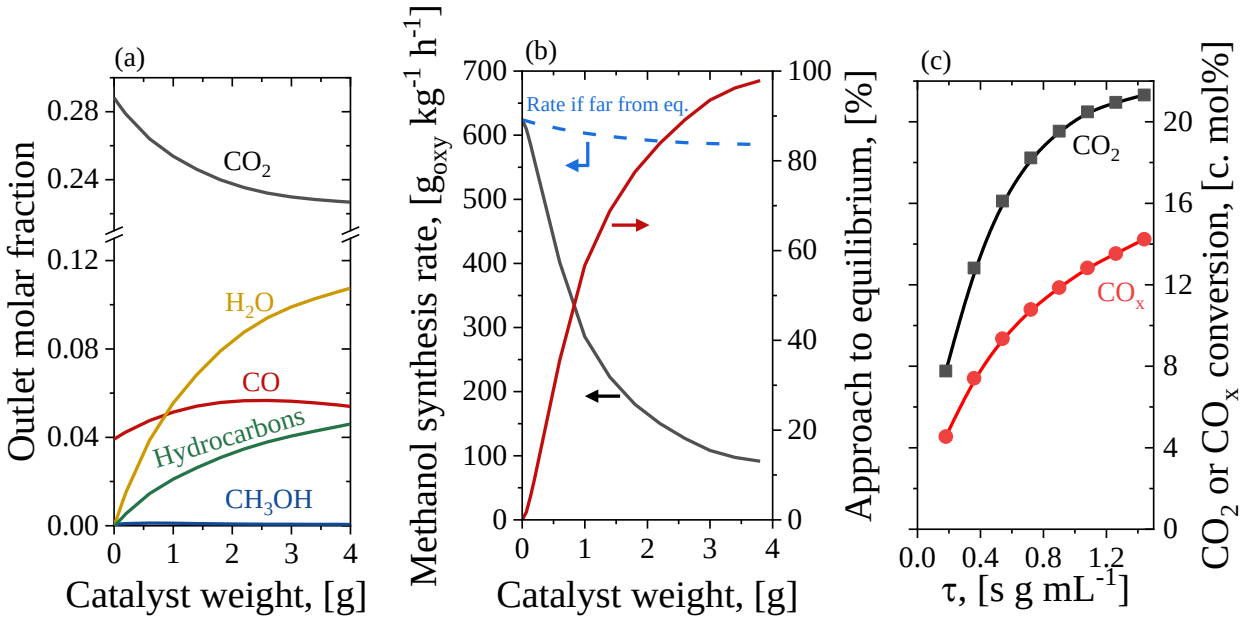


Fig. 9. (a) Simulated concentration profiles, (b) methanol synthesis rate and approach to equilibrium of the CO_2 to methanol reaction through the catalyst bed. (c) The calculated CO_2 and CO_x to hydrocarbons conversion (carbon mol%) at different contact times. Reaction conditions: 30 bar, 340°C, 10 NL h^{-1}, feed composition $CO_2/CO/H_2/Ar$ = 24/4/64/3 vol% and catalyst loading of 4 g with 80 wt% ZnO/t-ZrO_2.

Fig. 9 (a & b) shows the simulated concentration profiles and methanol synthesis rate through the catalyst bed. The results illustrate that the formation of methanol and water is very rapid in the initial part of the bed. The model predicts that the methanol is directly converted to hydrocarbons leaving only a small amount of residual methanol. However, with the increasing partial pressure of water through the reaction zone, the methanol synthesis reaction approaches equilibrium, as illustrated in Fig. 9 (b) [30]. This causes both the methanol synthesis and the overall conversion of CO_2 to hydrocarbons to slow down. This model, which contains only thermodynamic restrictions on the methanol synthesis rate and not kinetic inhibitions is able to describe that a 4-fold increase in residence time only results in a 1.8-fold increase in conversion (Fig. 9 (c)) as seen experimentally (Fig. 7 (a)). This suggests that it is predominantly thermodynamic limitations, which cause the CO_2 conversion to slow down as the water concentration increases. This sensitivity of the methanol synthesis component to the water concentration highlights the importance of having a well-mixed and uniform distribution of the two catalysts and that diffusion limitations should be avoided, otherwise local zones within the reactor could be limited by equilibrium.

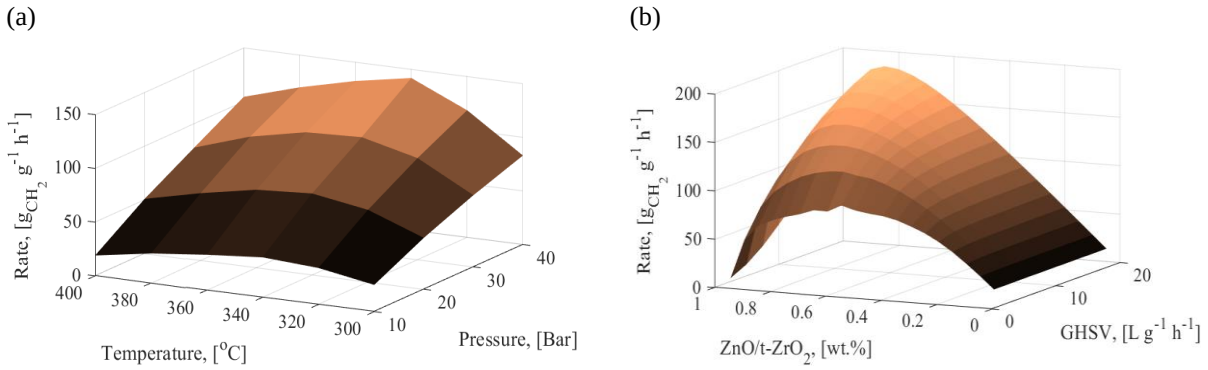


Fig. 10. The hydrocarbon formation rate (a) as a function of temperature and pressure, and (b) as a function of weight percentage of ZnO/t-ZrO$_2$ in the catalyst mixture and GHSV. Reaction conditions, unless otherwise stated: 30 bar, 340°C, 10 NL h^{-1}, feed composition CO$_2$/CO/H$_2$/Ar = 24/4/64/3 vol% and catalyst loading of 2g with 80 wt% ZnO/t-ZrO$_2$.

Fig. 10 (a) shows that the model predicts 340 ºC as the optimal reaction temperature for the hydrocarbon formation rate, which represents a balance between faster kinetics and a less favourable equilibrium at higher temperatures. However, this optimum depends on the oxide/zeolite mixing ratio and on the residence time (Fig S9). Increasing the pressure lowers the equilibrium limitation on the methanol synthesis and, thereby, increased the amount of CO_2 that can be converted into hydrocarbons (Fig. 9). However, the selectivity to aromatics decreases with increasing pressure (Fig. 7 (c)).

The kinetic analysis thus illustrates the inherently conflicting requirements to the hydrogenation of CO_2 into aromatics. To increase reaction rate and conversion it is favourable with high pressure and temperature (Fig. 10). However, the selectivity to aromatics oppositely benefits from low temperature and pressure (Fig. 7). Thus for the bi-functional catalytic system to have a high selectivity to aromatics, the system must operate at low CO_2 conversions, yielding a low concentration of products, that would be expensive to purify, and high costs of handling the high amount of gas that would need to be recycled. However, direct CO_2 conversion into an isoparaffin rich gasoline product is possible at a higher pressure, making the bi-functional catalytic system of potential interest for such applications.

3.6 What is the limit for aromatics selectivity with the bi-functional system

The present work achieved maximal aromatics selectivities of 33.2 carbon mol% with ZSM-5 and 42.4 carbon mol% ZSM-12, and these levels are most likely approaching the level that can be

achieved with these systems. It is generally accepted that the methanol dehydration over zeolites occurs through the hydrocarbon pool dual cycle mechanism, where olefins oligomerize in the olefinic cycle to form hydrocarbons with sizes that allow the carbenium ion cyclization [53,54]. This is followed by hydrogen transfer reactions, which forms paraffins and aromatics. These aromatics can react with methanol and produce methylated aromatic products, which can undergo cracking, forming light olefins, such as ethene and propene, through the paring or/and the side-chain methylation mechanism [40,53,55]. Olefins that do not undergo carbenium ion cyclization can be cracked through β-scission, forming light to medium olefins [56]. By assuming that the carbenium ion cyclization results in the formation of cycloalkanes, three alkenes (mono-enes) are required for the hydrogen transfer reaction to form aromatics. By further assuming that this alkene is ethene and that the aromatic product is tetra-methylated to C_{10} (durene, a common product from methanol dehydration over H-ZSM-5), the maximal aromatics selectivity is 62.5 carbon mol%. However, it is unlikely that ethene participates in the hydrogen transfer reactions, as it has to go through the formation of a very unstable primary carbenium ion and ethene is a product from the aromatic methylation mechanism. With propene or butene as hydrogen acceptors the maximal aromatics selectivity is 52.6 and 45.4 carbon mol% respectively and this is a more likely limit for the aromatics selectivity. It has been proposed that cycloalkane dehydrogenation can occur over metal oxide sites in modified ZSM-5 catalysts to increase the aromatic selectivity in the methanol-to-aromatics process [57,58]. However, thermodynamic equilibrium calculations of cyclohexane dehydrogenation to benzene showed that with the applied reaction temperature, pressure and high hydrogen partial pressure, such reactions are thermodynamically unfavourable (Fig S7), so this possibility can be ruled out. A carbonylation reaction between oxygenates and CO over H-ZSM-5 has showed a potential for creating new pathways for aromatics formation through acetic acid or/and methyl acetate, with the cost of faster deactivation [59,60]. However, despite the presence of 4 vol% of CO in the syngas in this study, this reaction pathway is unlikely to play a major role. The 42.4 carbon mol% aromatics selectivity achieved with ZSM-12 in this study must thus be regarded as very close to the ca. 45-52 carbon mol% level that can be regarded as the upper limit of aromatics selectivity. The present work thus constitutes an accurate mapping of the most important parameters for maximizing the selectivity in the direct conversion of CO_2 into aromatics.

4 Conclusions

Upon combining ZnO/t-ZrO_2 with zeolites, it was observed that the equilibrium limit for the methanol synthesis reaction was surpassed. This observation shows that localized methanol dehydration shifts the reaction towards the formation of hydrocarbons. However, when having a high partial pressure of hydrogen, both cracking and hydrogenation reactions limit the aromatic selectivity, producing mainly light paraffins and isoparaffins. These cracking and hydrogenation reactions are believed to be the primary factors contributing to the extended methanol dehydration lifespan of the H-ZSM-5 catalyst within the bi-functional catalyst mixture, as compared to methanol-to-hydrocarbon processes. The main hydrogenation activity was attributed to the acid sites, as evidenced by the higher acid site density and the longer residence time increased the selectivity towards saturated hydrocarbons for the H-ZSM-5 catalyst (achieved by reducing the weight fraction of the ZnO/t-ZrO_2 or the total mass loaded). Low temperature and pressure were necessary to decrease the hydrogenation activity and an aromatic selectivity of 33.2 carbon mol% was obtained at 320 °C and 10 bar. In contrast, the conversion for CO_2 to hydrocarbons exhibited an increase at higher temperatures and pressures. Substituting the H-ZSM-5 catalyst with zeolites featuring larger intersecting cavities (H-ZSM-11) or pores (H-ZSM-12) amplified the aromatic selectivity by promoting the methylation of aromatic products. Consequently, an aromatic selectivity of 42.4 carbon mol% was attained at a 9.8% CO_2 conversion to hydrocarbons, with hexamethylbenzene emerging as the predominant aromatic product.

The behaviour of the bi-functional catalytic system underwent evaluation through kinetic studies revealing that the water produced from the reverse-water-gas-shift, CO_2 hydrogenation to methanol, and methanol dehydration limited the methanol synthesis activity even at extremely low residual concentration of methanol. Consequently, doubling the residence time did not yield a corresponding twofold increase in CO_2 conversion, showing that the reaction was limited by thermodynamics. This observation elucidated the trends observed in the experimental data. To optimize the aromatics formation rate, it is essential to operate the process far from equilibrium. Such conditions would highly limit the CO_2 conversion to hydrocarbons, rendering the use of the bi-functional catalyst system for aromatics production notably inefficient. However, the system could be optimized for the production of an isoparaffin rich gasoline product.

References

[1] OECD, Global Plastics Outlook: Plastics use by polymer - projections, OECD Environ. Stat. (2022). https://doi.org/10.1787/b9bae4d1-en (accessed September 22, 2022).

[2] J.M. Garcia, M.L. Robertson, The future of plastics recycling, Science (80-.). 358 (2017) 870–872. https://doi.org/10.1126/science.aaq0324.

[3] P. Gao, S. Li, X. Bu, S. Dang, Z. Liu, H. Wang, L. Zhong, M. Qiu, C. Yang, J. Cai, W. Wei, Y. Sun, Direct conversion of CO2 into liquid fuels with high selectivity over a bifunctional catalyst, Nat. Chem. 9 (2017) 1019–1024. https://doi.org/10.1038/nchem.2794.

[4] O. Martin, A.J. Martín, C. Mondelli, S. Mitchell, T.F. Segawa, R. Hauert, C. Drouilly, D. Curulla-Ferré, J. Pérez-Ramírez, Indium oxide as a superior catalyst for methanol synthesis by CO2 hydrogenation, Angew. Chemie - Int. Ed. 55 (2016) 6261–6265. https://doi.org/10.1002/anie.201600943.

[5] N. Li, F. Jiao, X. Pan, Y. Ding, J. Feng, X. Bao, Size Effects of ZnO Nanoparticles in Bifunctional Catalysts for Selective Syngas Conversion, ACS Catal. 9 (2019) 960–966. https://doi.org/10.1021/acscatal.8b04105.

[6] Y. Wang, L. Tan, M. Tan, P. Zhang, Y. Fang, Y. Yoneyama, G. Yang, N. Tsubaki, Rationally Designing Bifunctional Catalysts as an Efficient Strategy to Boost CO2 Hydrogenation Producing Value-Added Aromatics, ACS Catal. 9 (2019) 895–901. https://doi.org/10.1021/acscatal.8b01344.

[7] Y. Wang, W. Gao, S. Kazumi, H. Li, G. Yang, N. Tsubaki, Direct and Oriented Conversion of CO2 into Value-Added Aromatics, Chem. Eur.J. 25 (2019) 5149–5153. https://doi.org/10.1002/chem.201806165.

[8] Z. Li, Y. Qu, J. Wang, H. Liu, M. Li, S. Miao, C. Li, Highly Selective Conversion of Carbon Dioxide to Aromatics over Tandem Catalysts, Joule. 3 (2019) 570–583. https://doi.org/10.1016/j.joule.2018.10.027.

[9] C. Zhou, J. Shi, W. Zhou, K. Cheng, Q. Zhang, J. Kang, Y. Wang, Highly Active ZnO-ZrO2 Aerogels Integrated with H-ZSM-5 for Aromatics Synthesis from Carbon Dioxide, ACS Catal. 10 (2020) 302–310. https://doi.org/10.1021/acscatal.9b04309.

[10] X. Zhang, A. Zhang, X. Jiang, J. Zhu, J. Liu, J. Li, G. Zhang, C. Song, X. Guo, Utilization of CO2 for aromatics production over ZnO/ZrO2-ZSM-5 tandem catalyst, J. CO2 Util. 29 (2019) 140–145. https://doi.org/10.1016/j.jcou.2018.12.002.

[11] P. Ticali, D. Salusso, R. Ahmad, C. Ahoba-Sam, A. Ramirez, G. Shterk, K.A. Lomachenko, E. Borfecchia, S. Morandi, L. Cavallo, J. Gascon, S. Bordiga, U. Olsbye, CO2 hydrogenation to methanol and hydrocarbons over bifunctional Zn-doped ZrO2 /zeolite catalysts, Catal. Sci. Technol. 11 (2021) 1249–1268. https://doi.org/10.1039/d0cy01550d.

[12] K. Cheng, W. Zhou, J. Kang, S. He, S. Shi, Q. Zhang, Y. Pan, W. Wen, Y. Wang, Bifunctional Catalysts for One-Step Conversion of Syngas into Aromatics with Excellent Selectivity and Stability, Chem. 3 (2017) 334–347. https://doi.org/10.1016/j.chempr.2017.05.007.

[13] Y. Ni, Z. Chen, Y. Fu, Y. Liu, W. Zhu, Z. Liu, Selective conversion of CO2 and H2 into aromatics, Nat. Commun. 9 (2018) 1–8. https://doi.org/10.1038/s41467-018-05880-4.

[14] X. Liu, M. Wang, H. Yin, J. Hu, K. Cheng, J. Kang, Q. Zhang, Y. Wang, Tandem Catalysis for Hydrogenation of CO and CO2 to Lower Olefins with Bifunctional Catalysts Composed of Spinel Oxide and SAPO-34, ACS Catal. 10 (2020) 8303–8314. https://doi.org/10.1021/acscatal.0c01579.

[15] X. Liu, M. Wang, C. Zhou, W. Zhou, K. Cheng, J. Kang, Q. Zhang, W. Deng, Y. Wang, Selective transformation of carbon dioxide into lower olefins with a bifunctional catalyst composed of ZnGa2O4 and SAPO-34, Chem. Commun. 54 (2017) 140–143. https://doi.org/10.1039/c7cc08642c.

[16] J. Zhang, M. Zhang, S. Chen, X. Wang, Z. Zhou, Y. Wu, T. Zhang, G. Yang, Y. Han, Y. Tan, Hydrogenation of CO2 into aromatics over a ZnCrOx-zeolite composite catalyst, Chem. Commun. 55 (2019) 973–976.

[17] W. Gao, L. Guo, Y. Cui, G. Yang, Y. He, C. Zeng, Selective Conversion of CO2 into para-Xylene over a ZnCr2O4-ZSM-5 Catalyst, ChemSusChem. 13 (2020) 6541–6545.

[18] D.L.S. Nieskens, J.D. Lunn, A. Malek, Understanding the Enhanced Lifetime of SAPO-34 in a Direct Syngas-to-Hydrocarbons Process, ACS Catal. 9 (2019) 691–700. https://doi.org/10.1021/acscatal.8b03465.

[19] P. Ticali, S. Morandi, G. Shterk, S. Ould-chikh, A. Ramirez, J. Gascon, S. Chung, J. Ruiz-martinez, S. Bordiga, PdZn/ZrO2 + SAPO-34 bifunctional catalyst for CO2 conversion : Further insights by spectroscopic characterization, Appl. Catal. A , Gen. 655 (2023) 1–9.

[20] A. Ramirez, P. Ticali, D. Salusso, T. Cordero-lanzac, S. Ould-chikh, C. Ahoba-sam, A.L. Bugaev, E. Borfecchia, S. Morandi, M. Signorile, S. Bordiga, J. Gascon, U. Olsbye,

Multifunctional Catalyst Combination for the Direct Conversion of CO2 to Propane, JACS Au. 1 (2021) 1719–1732. https://doi.org/10.1021/jacsau.1c00302.

[21] M. Tong, E. Hondo, L. Gapu Chizema, C. Du, Q. Ma, S. Mo, C. Lu, P. Lu, N. Tsubaki, Hydrogenation of CO2to LPG over CuZnZr/MeSAPO-34 catalysts, New J. Chem. 44 (2020) 9328–9336. https://doi.org/10.1039/d0nj00907e.

[22] J. Wang, G. Li, Z. Li, C. Tang, Z. Feng, H. An, H. Liu, T. Liu, C. Li, A highly selective and stable ZnO-ZrO2 solid solution catalyst for CO2 hydrogenation to methanol, Sci. Adv. 3 (2017) 1–11. https://doi.org/10.1126/sciadv.1701290.

[23] M.T. Nikolajsen, J.-C. Grivel, A. Gaur, L.P. Hansen, L. Baumgarten, N.C. Schjødt, U. V Mentzel, J.-D. Grundwaldt, J. Sehested, J.M. Christensen, M. Høj, Surface ZnOx on Zirconia is Highly Active for High Temperature Methanol Synthesis, Submitt. to J. Catal. XX (2023) 1–32.

[24] D.M. Bibby, B.N. Milestone, J.E. Patterson, L.P. Aldridce, Coke Formation in Zeolite ZSM-5, J. Catal. 97 (1986) 493–502.

[25] S. Ghosh, J. Sebastian, L. Olsson, D. Creaser, Experimental and kinetic modeling studies of methanol synthesis from CO2 hydrogenation using In2O3 catalyst, Chem. Eng. J. 416 (2021) 129120. https://doi.org/10.1016/j.cej.2021.129120.

[26] G.H. Graaf, J.G.M. Winkelman, Chemical Equilibria in Methanol Synthesis Including the Water − Gas Shift Reaction : A Critical Reassessment, Ind. Eng. Chem. Res. 55 (2016) 5854–5864. https://doi.org/10.1021/acs.iecr.6b00815.

[27] J.G. Van Bennekom, J.G.M. Winkelman, R.H. Venderbosch, S.D.G.B. Nieland, H.J. Heeres, Modeling and Experimental Studies on Phase and Chemical Equilibria in High-Pressure Methanol Synthesis, Am. Chem. Soc. 51 (2012) 12233–12243.

[28] P.M. Mathias, A Versatile Phase Equilibrium Equation of State, Ind. Eng. Chem. Process Des. Dev. 22 (1983) 385–391.

[29] G. Soave, Equilibrium constants from modified Redlich-Kwong equation of state, Chem. Eng. Sci. 27 (1972) 1197–1203.

[30] T. Cordero-Lanzac, A. Ramirez, M. Cruz-Fernandez, H.J. Zander, F. Joensen, S. Woolass, A. Meiswinkel, P. Styring, J. Gascon, U. Olsbye, A CO2 valorization plant to produce light hydrocarbons: Kinetic model, process design and life cycle assessment, J. CO2 Util. 67 (2023). https://doi.org/10.1016/j.jcou.2022.102337.

[31] B. Efron, Bootstrap Methods: Another Look at the Jackknife, Ann. Stat. 7 (1979) 1–26.

[32] S. Wang, L. Zhang, S. Li, Z. Qin, D. Shi, S. He, K. Yuan, P. Wang, T.S. Zhao, S. Fan, M. Dong, J. Li, W. Fan, J. Wang, Tuning the siting of aluminum in ZSM-11 zeolite and regulating its catalytic performance in the conversion of methanol to olefins, J. Catal. 377 (2019) 81–97. https://doi.org/10.1016/j.jcat.2019.07.028.

[33] S. Müller, Y. Liu, M. Vishnuvarthan, X. Sun, A.C. Van Veen, G.L. Haller, M. Sanchez-Sanchez, J.A. Lercher, Coke formation and deactivation pathways on H-ZSM-5 in the conversion of methanol to olefins, J. Catal. 325 (2015) 48–59. https://doi.org/10.1016/j.jcat.2015.02.013.

[34] P. Gao, S. Dang, S. Li, X. Bu, Z. Liu, M. Qiu, C. Yang, H. Wang, L. Zhong, Y. Han, Q. Liu, W. Wei, Y. Sun, Direct Production of Lower Olefins from CO2 Conversion via Bifunctional Catalysis, ACS Catal. 8 (2018) 571–578. https://doi.org/10.1021/acscatal.7b02649.

[35] Z. Li, J. Wang, Y. Qu, H. Liu, C. Tang, S. Miao, Z. Feng, H. An, C. Li, Highly Selective Conversion of Carbon Dioxide to Lower Olefins, ACS Catal. 7 (2017) 8544–8548. https://doi.org/10.1021/acscatal.7b03251.

[36] K. Cheng, B. Gu, X. Liu, J. Kang, Q. Zhang, Y. Wang, Direct and Highly Selective Conversion of Synthesis Gas into Lower Olefins: Design of a Bifunctional Catalyst Combining Methanol Synthesis and Carbon-Carbon Coupling, Angew. Chemie - Int. Ed. 55 (2016) 4725–4728. https://doi.org/10.1002/anie.201601208.

[37] J. Wang, A. Zhang, X. Jiang, C. Song, X. Guo, Highly selective conversion of CO2 to lower hydrocarbons (C2-C4) over bifunctional catalysts composed of In2O3-ZrO2 and zeolite, J. CO2 Util. 27 (2018) 81–88. https://doi.org/10.1016/j.jcou.2018.07.006.

[38] J. Wei, Q. Ge, R. Yao, Z. Wen, C. Fang, L. Guo, H. Xu, J. Sun, Directly converting CO2 into a gasoline fuel, Nat. Commun. 8 (2017) 1–8. https://doi.org/10.1038/ncomms15174.

[39] F. Jiao, J. Li, X. Pan, J. Xiao, H. Li, H. Ma, M. Wei, Y. Pan, Z. Zhou, M. Li, S. Miao, J. Li, Y. Zhu, D. Xiao, T. He, J. Yang, F. Qi, Q. Fu, X. Bao, Selective conversion of syngas to light olefins, Science (80-.). 351 (2016) 1065–1068. https://doi.org/10.1126/science.aaf1835.

[40] U. Olsbye, S. Svelle, M. Bjørgen, P. Beato, T.V.W. Janssens, F. Joensen, S. Bordiga, K.P. Lillerud, Conversion of methanol to hydrocarbons: How zeolite cavity and pore size

controls product selectivity, Angew. Chemie - Int. Ed. 51 (2012) 5810–5831. https://doi.org/10.1002/anie.201103657.

[41] M. Bjørgen, F. Joensen, M. Spangsberg Holm, U. Olsbye, K.P. Lillerud, S. Svelle, Methanol to gasoline over zeolite H-ZSM-5: Improved catalyst performance by treatment with NaOH, Appl. Catal. A Gen. 345 (2008) 43–50. https://doi.org/10.1016/j.apcata.2008.04.020.

[42] P. Castaño, J.M. Arandes, M. Olazar, J. Bilbao, B. Pawelec, U. Sedrán, Effect of hydrogen on the cracking mechanisms of cycloalkanes over zeolites, Catal. Today. 150 (2010) 363–367. https://doi.org/10.1016/j.cattod.2009.09.013.

[43] J. Yang, X. Pan, F. Jiao, J. Li, X. Bao, Direct conversion of syngas to aromatics, Chem. Commun. 53 (2017) 11146–11149. https://doi.org/10.1039/c7cc04768a.

[44] Y. Zhu, X. Pan, F. Jiao, J. Li, J. Yang, M. Ding, Y. Han, Z. Liu, X. Bao, Role of Manganese Oxide in Syngas Conversion to Light Olefins, ACS Catal. 7 (2017) 2800–2804. https://doi.org/10.1021/acscatal.7b00221.

[45] C. Ekici, C.R. Ho, J.F. DeWilde, L.T. Biegler, P.M. Witt, Optimization Modeling for Advanced Syngas to Olefin Reactive Systems, Ind. Eng. Chem. Res. 62 (2023) 2240–2254. https://doi.org/10.1021/acs.iecr.2c03135.

[46] M. Bjørgen, S. Svelle, F. Joensen, J. Nerlov, S. Kolboe, F. Bonino, L. Palumbo, S. Bordiga, U. Olsbye, Conversion of methanol to hydrocarbons over zeolite H-ZSM-5: On the origin of the olefinic species, J. Catal. 249 (2007) 195–207. https://doi.org/10.1016/j.jcat.2007.04.006.

[47] Y. Ding, F. Jiao, X. Pan, Y. Ji, M. Li, R. Si, Y. Pan, G. Hou, X. Bao, Effects of Proximity-Dependent Metal Migration on Bifunctional Composites Catalyzed Syngas to Olefins, Am. Chem. Soc. 11 (2021) 9729–9737.

[48] J. Grunwaldt, A. Perechodjuk, T.H. Vuong, J. Rabeah, In situ formation of ZnO x species for efficient propane dehydrogenation, Nature. 599 (2021) 234–238.

[49] J.F. Dewilde, C.R. Ho, J. Conner, A. Smith, A. V. Kirilin, A. Malek, P.M. Witt, Kinetics of Direct Olefin Synthesis from Syngas over Mixed Beds of Zn-Zr Oxides and SAPO-34, Ind. Eng. Chem. Res. 60 (2021) 14166–14175. https://doi.org/10.1021/acs.iecr.1c03246.

[50] L. Ren, J. Zhang, B. Wang, H. Xu, J. Jiang, Y. Guan, P. Wu, Syngas to light olefins over ZnAlOx and high-silica CHA prepared by boron-assisted hydrothermal synthesis, Fuel. 307 (2022) 121916–121926.

[51] C.D. Chang, A.J. Silvestri, The conversion of methanol and other O-compounds to hydrocarbons over zeolite catalysts, J. Catal. 47 (1977) 249–259. https://doi.org/10.1016/0021-9517(79)90103-9.

[52] C.D. Chang, C.T.W. Chu, R.F. Socha, Methanol conversion to olefins over ZSM-5. I. Effect of temperature and zeolite SiO2 Al2O3, J. Catal. 86 (1984) 289–296. https://doi.org/10.1016/0021-9517(84)90374-9.

[53] S. Ilias, A. Bhan, Mechanism of the Catalytic Conversion of Methanol to Hydrocarbons, ACS Catal. 3 (2013) 18–31.

[54] Y. V Joshi, K.T. Thomson, Brønsted Acid Catalyzed Cyclization of C7 and C8 Dienes in HZSM-5 : A Hybrid QM / MM Study and Comparison with C6 Diene Cyclization, (2008) 12825–12833.

[55] A. Sassi, M.A. Wildman, H.J. Ahn, P. Prasad, J.B. Nicholas, J.F. Haw, Methylbenzene Chemistry on Zeolite HBeta : Multiple Insights into Methanol-to-Olefin Catalysis, J. Phys. Chem. B. 106 (2002) 2294–2303.

[56] J.S. Buchanan, J.G. Santiesteban, W.O. Haag, Mechanistic Considerations in Acid-Catalyzed Cracking of Olefins, J. Catal. 158 (1996) 279–287.

[57] I. Pinilla-Herrero, E. Borfecchia, J. Holzinger, U. V. Mentzel, F. Joensen, K.A. Lomachenko, S. Bordiga, C. Lamberti, G. Berlier, U. Olsbye, S. Svelle, J. Skibsted, P. Beato, High Zn/Al ratios enhance dehydrogenation vs hydrogen transfer reactions of Zn-ZSM-5 catalytic systems in methanol conversion to aromatics, J. Catal. 362 (2018) 146–163. https://doi.org/10.1016/j.jcat.2018.03.032.

[58] P. Gao, Q. Wang, J. Xu, G. Qi, C. Wang, X. Zhou, X. Zhao, N. Feng, X. Liu, F. Deng, Brønsted/Lewis Acid Synergy in Methanol-to-Aromatics Conversion on Ga-Modified ZSM-5 Zeolites, As Studied by Solid-State NMR Spectroscopy, ACS Catal. 8 (2018) 69–74. https://doi.org/10.1021/acscatal.7b03211.

[59] D.B. Rasmussen, J.M. Christensen, B. Temel, F. Studt, P.G. Moses, J. Rossmeisl, A. Riisager, A.D. Jensen, Ketene as a Reaction Intermediate in the Carbonylation of Dimethyl Ether to Methyl Acetate over Mordenite, Angew. Chemie - Int. Ed. 54 (2015) 7261–7264. https://doi.org/10.1002/anie.201410974.

[60] Z. Chen, Y. Ni, Y. Zhi, F. Wen, Z. Zhou, Y. Wei, W. Zhu, Z. Liu, Coupling of Methanol and Carbon Monoxide over H-ZSM-5 to Form Aromatics, Angew. Chemie - Int. Ed. 57

(2018) 12549–12553. https://doi.org/10.1002/anie.201807814.

5 ZnO supported on Zinc Spinel Structures Enables the Direct Conversion of CO_2 to Olefins when Combined with Acidic CHA Catalysts

On the next page, the manuscript with the title: *ZnO supported on Zinc Spinel Structures Enables the Direct Conversion of CO_2 to Olefins when Combined with Acidic CHA Catalysts* are reprinted.

This manuscript is still under preparation.

The scientist highlights:

- Zinc aluminate and zinc gallate with over stoichiometric Zn-loading are active for methanol synthesis and enables the production of light olefins from CO_2 when combined with SAPO-34.
- XRD and XAS identified that the methanol activity correlated with the amount of surface ZnO supported on the spinel surfaces and was concluded to be the main active site.
- In-situ XAS analysis showed that the surface ZnO was unstable and sintered into larger crystalline ZnO with the change from reducing to oxidising atmospheres.
- In-situ DRIFT analysis showed that formation of methanol proceeds through the formate pathway and that methanol functions as an intermediate for the production of olefins.
- Co-feeding CO to the CO_2/H_2 feed improved the CO_2 to hydrocarbon conversion without altering the product selectivity and thus demonstrate a strategy to improve the activity and selectivity limitation for bi-functional catalysts.

ZnO supported on Zinc Spinel Structures Enables the Direct Conversion of CO_2 to Olefins when Combined with Acidic CHA Catalysts

M. T. Nikolajsen[1], K. Jordahn[1], L. D. Nilsson[1], N. C. Schjødt[2], U. V. Mentzel[2], J. Sehested[2], R. Y. Brogaard[2], J. M. Christensen[1] and M. Høj[1*]

[1] Department of Chemical Engineering, Technical University of Denmark (DTU), Kgs. Lyngby, 2800 (Denmark).

[2] Topsoe A/S, Kgs. Lyngby, 2800 (Denmark).

[*]Corresponding author: mh@kt.dtu.dk

Abstract

Bi-functional oxide-zeotype catalytic systems have shown promise for the selective production of light olefins from CO_2, but at low CO_2 to hydrocarbon conversion. Knowledge of the active sites for methanol synthesis over the oxide and the synergy with the zeotype at different operating conditions can guide future improvement of such systems. We here show that the methanol synthesis activity for zinc aluminate and gallate ($ZnAl_2O_4$ and $ZnGa_2O_4$) was dependent on the Zn-loading, and optimized activity was obtained at loadings above stoichiometric, Zn/(Zn + M) >0.33. This allowed for the creation of a surface supported ZnO phase, which was selective for the production of methanol and DME. The concentration of these sites controlled the CO_2 conversion. However, too high Zn-loading removed these sites, with the creation of crystalline ZnO, which had lower activity. In-situ XAS showed that the surface ZnO sintered to form crystalline ZnO when exposed to changing reductive and oxidative atmospheres, resulting in decreased methanol synthesis activity. Furthermore, in-situ DRIFTS analysis showed that the production of methanol proceeded through a formate pathway, where CO_2 adsorbed as carbonate that hydrogenated into formate and further into methoxy, which desorbed as methanol. Combining the Zn-spinel catalysts with H-SAPO-34 showed a light olefin selectivity > 70 carbon mol% but at a low CO_2 to hydrocarbon conversion of ~3 %. Increasing the pressure increased the CO_2 to hydrocarbon conversion, but this also increased hydrogenation activity and reduced the olefin selectivity. A powerful strategy to improve the CO_2 to hydrocarbon conversion without affecting the olefin selectivity was to co-feed CO. Co-feeding CO hampered the reverse-water-gas-shift reaction rate by limiting the thermodynamic driving force. This reduced the production of water in the reactor, which improved the thermodynamic driving force of the CO_2 to methanol reaction. Lastly, the lifetime of the $ZnAl_2O_4$ and H-SAPO-34 outperformed the methanol-to-olefin process, but solid-state titration of Zn onto the

solid acid and metal oxide sintering did reduce the CO_2 conversion and light olefin selectivity with time on stream.

1 Introduction

Light olefins, particularly ethylene and propylene, are important chemicals used in the annual production of around 200 million tons of plastic materials. Demands for plastic materials are forecasted to increase by ~20 % by 2030 [1]. Ethylene and propylene are mainly produced from steam cracking of natural gas or naphtha and fluid catalytic cracking of heavier crude oil fractions. The production of plastic materials generates ~1.6 billion tons of CO_2 equivalent, which accounts for around 3 % of the global greenhouse gas emissions [1]. Thus, finding alternative ways of producing these chemicals is essential to reduce their impact. Combining captured or biomass generated CO_2 with H_2 produced from water electrolysis for the production of light olefins could be an attractive pathway and has received increasing interest in literature [2–5]. Two CO_2 utilization technologies have shown some promising performance: The combination of reverse-water-gas-shift with Fischer-Tropsch synthesis or the combination of methanol synthesis with the methanol-to-hydrocarbons reaction. Recent research has demonstrated that an iron based Fischer-Tropsch catalyst promoted with alkaline metal enhanced the light olefin selectivity [6–9], but the polymerization reaction followed the Anderson-Schulz-Flory distribution limiting the C_{2-4} selectivity to ~60 % [10]. However, the combined methanol synthesis and methanol-to-hydrocarbon process showed up to ≥80 selectivity towards light olefins [2,3,11].

When mixing a methanol synthesis catalyst with solid acids within one reactor, the immediate dehydration of the methanol enables the direct conversion of CO_2 into hydrocarbons [11]. The local methanol removal ensures that the methanol equilibrium conversion can be exceeded thereby creating a more efficient production of hydrocarbons. The local methanol removal can be achieved by using compromised reactor conditions, compared to the high pressure and high temperatures necessary for the methanol synthesis and methanol-to-hydrocarbon reactions, respectively [12]. High CO_2 conversion, low CO selectivity and low olefin hydrogenation activity are essential for the efficient production of light olefins. Oxide catalysts without metallic sites, such as Cu or Pd [13–16], and CHA structured solid acids with low acid site density and strength and low H_2 partial pressure are required [17,18] to ensure minimal olefin hydrogenation. For this application, a Zn-based metal oxide catalyst combined with H-SAPO-34 has shown promising results for the direct

conversion of CO_2 to olefins [3,4,19]. Lui et al. [19] reported a light olefin selectivity of 86 %, obtained by combining $ZnGa_2O_4$ and H-SAPO-34. This high olefin selectivity was obtained at a CO_2 to hydrocarbon conversion of ~6 % at 370 ºC and 30 bar. A similar high olefin selectivity of 87 % was found for the combination of $ZnAl_2O_4$ and H-SAPO-34 [4]. However, the high olefin selectivity was achieved at low CO_2 to hydrocarbon conversion of ~6 % at 370 ºC and 30 bar. These results demonstrated that the Zn-spinel structure had low olefin hydrogenation activity, but its methanol synthesis activity should be optimized. It has been suggested that the methanol synthesis activity depends on the concentration of surface available oxygen vacancies, which are constructed when Zn is incorporated into the structure [4,19,20]. However, the methanol synthesis activity over Zn chromate has shown to be dependent on small ZnO sites constructed on the surface when a non-stoichiometric Zn loading was used [21–23]. The formation of surface ZnO has shown a great impact on the methanol synthesis activity for the $ZnAl_2O_4$ [24].

This study provides fundamental information about the active sites for the methanol synthesis reaction over $ZnAl_2O_4$ and $ZnGa_2O_4$ Zn-spinel catalysts. Particularly the relative importance of Zn bound in the spinel structure and the surface ZnO. To achieve this, a series of $ZnAl_2O_4$ and $ZnGa_2O_4$ with varying Zn-loadings were prepared by co-precipitation. Furthermore, the Zn-spinel catalysts were combined with H-SAPO-34 for the direct conversion of CO_2 into light olefins to optimize reaction conditions to improve both CO_2 conversion and light olefin selectivity. The Zn-spinel catalysts were characterized by X-ray diffraction (XRD), inductively coupled plasma optical emission spectroscopy (ICP-OES), X-ray absorption spectroscopy (XAS), and N_2 adsorption/desorption (BET). Furthermore, the reaction species involved in the CO_2 hydrogenation reaction on the surface of the catalyst were analyzed by in-situ diffuse reflectance infrared Fourier transform spectroscopy (DRIFTS). The changes in the structure of the supported ZnO were investigated by in-situ XAS under reducing and oxidizing conditions. The solid acids were characterized by XRD, X-ray fluorescence (XRF), and NH_3-temperature programmed desorption.

2 Materials and Method

2.1 Catalyst preparation

A series of $ZnAl_2O_4$ and $ZnGa_2O_4$ catalysts with different Zn loading between ~20 to ~50 mol% were prepared by the co-precipitation method proposed by Liu et al. [19]. As an example, 500 mL solution of 28.3 g $Zn(NO_3)_2{\cdot}6H_2O$ and 55.8 g of the $Al(NO_3)_3{\cdot}9H_2O$ was added to a beaker for the

$ZnAl_2O_4$ with a Zn loading of 39 mol%. The prepared solution was heated to 70 ºC and ammonium hydroxide was added dropwise under vigorous stirring to reach pH 7. The mixture was aged for 120 min at 70 ºC, filtered, and washed with demineralized water. The collected solid was dried at 100 ºC overnight and calcined in air at 500 ºC for five hours.

The NH_4-SAPO-34 sample was obtained from ACS Material®. Zn-SAPO-34 was prepared by incipient wetness impregnation with a $Zn(NO_3)_2 \cdot 6H_2O$ solution to prepare ~1 wt% Zn onto the NH_4-SAPO-34. Afterwards, the impregnated sample was dried overnight at 100 ºC. The zeotypes were calcined at 550 ºC for 3 hours to convert the ammonium-cation to a proton.

The bifunctional catalysts were physically mixed as granulates of 150-300µm with 80 wt% metal oxide to 20 wt% H-SAPO-34.

2.2 Catalyst characterization

XRD analysis was conducted with a PanAlytical X′Pert Pro instrument in Bragg-Brentano Geometry in reflectance mode using a Cu K_α radiation source (λ = 1.541 Å) at ambient conditions. The scan range was 5–70° with a step size of 0.017°. The Rietveld analysis was performed using the Topas software. ICP-OES analysis was conducted on an Agilent 700 Series instrument using argon as plasmogene to analyze the elemental composition. The specific surface area of the metal oxide was analyzed with the 3P instrument Sync440 and the N_2 adsorption isotherm was analyzed by the Brunauer-Emmett-Teller method. Details of the NH_3-TPD procedure can be found in previous work [25].

XRF was measured on a Bruker S2 Puma instrument using a silver anode and an energy dispersive HighSense XP detector. The spot size was limited by an 18 mm mask and the powder samples were loaded as prepared in 20 mm plastic sample cups with 4 µm polypropylene foil. Quantification was done using Bruker's standardless methods in the Spectra Elements software.

Ex-situ X-ray absorption spectroscopy (XAS) of the Zn K absorption edge was recorded in transmission mode at the MAX IV synchrotron at the Balder beamline. For the $ZnAl_2O_4$ and $ZnGa_2O_4$, boron nitride diluted catalyst pellets were pressed as self-sustaining wafers and scanned. These catalyst pellets were prepared with 20 and 30 mg of $ZnAl_2O_4$ or $ZnGa_2O_4$, respectively, together with 125 mg of boron nitride. The ZnO reference was prepared with 10 mg of ZnO and 125 mg of boron nitride. After averaging 4 to 8 scans, EXAFS fitting was possible up to k = 13 to 14 $Å^{-1}$ and

R = 1 to 4.5 Å. Basic XAS data treatment of normalizing, background subtraction, and Fourier transforming was done using Athena [26]. Linear combination fitting was conducted using a (0.14)ZnO/t-ZrO_2 sample with no ZnO visible from XRD and no Zn-Zn backscattering in FT-EXAFS [27], bulk ZnO, and low Zn loading of the spinel structures (no ZnO was visible from XRD) as references for surface ZnO sites, crystalline ZnO and Zn bound in the spinel structure, respectively. This provided insights into the amount of zinc present in these phases.

In-situ XAS experiments were conducted at the Swiss Light Source synchrotron at the SuperXAS beamline. Quartz capillaries (length of 80 mm, outer diameter 0.8 mm with 0.01 mm wall thickness) were loaded with 100-200 µm $ZnAl_2O_4$ or $ZnGa_2O_4$ particles diluted 1:8 in inert α-Al_2O_3. To ensure a pressure tolerance of 20 bar, the loaded capillaries were glued using Araldite Rapid Epoxy to a sample holder and cured for several hours. Hereafter, the sample holder was connected to the flow setup, where H_2, 10% CO/He, CO_2, 10% O_2/He and He gasses were connected. The capillaries were heated by radiative heaters, proprietary to the SuperXAS beamline, and the off gases were analyzed by a mass spectrometer. The experimental procedure included dehydration of the catalysts in O_2/He with a heating ramp of 10 °C /min to 400 °C at 2 or 15 bar, followed by cooling to room temperature. Hereafter, the gas was switched to a syngas mixture ($CO/CO_2/H_2$/He = 5/12/37/46, filtered through an active carbon filter to remove nickel carbonyls) or H_2. When a stable MS signal was achieved, the reactor was heated to 400 °C at 10 °C /min and kept at 400 °C for 2 hours. After this, periodic switching between syngas or H_2 and O_2/He was conducted in the time interval of 10 min for a total of 180 min, followed by cooling to room temperature. Time resolved spectra were continuously recorded in fluorescence mode in the middle of the catalytic bed through all the above-mentioned steps. The spectra were recorded in QEXAFS mode at 1 Hz oscillation of the monochromator. Data importing, energy calibration, rebinning, averaging, and exporting were done using the ProQEXAFS software proprietary to the beamline. Further details can be found in [27].

The reaction mechanism of the methanol synthesis over (0.39)$ZnAl_2O_4$ and (0.37)$ZnGa_2O_4$ was investigated by CO_2 adsorption and He temperature-programmed-desorption with the use of in-situ diffuse reflectance infrared Fourier transform spectroscopy (DRIFTS). A Harrick High Pressure Praying Mantis cell equipped with pure ZnSe windows was placed in a Vertex 70 infrared spectrometer with a liquid nitrogen cooled LN-MCT VP detector. The catalysts were diluted in

CaF_2 to achieve a 10 wt% mixture to improve the signal and scanned with a resolution of 4 cm^{-1} from 650 to 4000 cm^{-1}. Every measurement was achieved by averaging 200 scans. The sample was pretreated under He flow at 400 °C and 20 bar for 2 hours and then cooled to the reaction temperature, where a background spectrum was acquired. For the CO_2 adsorption experiment, the gas was switched to CO_2/He where the development of peaks was continuously monitored for 60 min. Hereafter, the gas was switched to H_2/He, and the change and disappearance of surface species were continuously monitored for 60 min. The He and H_2 TPD/TPR experiments were conducted after steady-state methanol synthesis at 320 ºC and 20 bar (260 ºC for the H_2-TPR). For the He-TPD, the reactor was cooled to room temperature and the pressure was relieved to atmospheric pressure. Only the temperature was lowered for the H_2-TPR. When a stable MS signal was achieved, the temperature was increased to 460 °C by ~6 °C/min, where the disappearance and development of peaks were continuously monitored.

2.3 Catalytic activity evaluation

The measurements of the methanol synthesis activity were conducted in a high-pressure flow reactor setup using a copper-lined reactor tube with an inner diameter of ¼ inch. Typically, 750 mg of the catalyst with a grain size of 300-600 µm diluted in 750 mg inert α-Al_2O_3 was loaded into the reactor. Synthesis gas CO_2/CO/H_2/Ar with the composition 29/4/64/3 vol% was introduced into the reactor at various temperatures in the range of 280-400 ºC and 50 barg. The reaction temperature was adjusted by an electric furnace controlled by a K-type thermocouple placed right below the catalyst bed inside the reactor tube. The effluent gas was analyzed by an online GC (Agilent 7890B) equipped with a thermal conductivity detector (TCD) and a flame ionization detector (FID). The GC column connected to the flame ionization detector was RTX-DHA-150 (150m, 0.25 mmID, and 1.0µm df). A combination of Shincarbon ST and MS5A columns using helium or argon carrier gas were connected to the TCD detectors for quantification of CO, CO_2, Ar, and H_2.

A similar reactor setup was used for the bi-functional catalyst activity measurements. These were conducted in a quartz-lined reactor tube with an inner diameter of 4 mm. Typically, 500 mg of total catalyst, 400 mg metal oxide, and 100 mg zeotype with both components sieved to a grain size of 150-300 µm, was loaded into the reactor tube. The activity measurements were conducted using a synthesis gas CO_2/H_2/Ar with the composition 23/69/8 vol% at 10 barg and 400 ºC. The

reaction temperature was controlled by a N-type thermocouple placed right above the catalyst bed inside the reactor tube and an electric furnace with three heating zones. No pre-treatment was performed on the catalysts before the catalytic testing. The internal standard, argon, was used to account for the decrease in reaction volume. The carbon balance closed at an average of 99.7 % ± 0.5 % for all the experiments. The effluent gas was analyzed by an online GC (ThermoFisher Trace 1300, assembled by Global Analyzer Solutions) equipped with a thermal conductivity detector (TCD) and a flame ionization detector (FID). The GC column connected to the flame ionization detector was Rt-Q-bond (30m, 0.32 mmID, and 10µm df), which separated the formed hydrocarbon products from C_1 to C_6. A combination of Hayesep N, XL Sulfur, and Molsieve 5A columns were connected to the TCD detectors for quantification of CO, CO_2, and Ar. The CO_2 conversion, oxygenate (CH_3OH + CH_3OCH_3) selectivity, and oxygenate formation rate were calculated by Eq. (1) to (4).

$$\dot{F}_{i,out} = \dot{V}_{in} \cdot \frac{y_{Ar,in}}{y_{Ar,out}} \cdot y_{i,out} \cdot V_m^{-1} \tag{1}$$

$$X_{CO_2} = 1 - \frac{\dot{F}_{CO_2,out}}{\dot{F}_{CO_2,in}} \tag{2}$$

$$S_{Oxy} = \frac{\dot{F}_{CH_3OH,out} + 2 \cdot \dot{F}_{CH_3OCH_3,out}}{\dot{F}_{CO_2,in} - \dot{F}_{CO_2,out}} \cdot 100\% \tag{3}$$

$$Rate_{oxy} = \frac{\left(\dot{F}_{CH_3OH,out} + 2 \cdot \dot{F}_{CH_3OCH_3,out}\right) \cdot M_{w,CH_3OH}}{m_c} \tag{4}$$

Where $\dot{V}$ is the volumetric flow rate at standard conditions, V_m is the molar volume, m_c is the weight of the catalyst, and M_w is the molar mass. $\dot{F}_i$ and y_i are the molar flow rate and molar fraction of component i. The hydrocarbon selectivity within hydrocarbons (oxygenates included) was calculated by Eq. (5) to (6).

$$S_{HC,i} = \frac{n_{c,i} \cdot \dot{F}_{HC,i}}{\sum_{i=1}^{N} n_{c,i} \cdot \dot{F}_{HC,i}} \cdot 100\% \tag{5}$$

$$Rate_{C_{2-4=}} = \frac{\left(\dot{F}_{C_2H_6,out} + \dot{F}_{C_3H_8,out} + \dot{F}_{C_4H_{10},out}\right) \cdot M_{w,CH_2}}{m_c} \quad (6)$$

Where $n_{c,i}$ is the number of carbon atoms within the hydrocarbon product. The hydrogen index was calculated by Eq. (7).

$$Hydrogen\ index = \frac{\sum_{i=1}^{N} n_{H,i} \cdot \dot{F}_{HC,i}}{\dot{F}_{CO_2,in} \cdot X_{CO_2} \cdot (1 - S_{CO}) \cdot 2} \quad (7)$$

Where $n_{h,i}$ is the number of hydrogen atoms within the hydrocarbon product. The conversion to CH_2 was calculated by the CO_2 conversion to hydrocarbons multiplied by 2. This demonstrates the amount of hydrogen coming from the hydrocarbon pool species generated from methanol dehydration. If no gaseous hydrogen was incorporated into the product, the hydrogen index should be 1, and net hydrogenation or dehydrogenation resulted in a hydrogen index >1 or <1, respectively.

3 Results and Discussion

3.1 The methanol synthesis activity of the supported ZnO

Prior research conducted by our group has demonstrated that the primary active sites within the ZnO-ZrO_2 catalyst are supported surface ZnO species, rather than Zn integrated as a solid solution within the tetragonal ZrO_2 lattice or crystalline ZnO [27]. In order to enhance the methanol synthesis activity and discern the active sites associated with Zn-spinel structures, a series of catalysts with different Zn loadings were prepared and tested in a fixed bed reactor. The methanol synthesis rate depended on the Zn-loading of the Zn-spinel structures, as demonstrated in Fig. 1 (a). Exceeding the spinel stoichiometric Zn-loading of 33 mol% ($ZnMe_2O_4$) improved the methanol synthesis rate significantly. This improvement was due to the increase in CO_2 conversion and oxygenate selectivity (Fig. 1 (b)). The XRD patterns of the catalysts mainly showed the spinel structure as illustrated in Fig. 1 (c) and Fig S1. As the Zn loading further increased beyond stoichiometric Zn, crystalline ZnO became visible by XRD. This caused the methanol synthesis rate to decline (Fig. 1 (a)) due to a decrease in the CO_2 conversion. This suggests that the sintering of the ZnO phase led to the elimination of the active surface area, where the active sites might consist of small, well-dispersed, supported ZnO particles [28], or a more amorphous phase in which the ZnO phase did

not adopt a repetitive crystalline structure [24]. Together, these results suggest that the active phase was not inherent to the spinel structures themselves [4,19,29], nor the crystalline ZnO, but rather to a ZnO phase that formed on the surface of the spinel structure [21–24,30].

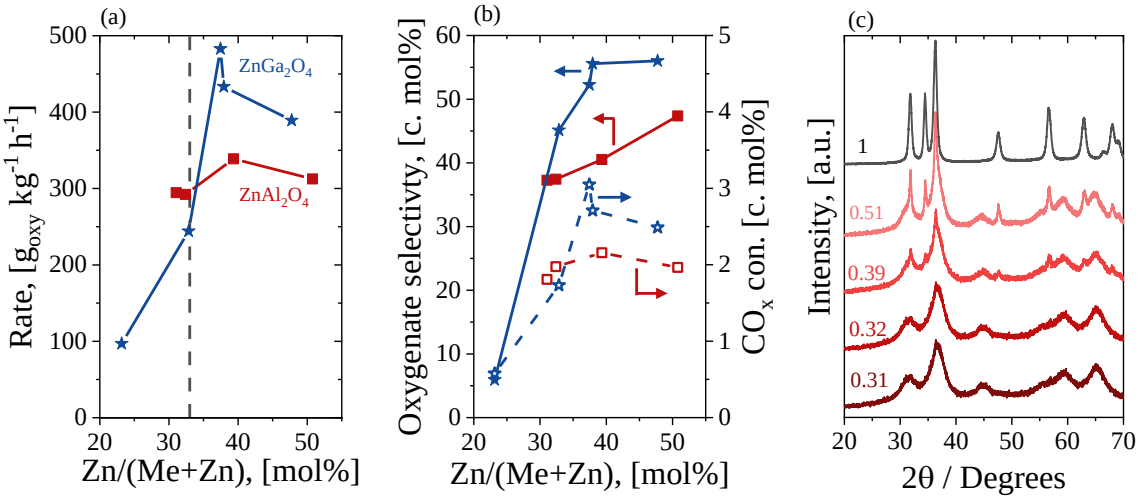


Fig. 1. (a) The oxygenate formation rate and (b) the oxygenate selectivity and CO2 conversion to hydrocarbons (CO_x con.) against the Zn loading within the spinel structures. (c) The XRD pattern of the as prepared $ZnAl_2O_4$ catalyst with different Zn loading from 0.31 to 0.51 mol fraction (1 for pure ZnO). Reaction conditions: 320 ºC, 50 bar, 31.2 NL/h, 0.75 g catalyst, gas composition of $CO_2/CO/H_2/Ar$ 29/4/64/3 Vol%.

XAS analysis of the Zn K-edge was conducted to further investigate the nature of the ZnO phase present in the spinel catalysts. The X-ray absorption near edge structure (XANES) and the Fourier-transformed k^3-weighted extended X-ray absorption fine structure (FT-EXAFS) spectra of the as-prepared $ZnAl_2O_4$ catalysts and ZnO are presented in Fig. 2 (a) and (b). A similar analysis for the $ZnGa_2O_4$ was conducted and can be found in Fig. S1. Fitting the two nearest neighbor shells to the FT-EXAFS spectrum of the under stoichiometric $ZnAl_2O_4$ sample, using paths calculated for $ZnAl_2O_4$ (ICSD 196109), found Zn-O at 1.96 Å, Zn-Al at 3.34 Å, and Zn-Zn at 3.50 Å. When using similar paths calculated for $ZnGa_2O_4$ (ICSD 81108) to fit the under stoichiometric $ZnGa_2O_4$ sample found Zn-O at 1.98 Å, Zn-Ga 3.44 Å, and Zn-Zn 3.57 Å. This confirmed that most Zn in these samples was present in the spinel structure, where Zn atoms are tetrahedrally coordinated within the octahedrally coordinated aluminum oxide or gallium oxide structure. Changes in both the XANES (Fig. 2 (a)) and EXAFS (Fig. 2 (b)) spectra were observed as the Zn-loading increased. Signals associated with crystalline ZnO (ICSD 57450) became visible at high Zn-loadings, in

agreement with the observations from the XRD analysis (Fig. 1 (c)). The EXAFS fits of the standards and the Zn-O, Zn-Zn (ZnO), and Zn-Al, Zn-Zn ($ZnAl_2O_4$) contribution to the fitted curve are visualized in Fig. S2. Similar fits for the $ZnGa_2O_4$ catalyst can be found in Fig S3.

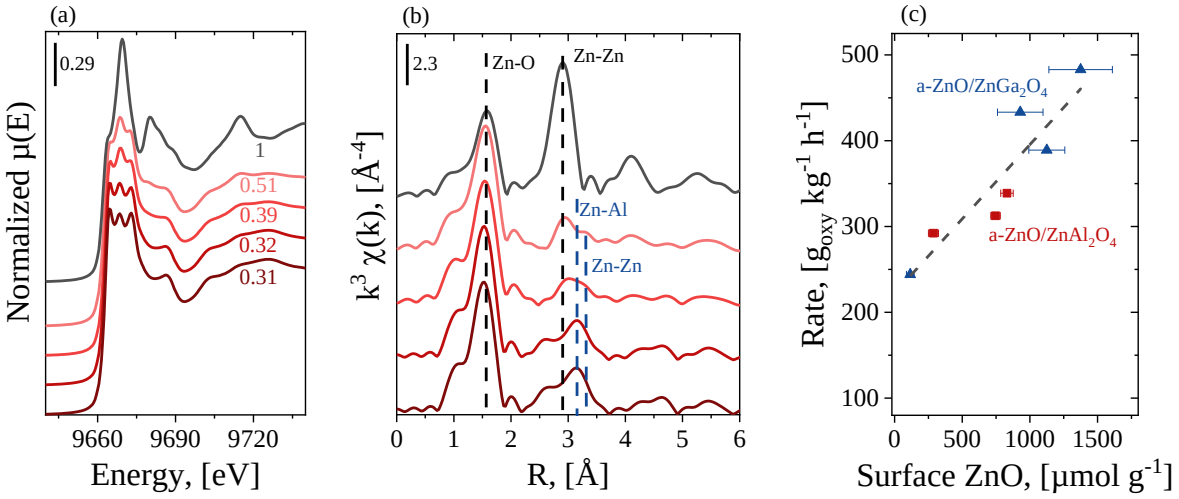


Fig. 2. (a) Zn K-edge XANES and (b) Fourier-transformed k^3-weighted EXAFS spectra, $ZnAl_2O_4$ catalysts with varying Zn loading from 0.31 to 0.51 mol fraction and ZnO (1) as references. The contribution of the $ZnAl_2O_4$ and ZnO phases on the EXAFS spectra were identified by 1st and 2nd shell EXAFS fitting with the ICSF 196109 and ICSD 57450 standard, respectively. (c) The oxygenate formation rate against the calculated amount of the surface ZnO species from linear combination fitting [27]*. Reaction conditions: 320 ºC, 50 bar, 31.2 NL/h, 0.75 g catalyst, gas composition of CO_2/CO/H_2/Ar 29/4/64/3 Vol%.*

Table 1. Specific surface area (BET), bulk metal loading, the weight percentage of crystalline, hexagonal ZnO determined by XRD, and the Zn percentage present as surface ZnO or crystalline ZnO determined by XANES.

Catalyst	**BET** [m^2/g]	**Bulk Zn/(Me+Zn)[a]** [mol%]	**Cryst. ZnO[b]** [wt%]	**Surface ZnO[c]** [mol%]	**Cryst. ZnO[c]** [mol%]
(0.31)$ZnAl_2O_4$	167	31.1	n.d.	0	0
(0.32)$ZnAl_2O_4$	135	32.4	n.d.	5.8 ± 0.8	3.3 ± 0.9
(0.39)$ZnAl_2O_4$	133	39.3	12.3	14 ± 0.8	14 ± 1.1
(0.51)$ZnAl_2O_4$	96.3	50.8	25.6	10 ± 0.5	19 ± 0.7
(0.23)$ZnGa_2O_4$	107	23.2	n.d.	0	0
(0.33)$ZnGa_2O_4$	50.7	32.8	n.d.	2 ± 0.8	4.9 ± 1.0
(0.37)$ZnGa_2O_4$	96	37.4	n.d.	24 ± 6.0	3.5 ± 7.8
(0.38)$ZnGa_2O_4$	86.3	37.9	0.4	16 ± 4.2	9.2 ± 2.3
(0.48)$ZnGa_2O_4$	75.2	47.7	7	15 ± 2.6	26 ± 2.0

[a]determined by ICP-OES, Me denotes the support metal (Al or Ga), [b]determined by Rietveld refinement of XRD data, [c]determined by linear combination fitting of XANES data. n.d. denotes not detected.

Linear combination fitting of the XANES spectra was conducted to further understand the changes in ZnO phases present in the catalysts between low and high Zn-loadings. In previous work, surface, amorphous ZnO was observed at low Zn loadings for ZnO supported on alumina stabilized tetragonal zirconia catalysts [27]. This catalyst was used as a spectral reference for supported amorphous ZnO. The spectra of the under stoichiometric spinel catalysts and ZnO were used as references for the spinel bound Zn and crystalline ZnO respectively. Good fits were obtained by using these three references (Fig S2 and S3), showing that the changes in the spectra were caused by the formation of an amorphous, surface ZnO phase that at high Zn loadings formed crystalline ZnO. The outcomes of linear combination fitting, as presented in Table 1, indicate that methanol synthesis activity increased associated with the formation of the amorphous ZnO phase, while it declined with the formation of crystalline ZnO (Fig. 1 (a) and Table 1). By utilizing the bulk concentration determined from ICP analysis and the fraction of Zn present as the surface ZnO phase (Table 1), the amount of the surface ZnO phase in the catalysts was estimated [27]. The estimated amount exhibited a strong correlation with the methanol synthesis rate, as depicted in Fig. 2 (c). This finding shows that the surface ZnO phase was the primary active site for methanol synthesis and that improving the amount of this phase, e.g. by increasing the surface area available for its support, will enhance the methanol synthesis activity [24,27]. The spinel phases themselves did show methanol synthesis activity, as the correlation in Fig. 2 (c) does not show zero rate if no surface ZnO was present, but they became more selective towards oxygenates rather than CO with the formation of surface ZnO Fig. 1 (a).

3.2 Changes in the ZnO phase under reducing and oxidizing atmospheres

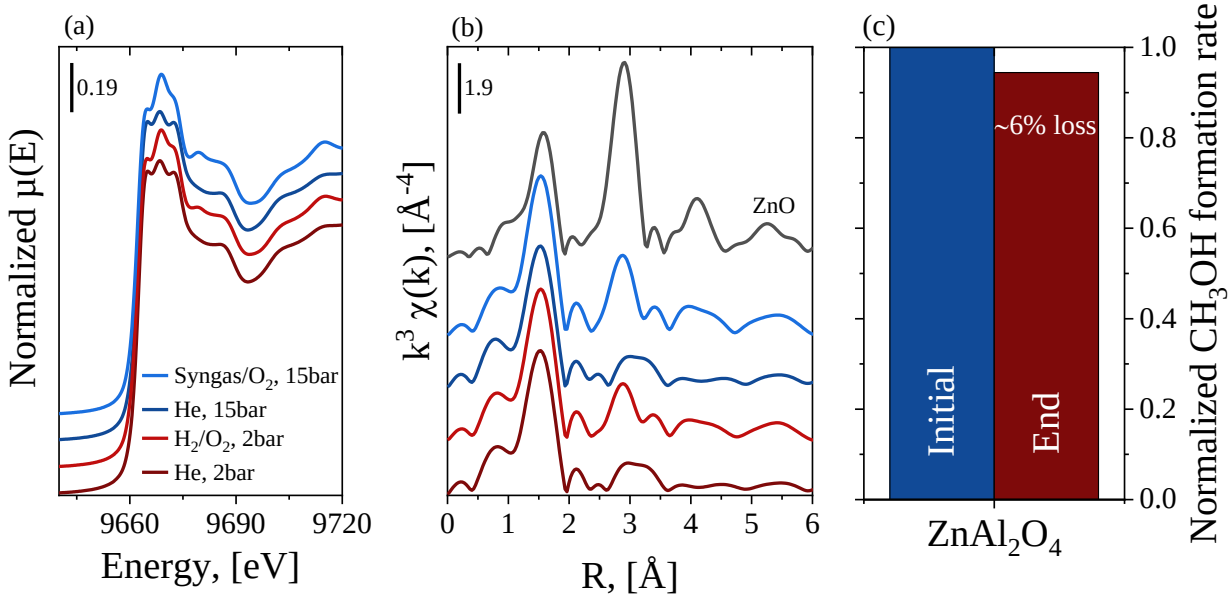


Fig. 3. (a) Zn K-edge XANES and (b) the Fourier-transformed k^3-weighted EXAFS spectra of the (0.39) $ZnAl_2O_4$ obtained at room temperature after the dehydration step and periodic switching between the syngas mixture or H_2 and O_2 through 18 switches. (c) The normalized CH_3OH formation rate for the first cycle (initial) and the 9th cycle (end) determined from the MS signal at m/z = 31. Reaction conditions: 400 °C, 2 or 15 barg, 50 NmL/h, catalyst loading of ~2.5 mg (diluted 1:8 in inert α-Al_2O_3), feed gas composition of CO_2/CO/H_2/He 12/5/37/46 or O_2/He of 10/90.

In-situ XAS analysis at the Zn K-edge was conducted on the most active spinel catalysts under methanol synthesis conditions and under changing reducing and oxidizing atmospheres, simulating catalyst regeneration in a bi-functional catalyst system. The XANES and EXAFS spectra obtained at room temperature after the dehydration step and after the periodic switching between H_2 or syngas and O_2 are illustrated in Fig. 3 (a) and (b) for the (0.39)$ZnAl_2O_4$ catalyst. The dehydration step did not change the structure of the catalysts compared to the as-prepared state (Fig. 2 (a-b)). However, the periodic switching between reducing and oxidizing gasses caused the formation of crystalline ZnO, which deactivated the catalyst (Fig. 3 (c)). Using both H_2 and a syngas mixture as the reducing gas gave similar results (Fig. 3 (a-b)). Thus, the sintering of the surface ZnO phase into crystalline ZnO under oscillating conditions led to catalyst deactivation, providing additional confirmation that the primary methanol synthesis activity did not stem from the crystalline ZnO. A similar experiment was conducted for the (0.37)$ZnGa_2O_4$ catalyst as shown in Fig S6. Linear combination fitting of the (0.37)$ZnGa_2O_4$ revealed that the crystalline ZnO fraction doubled after oscillating between syngas and O_2, as illustrated in Fig S6. The instability of the surface ZnO phase under the oscillating conditions indicates that Zn became mobile and sintered. It is plausible that

Zn exhibits mobility under reducing conditions, as these conditions may contribute to a partial reduction of the surface ZnO [27]. Shifting to oxidizing conditions reoxidizes the more sintered ZnO. Such mobility of the ZnO under reducing conditions could be important for the observed solid-state titration of ZnO into zeolite components in bi-functional catalytic systems [31–33]. Furthermore, zinc mobility under reducing atmospheres is debated in literature to have an important effect on copper based methanol synthesis catalysts as well [34–36]. The deactivation behavior of the metal oxide catalysts under alternating reducing-oxidizing conditions could be a significant drawback when used together with H-SAPO-34. H-SAPO-34 deactivates fast due to carbon deposits hindering access to the acid sites under methanol-to-olefins conditions [37]. Oxidative removal of such carbon deposits when using the bi-functional catalytic system would deactivate the methanol synthesis catalyst. However, great stability has been demonstrated when combining metal oxides solid with CHA acids [2–4,18,19,38], so oxidative regeneration may be unnecessary.

3.3 The CO_2 hydrogenation to methanol synthesis mechanism

To investigate the CO_2 hydrogenation reaction over the Zn-containing spinel structures in-situ DRIFTS was employed to monitor the evolution of surface species during CO_2 adsorption, followed by H_2 treatment, and He-TPD after reaching a steady state in methanol synthesis. In Fig. 4 (a), the initial CO_2 adsorption on the $ZnAl_2O_4$ catalyst shows the formation of carbonate ($*CO_3$) at 1371 and 1552 cm^{-1} [39–42]. The surface carbonate rapidly hydrogenated into formate (*HCOO), observed at 1363, 1375, 1598, and 2850 cm^{-1}, when the CO_2 gas was changed to H_2 (Fig. 4 (a-b) and Fig. S7) [40,43,44]. At constant H_2 flow, the formate signals started to disappear with concurrent formation of water and CH_4, as detected in the gas phase as the "hedgehog" signal due to water rotational modes around 1300-2000 cm^{-1}, and peak at 1306 cm^{-1}, respectively (Fig. 4 (a)). Both the $ZnAl_2O_4$ and $ZnGa_2O_4$ catalysts showed low selectivity towards CH_4 under the methanol synthesis conditions, but the high IR absorption cross-section for CH_4 is believed to be the reason for the strong signal observed. CH_4 formation was observed by Ye et al. [45] over a similar $ZnAl_2O_4$ catalyst. Repeating this experiment at 260 ºC showed the formation of carbonate, which again rapidly hydrogenated into formate. However, the fast removal of formate peaks by further hydrogenation in constant H_2 flow was not observed (Fig S7). This could indicate that formate hydrogenation proceeds much slower and requires more energy to overcome the activation energy barrier than carbonate hydrogenation.

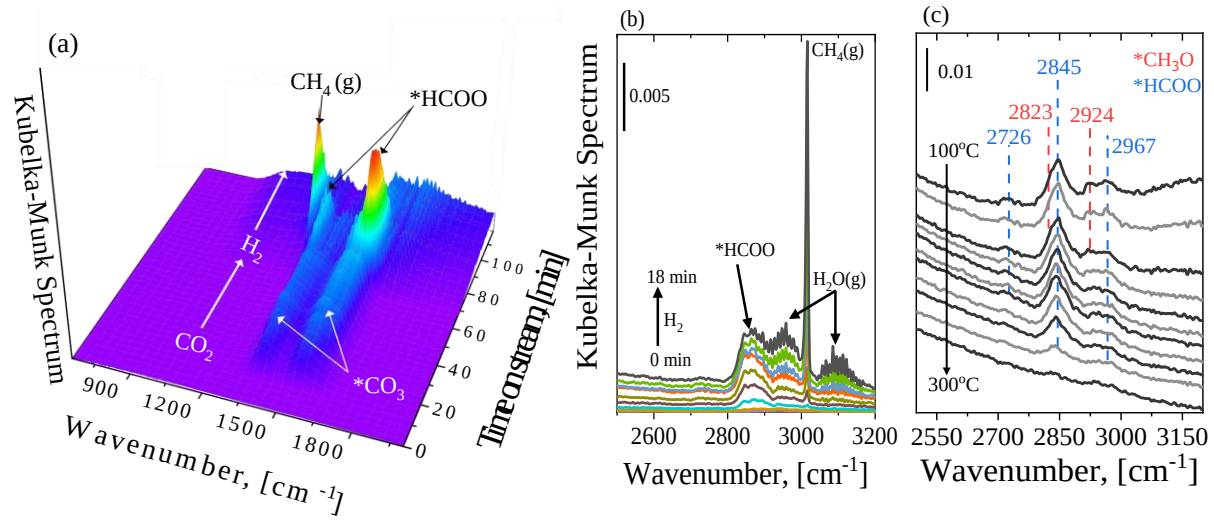


Fig. 4. In-situ DRIFTS measurements. (a) CO_2 adsorption followed by H_2 treatment on (0.39)$ZnAl_2O_4$ at 20 bar and 320 °C. (b) The initial change in IR signals for the H_2 treatment after CO_2 adsorption (c) TPD in He at 1 bar after steady-state methanol formation at 320 °C and 20 bar.

Ye et al. [45] investigated methanol adsorption on the $ZnAl_2O_4$ catalyst and found signals for methoxy at 2982 and 2891 cm^{-1}. These signals only appeared at 2823 and 2924 cm^{-1} after the $ZnAl_2O_4$ was subjected to steady-state methanol synthesis at 320 °C and 20 bar and then cooled to room temperature (Fig. 4 (b)). The methoxy signals quickly disappeared upon heating in He. Hence, the formation of methanol could proceed through a methoxy intermediate, which rapidly hydrogenated and desorbed as methanol, and thereby only visible at low temperatures. By further heating in helium, the formate signal disappeared at around 300 ºC, showing that formate was strongly adsorbed to the surface (Fig. 4 (c)). The same analysis was conducted for the $ZnGa_2O_4$ catalyst, which showed similar behavior as to the $ZnAl_2O_4$ catalyst and can be found in Fig. S8. A notable difference was that the formate signals for the $ZnGa_2O_4$ were removed at 324 ºC (Fig S8). In previous work, similar experiments for the ZnO/t-ZrO_2 catalysts showed that the formate signals disappeared at 370 ºC [27]. The stronger adsorption of the formate on the ZnO/t-ZrO_2 could be responsible for its superior methanol selectivity since both methanol selectivity and formate desorption temperature followed the order ZnO/t-ZrO_2>$ZnGa_2O_4$>$ZnAl_2O_4$.

Overall, it is proposed that the CO_2 hydrogenation into methanol over non-stoichiometric Zn-spinel structures occurred through CO_2 adsorption as carbonate followed by fast hydrogenation into formate. Formate hydrogenation into methoxy occurred at a slower rate and appeared as the rate determining step, while formed methoxy rapidly hydrogenated and desorbed as methanol [45].

3.4 Direct CO_2 hydrogenation into olefins

The measurements of direct CO_2 hydrogenation to olefins activity were conducted by physical mixing of granulates of the metal oxide and H-SAPO-34 within one reactor. By combining the (0.39)$ZnAl_2O_4$ with H-SAPO-34, a light olefin selectivity of 80 mol% on a carbon basis at 10 bar and 400 ºC was obtained (Fig. 5 (a)). This light olefin selectivity was achieved with a CO_2 to hydrocarbon conversion (CO_x conversion) of 2.9 mol%. By changing the metal oxide component to the (0.37)$ZnGa_2O_4$ or the (0.18)ZnO/t-ZrO_2 catalyst, the CO_x conversion increased to 3.8 and 5.4 mol%, respectively. Detailed analysis of the methanol synthesis activity of the ZnO/t-ZrO_2 catalyst is published elsewhere [27]. The improvements in the CO_x conversion were achieved with the drawback of a decrease in light olefin selectivity to 72 and 67 mol%. However, due to the enhanced CO_x conversion, the light olefin formation rates were 22 and 11 $g_{C2-4=}$ kg^{-1} h^{-1} for the ZnO/t-ZrO_2 and the $ZnAl_2O_4$ catalyst (Fig S9).

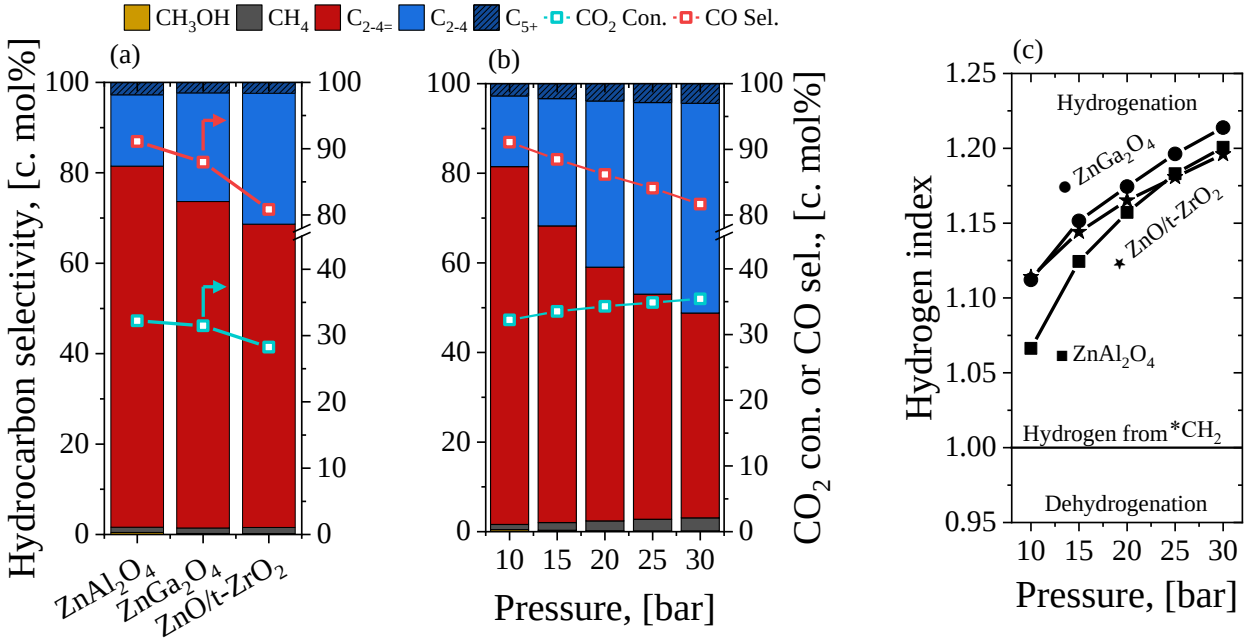


Fig. 5. The CO_2 conversion (con.), CO selectivity (sel.), and the hydrocarbon selectivity (a) for different metal oxide catalysts with H-SAPO-34 and (b) for different pressures over $ZnAl_2O_4$+H-SAPO-34. (c) The hydrogen index with increasing pressure. Reaction condition: 400 °C, 10 bar (unless else stated), 2.5 NL/h, and catalyst loading of 500 mg.

Increasing the reactor pressure improved the CO_x conversion for the $ZnAl_2O_4$ catalyst, as illustrated in Fig. 5 (b). In Fig. 5 (c), the calculated hydrogen index as a function of pressure for all three catalyst combinations is visualized. A hydrogen index of one corresponds to no incorporation

of gaseous H_2 into the product, meaning that all hydrogen stored in the product came from methanol dehydration, forming the "CH_2" hydrocarbon pool specie. A hydrogen index above or below one corresponds to hydrogenation or dehydrogenation, respectively. The result in Fig. 5 (c) shows, that the catalyst mixture of the metal oxide and H-SAPO-34 all resulted in net hydrogenation. As the pressure increased, the incorporation of gaseous H_2 increased, which explains the decreased light olefin selectivity with increasing pressure observed in Fig. 5 (b). At low pressures, the $ZnAl_2O_4$ catalyst had a hydrogen index closer to one, compared to the other catalysts, showing less hydrogenation activity. However, similar hydrogen activity was observed for all three catalyst mixtures when the pressure increased to ≥20 bar.

To investigate how performance changes with the presence of CO in the feed gas, CO co-feeding experiments were conducted, which mimic the process of recycling unconverted gas back to the reactor. The CO co-feeding was conducted according to two different strategies. The results represented in Fig. 6 were obtained by replacing CO_2 with CO while keeping the total amount of carbon constant. Experiments where the CO or the CO_2 partial pressures were kept constant while co-feeding of either CO_2 or CO can be found in Fig. S10.

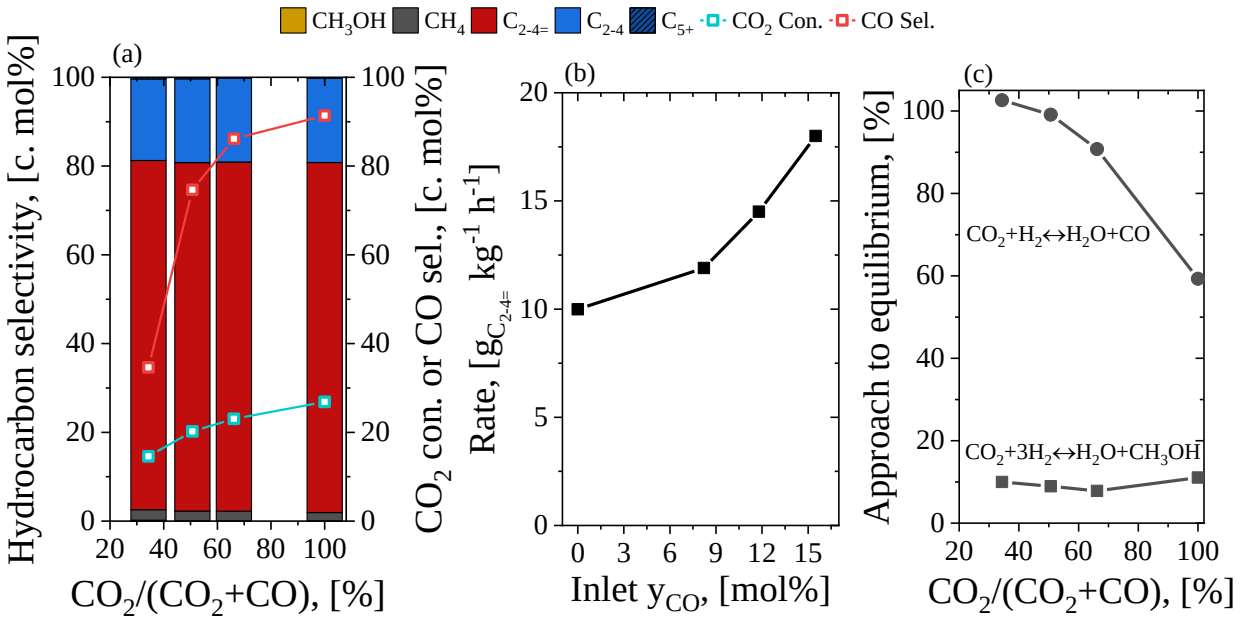


Fig. 6. (a) The CO_2 conversion (con.), CO selectivity (sel.), and the hydrocarbon selectivity with change in the amount of CO and CO_2 in the feed gas. (b) The light olefins formation rate with increased CO concentration in the feed. (c) The approach to equilibrium for the reverse-water-gas-shift and the methanol synthesis reaction with the change in CO_2/CO feed concentration. Reaction conditions: 380 °C, 10 bar, 3.5 NL/h, and catalyst loading of 700 mg.

As depicted in Fig. 6 (a), having more CO in the feed gas led to a decrease in both CO selectivity and CO_2 conversion. The CO selectivity dropped from 91 to 35 %, where the CO_2 conversion only decreased from 27 to 15 %, resulting in an increased overall CO_x conversion from 2.3 to 9.5 %. This was achieved without affecting the olefin selectivity, which remained constant at 79 mol% (Fig. 6 (a)). Therefore, the increased presence of CO in the feed resulted in an enhanced rate of light olefin formation, rising from 10 to 18 $g_{C2-4=}\ kg^{-1}\ h^{-1}$, as illustrated in Fig. 6 (b). These results demonstrate a powerful strategy to minimize the CO selectivity and improve the light olefin formation rate for the bi-functional catalytic system, which could be achieved by recycling gas to the reactor [4,46].

Several factors may account for the enhanced CO_x conversion observed during CO co-feeding. Firstly, CO could potentially serve as the primary carbon source for the initial methanol synthesis. Also, CO may aid in the removal of water, an inhibitor of the metal oxide that slows the methanol synthesis activity [47]. Additionally, CO may generate oxygen vacancies that boost the CO_2 hydrogenation rate [48]. Lastly, CO may facilitate the carbonylation of hydrocarbon pool species [49]. The DRIFTS data in Section 3.3 together with the fact that $ZnAl_2O_4$ catalysts have demonstrated great reverse-water-gas-shift activity [50], and as the rate of this reaction is much faster than CO or CO_2 hydrogenation into methanol, it is unlikely that CO is the primary carbon source for methanol synthesis. Previous kinetic analysis of a bi-functional catalytic system showed that a small amount of residual methanol together with a high amount of water, produced from the reverse-water-gas-shift, methanol synthesis, and methanol dehydration reactions, reduced the thermodynamic driving force by approaching the methanol equilibrium if immediate methanol conversion did not occur [25]. Fig. 6 (c) shows that the reverse-water-gas-shift reaction reached equilibrium when a high amount of CO was co-fed. Therefore, the production of water from this reaction was reduced and the total amount of water in the reactor was significantly reduced (water outlet mol% decreased from 7.1 to 2.0). Thus, the enhanced activity could be due to the improved thermodynamic driving force for the CO_2 to methanol hydrogenation reaction. Attenuation of the H-SAPO-34 acidity has been observed due to competitive water adsorption. Thus, high water concentration decreased the dehydration activity of the solid acid and thereby increased the residual methanol concentration, forcing the methanol synthesis reaction closer to equilibrium [51]. However, as illustrated in Fig. 6 (c), the outlet gas was far from CO_2 to methanol equilibrium, but this could be misguiding if the catalyst bed was not perfectly mixed. Lastly, incorporation of CO into

the hydrocarbon pool species within the solid acid pores cannot be excluded [49,52], but it seems unlikely as no significant change was observed in the hydrocarbon distribution (Fig. 6 (a)).

The effect on the hydrocarbon distribution and light olefin formation rate with the change of residence time in the reactor when feeding CO_2/H_2 over the $ZnAl_2O_4$ and H-SAPO-34 is illustrated in Fig. 7. Short residence time allows unconverted methanol and dimethyl ether to pass through the reactor. At longer residence time, the oxygenates were converted and an increase in the light olefin selectivity was observed (Fig. 7 (a)). With extended residence time, the olefin selectivity began to decline, attributed to the hydrogenation of olefins into paraffins. The optimum olefin selectivity was obtained when all oxygenates were converted into olefins where the residence time remained sufficiently short to prevent olefin hydrogenation.

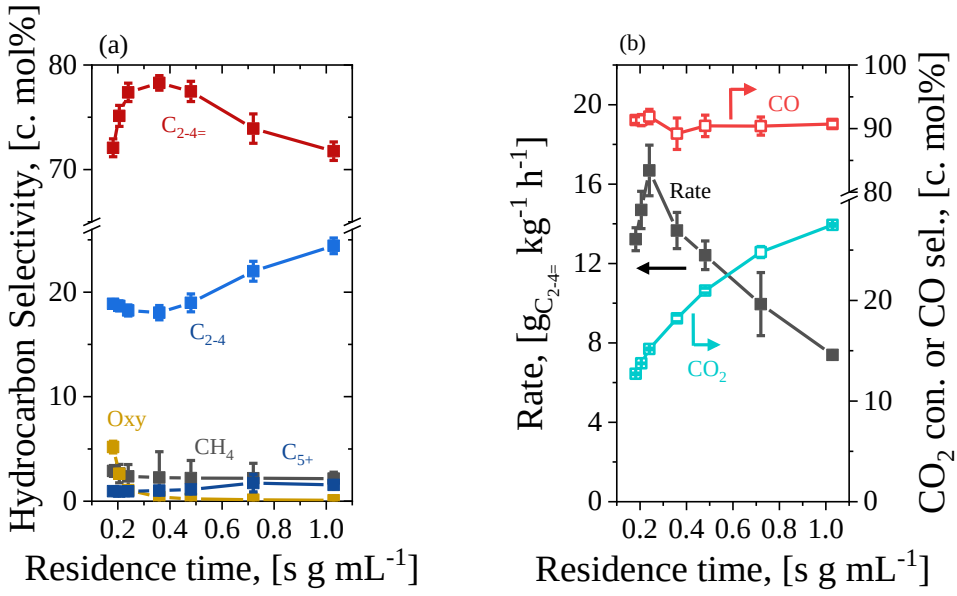


Fig. 7. (a) The hydrocarbon selectivity with change in the residence time. (b) The CO_2 conversion (con.), CO selectivity (sel.), and light olefins formation rate with the change in residence time. Reaction condition: 380 °C, 10 bar, 2.5, 3.5, 5.2, and 7 NL/h at the catalyst loading of 700 mg and repeated at 1.8, 2.7, 3.5, 5.3, 6.2 and 7 NL/h at the catalyst loading of 350 mg.

As illustrated in Fig. 7 (b), the CO selectivity did not change with the change in residence time staying at ~90 %. However, the CO_2 conversion increased from 12.7 to 27.5 % with a 5.7-time increase in the residence time. Previous work has revealed that this trend in CO_2 conversion can be attributed to the approach to equilibrium for the CO_2 to methanol reaction as more water is formed at a longer residence time [25]. The optimum light olefin formation rate was achieved at the residence time where all the oxygenates were converted and where the CO_2 hydrogenation

reaction was far from equilibrium, as depicted in Fig. 7 (b). The cause of the approach to equilibrium could be the effect of water attenuation of the acid sites, causing an increase in residual methanol within the reactor [51]. Hence, the breakthrough for the bi-functional catalyst systems for direct syngas to hydrocarbons may necessitate a reconsideration of reactor design to eliminate the high concentration of water[53].

The stability of the $ZnAl_2O_4$+H-SAPO-34 catalyst mixture was investigated and the results are illustrated in Fig. 8. A slow but steady deactivation was observed for the CO_2 conversion over 100 hours on stream. Greater changes were observed for the CO, light olefin, and light paraffin selectivity, mainly within the first 10 hours on stream. The decline in light olefin selectivity was attributed to an increase in hydrogenation activity, resulting in an elevated paraffin selectivity. Additionally, the CO selectivity increased showing a decrease in CO_2 converted into hydrocarbons within the initial 10 hours. After the first 10 hours, stable selectivities were observed for more than 90 hours. These results demonstrated a stable catalytic system, in sharp contrast to the methanol-to-olefins process. Similar trends with time on stream have been reported for bi-functional catalysts [3,18], but the cause of the stable performance is still not fully known.

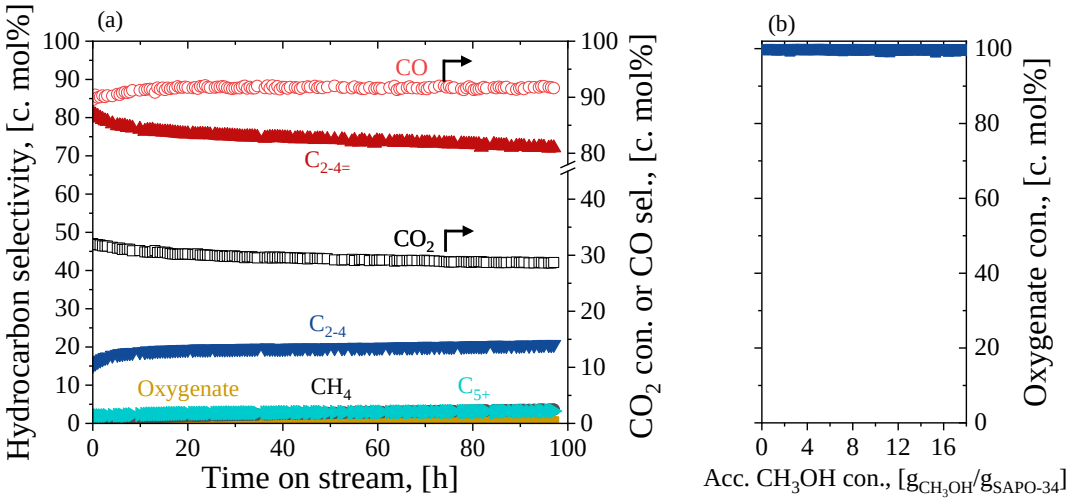


Fig. 8. (a) The CO_2 conversion (con.), CO selectivity (sel.), and the hydrocarbon selectivity with time on stream. (b) The oxygenate conversion (CH_3OH + CH_3OCH_3) at accumulated (acc.) methanol conversion pr. gram of H-SAPO-34. Reaction conditions: 400 °C, 10 bar, 2.5 NL/h, and catalyst loading of 500 mg.

The results in Fig. 8 (b) show that more than 18 g_{MeOH} pr $g_{SAPO-34}$ was converted without a significant drop in the methanol conversion. This surpasses the methanol-to-olefin process where the CHA structure is prone to fast deactivation by internal coke formation. Bleken et al. [37] showed

that SAPO-34 can convert approximately 20 g_{MeOH} pr $g_{SAPO-34}$ before the methanol conversion dropped to 20 %. The combination of the metal oxide, the solid acid, and the reaction atmosphere has an enhancing effect on the solid acid's lifetime. Improved lifetime for the methanol-to-olefins process has been demonstrated by co-feeding methanol with high partial pressure of H_2 [54–56]. This enhancement was attributed to a decrease in the rate of coke formation, resulting in smaller coke molecules, primarily mono- and diaromatics, as opposed to the tri- and tetraaromatic species typically formed during the methanol-to-olefins process [13,55]. Zhao et al. [56] proposed that hydrogenation of heavy aromatic deposits reactivates these aromatic species for the hydrocarbon pool mechanism and thus slows down the evolution of coke species. Furthermore, studies have shown that high partial pressures of water together with H_2 further reduce the amount of coke formed [51,56].

It has been proposed that when combining a Zn-based methanol synthesis catalyst with a solid acid catalyst, titration of acidic sites by Zn ion exchange into the solid acid can take place [31,32]. To simulate this, a SAPO-34 sample was impregnated with a small amount of Zn, denoted Zn-SAPO-34. This catalyst was combined with $ZnAl_2O_4$, tested for its direct CO_2 hydrogenation to olefin abilities, and compared to H-SAPO-34, as illustrated in Fig. 9 (a-b).

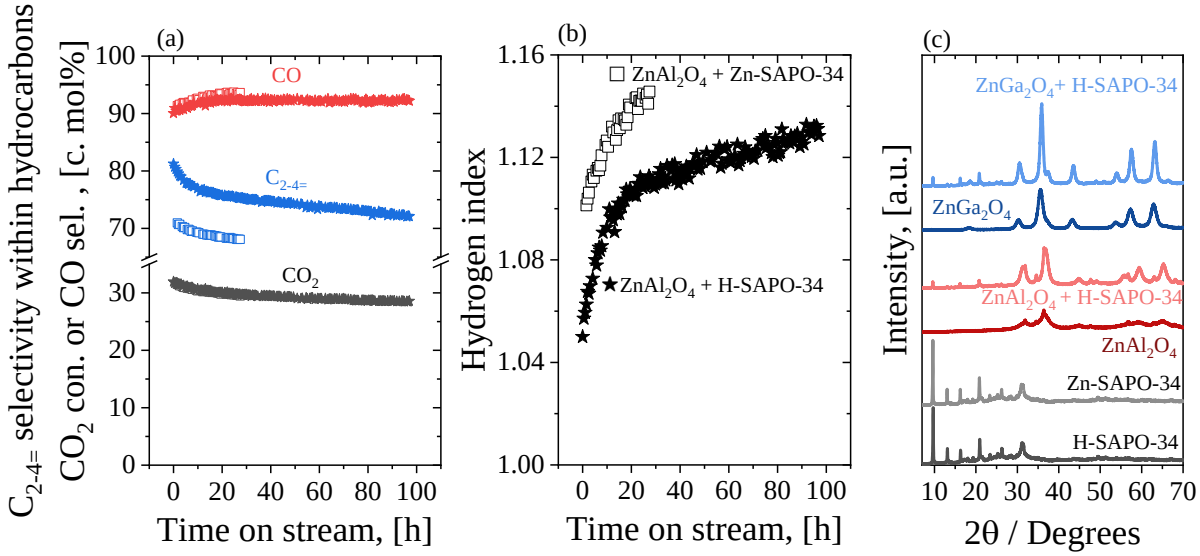


Fig. 9. (a) The CO_2 conversion (con.), CO selectivity (sel.), and light olefins selectivity, and (b) the hydrogen index with time on stream for the $ZnAl_2O_4$ mixed with H-SAPO-34 and Zn-SAPO-34. (c) The XRD patterns of the as-prepared catalysts and after exposure to the CO_2 to olefin reaction (the mixture of the metal oxide phase and the solid acid phase). Reaction conditions: 400 °C, 10 bar, 2.5 NL/h, and catalyst loading of 500 mg.

XRF analysis revealed the presence of 1.5 wt% Zn in the Zn-SAPO-34 sample, leading to a reduction in acid site density from 516 to 403 µmol/g, as determined by NH_3-TPD (Table S1). XRD analysis did not detect the presence of any crystalline ZnO in the Zn-SAPO-34 sample (Fig. 9 (c)), showing the absence of large ZnO clusters. Consequently, it was inferred that the Zn was well dispersed and occupied acid sites within the SAPO-34 crystals. Upon combination with $ZnAl_2O_4$, the CO_2 conversion and CO selectivity were identical to those observed with the $ZnAl_2O_4$/H-SAPO-34 catalyst (Fig. 9 (a)). However, the hydrogenation activity of the Zn-SAPO-34 catalyst, illustrated in the hydrogen index in Fig. 9 (b), was significantly higher yielding a higher selectivity towards paraffins. This suggests that Zn migration from $ZnAl_2O_4$ into H-SAPO-34 was responsible for the decrease in olefin selectivity, where the greatest change happens within the first 10 hours on stream (Fig. 9 (a-b)). Zn migration further altered the active site for the methanol synthesis reaction, which could explain the initial changes in the CO_2 and CO selectivity (Fig. 9 (a)).

XRD analysis of the catalysts after being exposed to CO_2 to olefins conditions (from experiments visualized in Fig. 5 (b) and S9) showed that both the $ZnAl_2O_4$ and ZnO crystals sintered, with an increase in particle size from 33 to 72 Å and from 109 to 230 Å, respectively. Similar sintering was observed for $ZnGa_2O_4$, where the particle size increased from 79 to 137 Å. Crystalline ZnO was not visible by XRD for the $ZnGa_2O_4$ catalyst. This demonstrated that the metal oxide candidate lost active surface area with time on stream and explained the slow and steady loss in the CO_2 conversion. Overall, this suggested that two deactivation phenomena occurred: Zn migration, which occurred initially, increasing the hydrogenation activity of the solid acid, and metal oxide sintering, which steadily removed the methanol synthesis active surface area.

4 Conclusions

To improve the methanol synthesis activity for $ZnAl_2O_4$ and $ZnGa_2O_4$, the Zn loading should exceed the stoichiometric spinel loading. Exceeding the stoichiometric loading created ZnO sites on the spinel structure's surface, which were quantified by XAS analysis. These sites had superior oxygenate selectivity and the concentration of such sites controlled the CO_2 conversion. However, at high Zn loading, the formation of crystalline ZnO removed these amorphous ZnO sites, resulting in a decrease in the methanol synthesis activity. In-situ XAS analysis confirmed that the primary active sites were the amorphous, surface ZnO since deactivation occurred with the formation of

crystalline ZnO when oscillating between reducing and oxidizing conditions. In-situ DRIFTS analysis showed that the CO_2 to methanol reaction over Zn containing spinel catalyst occurred through a formate pathway, where CO_2 adsorbed as carbonate, hydrogenated into formate, and further into methoxy, which desorbed as methanol. Fast hydrogenation of carbonate into formate was observed at both 260 and 320 ºC, while formate hydrogenation was mainly observed at 320 ºC, suggesting that formate hydrogenation was the rate-determining step.

When the Zn spinel catalysts were combined with H-SAPO-34 solid acid, a high olefin selectivity was observed. $ZnGa_2O_4$ had higher methanol synthesis activity and higher hydrogen index, showing a higher olefin hydrogenation activity than the $ZnAl_2O_4$ catalyst. By increasing the pressure, higher hydrocarbon yields were obtained at the expense of an increase in paraffin selectivity. This demonstrated a trade-off between the CO_2 conversion to hydrocarbons and the olefin selectivity. A strategy to improve the CO_2 conversion to hydrocarbons without affecting the olefin selectivity was to co-feed CO. Co-feeding CO decreased the rate of the reverse-water-gas-shift reaction by limiting the thermodynamic driving force. This caused minimal production of water in the reactor, which improved the thermodynamic driving force for the CO_2 to methanol reaction. Combining the $ZnAl_2O_4$ and H-SAPO-34 showed stable production of olefins for around 100 hours on stream, and showed that more than 18 g_{MeOH} pr $g_{SAPO-34}$ could be converted without any reduction in the methanol conversion. However, solid-state migration of Zn onto the solid acid and metal oxide sintering caused the slow deactivating trends observed. When Zn was impregnated on the solid acid, increased olefin hydrogenation was observed, explaining the initial decrease in the olefin selectivity observed within the first 10 hours on stream.

References

[1] OECD, Global Plastics Outlook: Plastics use by polymer - projections, OECD Environ. Stat. (2022). https://doi.org/10.1787/b9bae4d1-en (accessed September 22, 2022).

[2] P. Gao, S. Dang, S. Li, X. Bu, Z. Liu, M. Qiu, C. Yang, H. Wang, L. Zhong, Y. Han, Q. Liu, W. Wei, Y. Sun, Direct Production of Lower Olefins from CO2 Conversion via Bifunctional Catalysis, ACS Catal. 8 (2018) 571–578. https://doi.org/10.1021/acscatal.7b02649.

[3] Z. Li, J. Wang, Y. Qu, H. Liu, C. Tang, S. Miao, Z. Feng, H. An, C. Li, Highly Selective Conversion of Carbon Dioxide to Lower Olefins, ACS Catal. 7 (2017) 8544–8548. https://doi.org/10.1021/acscatal.7b03251.

[4] X. Liu, M. Wang, H. Yin, J. Hu, K. Cheng, J. Kang, Q. Zhang, Y. Wang, Tandem Catalysis for Hydrogenation of CO and CO2 to Lower Olefins with Bifunctional Catalysts Composed of Spinel Oxide and SAPO-34, ACS Catal. 10 (2020) 8303–8314. https://doi.org/10.1021/acscatal.0c01579.

[5] S. Dang, S. Li, C. Yang, X. Chen, X. Li, L. Zhong, P. Gao, Y. Sun, Selective Transformation of CO2 and H2 into Lower Olefins over In2O3-ZnZrOx/SAPO-34 Bifunctional Catalysts, ChemSusChem. 12 (2019) 3582–3591. https://doi.org/10.1002/cssc.201900958.

[6] J. Wang, Z. You, Q. Zhang, W. Deng, Y. Wang, Synthesis of lower olefins by hydrogenation of carbon dioxide over supported iron catalysts, Catal. Today. 215 (2013) 186–193. https://doi.org/10.1016/j.cattod.2013.03.031.

[7] T. Riedel, M. Claeys, H. Schulz, G. Schaub, S.-S. Nam, K.-W. Jun, M.-J. Choi, G. Kishan, K.-W. Lee, Comparative study of Fischer–Tropsch synthesis with H /CO and H2 /CO2 syngas using Fe-and Co-based catalysts, Appl. Catal. A Gen. 186 (1999) 201–213.

[8] Y. Yang, H.W. Xiang, Y.Y. Xu, L. Bai, Y.W. Li, Effect of potassium promoter on precipitated iron-manganese catalyst for Fischer-Tropsch synthesis, Appl. Catal. A Gen. 266 (2004) 181–194. https://doi.org/10.1016/j.apcata.2004.02.018.

[9] A. Ramirez, L. Gevers, A. Bavykina, S. Ould-Chikh, J. Gascon, Metal Organic Framework-Derived Iron Catalysts for the Direct Hydrogenation of CO2 to Short Chain Olefins, ACS Catal. 8 (2018) 9174–9182. https://doi.org/10.1021/acscatal.8b02892.

[10] W. Zhou, K. Cheng, J. Kang, C. Zhou, V. Subramanian, Q. Zhang, Y. Wang, New horizon in C1 chemistry: Breaking the selectivity limitation in transformation of syngas and

hydrogenation of CO2 into hydrocarbon chemicals and fuels, Chem. Soc. Rev. 48 (2019) 3193–3228. https://doi.org/10.1039/c8cs00502h.

[11] F. Jiao, J. Li, X. Pan, J. Xiao, H. Li, H. Ma, M. Wei, Y. Pan, Z. Zhou, M. Li, S. Miao, J. Li, Y. Zhu, D. Xiao, T. He, J. Yang, F. Qi, Q. Fu, X. Bao, Selective conversion of syngas to light olefins, Science (80-.). 351 (2016) 1065–1068. https://doi.org/10.1126/science.aaf1835.

[12] J. T.-Jørgensen, TOPSOE INTEGRATED GASOLINE SYNTHESIS - THE TIGAS PROCESS, Stud. Surf. Sci. Catal. 36 (1988) 293–305.

[13] D.L.S. Nieskens, J.D. Lunn, A. Malek, Understanding the Enhanced Lifetime of SAPO-34 in a Direct Syngas-to-Hydrocarbons Process, ACS Catal. 9 (2019) 691–700. https://doi.org/10.1021/acscatal.8b03465.

[14] P. Ticali, S. Morandi, G. Shterk, S. Ould-chikh, A. Ramirez, J. Gascon, S. Chung, J. Ruiz-martinez, S. Bordiga, PdZn/ZrO2 + SAPO-34 bifunctional catalyst for CO2 conversion : Further insights by spectroscopic characterization, Appl. Catal. A , Gen. 655 (2023) 1–9.

[15] A. Ramirez, P. Ticali, D. Salusso, T. Cordero-lanzac, S. Ould-chikh, C. Ahoba-sam, A.L. Bugaev, E. Borfecchia, S. Morandi, M. Signorile, S. Bordiga, J. Gascon, U. Olsbye, Multifunctional Catalyst Combination for the Direct Conversion of CO2 to Propane, JACS Au. 1 (2021) 1719–1732. https://doi.org/10.1021/jacsau.1c00302.

[16] M. Tong, E. Hondo, L. Gapu Chizema, C. Du, Q. Ma, S. Mo, C. Lu, P. Lu, N. Tsubaki, Hydrogenation of CO2to LPG over CuZnZr/MeSAPO-34 catalysts, New J. Chem. 44 (2020) 9328–9336. https://doi.org/10.1039/d0nj00907e.

[17] Z. Shi, M. Neurock, A. Bhan, Methanol-to-Ole fi ns Catalysis on HSSZ-13 and HSAPO-34 and Its Relationship to Acid Strength, ACS Catal. 11 (2021) 1222–1232. https://doi.org/10.1021/acscatal.0c04011.

[18] X. Liu, W. Zhou, Y. Yang, K. Cheng, J. Kang, L. Zhang, G. Zhang, X. Min, Q. Zhang, Y. Wang, Design of efficient bifunctional catalysts for direct conversion of syngas into lower olefins: Via methanol/dimethyl ether intermediates, Chem. Sci. 9 (2018) 4708–4718. https://doi.org/10.1039/c8sc01597j.

[19] X. Liu, M. Wang, C. Zhou, W. Zhou, K. Cheng, J. Kang, Q. Zhang, W. Deng, Y. Wang, Selective transformation of carbon dioxide into lower olefins with a bifunctional catalyst composed of ZnGa2O4 and SAPO-34, Chem. Commun. 54 (2017) 140–143.

https://doi.org/10.1039/c7cc08642c.

[20] N. Li, Y. Zhu, F. Jiao, X. Pan, Q. Jiang, J. Cai, Y. Li, W. Tong, C. Xu, S. Qu, B. Bai, D. Miao, Z. Liu, X. Bao, Steering the reaction pathway of syngas-to-light olefins with coordination unsaturated sites of ZnGaOx spinel, Nat. Commun. 13 (2022) 1–8. https://doi.org/10.1038/s41467-022-30344-1.

[21] G. Del Piero, F. Trifiro, A. Vaccaria, Non-stoicheismetric Zn-Cr Spinel as Active Phase in the Catalytic Synthesis of Methanol, J. CHEM. SOC., CHEM. COMMUN. 3 (1984) 656–658.

[22] H. Song, D. Laudenschleger, J.J. Carey, H. Ruland, M. Nolan, M. Muhler, Spinel-Structured ZnCr2O4 with Excess Zn Is the Active ZnO/Cr2O3 Catalyst for High-Temperature Methanol Synthesis, ACS Catal. 7 (2017) 7610–7622. https://doi.org/10.1021/acscatal.7b01822.

[23] T. Ferruccio, A. Vaccari, Non-stoichiometry as key to modify the activity and selectivity of spinel-type catalysts for hydrogenation reactions, Struct. Sel. Relationships Heterog. Catal. 67 (1991) 157–167.

[24] X. Zhang, G. Zhang, W. Liu, F. Yuan, J. Wang, J. Zhu, X. Jiang, A. Zhang, F. Ding, C. Song, X. Guo, Reaction-driven surface reconstruction of ZnAl2O4 boosts the methanol selectivity in CO2 catalytic hydrogenation, Appl. Catal. B Environ. 284 (2021) 119700. https://doi.org/10.1016/j.apcatb.2020.119700.

[25] M.T. Nikolajsen, E.S. Kold, A.B. Møller, N.C. Schjødt, U. V Mentzel, J. Sehested, R.Y. Brogaard, J.M. Christensen, M. Høj, Direct CO2 Hydrogenation to Aromatics over Combined Catalysts Composed of Supported ZnO with Different Zeolite Topologies, In Perpartation. (2023).

[26] B. Ravel, M. Newville, ATHENA, ARTEMIS, HEPHAESTUS: data analysis for X-ray absorption spectroscopy using IFEFFIT, J. Synchrotron Rad. 12 (2005) 537–541.

[27] M.T. Nikolajsen, J.-C. Grivel, A. Gaur, L.P. Hansen, L. Baumgarten, N.C. Schjødt, U. V Mentzel, J.-D. Grundwaldt, J. Sehested, J.M. Christensen, M. Høj, Surface ZnOx on Zirconia is Highly Active for High Temperature Methanol Synthesis, Submitt. to J. Catal. XX (2023) 1–32.

[28] N. Li, F. Jiao, X. Pan, Y. Ding, J. Feng, X. Bao, Size Effects of ZnO Nanoparticles in Bifunctional Catalysts for Selective Syngas Conversion, ACS Catal. 9 (2019) 960–966.

https://doi.org/10.1021/acscatal.8b04105.

[29] W. De Hu, C.M. Wang, Y.D. Wang, J. Ke, G. Yang, Y.J. Du, W.M. Yang, First-principles-based microkinetic simulations of syngas to methanol conversion on ZnAl2O4 spinel oxide, Appl. Surf. Sci. 569 (2021) 151064. https://doi.org/10.1016/j.apsusc.2021.151064.

[30] J. Su, L. Zhang, H. Zhou, Y. Ye, X. Zheng, C. Liu, S. Liu, W. Jiao, X. Liu, C. Wang, Y. Wang, Z. Xie, Unveiling the Anti-Trap Effect for Bridging Intermediates on ZnAlOx/AlPO-18 Bifunctional Catalysts to Boost Syngas to Olefin Conversion, ACS Catal. 13 (2023) 2472–2481. https://doi.org/10.1021/acscatal.2c05918.

[31] Y. Wang, G. Wang, L.I. van der Wal, K. Cheng, Q. Zhang, K.P. de Jong, Y. Wang, Visualizing Element Migration over Bifunctional Metal-Zeolite Catalysts and its Impact on Catalysis, Angew. Chemie - Int. Ed. 60 (2021) 17735–17743. https://doi.org/10.1002/anie.202107264.

[32] Y. Ding, F. Jiao, X. Pan, Y. Ji, M. Li, R. Si, Y. Pan, G. Hou, X. Bao, Effects of Proximity-Dependent Metal Migration on Bifunctional Composites Catalyzed Syngas to Olefins, Am. Chem. Soc. 11 (2021) 9729–9737.

[33] B. Voss, A. Katerinopoulou, R. Montesano, J. Sehested, Zn and Si transport in dual-functioning catalyst for conversion of synthesis gas to dimethyl ether, Chem. Eng. J. 377 (2019) 121940. https://doi.org/10.1016/j.cej.2019.121940.

[34] V. Schott, H. Oberhofer, A. Birkner, M. Xu, Y. Wang, M. Muhler, K. Reuter, C. Wçll, Chemical Activity of Thin Oxide Layers : Strong Interactions with the Support Yield a New Thin-Film Phase of ZnO, Angew. Chemie - Int. Ed. 52 (2013) 11925–11929. https://doi.org/10.1002/anie.201302315.

[35] T. Lunkenbein, J. Schumann, M. Behrens, R. Schlçgl, M.G. Willinger, Formation of a ZnO Overlayer in Industrial Cu/ZnO/Al2O3 Catalysts Induced by Strong Metal – Support Interactions, Angew. Chemie - Int. Ed. 54 (2015) 4544–4548. https://doi.org/10.1002/anie.201411581.

[36] S. Kuld, M. Thorhauge, H. Falsig, C.F. Elkjær, S. Helveg, I. Chorkendorff, J. Sehested, Quantifying the promotion of Cu catalysts by ZnO for methanol synthesis, Science (80-.). 352 (2016) 969–974.

[37] F. Bleken, Æ.M. Bjørgen, Æ.L. Palumbo, S. Bordiga, Æ.S. Svelle, The Effect of Acid Strength on the Conversion of Methanol to Olefins Over Acidic Microporous Catalysts with

the CHA Topology, Top Catal. 52 (2009) 218–228. https://doi.org/10.1007/s11244-008-9158-0.

[38] S. Wang, P. Wang, D. Shi, S. He, L. Zhang, W. Yan, Z. Qin, J. Li, M. Dong, J. Wang, U. Olsbye, W. Fan, Direct Conversion of Syngas into Light Olefins with Low CO2 Emission, ACS Catal. 10 (2020) 2046–2059. https://doi.org/10.1021/acscatal.9b04629.

[39] Y. Zro, E. Ko, M. Kogler, T. Bielz, B. Klo, S. Penner, In Situ FT-IR Spectroscopic Study of CO2 and CO Adsorption on Y2O3, ZrO2 and Yttria-Stabilized ZrO2, J. Phys. Chem. C. 117 (2013) 17666–17673.

[40] S.E. Collins, M.A. Baltanás, A.L. Bonivardi, An infrared study of the intermediates of methanol synthesis from carbon dioxide over Pd/β -Ga2O3, J. Catal. 226 (2004) 410–421. https://doi.org/10.1016/j.jcat.2004.06.012.

[41] K. Pokrovski, K.T. Jung, A.T. Bell, Investigation of CO and CO 2 Adsorption on Tetragonal and Monoclinic Zirconia, Langmuir. 17 (2001) 4297–4303.

[42] S.M. Fehr, K. Nguyen, I. Krossing, Realistic Operando-DRIFTS Studies on Cu/ZnO Catalysts for CO2 Hydrogenation to Methanol – Direct Observation of Mono-ionized Defect Sites and Implications for Reaction Intermediates, ChemCatChem. 14 (2022). https://doi.org/10.1002/cctc.202101500.

[43] S. Tada, N. Ochiai, H. Kinoshita, M. Yoshida, N. Shimada, T. Joutsuka, M. Nishijima, T. Honma, N. Yamauchi, Y. Kobayashi, K. Iyoki, Active Sites on ZnxZr1– x O2– x Solid Solution Catalysts for CO2 -to-Methanol Hydrogenation, ACS Catal. 12 (2022) 7748–7759. https://pubs.acs.org/doi/10.1021/acscatal.2c01996.

[44] Y. Wang, S. Kattel, W. Gao, K. Li, P. Liu, G.J. Chen, H. Wang, Exploring the ternary interactions in Cu–ZnO–ZrO2 catalysts for efficient CO2 hydrogenation to methanol, Nat. Commun. 10 (2019) 1–8. http://dx.doi.org/10.1038/s41467-020-16342-1.

[45] A. Ye, Z. Li, J. Ding, W. Xiong, W. Huang, Synergistic Catalysis of Al and Zn Sites of Spinel ZnAl2O4Catalyst for CO Hydrogenation to Methanol and Dimethyl Ether, ACS Catal. 11 (2021) 10014–10019. https://doi.org/10.1021/acscatal.1c02742.

[46] Y. Ni, Z. Chen, Y. Fu, Y. Liu, W. Zhu, Z. Liu, Selective conversion of CO2 and H2 into aromatics, Nat. Commun. 9 (2018) 1–8. https://doi.org/10.1038/s41467-018-05880-4.

[47] N.D. Nielsen, A.D. Jensen, J.M. Christensen, The roles of CO and CO2 in high pressure methanol synthesis over Cu-based catalysts, J. Catal. 393 (2021) 324–334.

https://doi.org/10.1016/j.jcat.2020.11.035.

[48] O. Martin, A.J. Martín, C. Mondelli, S. Mitchell, T.F. Segawa, R. Hauert, C. Drouilly, D. Curulla-Ferré, J. Pérez-Ramírez, Indium oxide as a superior catalyst for methanol synthesis by CO2 hydrogenation, Angew. Chemie - Int. Ed. 55 (2016) 6261–6265. https://doi.org/10.1002/anie.201600943.

[49] Z. Chen, Y. Ni, Y. Zhi, F. Wen, Z. Zhou, Y. Wei, W. Zhu, Z. Liu, Coupling of Methanol and Carbon Monoxide over H-ZSM-5 to Form Aromatics, Angew. Chemie - Int. Ed. 57 (2018) 12549–12553. https://doi.org/10.1002/anie.201807814.

[50] N.C. Schjødt, S.L. Jørgensen, L.F. Lundegaard, P. Beato, R. Montesano, J. Sehested, Alkali promoted zinc-aluminum oxide as high temperature water gas shift catalyst, Appl. Catal. A Gen. 640 (2022). https://doi.org/10.1016/j.apcata.2022.118646.

[51] A.T. Aguayo, J. Bilbao, A. Ateka, A. Portillo, O. Parra, J. Ere, Effect of water and methanol concentration in the feed on the deactivation of In2O3 -ZrO2/SAPO-34 catalyst in the conversion of CO2/CO to olefins by hydrogenation, Fuel. 346 (2023) 128298–128307.

[52] D.B. Rasmussen, J.M. Christensen, B. Temel, F. Studt, P.G. Moses, J. Rossmeisl, A. Riisager, A.D. Jensen, Ketene as a Reaction Intermediate in the Carbonylation of Dimethyl Ether to Methyl Acetate over Mordenite, Angew. Chemie - Int. Ed. 54 (2015) 7261–7264. https://doi.org/10.1002/anie.201410974.

[53] S. Najari, G. Grof, S. Saeidi, Enhancement of hydrogenation of CO2 to hydrocarbons via In-Situ water removal, Int. J. Hydrogen Energy. 44 (2019) 24759–24781. https://doi.org/10.1016/j.ijhydene.2019.07.159.

[54] J. Xie, D.S. Firth, T. Cordero-lanzac, A. Airi, C. Negri, S. Øien-ødegaard, K.P. Lillerud, S. Bordiga, U. Olsbye, MAPO-18 Catalysts for the Methanol to Olefins Process: Influence of Catalyst Acidity in a High-Pressure Syngas (CO and H2) Environment, ACS Catal. 12 (2022) 1520–1531.

[55] S.S. Arora, D.L.S. Nieskens, A. Malek, A. Bhan, Lifetime improvement in methanol-to-olefins Catalysis Over Chabazite Materials By High-Pressure H2 Co-feeds, Nat. Catal. 1 (2018). http://dx.doi.org/10.1038/s41929-018-0125-2.

[56] X. Zhao, J. Li, P. Tian, L. Wang, X. Li, S. Lin, X. Guo, Z. Liu, Achieving a Superlong Lifetime in the Zeolite-Catalyzed MTO Reaction under High Pressure: Synergistic Effect of Hydrogen and Water, ACS Catal. 9 (2019) 3017–3025.

https://doi.org/10.1021/acscatal.8b04402.

6 Deactivation Phenomena for Bi-functional Catalysts Composed of ZnO/ZrO_2 and CHA Topology Solid Acid

On the next page, the manuscript with the title: *Deactivation Phenomena for Bi-functional Catalysts Composed of ZnO/ZrO_2 and CHA Topology Solid Acid* are reprinted.

This manuscript is still under preparation.

Deactivation Phenomena for Bi-functional Catalysts Composed of ZnO/ZrO_2 and CHA Topology Solid Acid

M. T. Nikolajsen[1], L. P. Hansen[2], N. C. Schjødt[2], U. V. Mentzel[2], J. Sehested[2], R. Y. Brogaard[2], J. M. Christensen[1] and M. Høj[1*]

[1] Department of Chemical Engineering, Technical University of Denmark (DTU), Kgs. Lyngby, 2800 (Denmark).

[2] Topsoe A/S, Kgs. Lyngby, 2800 (Denmark).

[*]Corresponding author: mh@kt.dtu.dk

1 Materials and Method

1.1 Catalyst preparation

The $ZnO/t\text{-}ZrO_2$ catalyst was prepared by the incipient wetness impregnation method. Before impregnation, the $t\text{-}ZrO_2$ support was dried overnight at 120 ºC and the precise water uptake was determined of the dried support. A solution of $Zn(NO_3)_2{\cdot}6H_2O$ with the volume determined by the water uptake was prepared to achieve 18 mol% Zn/(Zr+Zn). The prepared solution was then added to the $t\text{-}ZrO_2$ support and the impregnated catalyst was dried overnight at 100 ºC. Finally, the dried catalyst was calcined in air at 500 ºC for five hours. The $t\text{-}ZrO_2$ support had a surface area of 145 145 m^2/g (stabilized by Al_2O_3) and was provided by Saint-Gobain NorPro.

The NH_4-SAPO-34 samples were obtained from ACS Material®. The NH_4-SAPO-34 was calcined at 550 ºC for 3 hours to convert the ammonium-cation to a proton.

The bifunctional catalysts were physically mixed as granulates of 150-300µm with 80 wt% metal oxide to 20 wt% H-SAPO-34.

The spent bi-functional catalyst was obtained from an experiment where the pressure was changed from 10 to 30 bar in 5 bar intervals and afterwards returned to 10 bar at 400 ºC and 5000 mL/g/h. The total hours on stream for this experiment was 21 hours. The second spent bi-functional catalyst was obtained after 80 hours on stream at constant conditions (400 ºC, 10 bar and 5000 mL/g/h) which was then treated in an oxidative regeneration environment and finally used for activity test at the same conditions for 38 hours.

1.2 Catalyst characterization

XRD analysis was conducted with a PanAlytical X′Pert Pro instrument in Bragg-Brentano Geometry in reflectance mode using a Cu K_α radiation source (λ = 1.541 Å) at ambient conditions. The scan

range was 5–70° with a step size of 0.017°. The Rietveld analysis was performed using the Topas software.

Transmission electron microscopy imaging of the catalysts was performed on a Thermo Fisher Spectra 200 X-CFEG (S)TEM microscope equipped with Dual-X EDS detectors. The catalyst samples were crushed in a mortar and dispersed in absolute ethanol (99.9%) before drop casting on a Cu-TEM grid covered with lacey carbon film (SPI supplies). Images and energy dispersive X-ray (EDX) spectroscopy maps were acquired in scanning transmission mode (STEM) with a probe current of 0.2 nA and a probe convergence angle of 30 mrad. Detector collection angles of 0-22 mrad and 56-200 mrad were applied for the bright-field (BF) and high-angular annular dark field (HAADF) detector, respectively. The EDX maps were acquired continuously scanning for >10 minutes to obtain decent signals and were post-processed in Velox 3.8 to generate element composite images with pixel-averaged smoothing.

In-situ XAS experiments were conducted at the Swiss Light Source synchrotron at the SuperXAS beamline. Quartz capillaries (length of 80 mm, outer diameter 0.8 mm with 0.01 mm wall thickness) were loaded with 100-200 µm $ZnAl_2O_4$ or $ZnGa_2O_4$ particles diluted 1:8 in inert α-Al_2O_3. To ensure a pressure tolerance of 20 bar, the loaded capillaries were glued using Araldite Rapid Epoxy to a sample holder and cured for several hours. Hereafter, the sample holder was connected to the flow setup, where H_2, 10% CO/He, CO_2, 10% O_2/He and He gasses were connected. The capillaries were heated by radiative heaters, proprietary of the SuperXAS beamline and the off gases were analyzed by a mass spectrometer. The experimental procedure included dehydration of the catalysts in O_2/He with a heating ramp of 10 °C /min to 400 °C at 2 or 15 bar, followed by cooling to room temperature. Hereafter, the gas was switched to a syngas mixture ($CO/CO_2/H_2$/He = 5/12/37/46, filtered through an active carbon filter to remove nickel carbonyls) or H_2. When a stable MS signal was achieved, the reactor was heated to 400 °C at 10 °C /min and kept at 400 °C for 2 hours. After this, periodic switching between syngas or H_2 and O_2/He was conducted in the time interval of 10 min for a total of 180 min, followed by cooling to room temperature. Time resolved spectra were continuously recorded in fluorescence mode in the middle of the catalytic bed through all the above-mentioned steps. The spectra were recorded in QEXAFS mode at 1 Hz oscillation of the monochromator. Data importing, energy calibration, rebinning, averaging and exporting was done using the ProQEXAFS software proprietary of the beamline. Further details can be found in [1].

1.3 Catalytic activity evaluation and oxidative regeneration

A high-pressure flow reactor setup was used for the bifunctional catalyst activity measurements. These were conducted in a quartz-lined reactor tube with an inner diameter of 4 mm. Typically, 500 mg of total catalyst, 400 mg metal oxide and 100 mg zeotype with both components sieved to a grain size of 150-300 µm, was loaded into the reactor tube. The activity measurements were conducted using a synthesis gas $CO_2/H_2/Ar$ with the composition 23/69/8 vol% at 10 barg and 400 ºC. The reaction temperature was controlled by a N-type thermocouple placed right above the catalyst bed inside the reactor tube and an electric furnace with three heating zones. No pre-treatment was performed to the catalysts before the catalytic testing. The internal standard, argon, was used to account for the decrease in reaction volume. The effluent gas was analyzed by an online GC (ThermoFisher Trace 1300, assembled by Global Analyzer Solutions) equipped with a thermal conductivity detector (TCD) and a flame ionization detector (FID). The GC column connected to the flame ionization detector was Rt-Q-bond (30m, 0.32 mmID and 10µm df), which separated the formed hydrocarbon products from C_1 to C_6. A combination of Hayesep N, XL Sulfur and Molsieve 5A columns were connected to the TCD detector for quantification of CO, CO_2, and Ar. The CO_2 conversion, oxygenate (CH_3OH + CH_3OCH_3) selectivity, and oxygenate formation rate were calculated by Eq. (1) to (3).

$$\dot{F}_{i,out} = \dot{V}_{in} \cdot \frac{y_{Ar,in}}{y_{Ar,out}} \cdot y_{i,out} \cdot V_m^{-1} \quad (1)$$

$$X_{CO_2} = 1 - \frac{\dot{F}_{CO_2,out}}{\dot{F}_{CO_2,in}} \quad (2)$$

$$S_{Oxy} = \frac{\dot{F}_{CH_3OH,out} + 2 \cdot \dot{F}_{CH_3OCH_3,out}}{\dot{F}_{CO_2,in} - \dot{F}_{CO_2,out}} \cdot 100\% \quad (3)$$

Where $\dot{V}$ is the volumetric flow rate at standard conditions, V_m is the molar volume, m_c is the weight of the catalyst, and M_w is the molar mass. $\dot{F}_i$ and y_i are the molar flow rate and molar fraction of component i. The hydrocarbon selectivity within hydrocarbons (oxygenates included) was calculated by Eq. (4).

$$S_{HC,i} = \frac{n_{c,i} \cdot \dot{F}_{HC,i}}{\sum_{i=1}^{N} n_{c,i} \cdot \dot{F}_{HC,i}} \cdot 100\% \quad (4)$$

Where $n_{c,i}$ is the number of carbon atoms within the hydrocarbon product.

For the oxidative regeneration, the reactor was heated with a temperature ramp of 5 ºC/min to 500ºC in a gas flow of 100 mL/min of 5 vol% oxygen diluted in nitrogen at 1 atm for the first 185 min. Hereafter, a 10 vol% oxygen mixture was applied at 500 ºC to ensure complete carbon removal. The setup was connected to an FT-IR, in which it was possible to monitor the amount of CO_2 and CO formed during oxidative regeneration.

2 Results and Discussion

2.1 Bi-functional catalyst activity and selectivity

ZnO supported on tetragonal zirconia (t-ZrO_2) was shown to selectively produce methanol form CO_2 at elevated temperatures, making them promising candidates when combined with solid acids, for the combined methanol synthesis and methanol dehydration reaction. The methanol synthesis rate for the ZnO/t-ZrO_2 correlated with the amount of ZnO surface domains on the t-ZrO_2 surface and the optimal catalyst was obtained with a Zn-loading for 18 mol% for the used t-ZrO_2 support with an SSA of 145 m^2/g [1]. Fig. 1 show the results for direct conversion of CO_2 into light olefins when combining the optimized ZnO/t-ZrO_2 and SAPO-34 catalyst at different reaction conditions.

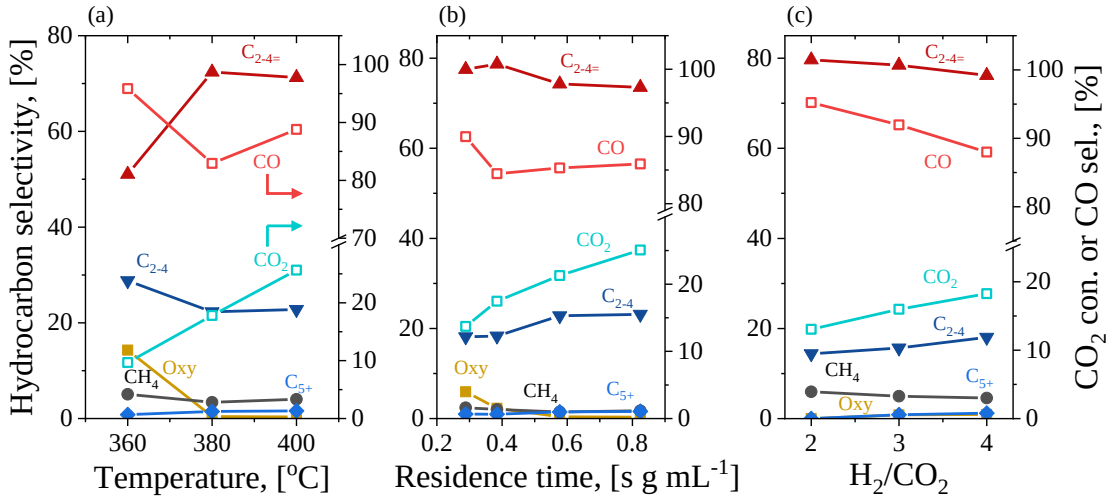


Fig. 1. CO_2 conversion and CO and hydrocarbons selectivities at different (a) temperatures, (b) residence times and (c) H_2/CO_2 ratios. Reaction conditons: 10 bar, 5000 mL/g/h, (c) 7500 mL/g/h, (b-c) 380 ºC, $CO_2/H_2/Ar$ = 23/69/8 vol%, and catalyst ZnO/t-ZrO_2 + SAPO-34 mixed 4:1.

Operating the bi-functional catalysts at 360 ºC resulted in low methanol dehydration activity over the SAPO-34 catalyst, as evident form the significant amount of unconverted oxygenates (mostly methanol) leaving the reactor, as illustrated in Fig. 1 (a). The high concentration of unconverted methanol in the reactor inhibited the CO_2 hydrogenation reaction, as this reaction approached equilibrium (Fig. S1). Furthermore, most of the converted CO_2 formed CO through the reverse-water-gas-shift reaction yielding a high CO selectivity. Upon increasing the temperature by 20 ºC, the methanol dehydration activity improved, now converting all the oxygenates to hydrocarbons. This also improved the CO_2 hydrogenation, because the methanol partial pressure was reduced, ensuring that the CO_2 hydrogenation reaction was further from equilibrium. Furthermore, the rate of the reaction increased with temperature. More importantly, the CO selectivity decreased, showing that more of the converted CO_2 formed hydrocarbons. As the reverse-water-gas-shift reaction is endothermic, it could at first seem counter-intuitive that the CO selectivity decreased with increasing temperature. However, the production of water from the CO_2 hydrogenation and the methanol dehydration reactions forced the reverse-water-gas-shift reaction closer to equilibrium and thereby limited the CO formation rate. As shown in Fig. 1 (b), a similar trend in the CO selectivity was observed when going from short residence time, where there was unconverted oxygenates in the reactor outlet, to longer residence time where complete oxygenate conversion was achieved. This change in the thermodynamic driving force for the reverse-water-gas-shift reaction, thus explains the improved CO selectivity. As the reverse water gas shift equilibrium constant increased at higher temperatures, the CO selectivity again increased when increasing the reaction temperature to 400 ºC, as illustrated in Fig. 1 (a). Going from 380 to 400 ºC did not significantly change the light olefin selectivity, which stayed above 70 % on carbon basis. The highest selectivity was obtained at residence times allowing for complete oxygenate conversion, but at even longer residence times, the light olefin selectivity decreased, likely due to hydrogenation reactions forming light paraffins (Fig. 1 (b)). At complete oxygenate conversion, the CO_2 conversion increased with increasing residence time, revealing a trade-off between CO_2 conversion and light olefin selectivity [2,3]. In Fig. 1 (c), the results for increasing the CO_2/H_2 ratio in the feed show improved CO_2 to hydrocarbons conversion from 0.7 to 2.2 %, at the expense of a slightly more hydrogenated product causing the light olefin selectivity to decrease from 79 to 76 %. Operating the bi-functional catalysts with a H_2/CO_2 ratio of four increased the olefin yield by a factor of three. Similar improvement was also found for the In_2O_3-ZrO_2/SAPO-34 catalyst by increasing the H_2/CO_2

ratio, but by increasing the pressure the hydrogen incorporation increased exponentially [3]. Therefore, this strategy is only applicable at low-pressure operation, where the CO_2 to hydrocarbon conversion is low.

2.2 Bi-functional catalysts stability and oxidative regeneration

The results shown in Fig. 1, demonstrate that it was possible to produce light olefins with a selectivity above 70 % on carbon basis at a CO_2 conversion to hydrocarbons of ~3 %. When converting methanol over solid acids with the chabazite topology in the methanol-to-olefin process, fast deactivation occurs [4,5]. This deactivation occurs due to the formation of coke precursors (methylated aromatics and/or poly-aromatic species) within the cages of the chabazite crystal, which cannot diffuse out through the small pore openings connecting the cages [4,6]. Therefore, it is of great interest to investigate the stability of bi-functional catalysts composed of metal oxides and chabazite solid acids. In Fig. 2 (a) the results from stability measurement of the bi-functional catalyst conducted over 80 hours on stream are illustrated. The results showed a minor drop in the CO_2 conversion and a minor increase in the CO selectivity during the 80 hours on stream. The accumulated amount of methanol converted per g of SAPO-34 reached 22 g, which indicate a superior stability compared to the methanol-to-olefin reaction, where significant deactivation occurs within 18 g methanol converted per g SAPO-34 [5]. Thus, the coking mechanism for the SAPO-34 catalyst under the reaction conditions applied to the bi-functional catalysts changed, which improved the catalysts lifetime. The retained coke precursor molecules observed in SAPO-34 catalysts, used in similar bi-functional catalyst experiments, was smaller and consisted mostly of mono- and diaromatics, as compared to tri- and tetraaromatic species for the methanol-to-olefins reaction [7]. The change in the nature of the coke species could be explained by induced cracking reactions at the high hydrogen partial pressure [8], and/or that hydrogenation of aromatic molecules slowed down the evolution of coke species [9].

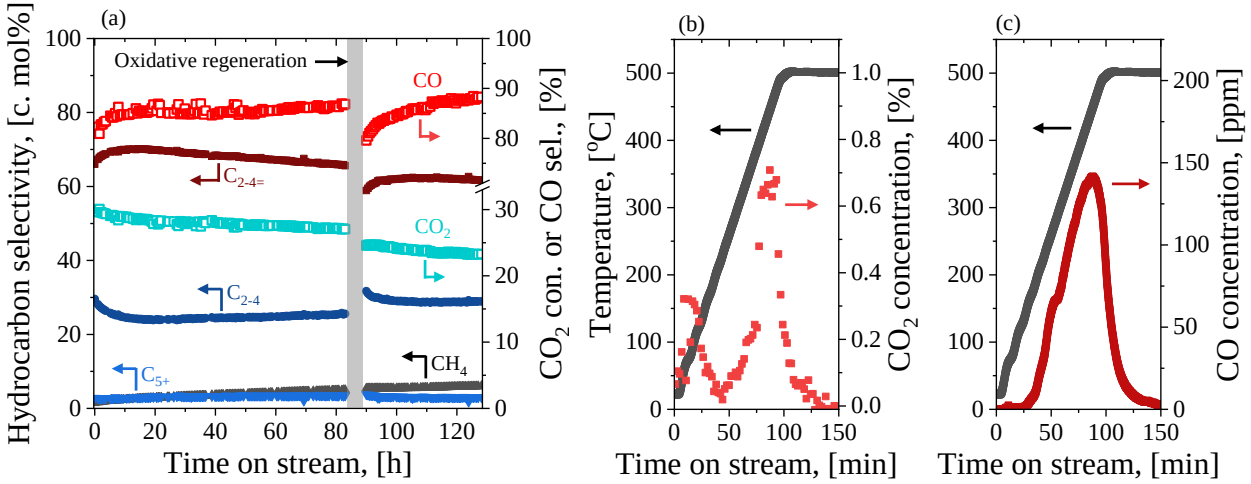


Fig. 2. (a) CO_2 conversion and CO and hydrocarbons selectivities with time on stream before and after catalyst regeneration. (b) and (c) Concentration of CO_2 and CO in the effluent gas and the temperature with time on stream for the oxidative regeneration of the ZnO/t-ZrO_2+SAPO-34 catalyst. Reaction conditions: (a) 400 ºC, 10 bar, 5000 mL/g/h, $CO_2/H_2/Ar$ = 23/69/8 vol%, and catalyst ZnO/t-ZrO_2 + SAPO-34 mixed 4:1. (b-c) 1 atm, 100 mL/min, 5 vol% oxygen in nitrogen.

As shown in Fig. 2 (a), the CO_2 conversion to hydrocarbons decreased slowly with time on stream, which indicated that a slower deactivation occurred. Coking, formed at a rate lower than expected for methanol to olefins, could be responsible for the change in activity, as the formation of carbon deposits was evident from the color of the SAPO-34 grains after reaction, which had turned from white to gray/black. Therefore, it is likely that the bi-functional catalysts would need to be regenerated at some point. Normally, regeneration of methanol to hydrocarbons solid acid catalysts occurs through oxidative treatment, where the carbon deposits are oxidized with air or diluted air at high temperature. To investigate the effect of such treatment, an oxidative regeneration of the bi-functional catalysts operated for more than 80 hours was conducted. It is clear from the CO_2 and CO concentration profiles in Fig. 2 (a) and (b) that carbon deposits were retained in the SAPO-34 catalyst. Most bi-functional catalysts reported in the literature have only been tested for ≤ 100 hours on stream and with high amount of SAPO-34 in the catalyst mixture, which likely masks deactivation by coking, as only a fraction of the loaded SAPO-34 needs to be active to achieve full conversion of the intermediate methanol [10–12]. Since coke molecules were retained in the SAPO-34 catalyst, regeneration would most likely be necessary at some point. However, the oxidative regeneration resulted in an even less active bi-functional catalyst than immediately before the regeneration, as evident from the drop in CO_2 conversion after regeneration, as illustrated in Fig. 2 (a). Furthermore, the regeneration induced the olefin hydrogenation activity, causing higher light paraffin selectivity.

As shown in Fig. 2 (a), the initial CO selectivity was low, both for the fresh and the regenerated catalyst, but it increased rapidly within the first 10 hours, before it stabilized and showed slower increase with time on stream. The initial low CO selectivity could be the result of a highly active SAPO-34 catalyst that efficiently dehydrated the methanol, which formed water that inhibited the reverse-water-gas-shift reaction. The initial rapid increase in the CO selectivity could be the result of the formation of carbon deposits within the cages, but due to hydrogenation the evaluation of larger coke species was slow [9]. The opposite trend was observed for the light paraffins selectivity, which decreases rapidly within the first 10 hours. It is well established that a high acidity of the solid acid applied in bi-functional catalysts results in high hydrogenation activity [5,13,14]. The attenuation of acid sites by carbon deposits formed initially explained both the decrease in paraffins selectivity and the increase CO selectivity. Since this was observed both before and after the regeneration, suggests that the activity of the SAPO-34 catalysts was regained. Thus, the cause of the decrease in CO_2 conversion was most likely due to changes occurring to the metal oxide component.

2.3 The stability of the surface ZnO phase in reductive and oxidative atmospheres

To investigate the changes occurring for ZnO/t-ZrO_2 catalyst under operation, operando XAS at the Zn K-edge was conducted during catalyst dehydration, methanol synthesis conditions, and by switching between syngas and O_2 exposure for 9 cycles. The XANES and FT-EXAFS spectra illustrated in Fig. 3 (a) and (b) were obtained at room temperature after each treatment, all performed at 400 °C. The absorption edge at 9662 eV for the ZnO/t-ZrO_2 in the XANES spectra (Fig. 3 (a)) shows that the oxidation state was Zn^{2+} and did not change during the experiments. The adsorption edge for metallic Zn lies at 9659 eV, thus significant Zn reduction would be visible by a shift of the adsorption edge, which was not observed [15,16]. The dehydration and steady state methanol synthesis did not change the EXAFS spectra, as illustrated in Fig. 3 (b). The low Zn-Zn backscattering amplitude at 2.9 Å observed in the EXAFS spectra after these two treatments indicated that the ZnO was present as the highly active surface ZnO phase [1]. This shows that under catalyst dehydration and steady state methanol synthesis the main active sites were maintained [1].

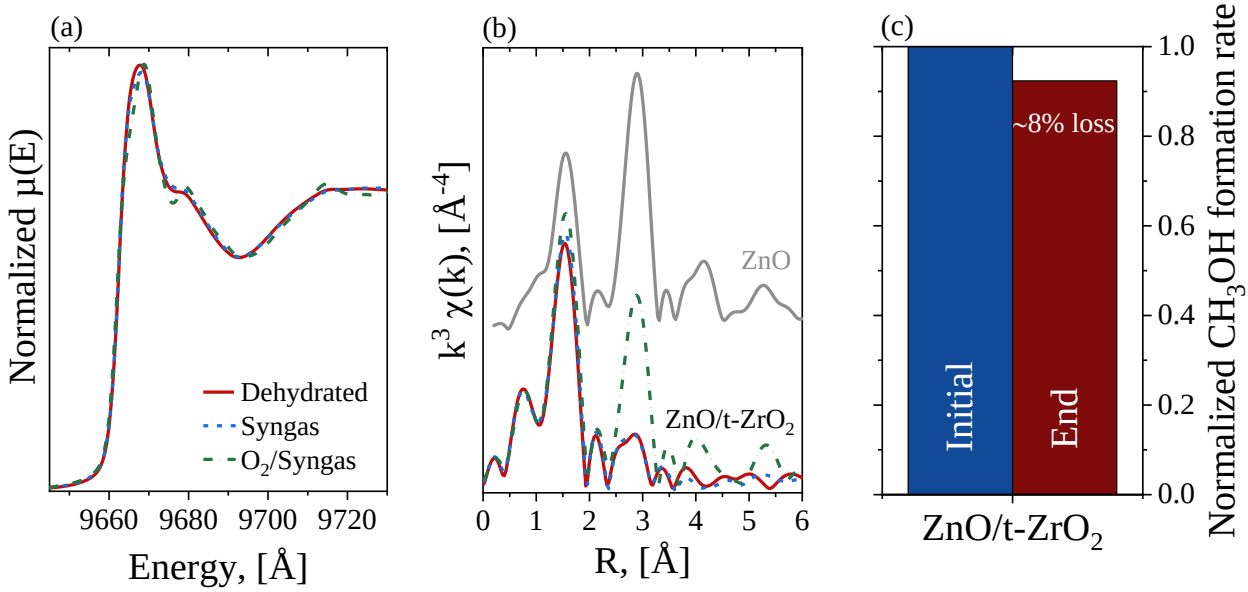


Fig. 3. (a) Zn K-edge XANES and (b) the Fourier-transformed k^3-weighted EXAFS spectra of the ZnO/t-ZrO_2 catalyst obtained at room temperature after the dehydration step, steady state methanol synthesis in syngas and periodic switching between the syngas mixture and O_2/He through 9 cycles. (c) The normalized CH_3OH formation rate for the first cycle (initial) and the 9th cycle (end) determined from the MS signal at m/z = 31. Reaction conditions: 400 °C, 15 barg, 50 NmL/h, catalyst loading of ~2.5 mg (diluted 1:4 in inert α-Al_2O_3), feed gas composition of CO_2/CO/H_2/He 12/5/37/46 or O_2/He of 10/90.

However, when the catalyst was exposed to cyclic changes between reducing and oxidizing conditions, an irreversible formation of crystalline ZnO was observed from a significant increase in the Zn-Zn backscattering amplitude (Fig. 3 (b)). The conversion of the surface ZnO to crystalline ZnO deactivated the catalyst, as illustrated in Fig. 3 (c). Thus, the oxidative regeneration of the bi-functional catalyst composed of ZnO/t-ZrO_2 could result in the sintering of the surface ZnO phase into larger crystalline ZnO particles. This explains the observed decrease in CO_2 conversion after oxidative regeneration of the bi-functional catalysts (Fig. 2 (a)), and also the increased hydrogenation activity, as larger ZnO crystals have showed to increase the light paraffins selectivity for bi-functional catalysts [17]. The sintering of the ZnO phase in oxygen rich atmospheres questions the ability of using Zn-based metal oxides as the methanol synthesis component in bi-functional catalyst, if oxidative regeneration is necessary to regain the activity.

2.4 Deactivation by ZnO sintering and internal carbon deposition

X-ray diffraction (XRD) analysis on the pure t-ZrO_2 support, the SAPO-34, the prepared ZnO/t-ZrO_2 catalysts and spent bi-functional catalysts from two different experiments were conducted. In Fig. 4 (a), the XRD patterns for the SAPO-34 and t-ZrO_2 support confirmed that the main crystal phases were chabazite and tetragonal zirconia. For the as prepared catalyst ~1 wt% hexagonal ZnO was visible, but no structural changes were observed for the t-ZrO_2 support. This indicate that ZnO was only present on the zirconia surface and did not migrate into the ZrO_2 lattice. The first spent bi-

functional catalyst was obtained from an experiment where the pressure was changed from 10 to 30 bar in 5 bar intervals and afterwards returned to 10 bar. The total time on stream for this experiment was 21 hours and catalytic performance can be found in Fig. S2. The second spent bi-functional catalyst was obtained after oxidative regeneration and the activity test shown in Fig. 2 (a). The XRD patterns, illustrated in Fig. 4 (a), for the spent bi-functional catalysts show the presence of the mixture of t-ZrO_2 and SAPO-34. The t-ZrO_2 lattice parameters did not change during the two experiments and Rietveld refinement showed little change to the crystallite size, which increased from 83 to 99 Å, as shown in Fig. 4 (b). If the Zn migrated into the t-ZrO_2 structure, a systemic peak shift to higher angles should be visible in Fig. 4 (a), which was not the case [18]. These results show that the t-ZrO_2 structure was stable under the CO_2 conversion to olefins conditions and that the Zn did not interfere with the t-ZrO_2 lattice.

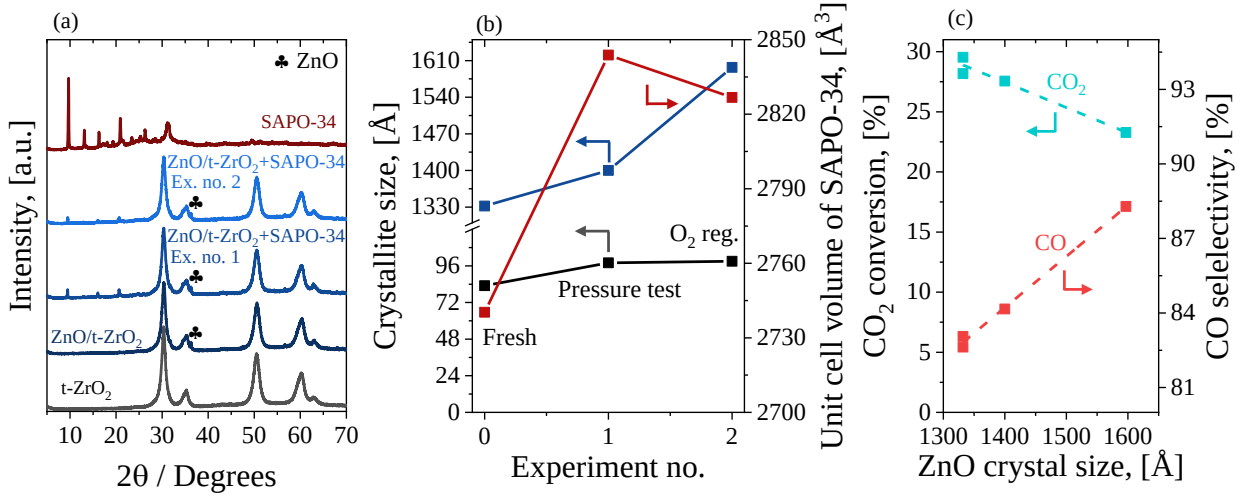


Fig. 4. (a) XRD patterns of t-ZrO_2, ZnO/t-ZrO_2, SAPO-34, and spent bi-functional catalysts composed of ZnO/t-ZrO_2 and SAPO-34 mixed 4:1. (b) The ZrO_2 and ZnO crystallite size and the unit cell volume of the SAPO-34 catalyst from fresh and spent bi-functional catalysts after experiments 1 and 2. Experiment 1 was operated at increasing pressures from 10 to 30 bar at 5 bars interval at 400 ºC for a total of 21 hours on stream. Experiment 2 was the stability test before and after the oxidative regeneration (Fig. 2 (a)). (c) The fresh and spent CO_2 conversion and CO selectivity predicted against the ZnO crystal size. Reaction conditions: 400 ºC, 10 bar, 5000 mL/g/h, $CO_2/H_2/Ar$ = 23/69/8 vol%, and the catalyst ZnO/t-ZrO_2 + SAPO-34 mixed 4:1.

Rietveld refinement showed that the small amount of h-ZnO did not change significantly and was maintained at ~1 wt%. However, the ZnO sintered under reaction conditions creating larger ZnO crystals, as shown in Fig. 4 (b). The initial and final CO_2 conversion and CO selectivity for the two experiments in Fig. 4 (c), show that the sintering of the ZnO phase may be one reason for reduced CO_2 to hydrocarbons conversion. By estimating the ZnO surface area from the crystallite size, the surface area decreased from 8 to 7 m^2/g. This extremely low surface area will result in negligible methanol synthesis activity showing that these crystals cannot be the main active sites. The loss of

ZnO crystal surface area can thereby not explain the change in the activity alone (Fig. 4 (c)). However, the creation of these larger ZnO crystals could reveal a loss of the highly active surface ZnO domains, which were not detected by XRD as they were not present in a repeated crystalline structure. Thus, the decrease in activity was most likely related to the loss of these sites, as they sinter into larger ZnO crystals. This loss in activity with the formation of more crystalline ZnO was in line with the observations for the in-situ XAS analysis in Fig. 3. However, an increase in the amount of h-ZnO detected by XRD as the surface ZnO sinter would be expected, but was not observed. The ZnO/t-ZrO_2 dilution in SAPO-34 increased the complexity of the diffraction patterns and the overall small amount of h-ZnO could explain that changes in the amount of h-ZnO were difficult to observe.

The unit cell volume of the SAPO-34 crystals increased for the spent bi-functional catalysts. This suggest that carbon deposits were formed within the SAPO-34 cages that increased the strain on the lattice, which slightly increased the unit cell volume [19]. The formation of carbon deposits would affect the methanol dehydration rate, while could change the thermodynamic driving force, explaining the loss in activity shown in Fig. 4 (c). This makes it difficult to decouple the deactivation effect caused by carbon deposits and/or by surface ZnO sintering, but indicates that both deactivation phenomena occurred for bi-functional catalysts.

2.5 Zinc migration

For further clarification of the deactivation phenomena occurring for the bi-functional catalysts, high-resolution transmission electron microcopy (HR-TEM) was conducted on the spent bi-functional catalysts, the SAPO-34, and the ZnO/t-ZrO_2 catalyst. The images and the EDX spectroscopy maps acquired in scanning transmission mode of multiple particles for the ZnO/t-ZrO_2 and the spent bi-functional catalyst are illustrated in Fig. 7 (a) and (b), respectively. The mapping of Zn, Zr, and Al were chosen as Zn and Zr show the metal oxide component, while Al comes from the SAPO-34 crystals, making them clearly distinguishable. The results in Fig. 7, show that the Zn was well dispersed on the t-ZrO_2 support on the as-prepared ZnO/t-ZrO_2 catalyst, but after the CO_2 conversion to olefins reaction, larger surface domains of Zn were visible. This demonstrates that Zn became mobile under reaction conditions and sintered into larger particles rich in Zn. This sintering resulted in a less active methanol synthesis catalyst and may explain some of the deactivation observed with time on stream (Fig. 2 (a)). Zooming in on a ZnO/t-ZrO_2 particle for the spent bi-functional catalyst showed that smaller ZnO surface domains were still present (Fig. S3), which are believed to be the main active sites and their presences was the reason of the remaining CO_2 hydrogenation activity [1].

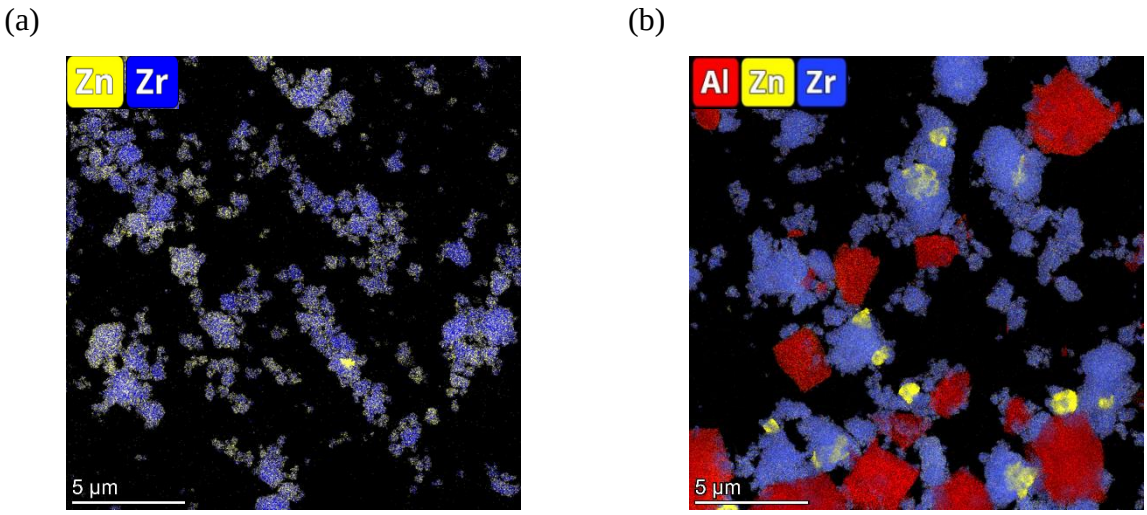


Fig. 5. TEM-EDX element map of Zn, Zr and Al of the (a) as prepared ZnO/t-ZrO_2 catalyst and (b) the spent ZnO/t-ZrO_2+SAPO-34 bi-functional catalyst.

Large surface Zn particles were also observed for the regenerated bi-functional catalyst as illustrated Fig. S4. The ZnO/t-ZrO_2 component in the regenerated bi-functional catalyst showed evidence for ZnO lattice fringes (~2.60 Å) in the HR-TEM image in Fig. 6 [13]. Thus, the exposure to high temperature and oxygen sintered the ZnO into larger particles and formed ZnO crystals, which was in line with the results observed from the in-situ XAS analysis. This formation of crystalline ZnO inhibited the methanol synthesis activity.

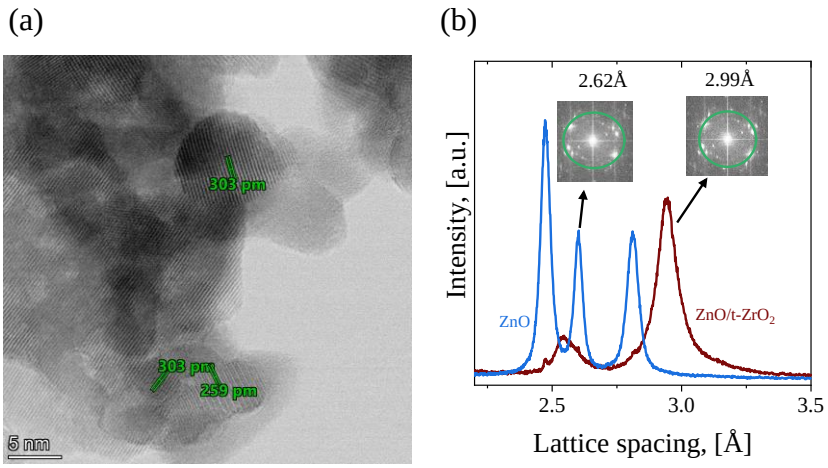


Fig. 6. (a) High-resolution transmission electron microscopy image (bright field) of the ZnO/t-ZrO_2 competent of the regenerated bi-functional catalyst. (b) The intensity against the lattice spacing from the XRD analysis and the comparison with the observed lattice spacing from electron diffraction obtained from the Fourier transformed HR-TEM image (a).

The Zn mobility was not only evident form the sintering of the ZnO surface domains, Zn was found to migrate into the SAPO-34 catalyst as well [20,21]. The EDX spectroscopy maps at the interface between the ZnO/t-ZrO_2 and SAPO-34 components shown in Fig. 7, demonstrate that Zn was not

only present on the t-ZrO_2 surface, but had also migrated into the SAPO-34 catalyst. A steady decrease in the olefin selectivity was observed in Fig. 2 (a) from 10 to 85 hours on stream, after the initial carbon deposit formation within the first 10 hours on stream. Zn migration into SAPO-34 catalysts have shown to increase the olefin hydrogenation activity [21], and could thereby explain the steady decrease in the light olefins selectivity and the corresponding steady increase in light paraffins selectivity as Zn migrates into the SAPO-34 catalyst. The methanol synthesis activity for Zn containing SAPO-34 is unknown but believed to be negligible compared to the activity of the ZnO/t-ZrO_2 catalyst. Thus, Zn migration from the ZnO/t-ZrO_2 component to the SAPO-34 would result in a decrease in the methanol synthesis rate.

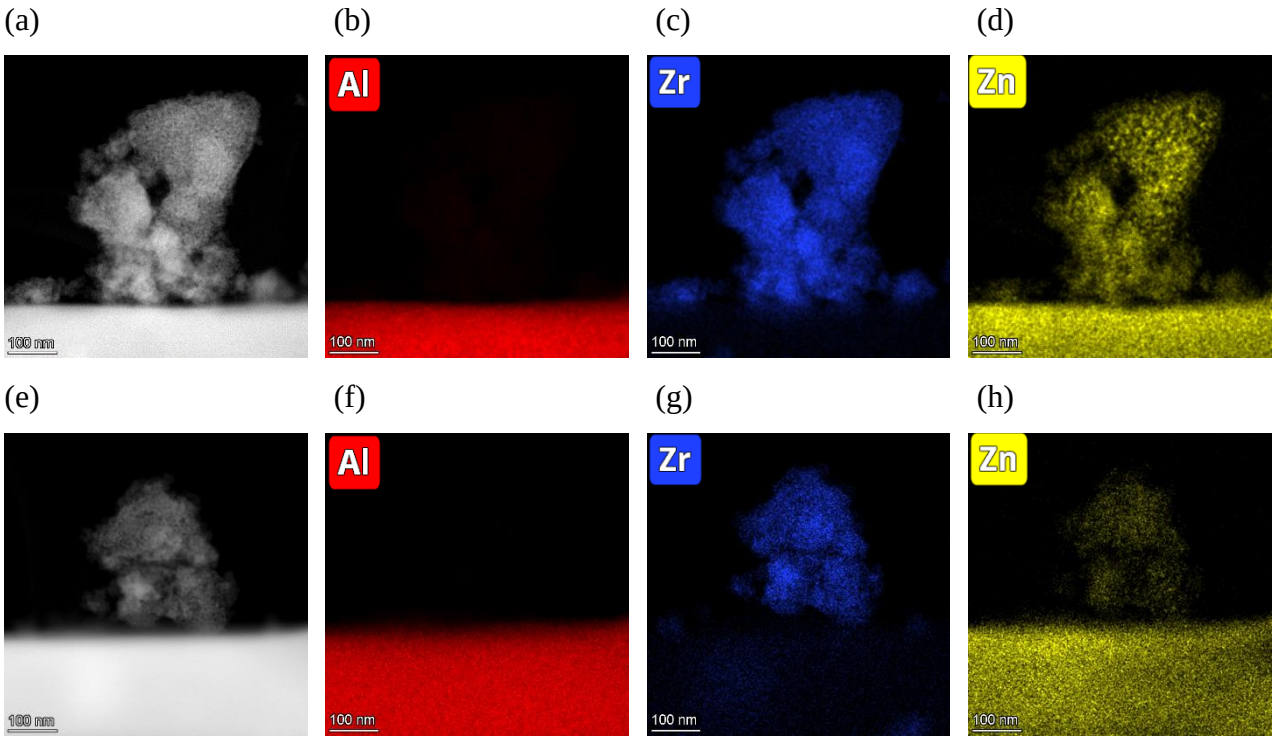


Fig. 7. High-angle annular dark field transmission electron microscopy image of (a) spent bi-functional catalyst and (e) spent oxidative regenerated bi-functional catalyst. EDX element map of Al, Zr and Zn of the spent bi-functional catalyst (b-d) and spent oxidative regenerated bi-functional catalyst (f-h).

As shown in Fig. 8 (a) and (b), the SAPO-34 was present as well-defined, box shaped crystals, easily distinguished from the more random structured metal oxide. The EDX intensity through a SAPO-34 crystal, through the path highlighted with the green arrow in Fig. 8 (b), showed that the migrated Zn was mostly present close to the periphery of the SAPO-34 crystal. This was evident by the high Zn intensity close to the SAPO-34 edges, while the intensity decreased at the crystal centre, as shown in Fig. 8 (c). The increase in the Zn and Zr intensities near the middle of the crystal was due to the presences of ZnO/t-ZrO_2 particles lying on top of the SAPO-34 crystal. However, the decrease in the

Zn intensity through the SAPO-34 crystal suggested that diffusion limitations limited the Zn migration into the centre of the crystal. Similar intensity profile was obtained from zooming in on a small ZnO/t-ZrO2 particle located at the edge a SAPO-34 crystal, clearly showing highest Zn intensity in the edge of the crystal (Fig. S5).

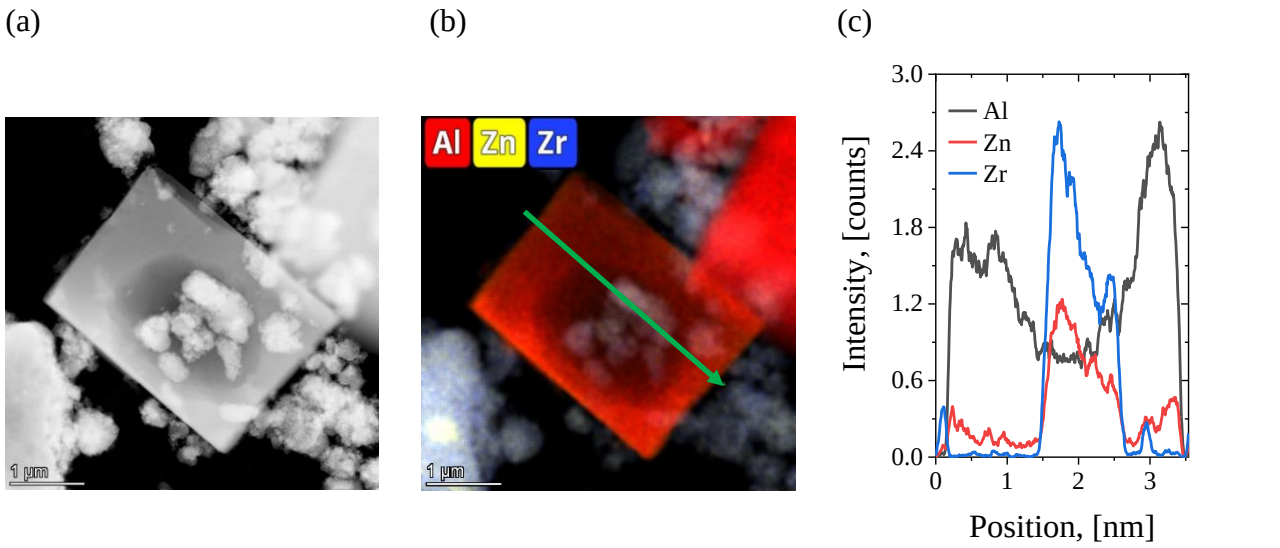


Fig. 8. (a) High-angle annular dark field transmission electron microscopy image and (b) EDX element map of Al, Zr and Zn of the spent bi-functional catalyst. (b) The green arrow highlights the path for which the intensities of Zn, Al and Zr were recorded. (c) The intensity of the Al, Zn and Zr through the SAPO-34 crystal.

3 Conclusions

The combination of the mixed oxide ZnO/t-ZrO_2 and SAPO-34 enabled the direct conversion of CO_2 into light olefins. Temperatures above 360 ºC were necessary to ensure complete oxygenate conversion over the SAPO-34 catalyst. Complete oxygenate conversion significantly altered the thermodynamic driving force for the reverse-water-gas-shift and the CO_2 hydrogenation reactions. For maximizing the selectivity towards light olefins, it was necessary to operate the reactor at low CO_2 to hydrocarbon conversions, using low pressure and a residence time just long enough to allow complete oxygenate conversion. Increasing the H_2/CO_2 ratio increased the CO_2 to hydrocarbons conversion without dramatically reducing in the light olefins selectivity at low operating pressure.

Great stability of the bi-functional catalyst was observed for over 80 hours on stream yielding a methanol conversion capacity above 22 g per g SAPO-34. This conversion capacity was superior to the methanol-to-olefins process. However, some deactivation occured with time on stream evident from the decreasing CO_2 conversion and changes in the product selectivities. Oxidative regeneration of the bi-functional catalyst confirmed the presence of carbon deposits. This treatment regained the activity of the SAPO-34 catalyst, but altered the metal oxide component, causing a lower CO_2 hydrogenation to methanol rate.

Operando XAS showed that in an oxygen rich atmosphere, ZnO sintering formed more crystalline ZnO, which showed lower methanol formation activity. HR-TEM analysis confirmed the presence of crystalline ZnO after the oxidative regeneration, as ZnO lattice fringes were identified. Thus, oxidative regeneration of the bi-functional catalyst negatively affect the Zn-based metal oxide's activity. XRD analysis of spent bi-functional catalysts indicated ZnO sintering and SAPO-34 unit cell expansion, as internal carbon deposits were formed, which explained the immediate loss in activity within 10 hours on stream. The TEM-EDX spectroscopy maps acquired for the spent bi-functional catalysts showed evidence for ZnO sintering and Zn migration into the SAPO-34 catalyst. The loss of Zn by migration and the sintering of the ZnO surface domains negatively affected the CO_2 hydrogenation rate and explained the steady decrease in olefin selectivity observed after 10 hours on stream. Three deactivation phenomena for the bi-functional catalysts were thus identified: carbon deposition in SAPO-34, surface ZnO sintering to crystalline h-ZnO and Zn migration from the metal oxide to SAPO-34. If the SAPO-34 catalyst needs regeneration, an oxidative regeneration method will result in formation of crystalline ZnO, which will cause further deactivation of the ZnO/t-ZrO_2 catalyst.

References

[1] M.T. Nikolajsen, J.-C. Grivel, A. Gaur, L.P. Hansen, L. Baumgarten, N.C. Schjødt, U. V Mentzel, J.-D. Grundwaldt, J. Sehested, J.M. Christensen, M. Høj, Surface ZnOx on Zirconia is Highly Active for High Temperature Methanol Synthesis, Submitt. to J. Catal. XX (2023) 1–32.

[2] Z. Li, J. Wang, Y. Qu, H. Liu, C. Tang, S. Miao, Z. Feng, H. An, C. Li, Highly Selective Conversion of Carbon Dioxide to Lower Olefins, ACS Catal. 7 (2017) 8544–8548. https://doi.org/10.1021/acscatal.7b03251.

[3] P. Gao, S. Dang, S. Li, X. Bu, Z. Liu, M. Qiu, C. Yang, H. Wang, L. Zhong, Y. Han, Q. Liu, W. Wei, Y. Sun, Direct Production of Lower Olefins from CO2 Conversion via Bifunctional Catalysis, ACS Catal. 8 (2018) 571–578. https://doi.org/10.1021/acscatal.7b02649.

[4] B.P.C. Hereijgers, F. Bleken, M.H. Nilsen, S. Svelle, K.P. Lillerud, M. Bjørgen, B.M. Weckhuysen, U. Olsbye, Product shape selectivity dominates the Methanol-to-Olefins (MTO) reaction over H-SAPO-34 catalysts, J. Catal. 264 (2009) 77–87. https://doi.org/10.1016/j.jcat.2009.03.009.

[5] F. Bleken, Æ.M. Bjørgen, Æ.L. Palumbo, S. Bordiga, Æ.S. Svelle, The Effect of Acid Strength on the Conversion of Methanol to Olefins Over Acidic Microporous Catalysts with the CHA Topology, Top Catal. 52 (2009) 218–228. https://doi.org/10.1007/s11244-008-9158-0.

[6] D.M. Marcus, W. Song, L.L. Ng, J.F. Haw, Aromatic hydrocarbon formation in HSAPO-18 catalysts: cage topology and acid site density, Langmuir. 18 (2002) 8386–8391. https://doi.org/10.1021/la011556i.

[7] D.L.S. Nieskens, J.D. Lunn, A. Malek, Understanding the Enhanced Lifetime of SAPO-34 in a Direct Syngas-to-Hydrocarbons Process, ACS Catal. 9 (2019) 691–700. https://doi.org/10.1021/acscatal.8b03465.

[8] P. Castaño, J.M. Arandes, M. Olazar, J. Bilbao, B. Pawelec, U. Sedrán, Effect of hydrogen on the cracking mechanisms of cycloalkanes over zeolites, Catal. Today. 150 (2010) 363–367. https://doi.org/10.1016/j.cattod.2009.09.013.

[9] X. Zhao, J. Li, P. Tian, L. Wang, X. Li, S. Lin, X. Guo, Z. Liu, Achieving a Superlong Lifetime in the Zeolite-Catalyzed MTO Reaction under High Pressure: Synergistic Effect of Hydrogen and Water, ACS Catal. 9 (2019) 3017–3025. https://doi.org/10.1021/acscatal.8b04402.

[10] T. Numpilai, C. Wattanakit, M. Chareonpanich, J. Limtrakul, T. Witoon, Optimization of synthesis condition for CO2 hydrogenation to light olefins over In2O3 admixed with SAPO-

34, Energy Convers. Manag. 180 (2019) 511–523.

[11] S. Dang, S. Li, C. Yang, X. Chen, X. Li, L. Zhong, P. Gao, Y. Sun, Selective Transformation of CO2 and H2 into Lower Olefins over In2O3-ZnZrOx/SAPO-34 Bifunctional Catalysts, ChemSusChem. 12 (2019) 3582–3591. https://doi.org/10.1002/cssc.201900958.

[12] S. Wang, P. Wang, D. Shi, S. He, L. Zhang, W. Yan, Z. Qin, J. Li, M. Dong, J. Wang, U. Olsbye, W. Fan, Direct Conversion of Syngas into Light Olefins with Low CO2 Emission, ACS Catal. 10 (2020) 2046–2059. https://doi.org/10.1021/acscatal.9b04629.

[13] K. Cheng, W. Zhou, J. Kang, S. He, S. Shi, Q. Zhang, Y. Pan, W. Wen, Y. Wang, Bifunctional Catalysts for One-Step Conversion of Syngas into Aromatics with Excellent Selectivity and Stability, Chem. 3 (2017) 334–347. https://doi.org/10.1016/j.chempr.2017.05.007.

[14] S. Bordiga, L. Regli, D. Cocina, C. Lamberti, M. Bjørgen, K.P. Lillerud, Assessing the acidity of high silica chabazite H-SSZ-13 by FTIR using CO as molecular probe: Comparison with H-SAPO-34, J. Phys. Chem. B. 109 (2005) 2779–2784. https://doi.org/10.1021/jp045498w.

[15] S. Han, D. Zhao, T. Otroshchenko, H. Lund, U. Bentrup, V.A. Kondratenko, N. Rockstroh, S. Bartling, D.E. Doronkin, J.D. Grunwaldt, U. Rodemerck, D. Linke, M. Gao, G. Jiang, E. V. Kondratenko, Elucidating the Nature of Active Sites and Fundamentals for their Creation in Zn-Containing ZrO2-Based Catalysts for Nonoxidative Propane Dehydrogenation, ACS Catal. 10 (2020) 8933–8949. https://doi.org/10.1021/acscatal.0c01580.

[16] S. Tada, N. Ochiai, H. Kinoshita, M. Yoshida, N. Shimada, T. Joutsuka, M. Nishijima, T. Honma, N. Yamauchi, Y. Kobayashi, K. Iyoki, Active Sites on ZnxZr1– x O2– x Solid Solution Catalysts for CO2 -to-Methanol Hydrogenation, ACS Catal. 12 (2022) 7748–7759. https://pubs.acs.org/doi/10.1021/acscatal.2c01996.

[17] N. Li, F. Jiao, X. Pan, Y. Ding, J. Feng, X. Bao, Size Effects of ZnO Nanoparticles in Bifunctional Catalysts for Selective Syngas Conversion, ACS Catal. 9 (2019) 960–966. https://doi.org/10.1021/acscatal.8b04105.

[18] J. Wang, G. Li, Z. Li, C. Tang, Z. Feng, H. An, H. Liu, T. Liu, C. Li, A highly selective and stable ZnO-ZrO2 solid solution catalyst for CO2 hydrogenation to methanol, Sci. Adv. 3 (2017) 1–11. https://doi.org/10.1126/sciadv.1701290.

[19] D. Rojo-Gama, M. Nielsen, D.S. Wragg, M. Dyballa, J. Holzinger, H. Falsig, L.F. Lundegaard, P. Beato, R.Y. Brogaard, K.P. Lillerud, U. Olsbye, S. Svelle, A Straightforward Descriptor for the Deactivation of Zeolite Catalyst H-ZSM-5, ACS Catal. 7 (2017) 8235–8246. https://doi.org/10.1021/acscatal.7b02193.

[20] Y. Wang, G. Wang, L.I. van der Wal, K. Cheng, Q. Zhang, K.P. de Jong, Y. Wang, Visualizing Element Migration over Bifunctional Metal-Zeolite Catalysts and its Impact on Catalysis, Angew. Chemie - Int. Ed. 60 (2021) 17735–17743. https://doi.org/10.1002/anie.202107264.

[21] Y. Ding, F. Jiao, X. Pan, Y. Ji, M. Li, R. Si, Y. Pan, G. Hou, X. Bao, Effects of Proximity-Dependent Metal Migration on Bifunctional Composites Catalyzed Syngas to Olefins, Am. Chem. Soc. 11 (2021) 9729–9737.

7 Conclusions

The development of sufficient technologies are imperative for replacing the current production methodologies, which rely on fossil resources, in the manufacturing of vital chemicals, including plastic monomers, ethylene, propylene, and aromatic compounds. A promising route for the production of plastic monomers is the combination of the methanol synthesis and the methanol-to-hydrocarbon reaction within one reactor. However, it is still a challenge to achieve high selectivity for unsaturated hydrocarbons at high CO_2 conversion. Synthesizing a metal oxide catalyst, with high methanol synthesis activity at methanol dehydration relevant temperatures with minimal olefin hydrogenation activity, could potentially close the activity and selectivity gab.

The synthesis of supported ZnO on different oxides, TiO_2, m-ZrO_2, and t-ZrO_2 with the incipient wetness impregnation method showed that the t-ZrO_2 support allowed for creation of highly active ZnO surface domains for the methanol synthesis reaction. A lower activity of the m-ZrO_2 and TiO_2 support correlated with higher amount of hexagonal ZnO forming on their surfaces. Adding more ZnO on the t-ZrO_2 support initially improved the methanol synthesis activity and the best activity was achieved with a Zn-loading of 18 mol%. This Zn-loading was equivalent with the saturation of the t-ZrO_2 surface with a monolayer of the ZnO(0001) facet. The methanol synthesis activity declined as the Zn-loading increased beyond this saturation, as more hexagonal ZnO was replacing the monolayer. Comparing the performance of the ZnO/t-ZrO_2 prepared by impregnation and co-precipitation revealed a similar selective production of methanol. The impregnated sample did not show any integration of Zn into the ZrO_2 lattice by XRD analysis. Hence, a solid solution of ZnO in ZrO_2 was not important for the catalytic activity or selectivity. XPS analysis revealed that the co-precipitation and the impregnation methods resulted in catalysts where ZnO was mainly present on the zirconia surface. XAS analysis showed that only amorphous surface ZnO was present at the ZrO_2 surface at low Zn loadings. Comparing the methanol synthesis activity and the amount of surface ZnO determined from linear combination fitting revealed that these sites are the main active sites. TEM analysis confirmed that at low Zn-loadings, the ZnO was not adopting any crystalline structure and showed well-dispersed ZnO as domains of ~5 nm size on the ZrO_2 surface. This was observed for both the co-precipitated and impregnated samples. Activity measurements of two co-precipitated samples with the same bulk Zn mol%, but with a significant difference in the surface Zn concentration, demonstrated the importance of ZnO located on the zirconia surface. Modulation excitation spectroscopy coupled time resolved QEXAFS showed that these Zn sites were capable of reversible, partial reduction under

methanol synthesis conditions forming ZnO_x, where *x* was approximately 0.98. An interaction between ZnO and ZrO_2 was by XPS found to create a more electron deficient ZnO and the withdrawal of electrons from the Zn-O bonds likely induced the partial reducibility of this phase. The superior catalytic performance of the ZnO/t-ZrO_2 was linked to its ability to abstract oxygen from the ZnO surface domains, creating oxophilic sites that activates CO_2. In-situ DRIFTS analysis of CO_2 adsorption under methanol synthesis conditions showed a shift in the formed carbonate and formate species on the ZnO containing zirconia, compared to the bare zirconia support. Together, these findings suggested that the active phase was the partly reduced surface ZnO_x, which adsorbed CO_2, hydrogenated it into formate and further into methanol.

Other interesting metal oxides for the production of methanol was $ZnAl_2O_4$ and $ZnGa_2O_4$ oxides. The methanol synthesis activity of the Zn-based spinel catalysts was linked to the Zn-loading. Exceeding the stoichiometric spinel loading created ZnO sites on the surface of the spinel structure which resembles the surface ZnO domains forming on the ZrO_2 surface. This resemblance enabled the quantification of the amount of these sites on the spinel structure's surface by XAS analysis and linear combination fitting. The amount of these ZnO surface sites correlated with the methanol synthesis rate and these sites had superior oxygenate selectivity. At high Zn-loadings, these sites were removed as more crystalline ZnO were formed. The combination of EXAFS fitting and linear combination fitting of the Zn k-edge XANES spectra of the Zn-spinel structures with different Zn-loading confirmed the presence of the spinel structure, amorphous surface ZnO and crystalline ZnO at high Zn-loadings. Spinel structures with under stoichiometric Zn-loading resulted in the formation of the pure spinel structure. In-situ XAS analysis confirmed that the primary active sites were the amorphous, surface ZnO since deactivation occurred with the formation of crystalline ZnO when oscillating between reducing and oxidizing conditions. Similar to the ZnO/t-ZrO_2 catalyst, the methanol synthesis mechanism over the Zn-spinel catalyst occurred through a formate pathway, identified by in-situ DRIFTS. In this mechanism, CO_2 adsorbed as carbonate, hydrogenated into formate and further into methoxy, which desorbed as methanol. Fast hydrogenation of carbonate into formate was observed at both 260 and 320 ºC, while formate hydrogenation was mainly observed at 320 ºC, suggesting that formate hydrogenation was the rate-determining step.

The bi-functional catalysts composed of ZnO/t-ZrO_2 with ZSM-5, ZSM-11, and ZSM-12 enabled the direct conversion of CO_2 into hydrocarbons with substantial amount of aromatics. The local dehydration of the methanol ensured that the CO_2 hydrogenation equilibrium was exceeded showing higher

conversion of CO_2 than expected from equilibrium calculations at these reactor conditions. High temperatures, pressure, and hydrogen partial pressure induced the hydrogenation and/or the cracking reactions, revealing the main hydrocarbon product to be light paraffins and isoparaffins. However, these reactions could explain the improved lifetime observed for the H-ZSM-5 catalyst as cracking and hydrogenation reactions could remove and/or slow the evolution of deactivating carbon deposits. The hydrogenation activity of the ZnO/t-ZrO_2+ZSM-5 was concluded to occur over the Brønsted acid sites, as the increase in the Si/Al ratio induced the hydrogen incorporation. The highest aromatic selectivity for the ZnO/t-ZrO_2+ZSM-5 catalyst was obtained at low temperature and pressure to minimize the hydrogenation, but a low hydrocarbon yield was obtained at these conditions. When replacing the ZSM-5 zeolite with ZSM-11, and ZSM-12, the larger cages and pores induce the benzene methylation reactions and improve the aromatic selectivity. A 9.8 % CO_2 conversion to hydrocarbons with an aromatic selectivity of 42.4 carbon mol% was achieved when combining the ZnO/t-ZrO_2 and ZSM-12 zeolite.

The behaviour of the ZnO/t-ZrO_2 system was evaluated through kinetic studies showing that the water produced from the reverse-water-gas-shift, CO_2 hydrogenation to methanol, and methanol dehydration limited the methanol synthesis activity even at very low residual concentration of methanol. This explains the not linear increase in the CO_2 conversion at longer residence time, which was observed in the experimental data. The higher water content at higher residence time would inhibit the CO_2 hydrogenation reaction by thermodynamics. The kinetic model also found that to optimize the aromatics formation rate, the process should be operated far from equilibrium. Such conditions would highly limit the CO_2 conversion to hydrocarbons, resulting in a very ineffective process. However, the system could be optimized for the production of an isoparaffic rich gasoline product.

When combing the ZnO/t-ZrO_2, $ZnAl_2O_4$, or $ZnGa_2O_4$ with H-SAPO-34, the direct conversion of CO_2 into light olefins, rich in ethylene and propylene, was possible. The bi-functional catalyst activity order was ZnO/t-ZrO_2 > $ZnGa_2O_4$ > $ZnAl_2O_4$ showing higher hydrocarbon yields for the ZnO/t-ZrO_2 + SAPO-34 combination. However, the higher methanol synthesis activity also revealed high hydrogen index numbers, showing that the ZnO/t-ZrO_2 and $ZnGa_2O_4$ had higher olefin hydrogenation activity as well. When increasing the reaction pressure, a better compromise between the reverse-water-gas-shift and the CO_2 hydrogenation reaction improved the hydrocarbon yield but at the expense of induced olefin hydrogenation. These results highlight the gap between activity and selectivity between bi-functional catalysts. Changing the CO_2/H_2 feed ratio showed improved hydrocarbon yield for the ZnO/t-ZrO_2 +SAPO-34 catalyst but at the expense of a slightly higher hydrogen incorporation

in the hydrocarbon product. It is believed that this strategy is only applicable at low operating pressure as the increase in pressure showed a great increase in hydrogenation activity which is supposed to be induced at higher hydrogen partial pressures. Another strategy to improve the hydrocarbon yield without affecting the olefin selectivity was to co-feed CO over the $ZnAl_2O_4$+SAPO-34 catalyst. Higher CO concentration in the feed changed the thermodynamic driving force for the reverse-water-gas-shift reaction causing less production of water from this reaction. The lower water content improved the CO_2 hydrogenation activity significantly, which improved the hydrocarbon yield of light olefins.

The $ZnAl_2O_4$ and ZnO/t-ZrO_2, and SAPO-34 combination showed a stable production of olefins for over 80 hours on stream. This stability was found superior to the methanol-to-olefins process as the methanol conversion capacity reached 18 g methanol per g SAPO-34 without any loss in the methanol conversion. However, a deactivation phenomenon was observed for the bi-functional catalyst as the hydrocarbon yield and the light olefin selectivity decreased with time on stream. Investigation of spent ZnO/t-ZrO_2 and SAPO-34 by XRD and TEM showed that three deactivation phenomena occurred under the CO_2 to light olefins conditions. It was found that the surface ZnO sinters into larger ZnO crystals causing a decrease in the methanol synthesis activity. Furthermore, the mobility of Zn was visible by Zn migration into the SAPO-34 catalyst. When Zn was impregnated on the SAPO-34, increased olefin hydrogenation was observed, which could be the reason for the induced hydrogen incorporation with time on stream. At last, coke molecules were forming in the SAPO-34 crystals expanding the unit cell volume. It was not possible to decouple the effect of these deactivation phenomena on the stability of the bi-functional catalyst. However, if oxidative regeneration is required to regain activity by removeing deactivating carbon deposits, it would result in sintering and formation of crystalline ZnO, as identified by in-situ XAS and ex-situ TEM analysis. This will cause a decline in the methanol synthesis activity for the metal oxide and thereby hamper the activity of the bi-functional catalyst.

8 Future work

In this project, it was found that Zn-based mixed oxides were capable of producing methanol at elevated temperatures, making them good candidates for the bi-functional catalytic system. However, one unanswered question was where the primary olefin hydrogenation occurred. Results suggested that the highly active methanol synthesis catalysts, the ZnO/t-ZrO_2 and $ZnGa_2O_4$, also induced the hydrogen incorporation, compared to the more inactive $ZnAl_2O_4$ oxide. Changing the acid site density for the ZSM-5 zeolite had great influence on the saturation degree of the hydrocarbon product obtained. Therefore, it was planned to conduct propene hydrogenation experiments over the metal oxide and zeolite/zeotype catalysts in relevant atmospheres present in the bi-functional catalytic conversion of CO_2. These experiments could clarify the precise origin of the olefin hydrogenation activity and may provide further insights for improving the synthesis of the catalysts to obtain a bi-functional catalyst with the best compromise between activity and selectivity.

The activity measurement of the ZnO/t-ZrO_2+ZSM-5 catalyst indicated that the primary hydrogen activity stems from the acidity of the zeolite. Altering of the acidity of shape selective solid acids could be obtained by synthesizing new materials where alternative T-atoms (section 2.2.1) is incorporated into the structure. Reducing the acid site density and its strength are important to achieve a bi-functional catalyst that can be operated at conditions improving the hydrocarbon yield without saturating the product.

The kinetic modelling of the bi-functional catalyst showed that the optimal mixing ratio of the catalyst components were dependent on the methanol synthesis activity and the methanol dehydration activity. If the reaction was limited by the methanol dehydration, a higher zeolite content would be necessary to optimize the hydrocarbon yield and vice versa. Experimental confirmation of this model insight would be valuable for guiding future research on the bi-functional catalyst and may explain the inconsistency in the reported performance of the bi-functional catalyst.

CO co-feeding experiments showed that minimizing the water constitution form the reverse-water-gas-shift reaction had great impact on the CO_2 hydrogenation activity. Research in alternative reactor designs, such as membrane reactors, where water formed from all the reactions could be removed along the catalyst bed could reveal an optimized bi-functional catalytic concept. Such reactors could further minimize the activity and selectivity gap, as they could be operated at milder conditions without reaching thermodynamic limitations. Another alternative could be the discovery of metal oxides

that are highly active for CO hydrogenation to methanol reactions, similar to the Cu/MgO catalyst. With methanol forming form CO hydrogenation would minimize the production of water allow the use of a dry synthesis gas feed. However, for this to be successful, the formed water must not have an inhibiting effect on such “theoretical” oxide materials.

9 Appendix

9.1 Supporting information: Surface ZnO_x on Zirconia is Highly Active for High Temperature Methanol Synthesis

Supporting Information: Surface ZnO_x on Zirconia is Highly Active for High Temperature Methanol Synthesis

M. T. Nikolajsen[1], J. Grivel[2], A. Gaur[3], L. P. Hansen[4], L. Baumgarten[3], N. C. Schjødt[4], U. V. Mentzel[4], J-D. Grunwaldt[3], J. Sehested[4], J. M. Christensen[1] and M. Høj[1*]

[1] Department of Chemical Engineering, Technical University of Denmark (DTU), Kgs. Lyngby, 2800 (Denmark).

[2]Department of Energy Conversion and Storage, Technical University of Denmark (DTU), Kgs. Lyngby, 2800 (Denmark).

[3] Institute for Chemical Technology and Polymer Chemistry, Karlsruhe Institute of Technology, Karlsruhe, 76131, (Germany)

[4] Topsoe A/S, Kgs. Lyngby, 2800 (Denmark).

[*]Corresponding author: mh@kt.dtu.dk

Table S1. Approach to equilibrium calculated as the percentage ratio between the reaction coefficient and the equilibrium constants for the reverse-water-gas-shift and the CO_2 hydrogenation to methanol reactions. The equilibrium constants used were calculated with the empirical correlations published by Graaf et al. [1].

			Approach to equilibrium, Q/K_{eq}	
Catalysts	T, [°C]	P, [bar]	$CO_2+H_2 \rightarrow CO+H_2O$	$CO_2+3H_2 \rightarrow CH_3OH+H_2O$
ZnO	320	50	0.49%	2.61%
(0.13)ZnO/SiO_2	320	50	0.06%	0.70%
(0.13)ZnO/m-ZrO_2	320	50	0.41%	9.87%
(0.13)ZnO/TiO_2	320	50	0.63%	14.36%
(0.13)ZnO/t-ZrO_2-CeO_2	320	50	0.28%	12.26%
(0.13)ZnO/t-ZrO_2	320	50	0.36%	16.19%
(0.18)ZnO/t-ZrO_2	320	50	0.46%	21.25%
(0.29)ZnO/t-ZrO_2	320	50	0.53%	29.16%
(0.44)ZnO/t-ZrO_2	320	50	0.44%	24.70%
(0.11)ZnO-ZrO_2	320	50	0.12%	4.65%

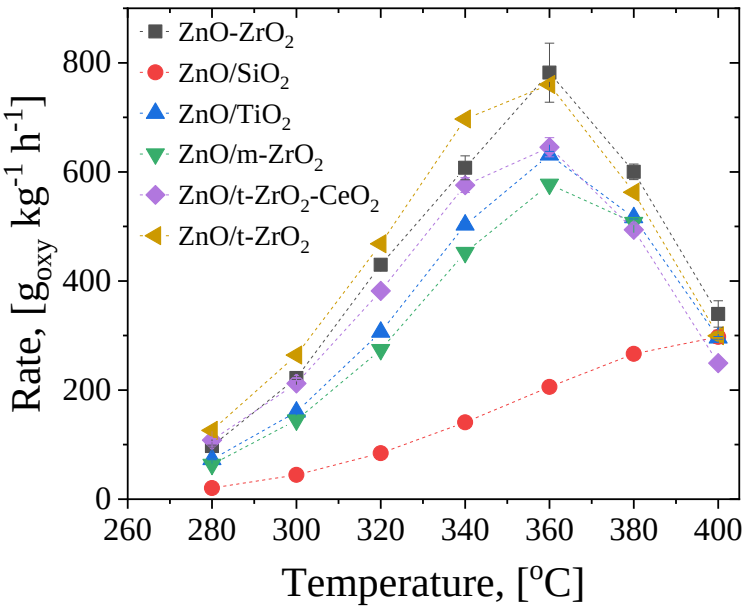


Fig. S1. The oxygenate (CH_3OH+ CH_3OCH_3) formation rate for ZnO supported on different metal oxides compared to the co-precipitated $ZnO\text{-}ZrO_2$. Conditions: 50 barg, 15 NL/h, catalyst loading of 300 mg, feed gas composition of $CO_2/H_2/Ar$ 20/60/20.

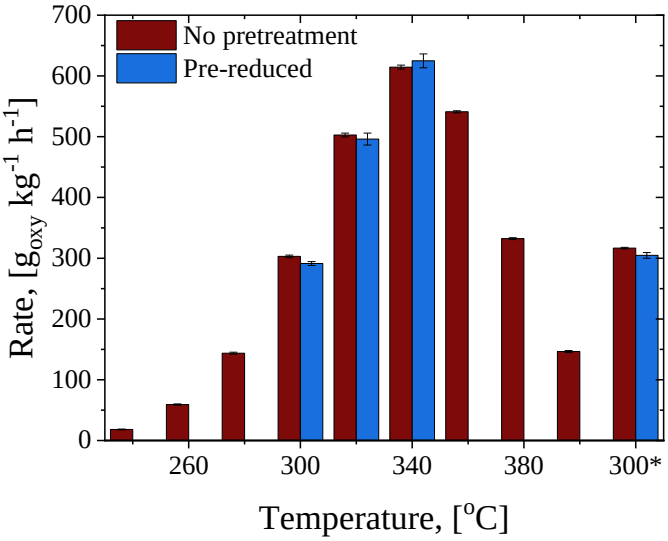


Fig. S2. The oxygenate (CH_3OH+ CH_3OCH_3) formation rate with and without pre-reduction of the co-precipitated $ZnO\text{-}ZrO_2$ in $CO/H_2/Ar$.* represent data when returned to 300 °C after reaction at 400°C. Conditions: 50 barg, 15 NL/h, catalyst loading of 300 mg, feed gas composition of $CO_2/H_2/Ar$ 20/60/20.*

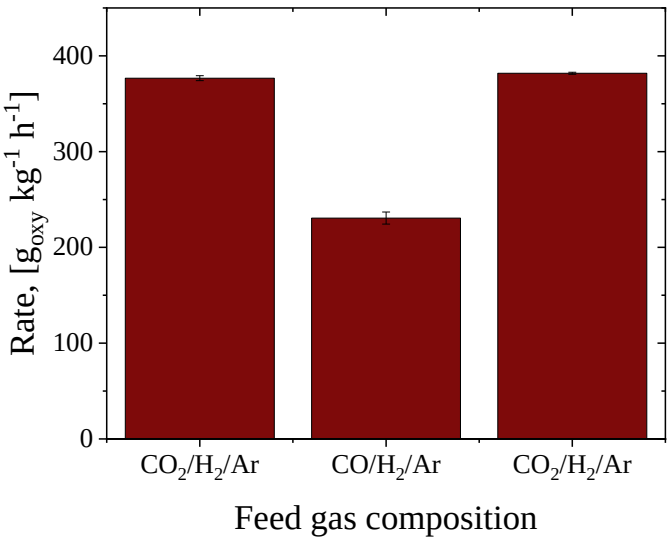


Fig. S3. The oxygenate (CH_3OH+ CH_3OCH_3) formation rate when shifting between CO_2/H_2, CO/H_2 and back to CO_2/H_2. Conditions: 320 °C 50 barg, 15 NL/h, catalyst loading of 300 mg, feed gas composition of $CO_2/H_2/Ar$ 20/60/20 or $CO/H_2/Ar$ 20/60/20.

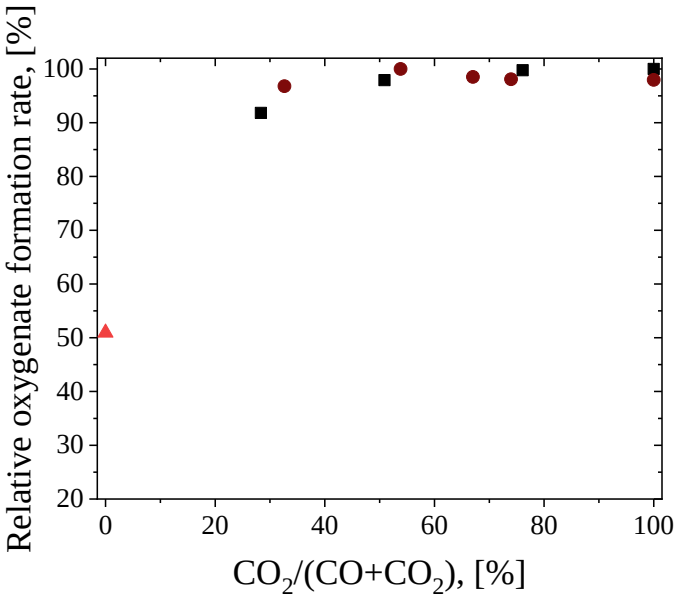


Fig. S4. Relative oxygenate (CH_3OH+ CH_3OCH_3) formation rate at different feed compositions. Black squares represent data where the $CO+CO_2$ was kept constant (C_{total}/H_2 1/3). Red circles represent data where CO_2 was kept constant (CO_2/H_2 1/3). Red triangle represent data when only CO and H_2 (1/3) are fed. Conditions: 320 °C 50 barg, 15 NL/h, catalyst loading of 300 mg.

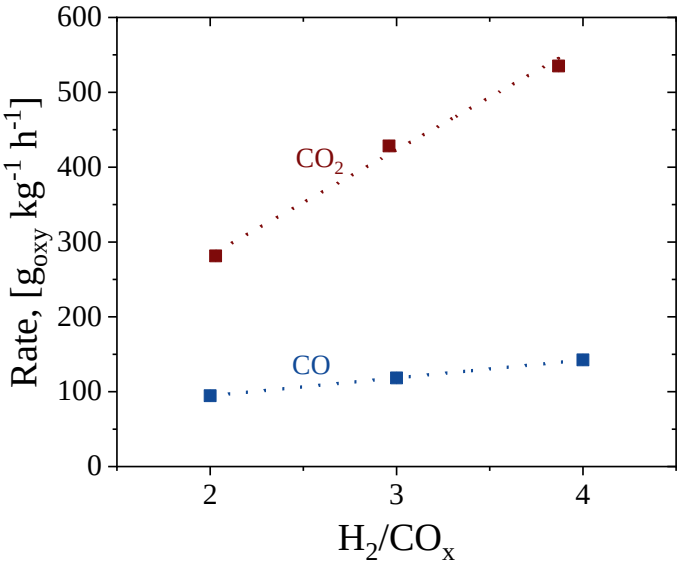


Fig. S5. The oxygenate (CH_3OH+ CH_3OCH_3) formation rate at different feed compositions. Conditions: 320 °C 50 barg, 15 NL/h, catalyst loading of 300 mg with the CO_2 vol% fixed at 20% or CO vol% fixed at 18%.

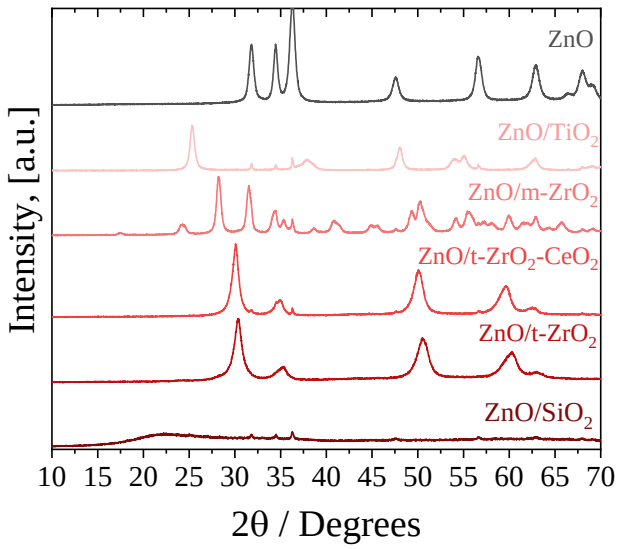


Fig. S6. XRD patterns of ZnO impregnated on different supports. All catalysts were prepared with ~13 mol% Zn/(Zn+M), where M is the supporting metal.

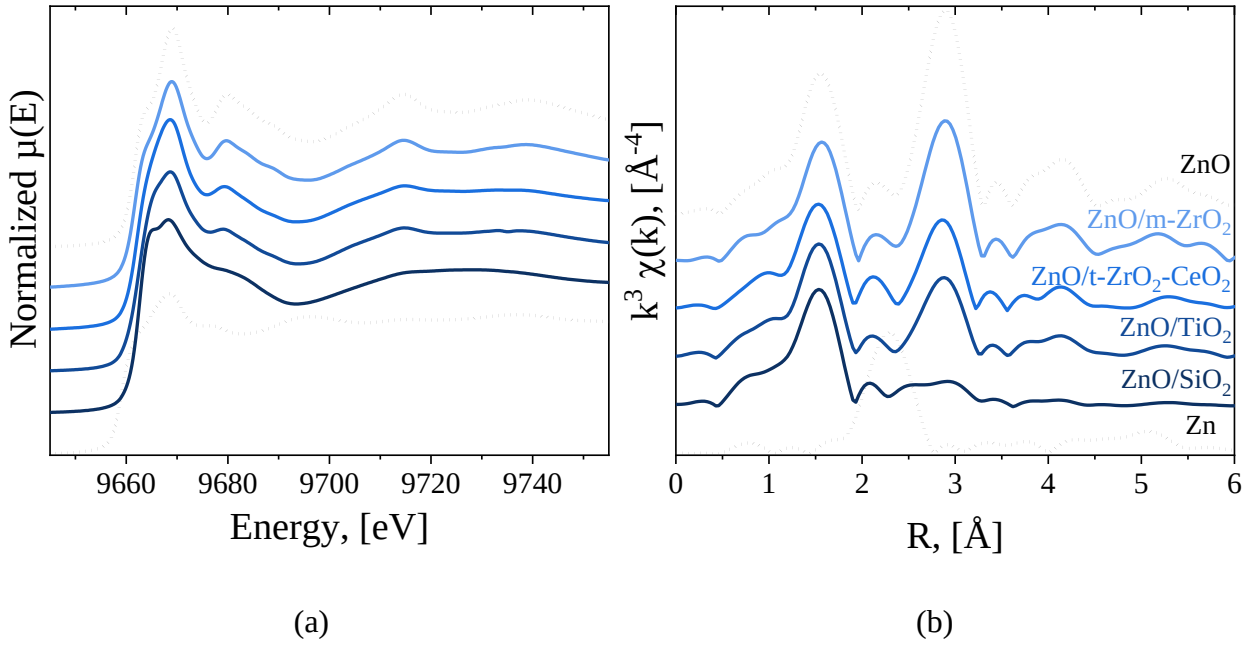
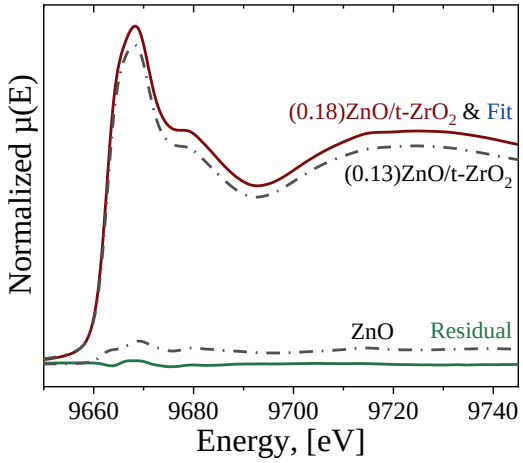


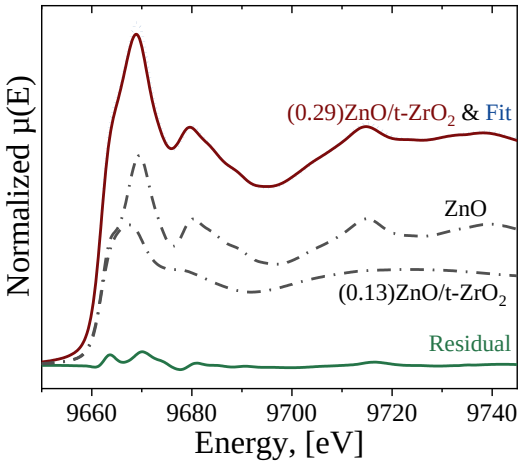
Fig. S7. (a) Zn K-edge XANES and (b) Fourier-transformed k^3-weighted EXAFS spectra of ZnO supported on different supports with Zn foil and ZnO as references.

Table S2. Results from the fitting of coordination number (CN), interatomic distances (R), energy shift (ΔE_0), and mean square deviation of interatomic distances (σ^2) for the first and second shell of ZnO on the catalyst samples. The fraction of surface ZnO, χ, calculated from Eq. (5).

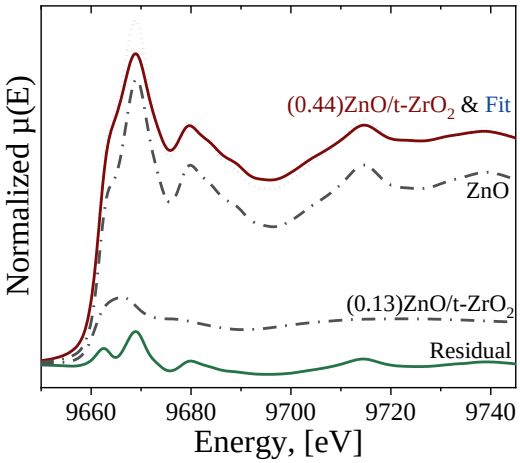
Catalysts	**χ** [%]	**shell**	**CN**	**R** [Å]	**σ²** [10^{-3}Å²]	**ΔE₀** [eV]	**R-factor**
ZnO-ZrO_2	100	Zn-O	3.2 ± 0.4	1.98 ± 0.00	7.9 ± 1.8	1.61 ± 1.60	0.029
(0.13)ZnO/t-ZrO_2	100	Zn-O	3.8 ± 0.5	1.98 ± 0.00	7.5 ± 1.8	0.59 ± 1.72	0.031
(0.18)ZnO/t-ZrO_2	73 ± 18	Zn-O Zn-Zn	3.7 ± 0.2 3.3 ± 2.2	1.97 ± 0.01 3.24 ± 0.01	7.2 ± 0.7 17 ± 5.7	0.88 ± 0.76	0.004
(0.29)ZnO/t-ZrO_2	44 ± 9	Zn-O Zn-Zn	3.2 ± 0.2 6.8 ± 1.1	1.97 ± 0.00 3.23 ± 0.01	5.2 ± 0.7 10 ± 1.1	2.80 ± 0.58	0.003
(0.44)ZnO/t-ZrO_2	32 ± 11	Zn-O Zn-Zn	2.8 ± 0.6 8.1 ± 1.3	1.97 ± 0.01 3.23 ± 0.01	5.0 ± 0.9 11 ± 1.1	3.49 ± 0.70	0.004
ZnO/t-ZrO_2-CeO_2	75 ± 11	Zn-O Zn-Zn	3.5 ± 0.5 3.0 ± 1.3	1.97 ± 0.01 3.24 ± 0.01	4.9 ± 1.0 13 ± 1.4	3.91 ± 0.78	0.005
ZnO/m-ZrO_2	6 ± 18	Zn-O Zn-Zn	3.2 ± 0.3 11 ± 2.1	1.97 ± 0.01 3.21 ± 0.01	6.5 ± 1.7 6.6 ± 2.7	1.12 ± 1.42	0.022
ZnO/TiO_2	53 ± 15	Zn-O Zn-Zn	3.5 ± 0.3 5.7 ± 1.8	1.97 ± 0.01 3.23 ± 0.01	5.9 ± 1.2 12 ± 2.4	1.12 ± 1.42	0.022
ZnO/SiO_2	56 ± 27	Zn-O Zn-Zn	3.7 ± 0.2 5.0 ± 3.3	1.95 ± 0.01 3.27 ± 0.01	6.4 ± 0.7 18 ± 5.9	1.14 ± 0.80	0.005


Normalized μ(E)
(0.18)ZnO/t-ZrO2 & Fit
(0.13)ZnO/t-ZrO2
ZnO
Residual
9660
9680
9700
9720
9740
Energy, [eV]

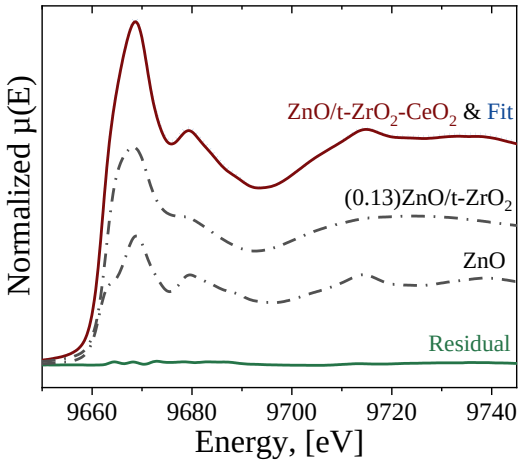
(a)


Normalized μ(E)
(0.29)ZnO/t-ZrO2 & Fit
ZnO
(0.13)ZnO/t-ZrO2
Residual
9660
9680
9700
9720
9740
Energy, [eV]

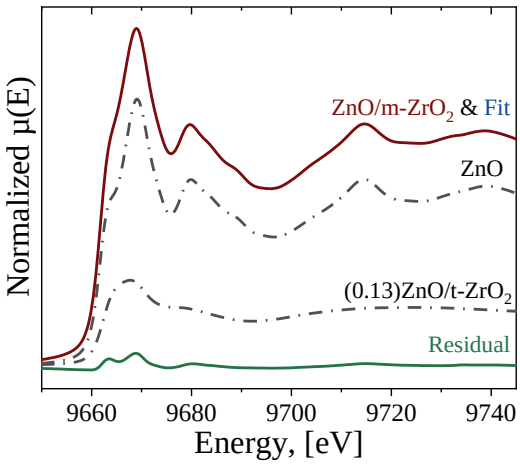
(b)


Normalized μ(E)
(0.44)ZnO/t-ZrO2 & Fit
ZnO
(0.13)ZnO/t-ZrO2
Residual
9660
9680
9700
9720
9740
Energy, [eV]

(c)


Normalized μ(E)
ZnO/t-ZrO2-CeO2 & Fit
(0.13)ZnO/t-ZrO2
ZnO
Residual
9660
9680
9700
9720
9740
Energy, [eV]

(d)


Normalized μ(E)
ZnO/m-ZrO2 & Fit
ZnO
(0.13)ZnO/t-ZrO2
Residual
9660
9680
9700
9720
9740
Energy, [eV]

(e)

Fig.S 8. Linear combination fitting results with (0.13)ZnO/t-ZrO_2 as reference for surface ZnO and ZnO as reference for crystalline ZnO. (a) (0.18)ZnO/t-ZrO_2, (b) (0.29)ZnO/t-ZrO_2, (c) (0.44)ZnO/t-ZrO_2, (d) ZnO/t-ZrO_2-CeO_2, and (e) ZnO/m-ZrO_2. Dashed dotted lines represent the references used and the contributions are summed to give fitted model (dotted line). Green solid line represents the residual from the model fit and the data (solid red line).

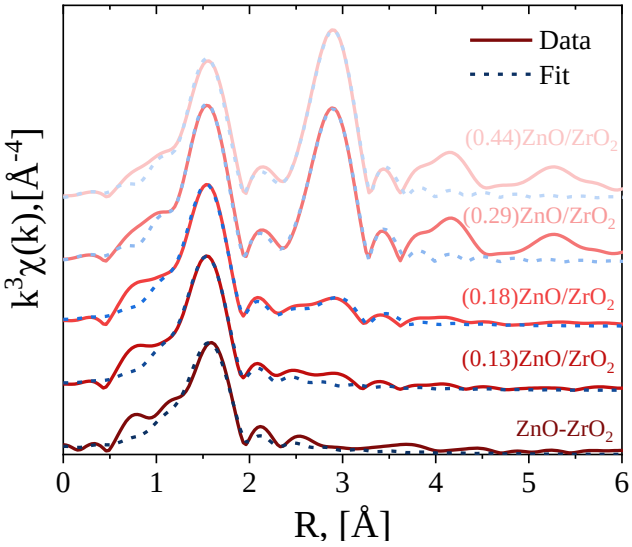


Fig. S9. The first and second shell fitting of the wurtzite ZnO structure model (ICSD 67849) on the Zn K-edge Fourier-transformed k^3-weighted EXAFS spectra of ZnO on ZrO_2 catalysts.

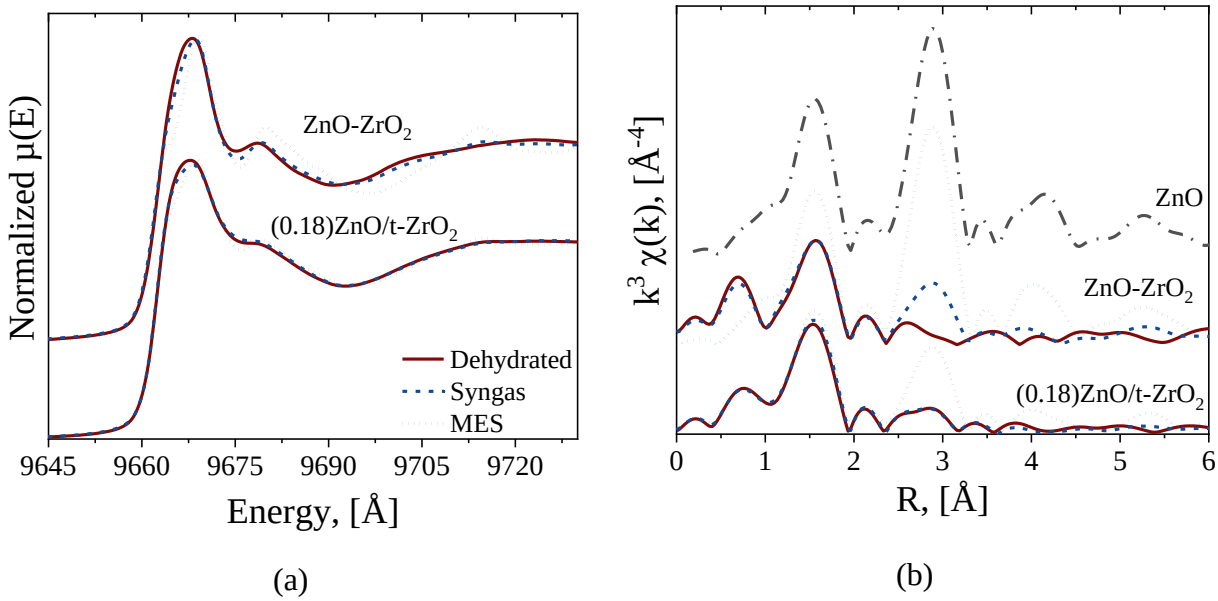


Fig. S10. In-situ (a) Zn K-edge XANES and (b) Fourier-transformed k^3-weighted EXAFS spectra of ZnO on ZrO_2 catalysts after dehydration, methanol synthesis in syngas and MES experiments. Spectra recorded at 15 bar and ~40 °C.

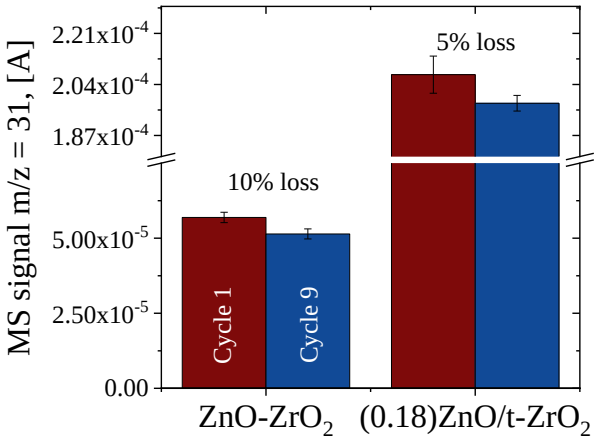


Fig. S11. MS signal ion current for m/z = 31 for MES cycle 1 and 9.

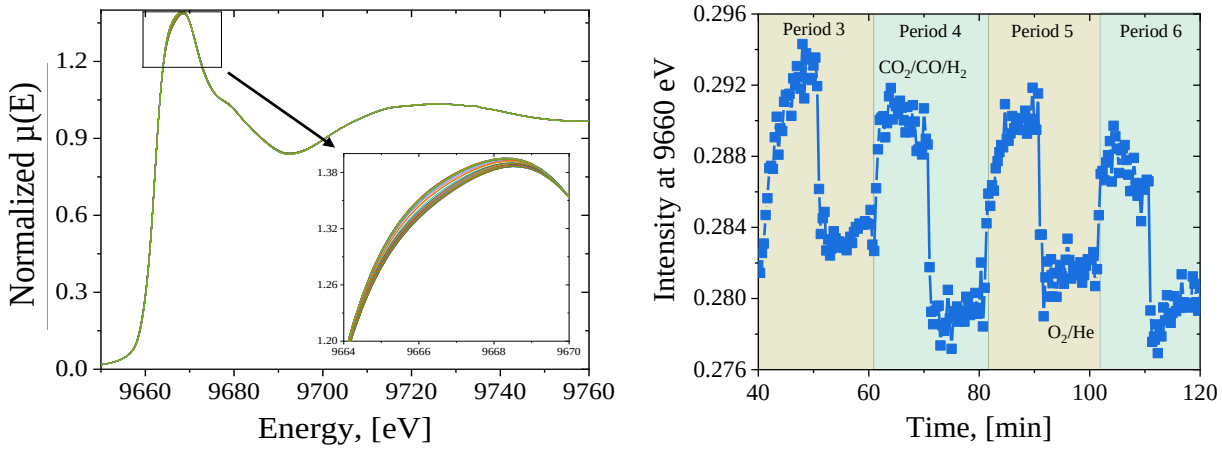


Fig. S12. (a) The periods 2-9 averaged time resolve Zn K-edge XANES spectra. (b) The intensity change at 9660 eV with the change from oxidizing and reducing atmospheres.

The thermodynamic reduction potential for bulk ZnO

By assuming that the reverse-water-gas-shift reaction is in equilibrium at 400 °C, the thermodynamic reduction potential for bulk ZnO can be calculated using Eqs. (39) and (40).

$$ZnO(s) + H_2 \rightarrow Zn(s) + H_2O, \qquad \Delta G_{r,400^\circ C} = 78.5\ kJ/mol \tag{39}$$

$$ZnO(s) + CO \rightarrow Zn(s) + CO_2, \qquad \Delta G_{r,400^\circ C} = 63.8\ kJ/mol \tag{40}$$

The large positive Gibbs free energy shows no potential for bulk crystalline ZnO reduction to metallic Zn at the conditions applied in the modulation excitation spectroscopy experiment. The partial reduction of ZnO observed was therefore concluded to happen only for the surface ZnO_x sites. The oxide-oxide interaction between the ZnO and ZrO_2 is hypothesised to stabilize and enable the ZnO reduction, which promotes the CO_2 hydrogenation activity.

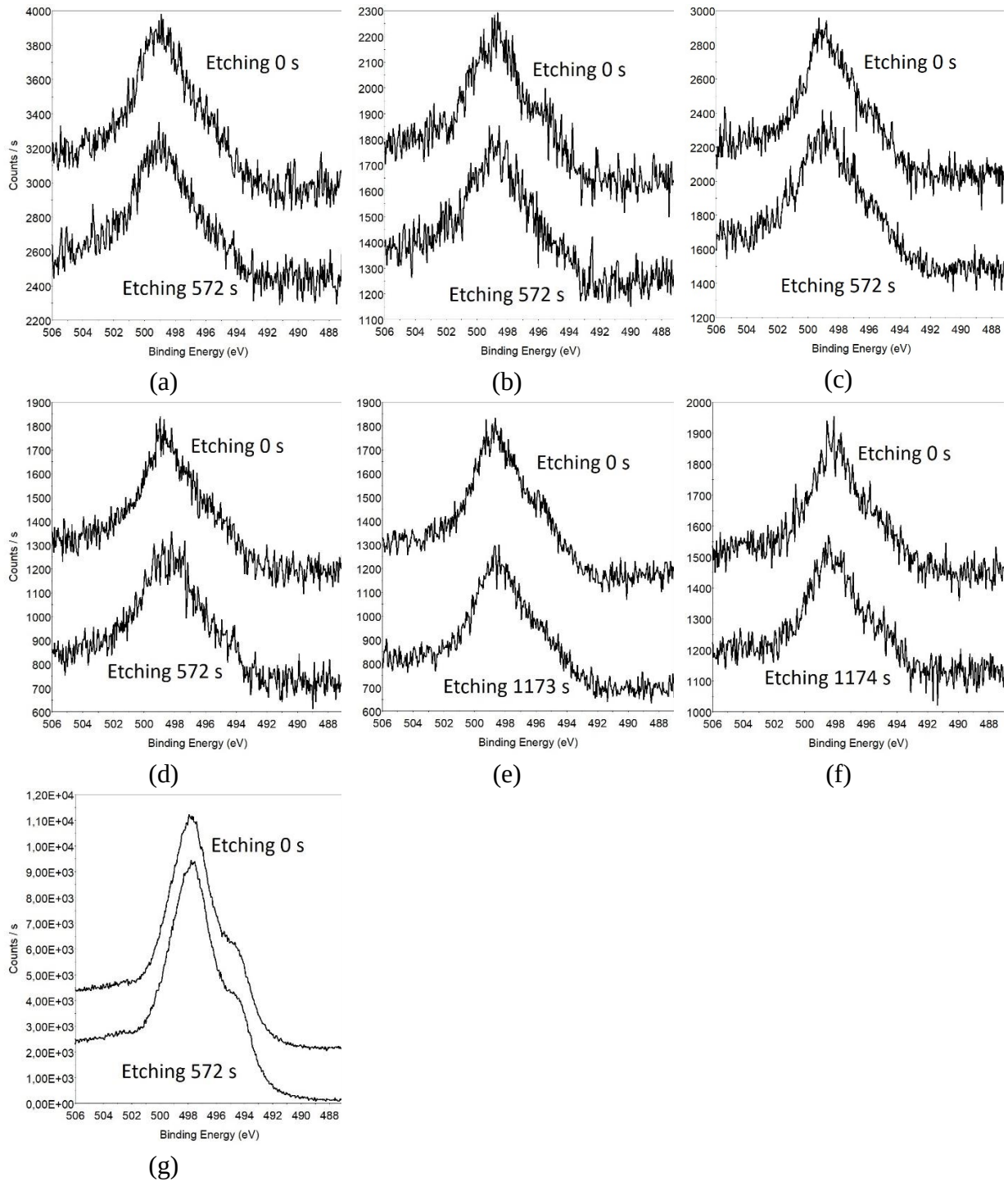
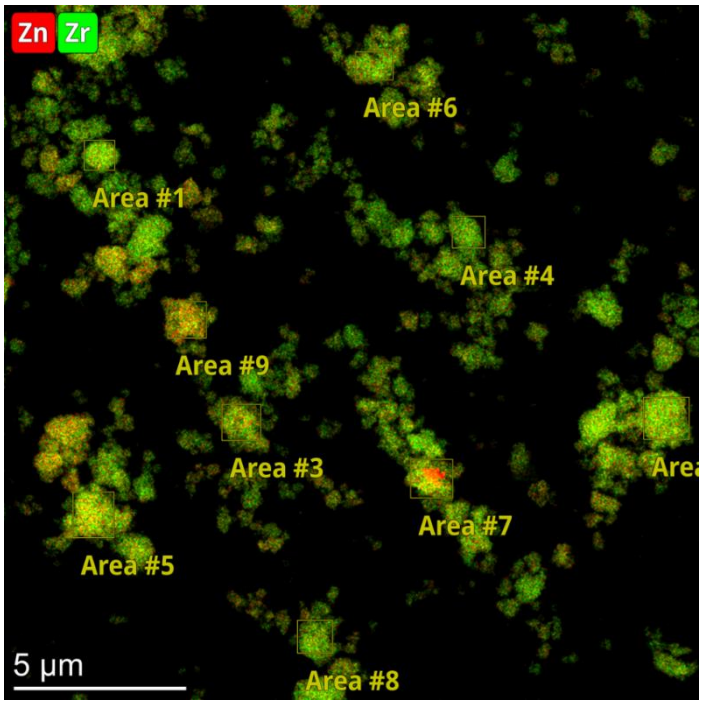


Fig. S13. XPS Zn LMM Auger peak for (a) (0.13)ZnO/t-ZrO_2, (b) (0.18)ZnO/t-ZrO_2, (c) (0.29)ZnO/t-ZrO_2, (d) (0.44)ZnO/t-ZrO_2, (e) ZnO-ZrO_2, (f) ZnO-ZrO_2-100 and (g) ZnO. The shape and position of the LMM Auger peak confirmed the oxidation state of Zn in the catalysts was Zn^{2+}.



	Zn/(Zn+Zr) Mol%
Area 1	7
Area 2	9
Area 3	12
Area 4	7
Area 5	11
Area 6	7
Area 7	19
Area 8	8
Area 9	15
Average	11
Standard deviation	4

Fig. S14. EDX maps of the Zn and Zr locations of the (0.13)ZnO/t-ZrO_2 sample.

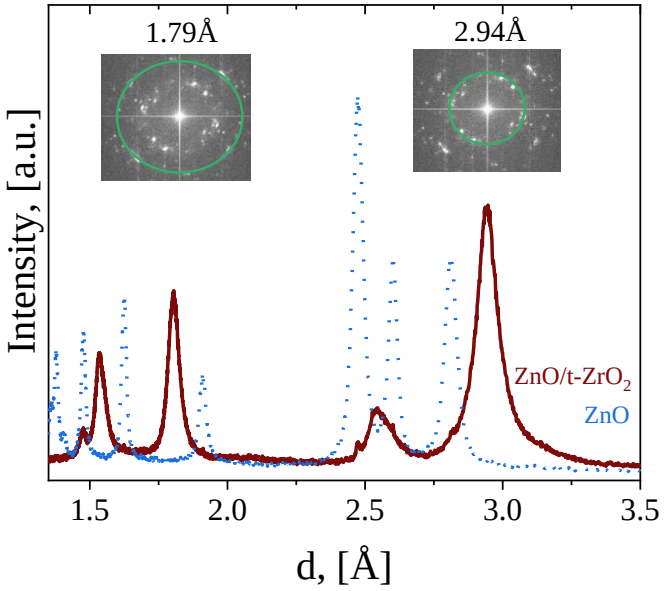
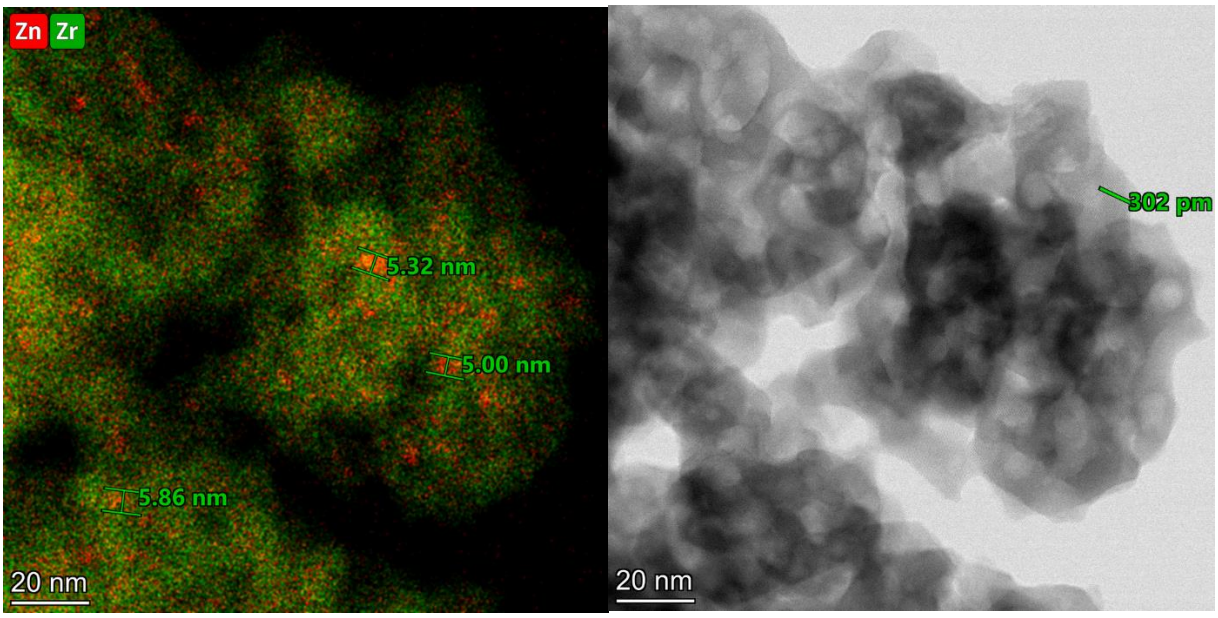
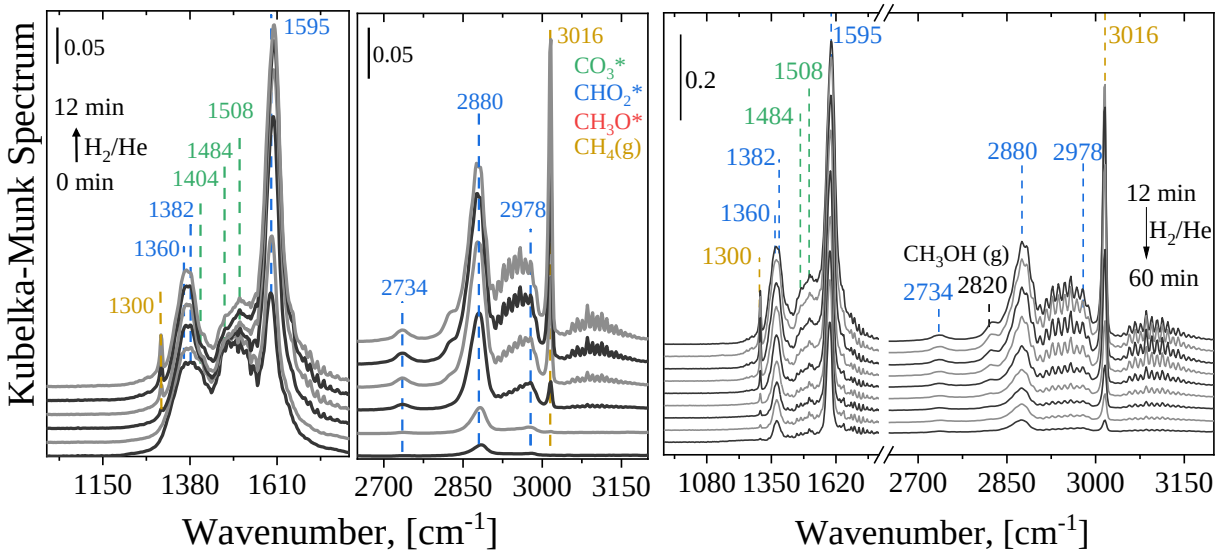


Fig. S15. Comparison of XRD results of ZnO and ZnO/t-ZrO_2 with Fourier transformed high-resolution TEM image.



(a) (b)

Fig. S16. (a) EDX maps of Zn and Zr location and (b) high-resolution STEM image (bright field) of the ZnO-ZrO_2 sample. The EDX quantification showed a mole fraction of Zn/(Zn+Zr) = 0.073 from this particular image area.



(a) (b)

Fig. S17. In-situ DRIFTS measurement of hydrogen treatment after CO_2 adsorption for the (0.13)ZnO/t-ZrO_2 sample at 20 bar and 320 °C (a) 0 to 12 min and (b) 12 to 60 min. The ZnO/t-ZrO_2 show very low selectivity towards CH_4 formation, but strong vibrational signals of gaseous CH_4 were observed at 1300 and 3016 cm^{-1} caused by continuous CH_4 accumulation in the large IR chamber dead volume.

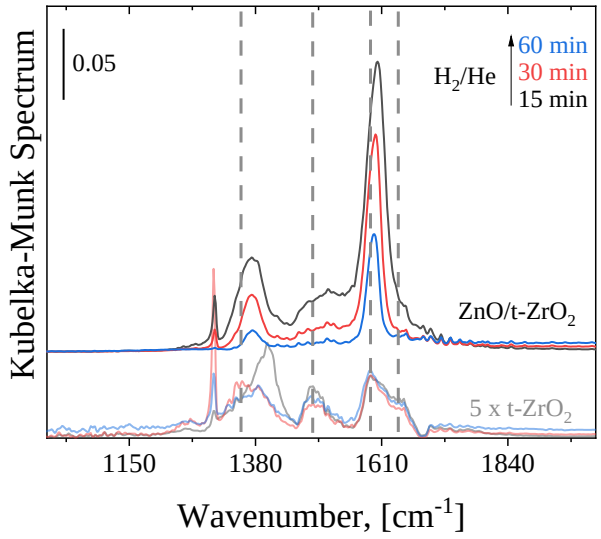


Fig. S18. In-situ DRIFTS measurements of H_2 treatment after CO_2 adsorption on (0.13)ZnO/t-ZrO2 and bare t-ZrO_2 support at 20 bar and 320 °C.

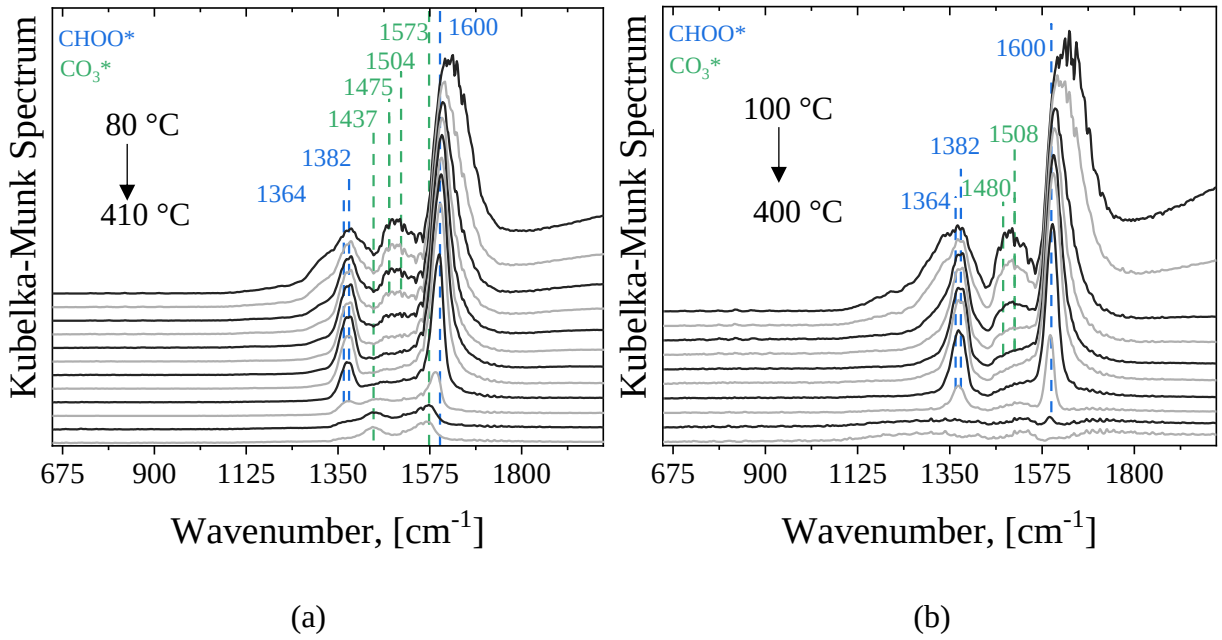


Fig. S19. In-situ DRIFTS measurements of (0.13)ZnO/t-ZrO_2 (a) TPD in He and (b) TPR in H_2 at 20 bar after steady-state methanol synthesis.

[1] G. H. Graaf and J. G. M. Winkelman, "Chemical Equilibria in Methanol Synthesis Including the Water − Gas Shift Reaction : A Critical Reassessment," *Ind. Eng. Chem. Res.*, vol. 55, pp. 5854–5864, 2016.

9.2 Supporting information: Direct CO_2 Hydrogenation to Aromatics over Combined Catalysts Composed of Supported ZnO with Different Zeolite Topologies

Supporting Information: Direct CO_2 Hydrogenation to Aromatics over Combined Catalysts Composed of Supported ZnO with Different Zeolite Topologies

M. T. Nikolajsen[1], Eva S. Kold[1], Amalie B. Møller[1], N. C. Schjødt[2], U. V. Mentzel[2], J. Sehested[2], R. Y. Brogaard[2], J. M. Christensen[1] and M. Høj[1*]

[1] Department of Chemical Engineering, Technical University of Denmark (DTU), Kgs. Lyngby, 2800 (Denmark).

[2] Topsoe A/S, Kgs. Lyngby, 2800 (Denmark).

[*]Corresponding author: mh@kt.dtu.dk

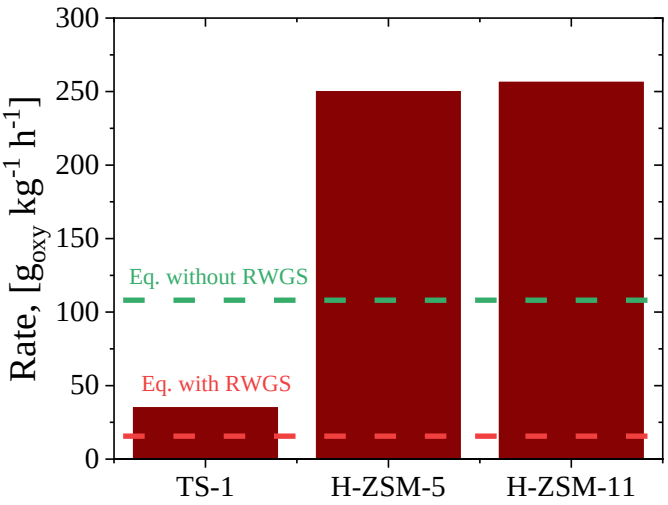


Fig. S1. The oxygenate formation rate for bifunctional catalyst compose of ZnO/t-ZrO_2 and zeolites. Green and red dashed lines represent the CO_2 hydrogenation to methanol equilibrium of no RWGS reaction occurs and if RWGS is in equilibrium. The oxygenate formation rate is based in the loaded amount of ZnO/t-ZrO_2. Reaction conditions: 30 bar, 340°C, 10 nL h^{-1}, feed composition CO_2/CO/H2/Ar of 24/4/64/3 vol% and catalyst loading of 2g with 80 wt% ZnO/t-ZrO_2.

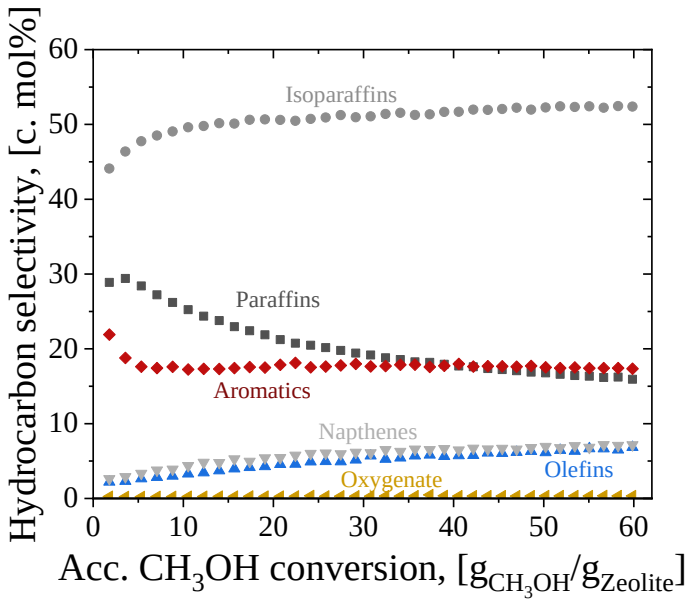


Fig. S2. Hydrocarbon (PIONA) selectivity with the accumulated (Acc.) amount of converted methanol pr. gram of zeolite. Reaction conditions: 30 bar, 340°C, 20 nL h^{-1}, feed composition $CO_2/CO/H_2/Ar$ of 24/4/64/3 vol% and catalyst loading of 4 g with 80 wt% ZnO/t-ZrO_2 and 20 wt% H-ZSM-5 (25).

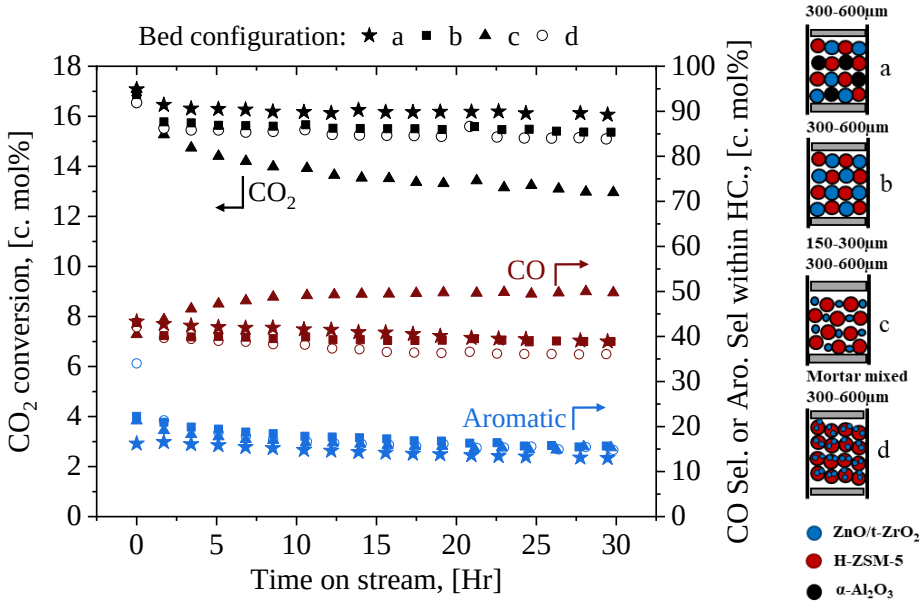


Fig. S3. CO_2 conversion, CO and Aromatic selectivity with time on stream mixed in different bed configurations. The bed configuration a to c consist of granulate mixing of ZnO/t-ZrO_2 where d consist of mortar mixed powders pressed as pellet and sieved to granulate. Reaction conditions: 30 bar, 340°C, 10 nL h^{-1}, feed composition $CO_2/CO/H_2/Ar$ of 24/4/64/3 vol% and catalyst loading of 2 g with 80 wt% ZnO/t-ZrO_2 and 20 wt% H-ZSM-5 (140).

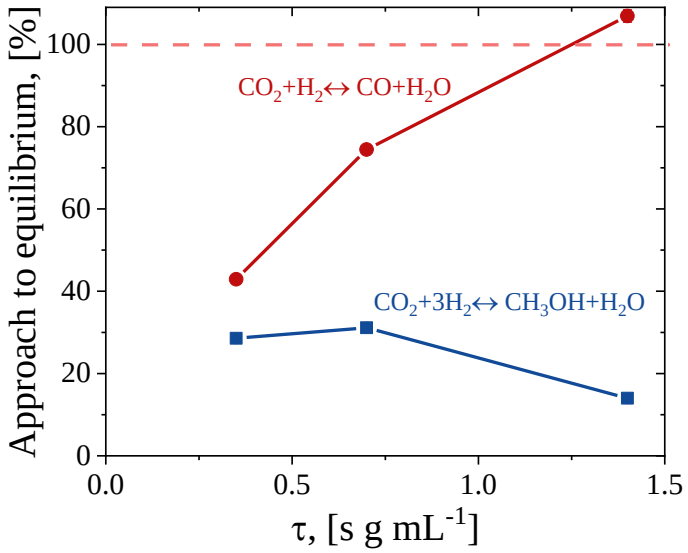


Fig. S4. The approach to equilibrium as a function of residence time over the bifunctional catalyst. Reaction conditions: 30 bar, 340ºC, 10 nL h^{-1}, feed composition $CO_2/CO/H_2/Ar$ 24/4/64/3 vol% and catalyst loading of 1, 2 or 4 g with 80 wt% ZnO/t-ZrO_2 mixed with H-ZSM-5(140).

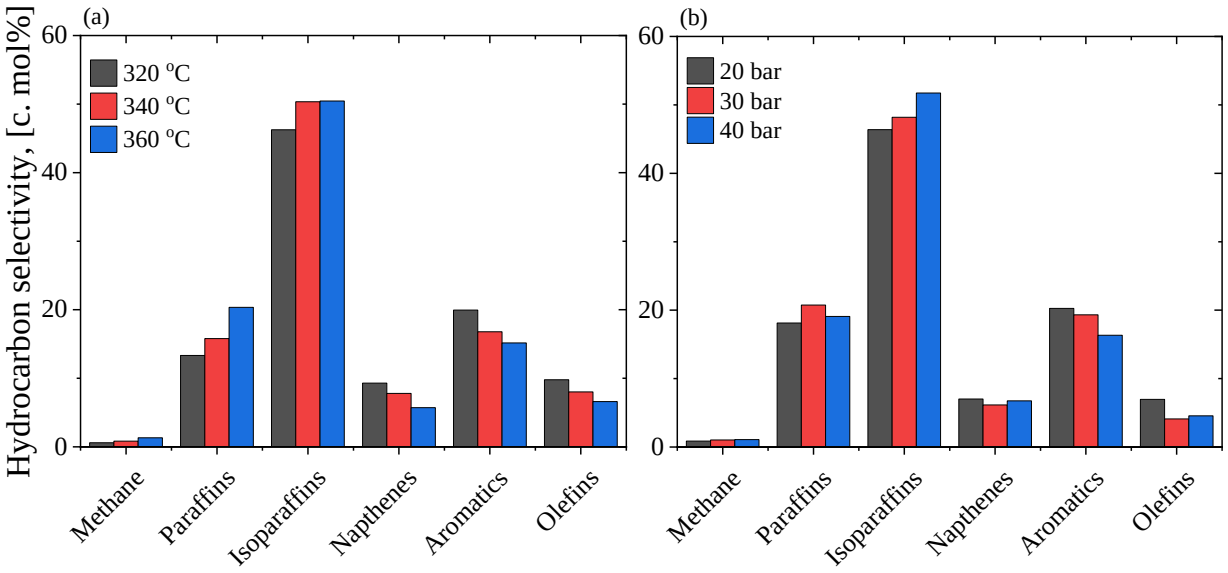


Fig. S5. The Hydrocarbon selectivity at different (a) temperatures and (b) pressure. Reaction conditions if not else are stated: 30 bar, 340ºC, 20 nL h^{-1}, feed composition $CO_2/CO/H_2/Ar$ of 24/4/64/3 vol% and catalyst loading of 4g with 80 wt% ZnO/t-ZrO_2 mixed with H-ZSM-5(40).

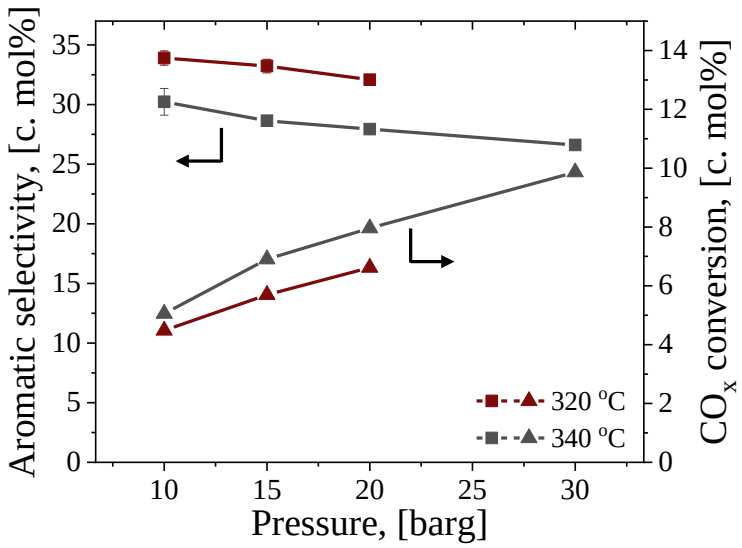


Fig. S6. Corrected initial aromatic selectivity (by correcting in aromatic selectivity by removing deactivation pattern with time on stream) and the CO_2 conversion to hydrocarbons (CO_x) at different temperatures and pressure. Reaction conditions: 20 nL h^{-1}, feed composition $CO_2/CO/H_2/Ar$ of 24/4/64/3 vol% and catalyst loading of 4g with 80 wt% ZnO/t-ZrO_2 mixed with H-ZSM-5(40).

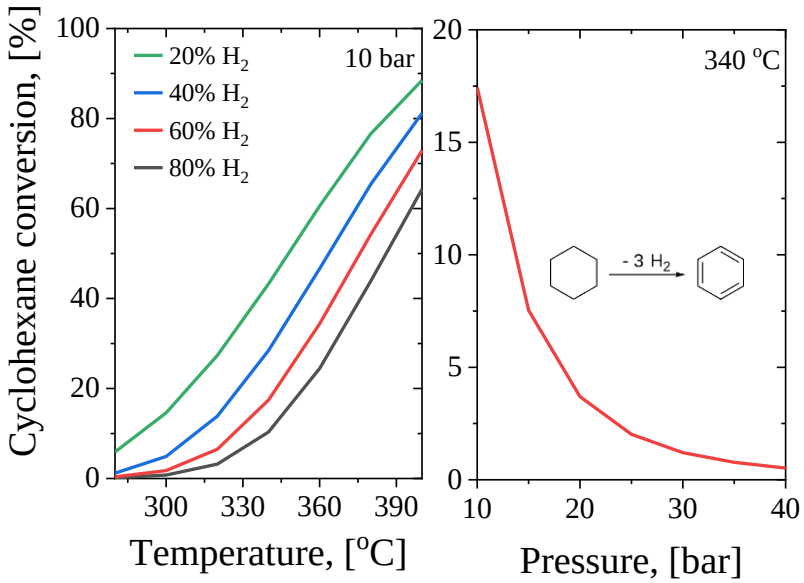


Fig. S7. Thermodynamic equilibrium conversion of cyclohexane to benzene at relevant bifunctional catalyst conditions.

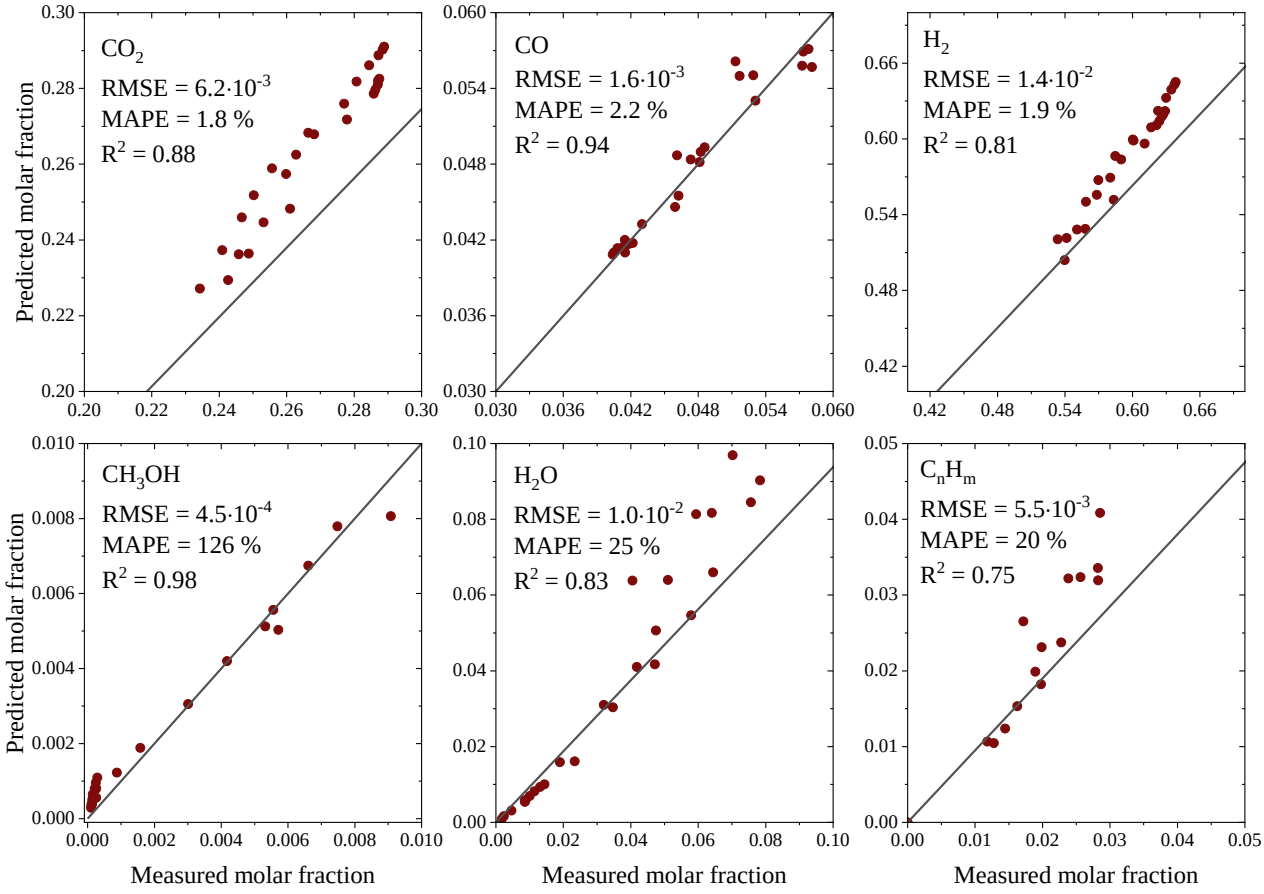


Fig. S8. Parity plots for the measured and predicted data.

Table S1. Data used for the parameter estimation.

	Reaction conditions						Outlet flow rates						Inlet molar fration					
Ex. no	T [K]	P [bar]	ZnO-ZrO2 [g]	Si/Al	H-ZSM-5 [g]	Vin [nL/h]	F CO mol/h	F CO_2 mol/h	F CH_3OH mol/h	F H_2 mol/h	F H_2O mol/h	F CH_3 mol/h	y CO	y CO_2	y CH_3OH	y H_2	y H_2O	y CH_3
1	513.00	50.85	0.76	1.00	0.00	31.2	5.62E-02	4.02E-01	1.22E-03	8.89E-01	2.46E-03	0.00E+00	4.07	29.18	64.71	0.06	0.00	0.00
2	533.00	50.85	0.76	1.00	0.00	31.2	5.64E-02	4.01E-01	2.19E-03	8.87E-01	3.36E-03	0.00E+00	4.07	29.18	64.71	0.06	0.00	0.00
3	553.00	50.85	0.76	1.00	0.00	31.2	5.68E-02	4.00E-01	4.19E-03	8.83E-01	6.47E-03	0.00E+00	4.07	29.18	64.71	0.06	0.00	0.00
4	573.00	50.85	0.76	1.00	0.00	31.2	5.77E-02	3.96E-01	7.95E-03	8.77E-01	1.20E-02	0.00E+00	4.07	29.18	64.71	0.06	0.00	0.00
5	573.00	51.01	1.25	1.00	0.00	50.1	9.27E-02	6.41E-01	1.19E-02	1.40E+00	1.98E-02	0.00E+00	3.97	28.79	63.47	0.06	0.00	0.00
6	573.00	51.01	1.25	1.00	0.00	31.1	5.85E-02	3.96E-01	1.04E-02	8.62E-01	1.82E-02	0.00E+00	3.97	28.79	63.47	0.06	0.00	0.00
7	573.00	41.01	1.25	1.00	0.00	31.1	5.80E-02	3.97E-01	9.16E-03	8.65E-01	1.59E-02	0.00E+00	3.97	28.79	63.47	0.06	0.00	0.00
8	573.00	31.01	1.25	1.00	0.00	31.1	5.76E-02	3.98E-01	7.71E-03	8.68E-01	1.39E-02	0.00E+00	3.97	28.79	63.47	0.06	0.00	0.00
9	573.00	21.01	1.25	1.00	0.00	31.1	5.72E-02	3.98E-01	5.78E-03	8.72E-01	1.19E-02	0.00E+00	3.97	28.79	63.47	0.06	0.00	0.00
10	593.00	50.85	0.76	1.00	0.00	31.2	5.98E-02	3.91E-01	1.26E-02	8.67E-01	2.01E-02	0.00E+00	4.07	29.18	64.71	0.06	0.00	0.00
11	613.00	50.85	0.76	1.00	0.00	31.2	6.44E-02	3.86E-01	1.53E-02	8.58E-01	2.64E-02	0.00E+00	4.07	29.18	64.71	0.06	0.00	0.00
12	613.00	51.02	1.25	1.00	0.00	50.1	1.03E-01	6.21E-01	2.68E-02	1.36E+00	5.22E-02	0.00E+00	3.97	28.79	63.47	0.06	0.00	0.00
13	593.13	11.01	1.60	40.00	0.40	10.4	2.24E-02	1.24E-01	5.42E-05	2.79E-01	1.61E-02	5.95E-03	3.91	28.82	64.10	0.00	0.00	0.00
14	593.15	16.01	1.60	40.00	0.40	10.3	2.22E-02	1.21E-01	6.51E-05	2.72E-01	1.93E-02	7.51E-03	3.91	28.82	64.10	0.00	0.00	0.00
15	593.16	21.01	1.60	40.00	0.40	10.2	2.21E-02	1.18E-01	6.85E-05	2.63E-01	2.15E-02	8.60E-03	3.91	28.82	64.10	0.00	0.00	0.00
16	613.14	11.01	1.60	40.00	0.40	10.2	2.60E-02	1.16E-01	4.65E-05	2.66E-01	2.15E-02	6.58E-03	3.91	28.82	64.10	0.00	0.00	0.00
17	613.12	16.00	1.60	40.00	0.40	10.0	2.55E-02	1.11E-01	5.77E-05	2.54E-01	2.58E-02	8.81E-03	3.91	28.82	64.10	0.00	0.00	0.00
18	613.15	21.01	1.60	40.00	0.40	9.8	2.53E-02	1.08E-01	7.24E-05	2.45E-01	2.82E-02	9.98E-03	3.91	28.82	64.10	0.00	0.00	0.00
19	613.16	31.01	1.60	40.00	0.40	9.7	2.51E-02	1.04E-01	1.01E-04	2.34E-01	3.27E-02	1.22E-02	3.91	28.82	64.10	0.00	0.00	0.00
19	593.16	11.01	1.60	40.00	0.40	10.1	2.14E-02	1.21E-01	5.74E-05	2.72E-01	1.45E-02	5.36E-03	3.91	28.82	64.10	0.00	0.00	0.00
20	613.20	31.01	3.21	40.00	0.80	20.9	4.94E-02	2.29E-01	2.01E-04	5.14E-01	5.98E-02	2.39E-02	3.89	28.55	64.38	0.00	0.00	0.00
21	613.15	21.01	3.21	40.00	0.80	21.0	4.82E-02	2.38E-01	1.82E-04	5.33E-01	4.79E-02	1.86E-02	3.89	28.55	64.38	0.00	0.00	0.00
22	613.14	41.01	3.21	40.00	0.80	20.8	4.94E-02	2.26E-01	2.73E-04	5.02E-01	6.53E-02	2.65E-02	3.89	28.55	64.38	0.00	0.00	0.00
23	633.16	31.01	3.21	40.00	0.80	21.0	5.78E-02	2.19E-01	2.41E-04	4.99E-01	7.32E-02	2.64E-02	3.89	28.55	64.38	0.00	0.00	0.00
24	593.10	31.01	3.21	40.00	0.80	21.3	4.38E-02	2.48E-01	2.30E-04	5.54E-01	3.85E-02	1.63E-02	3.89	28.55	64.38	0.00	0.00	0.00
25	613.18	31.01	3.21	40.00	0.80	21.1	4.86E-02	2.34E-01	2.40E-04	5.25E-01	5.59E-02	2.24E-02	3.89	28.55	64.38	0.00	0.00	0.00

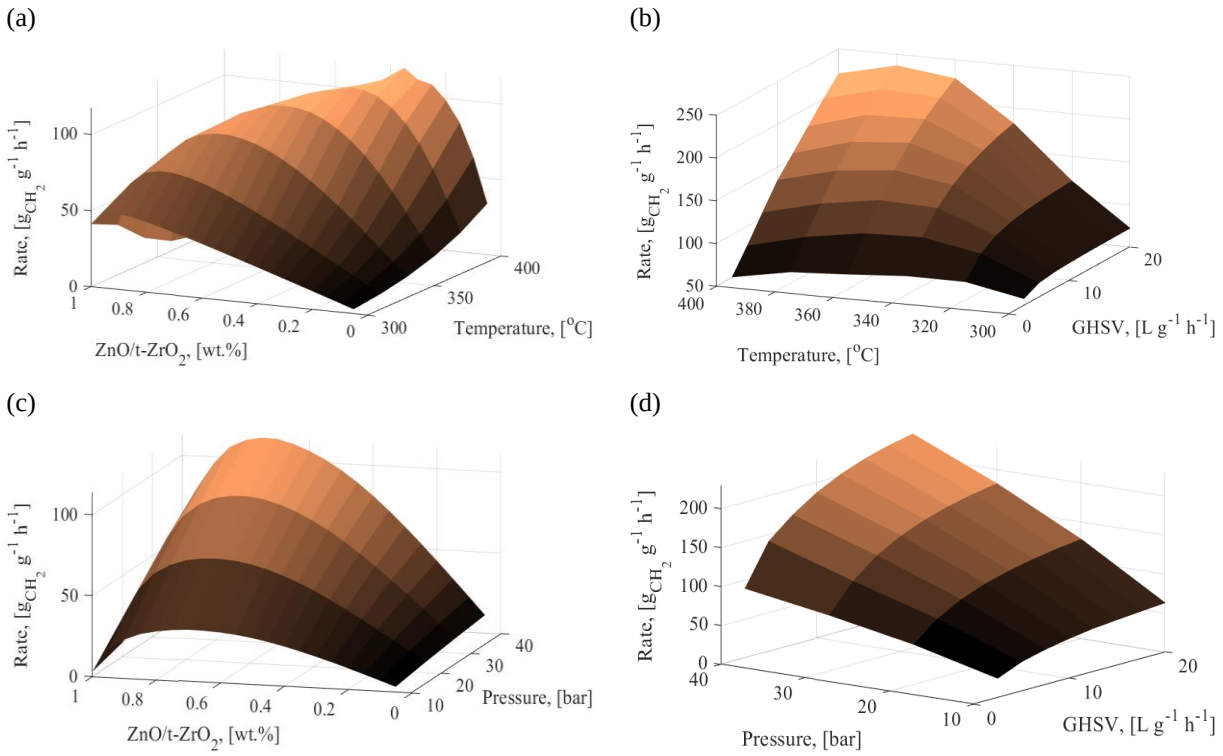


Fig. S9. The hydrocarbon formation rate (a) as a function of temperature and pressure, and (b) as a function of weight percentage of ZnO/t-ZrO_2 in the catalyst mixture and GHSV. Reaction conditions if not else stated: 30 bar, 340°C, 10 nL h^{-1}, feed composition CO_2/CO/H_2/Ar of 24/4/64/3 vol% and catalyst loading of 2g with 80 wt% ZnO/t-ZrO_2.

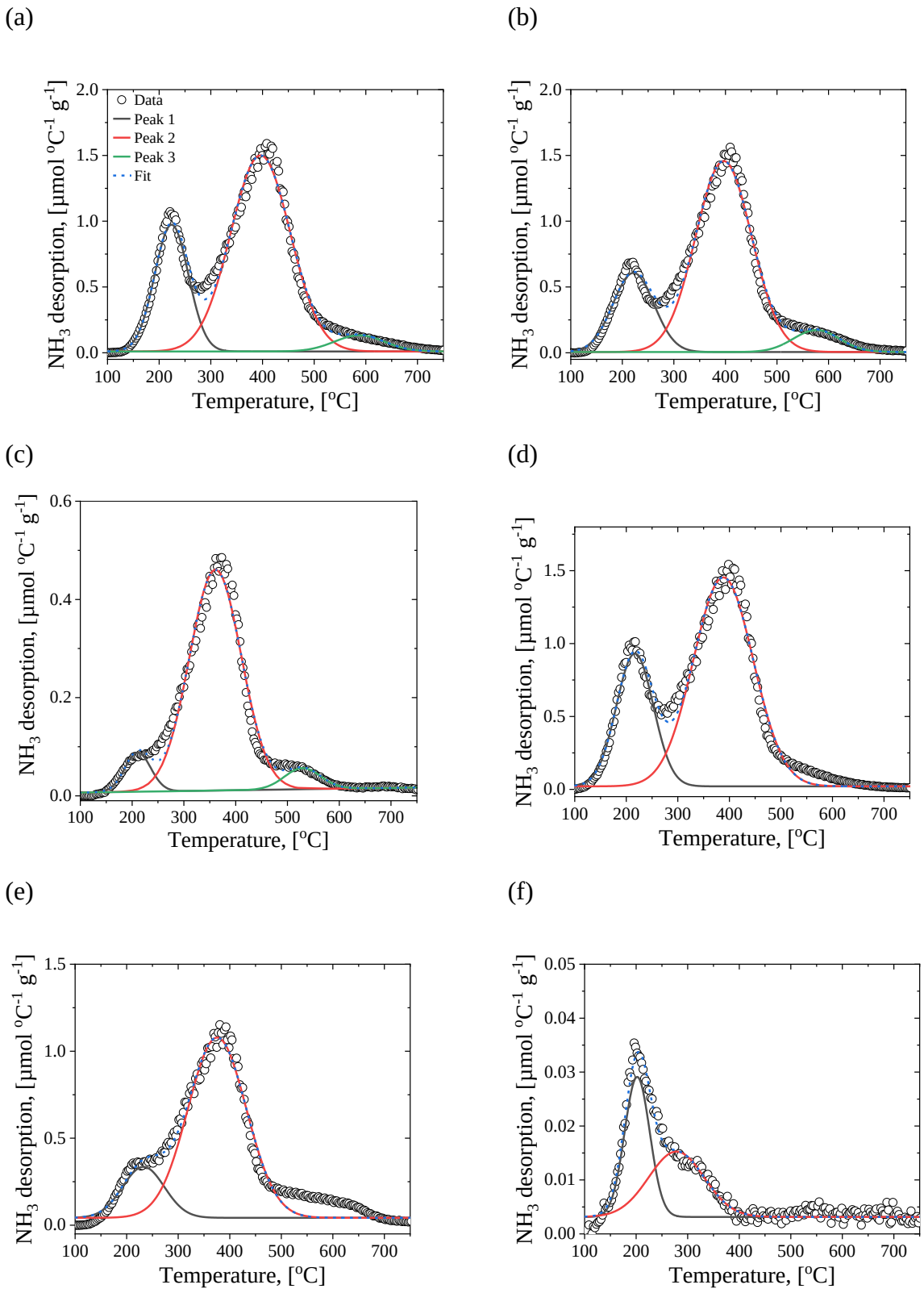


Fig. S10. NH_3 desorption rate against the temperature from the NH_3-TPD (a) ZSM-5 (25), (b) ZSM-5 (40), (c) ZSM-5 (140), (d) ZSM-11, (e) ZSM-12 and (f) TS-1.

9.3 Supporting information: ZnO supported on Zinc Spinel Structures Enables the Direct Conversion of CO2 to Olefins when Combined with Acidic CHA Catalysts

Supporting Information: ZnO supported on Zinc Spinel Structures Enables the Direct Conversion of CO_2 to Olefins when Combined with Acidic CHA Catalysts

M. T. Nikolajsen[1], K. Jordahn[1], L. D. Nilsson[1], N. C. Schjødt[2], U. V. Mentzel[2], J. Sehested[2], R. Y. Brogaard[2], J. M. Christensen[1] and M. Høj[1*]

[1] Department of Chemical Engineering, Technical University of Denmark (DTU), Kgs. Lyngby, 2800 (Denmark).

[2] Topsoe A/S, Kgs. Lyngby, 2800 (Denmark).

[*]Corresponding author: mh@kt.dtu.dk

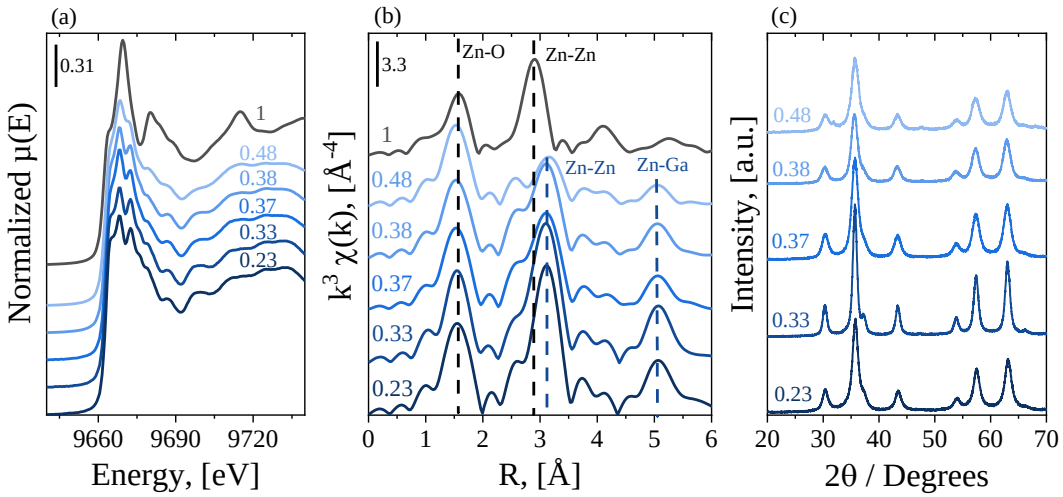


Fig. S1. (a) Zn K-edge XANES and (b) Fourier-transformed k^3-weighted EXAFS spectra, $ZnGa_2O_4$ catalysts with varying Zn loadings. (c) The XRD pattern of the as prepared $ZnGa_2O_4$ catalyst with different Zn loading from 0.23 to 0.48 mol fraction (1 for pure ZnO).The contribution of the $ZnGa_2O_4$ and ZnO phases on the EXAFS spectra were identified by EXAFS fitting with the ICSD 81108 and ICSD 57450 standard, respectively.

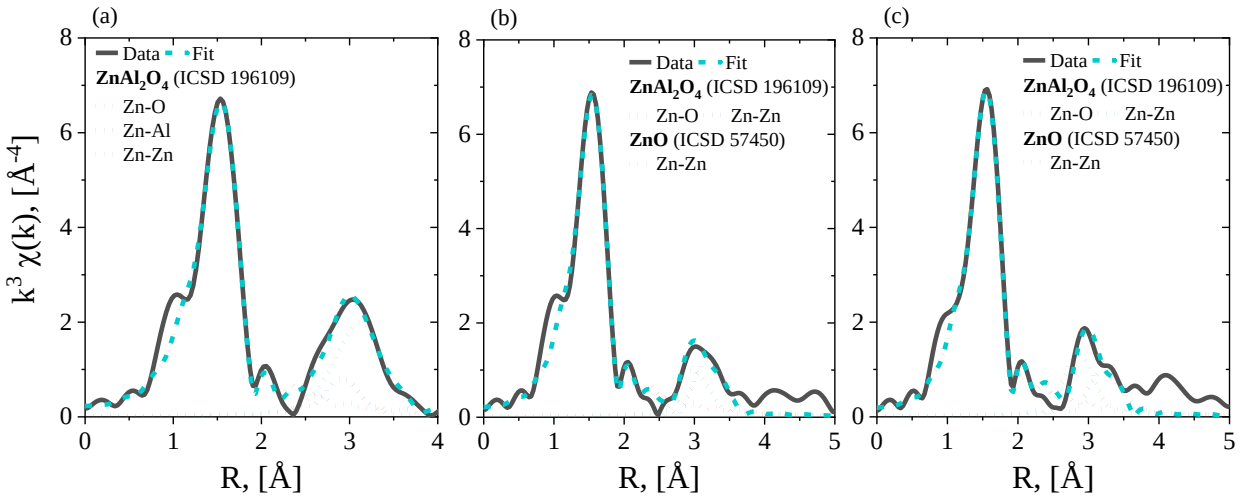


Fig. S2. The contribution of the $ZnAl_2O_4$ and ZnO phases on the EXAFS spectra with 1st and 2nd shell EXAFS fitting of (a) (0.32)$ZnAl_2O_4$, (b) (0.39)$ZnAl_2O_4$, and (0.51)$ZnAl_2O_4$ with the ICSF 196109 and ICSD 57450 standard, respectively.

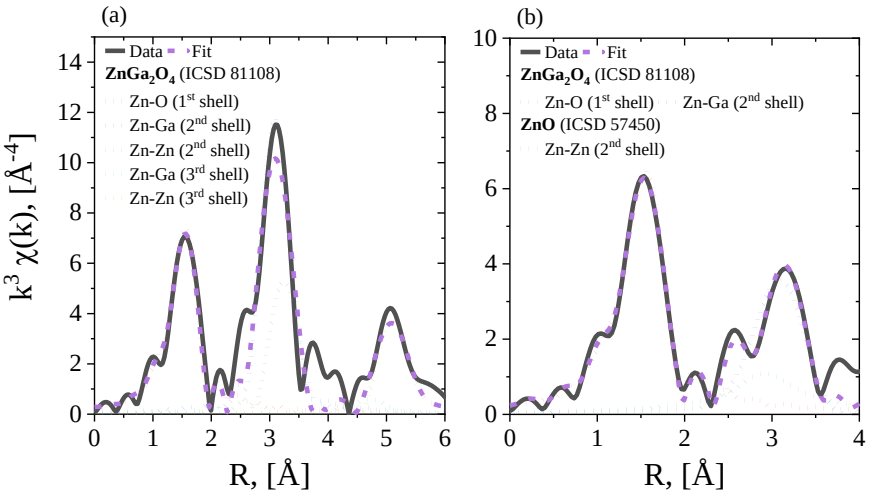
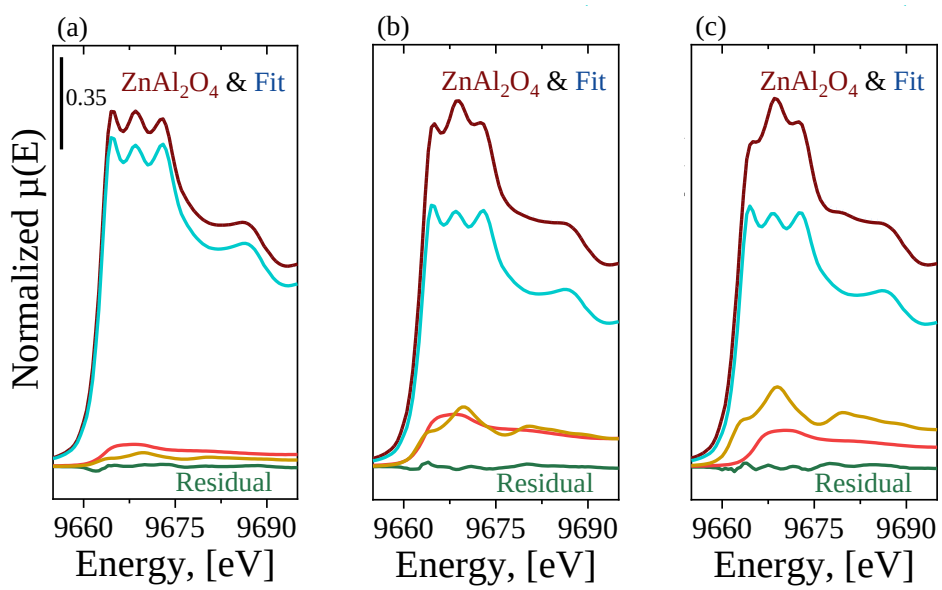
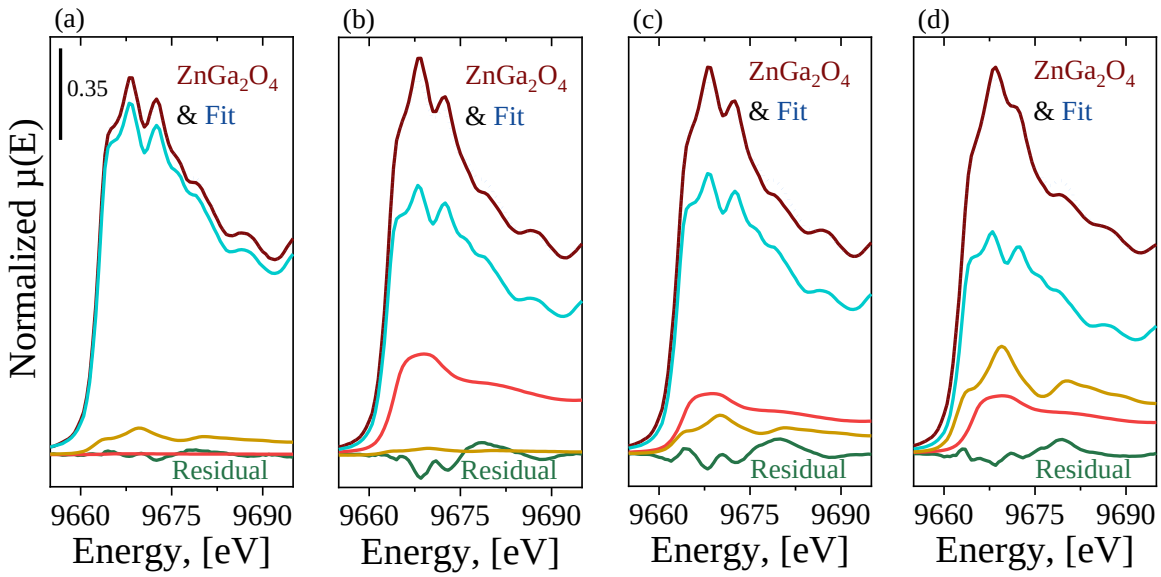


Fig. S3. The contribution of the $ZnGa_2O_4$ and ZnO phases on the EXAFS spectra with 1st and 2nd shell EXAFS fitting of (a) (0.23)$ZnGa_2O_4$ and (0.48)$ZnGa_2O_4$ with the ICSD 81108 and ICSD 57450 standard, respectively.



References: ZnO, (0.31)$ZnAl_2O_4$ and (0.14)ZnO/t-ZrO_2

Fig. S4. Linear combination fitting of Zn K-edge XANES of the (a) (0.32)$ZnAl_2O_4$, (b) (0.39)$ZnAl_2O_4$, and (0.51)$ZnAl_2O_4$ using the references ZnO, (0.31)$ZnAl_2O_4$ and (0.14)ZnO/t-ZrO_2.



References: ZnO, (0.23)$ZnGa_2O_4$ and (0.14)ZnO/t-ZrO_2

Fig. S5. Linear combination fitting of Zn K-edge XANES of the (a) (0.33)$ZnGa_2O_4$, (b) (0.37)$ZnGa_2O_4$, (c) (0.38)$ZnGa_2O_4$, and (0.48)$ZnGa_2O_4$ using the references ZnO, (0.23)$ZnGa_2O_4$ and (0.14)ZnO/t-ZrO_2.

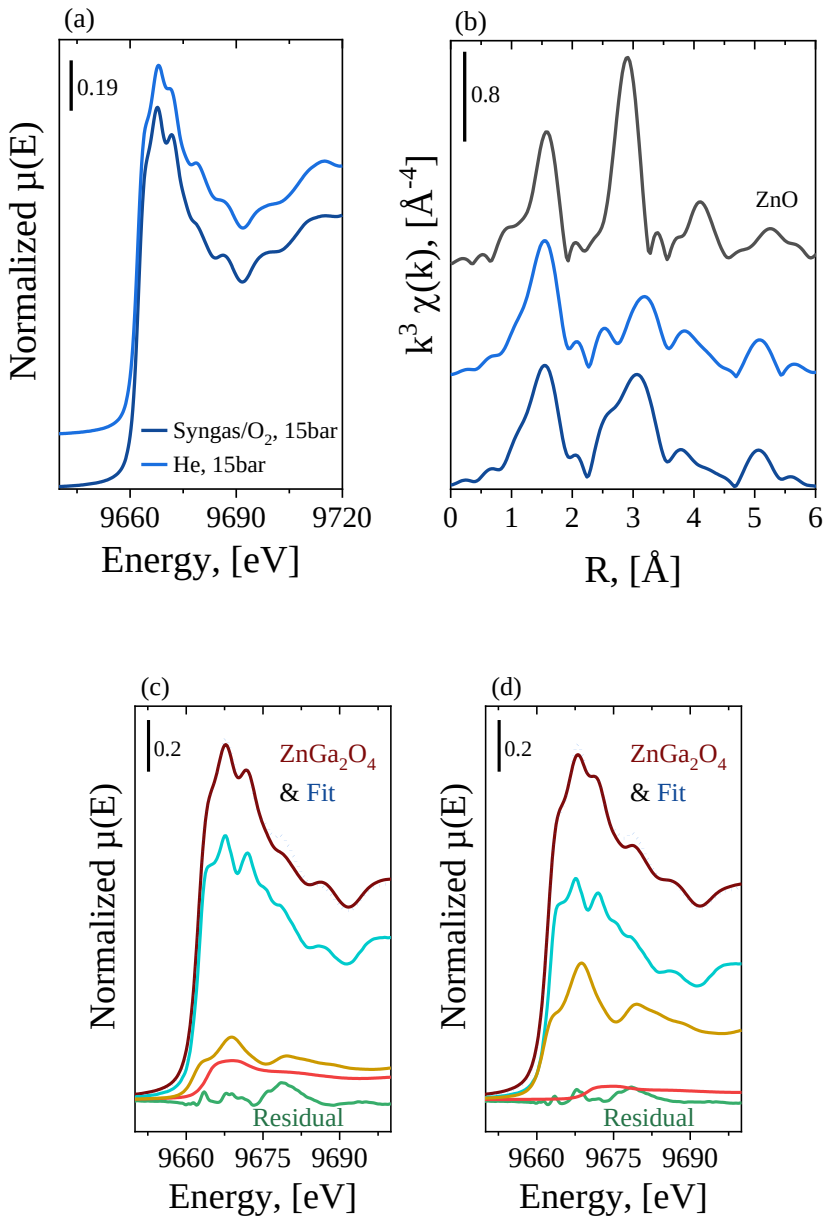


Fig. S6. (a) Zn K-edge XANES and (b) the Fourier-transformed k^3-weighted EXAFS spectra of the (0.37) $ZnGa_2O_4$ obtained at room temperature after the dehydration step and periodic switching between the syngas and O_2 through 18 switches. Linear combination fitting of Zn K-edge XANES of the (c) after dehydration, (d) after the switching between syngas and O_2, (c) using the references ZnO, (0.23)$ZnGa_2O_4$ and (0.14)ZnO/t-ZrO_2. Reaction conditions: 400 °C, 15 barg, 50 NmL/h, catalyst loading of ~2.5 mg (diluted 1:8 in inert α-Al_2O_3), feed gas composition of CO_2/CO/H_2/He 12/5/37/46 or O_2/He of 10/90.

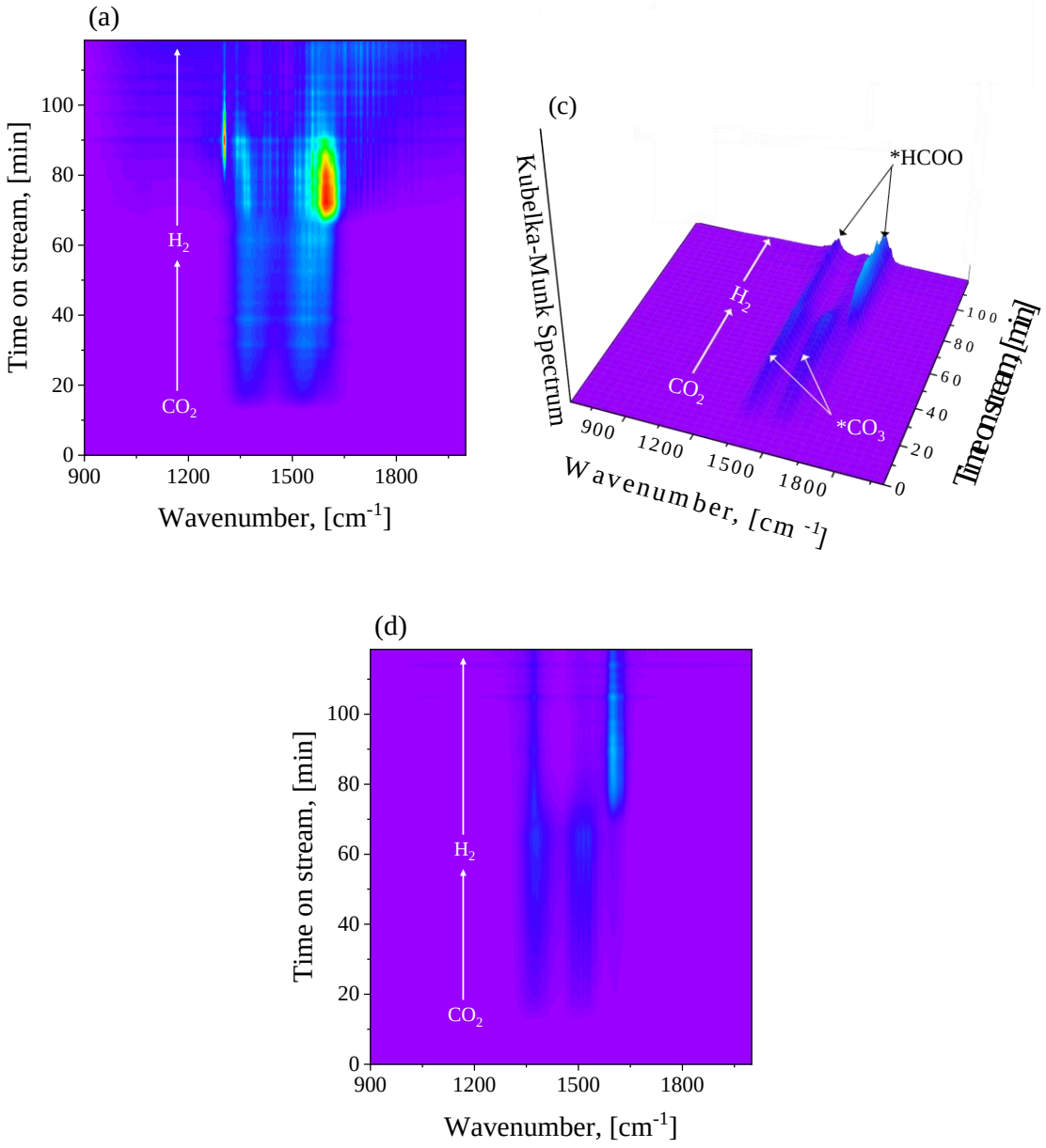


Fig. S7. (a) Contour plot for the In-situ DRIFTS measurements for CO_2 adsorption followed by H_2 treatment on (0.39)$ZnAl_2O_4$ at 20 bar and 320 °C. (b-c) In-situ DRIFTS measurements for CO_2 adsorption followed by H_2 treatment on (0.39)$ZnAl_2O_4$ at 20 bar and 260 °C.

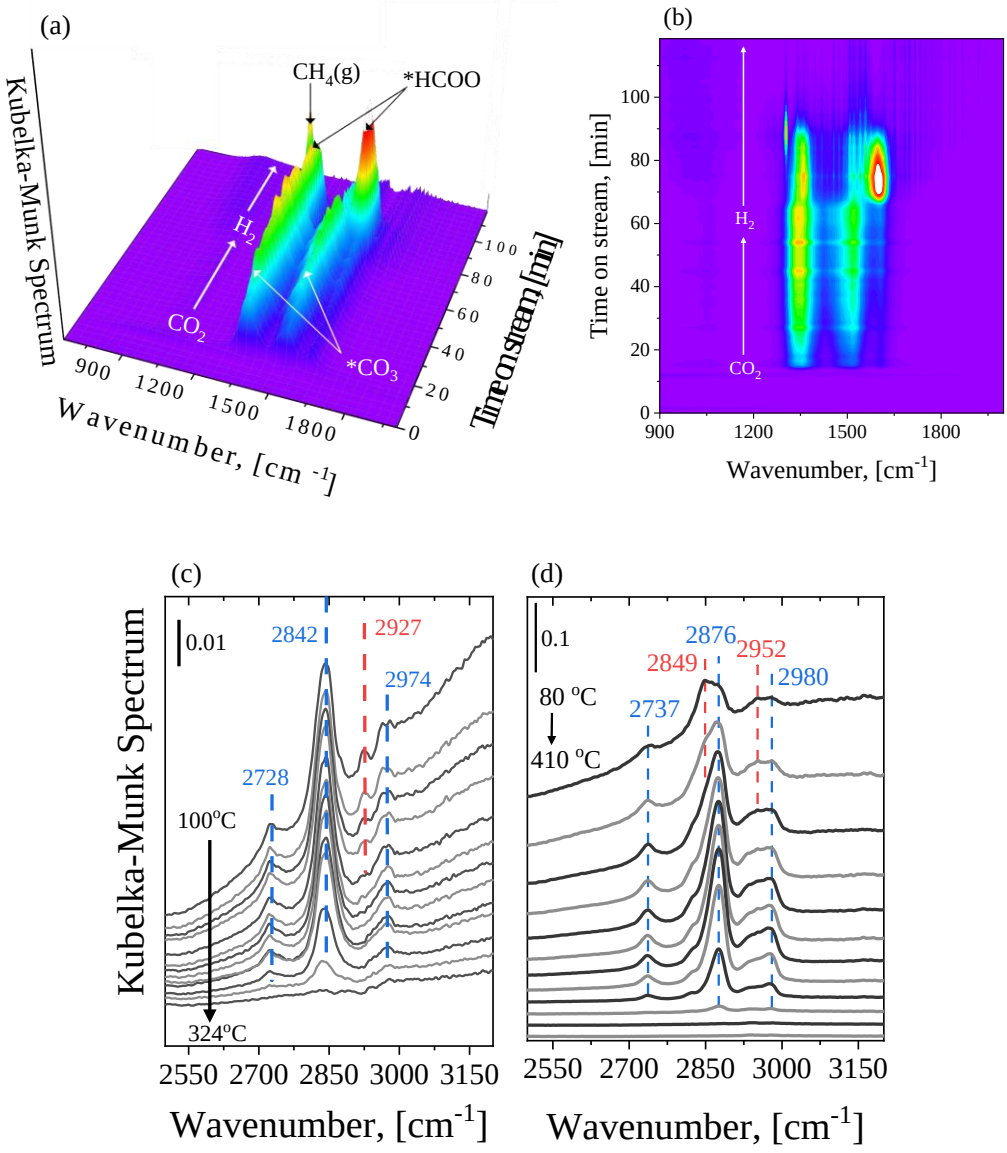


Fig. S8. (a-b) In-situ DRIFTS measurements for CO_2 adsorption followed by H_2 treatment on (0.37)$ZnGa_2O_4$ at 20 bar and 340 °C. TPD in He at 1 bar after steady-state methanol formation at 320 °C and 20 bar for (c) (0.37)$ZnGa_2O_4$ and (b) ZnO/t-ZrO_2. Blue numbers are peaks dedicated to formate and red numbers are peaks dedicated to methoxy.

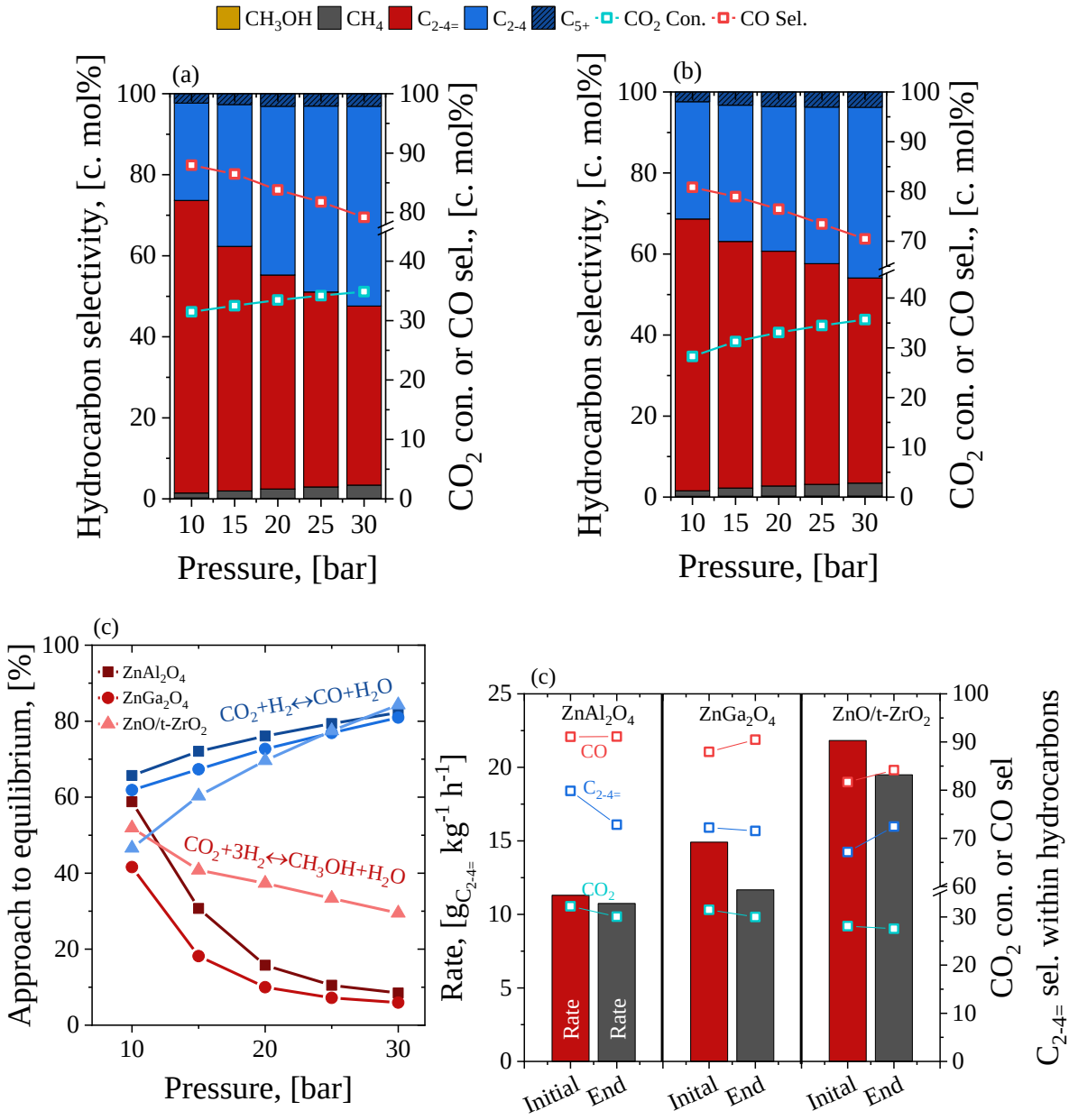


Fig. S9. The CO_2 conversion (con.), CO selectivity (sel.), and the hydrocarbon selectivity for different pressures over (a) $ZnGa_2O_4$+H-SAPO-34 and (b) ZnO/t-ZrO_2+H-SAPO-34. (c) The approach to equilibrium for the reverse-water-gas-shift and the methanol synthesis reaction with the change in Pressure. (d) The initial and spent (after the pressure experiment) light olefin formation rate, CO_2 conversion, CO and light olefin selectivity for the $ZnAl_2O_4$+H-SAPO-34, $ZnGa_2O_4$+H-SAPO-34, and ZnO/t-ZrO_2+H-SAPO-34 bi-functional catalysts. Reaction conditions: 400 °C, 10 bar (unless else stated), 2.5 NL/h and catalyst loading of 500 mg.

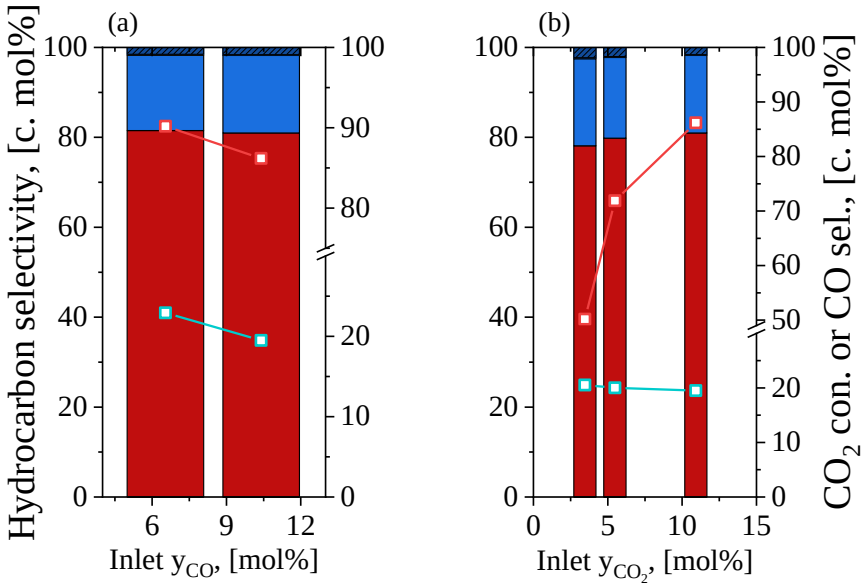


Fig. S10. The CO_2 conversion, CO selectivity and hydrocarbon selectivity with change in the inlet concentration of (a) CO at constant CO_2 concentration and (b) CO_2 at constant CO concentration. Reaction conditions: 380 °C, 10 bar, 3.5 NL/h and catalyst loading of 700 mg

Table S1. The Si/Al/P/Zn weight percentages and weak and strong acid densities for the zeolite samples.

Catalysts	**Si/Al/P/Zn [a] [wt%]**	**Weak acid sites[b], [µmol g^{-1}]**	**Strong acid sites[b], [µmol g^{-1}]**	**Total acid sites[b], [µmol g^{-1}]**
H-SAPO-34	40.4/10.1/49.5/0	98 ± 9.8	418 ± 4.5	516
Zn-SAPO-34	40.7/10.1/47.7/1.5	38 ± 2.3	365 ± 2.7	403

[a]determined by XRF, [b]determined by NH_3-TPD.

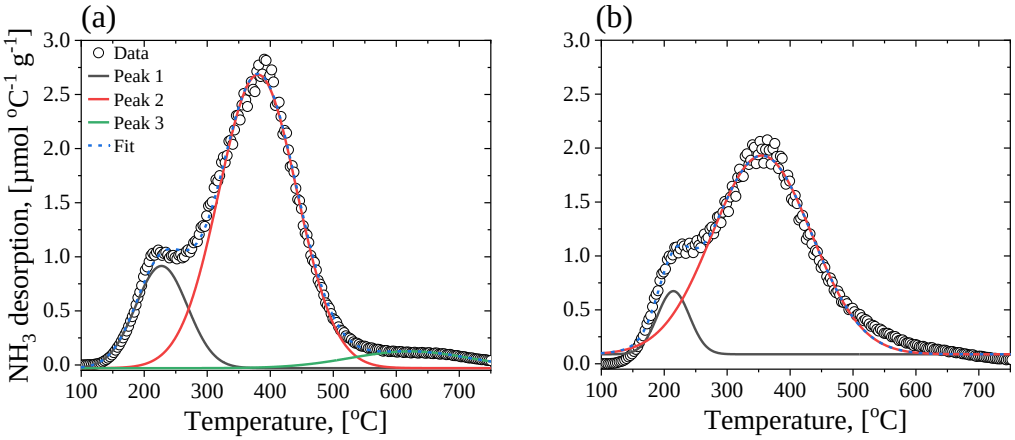


Fig. S11. NH_3 desorption rate against the temperature from the NH_3-TPD (a) SAPO-34 and (b) Zn-SAPO-34.

9.4 Supporting information: Deactivation Phenomena for Bi-functional Catalysts Composed of ZnO/ZrO2 and CHA Topology Solid Acid

Supporting Information: Deactivation Phenomena for Bi-functional Catalysts Composed of ZnO/ZrO_2 and CHA Topology Solid Acid

M. T. Nikolajsen[1], N. C. Schjødt[2], U. V. Mentzel[2], J. Sehested[2], R. Y. Brogaard[2], J. M. Christensen[1] and M. Høj[1*]

[1] Department of Chemical Engineering, Technical University of Denmark (DTU), Kgs. Lyngby, 2800 (Denmark).

[2] Topsoe A/S, Kgs. Lyngby, 2800 (Denmark).

[*]Corresponding author: mh@kt.dtu.dk

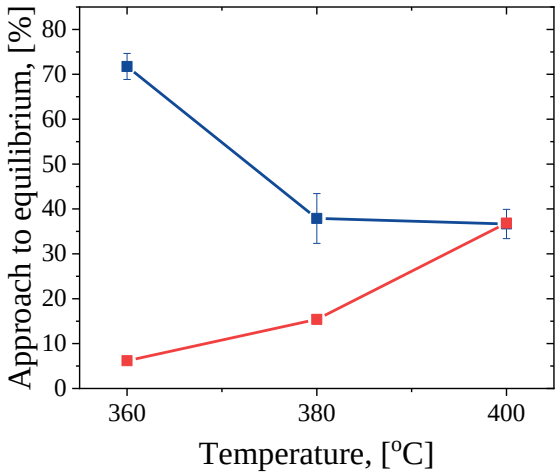


Fig. S1. The approach to equilibrium at different temperatures over ZnO/t-ZrO_2+H-SAPO-34. Reaction conditions: 400 °C, 2.5 NL/h, metal oxide:zeolite mixing mass ratio 4:1 and catalyst loading of 500 mg.

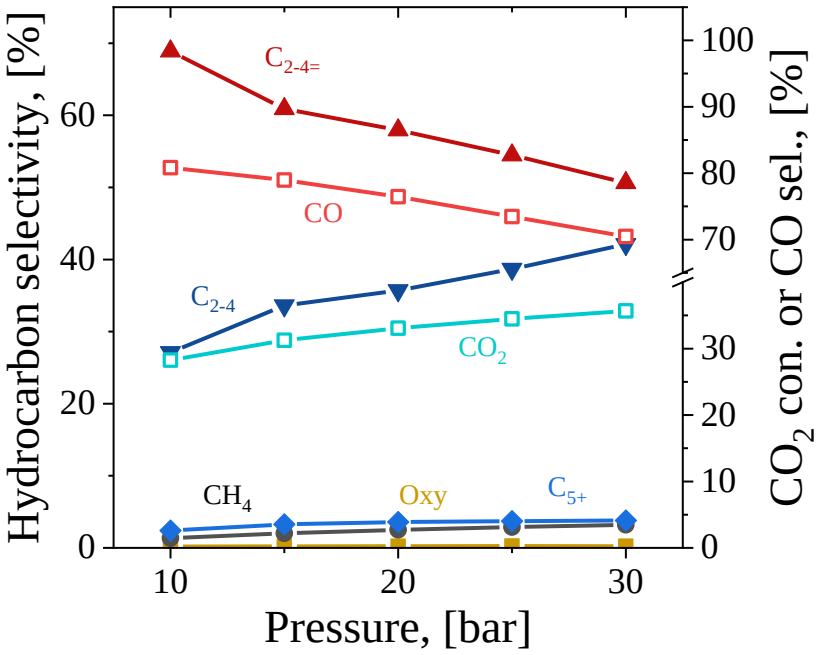


Fig. S2. The CO_2 conversion (con.), CO selectivity (sel.), and the hydrocarbon selectivities for different pressures over ZnO/t-ZrO_2+H-SAPO-34. Reaction conditions: 400 °C, 2.5 NL/h, metal oxide:zeolite mixing mass ratio 4:1 and catalyst loading of 500 mg.

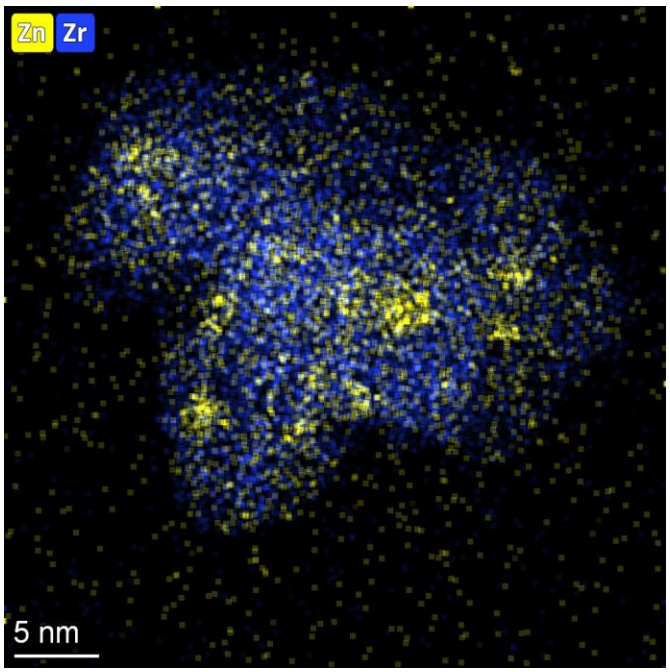


Fig. S3. TEM-EDX element map of Zn, Zr and Al of the ZnO/t-ZrO_2 component of the spent bi-functional catalyst.

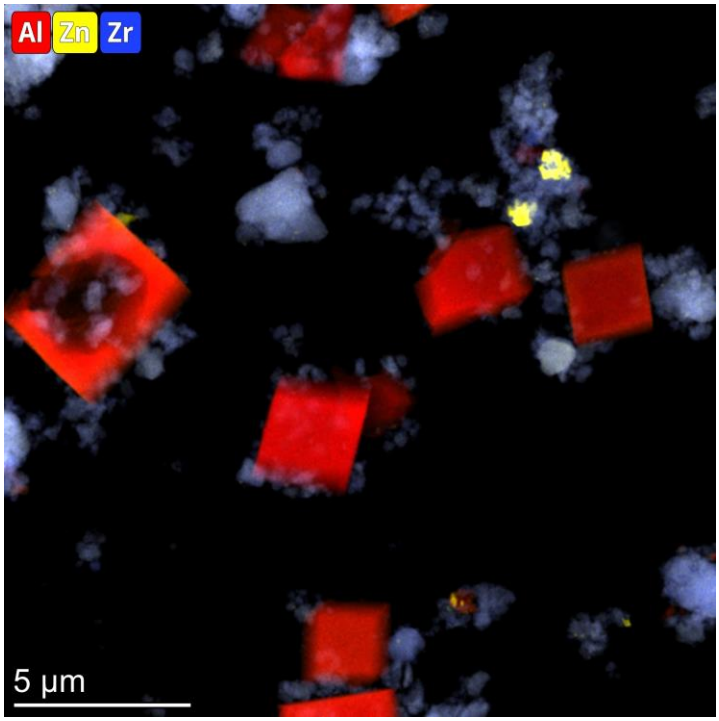


Fig. S4. TEM.-EDX element map of Zn, Zr and Al for the regenerated bi-functional catalyst.

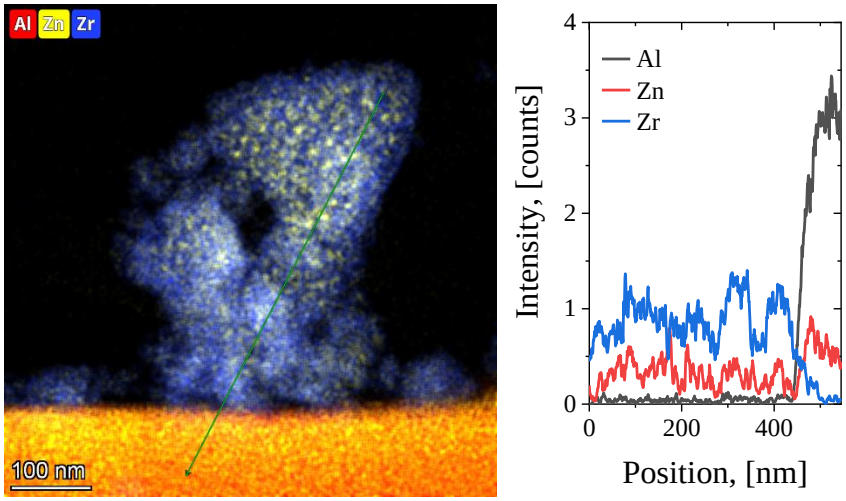


Fig. S5. TEM.-EDX element map of Zn, Zr and Al for the spent bi-functional catalyst and the element intensity profile through the path highlighted with the green arrow.